Coherent beam combining of high-brightness tapered semiconductor optical amplifiers

Philipp Albrodt

université
PARIS-SACLAY

Coherent beam combining of high brightness tapered semiconductor optical amplifiers

Thèse de doctorat de l'université Paris-Saclay

École doctorale n°572: ondes et matières (EDOM)
Spécialité de doctorat: Physique

Unité de recherche: Université Paris-Saclay, Institut d'Optique Graduate School, CNRS, Laboratoire Charles Fabry, 91127, Palaiseau, France.
Référent: Institut d'Optique

Thèse présentée et soutenue à Palaiseau, le 17/01/2020, par

Philipp ALBRODT

Composition du Jury

Philippe LECOEUR Directeur de Recherche, Université Paris-Saclay (C2N)	Président
Agnès DESFARGES-BERTHELEMOT Professeure des Universités, Université de Limoges (XLIM)	Rapporteuse
Mircea GUINA Professor, Tampere University (Optoelectronics Research Centre)	Rapporteur
Bernd SUMPF Privatdozent, Technische Universität Berlin Ferdinand-Braun-Institut, Leibniz-Institut für Höchstfrequenztechnik	Examinateur
Patrick GEORGES Directeur de Recherche, Université Paris-Saclay (LCF)	Directeur de thèse
Gaëlle LUCAS-LECLIN Maîtresse de conférences, Université Paris-Saclay (LCF)	Co-encadrante
Paul CRUMP Ferdinand-Braun-Institut, Leibniz-Institut für Höchstfrequenztechnik	Invité

Contents

Acknowledgments

Thank You!

I am grateful to all members of the Jury for having accepted to review my manuscript and for their participation at my PhD-defense.

I would like to thank Paul Crump for his extensive support during the last three years. This work would not have been possible without your important contribution. It has been a pleasure to work in a close collaboration with the FBH. In particular, I would like to thank Markus Niemeyer, Jonathan Decker and Martin Winterfeldt for their support and advice.

I want to thank our colleagues at DTU Fotonik (Ole Bjarlin Jensen, Anders Kragh Hansen and Muhammad Tahir Jamal) for their contribution to joined experiments and the corresponding publications. I am also grateful to Erik Larkins for many fruitful discussions and for supporting our work with important numerical simulations.

Merci!

Je remercie Frédéric Moron, Marc Apfel, Mondher Besbes et Jean-René Ruiller pour leur soutien important concernant le travail au niveau de l'électronique, de la mécanique et des modélisations numériques. Je tiens aussi à remercier l'équipe pédagogique avec laquelle j'ai interagi pendant mon monitorat.

Mes plus sincères remerciements vont à toute l'équipe du groupe Lasers du laboratoire Charles Fabry. Vous avez fait de ces trois années de thèse une expérience scientifique et humaine inoubliable. Je remercie Patrick pour sa sympathie, son soutien et pour les nombreuses discussions scientifiques. Je remercie Gaëlle pour son encadrement, son soutien et surtout pour avoir été de bonne humeur quasiment tous les jours. Merci à Marc pour quelques discussions scientifiques et un très grand nombre de discussions absolument non-scientifiques! Merci à Xavier pour m'avoir accueilli en tant que stagiaire il y a plus de quatre ans. Depuis nous avons fait de nombreux kilomètres ensemble - non seulement sur le plateau de Saclay en courant à midi, mais aussi dans Paris le soir. Je tiens aussi à remercier Fred, François et Sylvie qui complètent les membres permanents du groupe laser. J'ai beaucoup apprécié la bonne ambiance dans le groupe laser et c'est grâce à tous les membres permanents!

Merci à Michele pour tous les moments partagés pendant les nombreuses pauses café ou apéros afterwork. Tu as toujours été un moteur de motivation important au sein du groupe des doctorants. Je remercie Gaëtan, mon co-bureau, pour des nombreuses rigolades quand la porte de notre bureau était fermé (ou pas. . . .) et pour m'avoir appris des nombreuses expressions françaises. Merci à Pierre pour des nombreuses sorties en courant. Merci à Florent pour son sens d'humour exceptionnel!

J'ai eu la chance d'avoir pu travailler avec deux stagiaires exceptionnels, Jonas et Hector. Vous avez contribué une partie très importante dans la salle de manip. Je vous remercie je vous souhaite bonne chance pour la suite. Je remercie également tous les autres doctorants et doctorantes (Nour, Thomas, Tiphaine, Hussein) et je vous souhaite le meilleur pour votre fin de thèse.

Finalement je tiens à remercier chaleureusement tous les membres anciens du groupe laser (Loïc, Philippe, Guillaume, Paul, Romain, Anna, Igor, Kevin, Adrien , Julien . . .) en particulier je remercie Fabien Lesparre, avec lequel j'ai partagé mon bureau pendant un bon moment.

Danke!

Vielen Dank an meine Freunde aus Schul- und Studienzeiten aus Stuttgart und Umgebung. Viele von euch haben mich in Frankreich besucht und das waren immer besonders schöne Momente.

Ich bedanke mich von ganzem Herzen bei meinen Eltern und meinen lieben Geschwistern für die grenzenlose Unterstützung während meiner Zeit in Paris und während meines gesamten Studiums.

Vielen Dank liebe Franziska für viele besonders schöne Momente in Paris. Ich bin sehr froh, dass wir uns hier kennengelernt haben.

Introduction

The German language, my mother-tongue, is known for its compound nouns that are often hard to pronounce and hard to understand. The idiomatic German expression, "*eierlegende Wollmilchsau*" (literally "*egg-laying and milk-giving wool-pig*"), is only one colorful example and fortunately comparably graspable. It is used as a synonym for an extremely versatile all-in-one device having only advantages, which can replace several other devices easily. At the same time, it has however a certain latent ambiguity for something being obviously utopian and too good to be true. This said, the question arises whether there is a link between this idiomatic expression and the topic of this manuscript?

Lasers in general have become an incredibly useful and versatile tool not only for specific scientific purposes but also for countless applications that have changed our everyday life. Semiconductor lasers are, among the different sources of laser radiation, the most versatile as their spectral properties can be specifically designed. Furthermore, they can be produced in large quantities and are unbeatable in terms of compactness. In addition to that, they are also the most efficient sources of coherent laser light. The current state of the art of semiconductor laser-technology may be already somewhat close to the idea of the "eierlegende Wollmilchsau" in the perspective of a German-speaking Physicist in the early 1960s, at the advent of laser technology. But from today's perspective, it is clear that there are still many opportunities for the improvement of semiconductor laser systems, one of them being the increase in optical output power and brightness.

The optical output power of semiconductor laser emitters has significantly increased over the last two decades and still continues to increase, but is in the long run limited by material damage thresholds. That is the reason why high power semiconductor laser systems consist of multiple emitters that are combined into one laser beam in order to reach the targeted power level. Power is however not the only relevant parameter as other physical properties, such as spatial and spectral quality of the laser beam, are also important. Most applications of high power lasers require a specific wavelength. The optical power and the spatial properties determine together the brightness of a laser beam. A laser is particular bright if the optical power remains concentrated in a small surface area over a large propagation distance.

Approaches to increase the power of a laser system by beam combining methods can be classified in incoherent and coherent beam combining. Today's high power semiconductor laser systems rely on incoherent beam combining, where the optical powers from several beams are added by incoherent side-by-side addition, polarization coupling or spectral beam combining. On the one hand these approaches allows straightforward scaling of the optical output power, on the other hand these approach degrade spatial and/or spectral properties of the laser beam. As a result, incoherent beam combining methods are not infinitely scalable, as the resulting large optical spectrum or low brightness of the final beam may no longer meet the requirements for certain demanding applications. In contrast to that, coherent beam combining relies on the constructive interference of several coherent electromagnetic fields and allows to increase the total optical power while spatial and spectral properties of the laser light are maintained. It allows even to suppress imperfections of the individual emitters, such as depolarized light or un-wanted stray-light around the main laser beam. Coherent beam combining is on paper an ideal approach to scale the output power and brightness of laser sources in order to get another step closer to the idea of the perfect all-in-one laser source.

Although coherent beam combining has been demonstrated in many configurations with semicon-

ductor lasers and other laser sources, it is still an exploratory field of research and commercially available semiconductor laser systems do not make use of this combining approach. One reason may be that coherent beam combining is not as straightforward as other combining approaches. It is indeed technologically challenging to combine laser beams coherently in a simple, stable and efficient way. Many of the past demonstrations of coherently combined semiconductor emitters were too complicated, too unstable or too in-efficient in order to be interesting for applications on a large scale. In this context, one may see a parallel between coherent beam combining of semiconductor lasers and the picture of the "eierlegende Wollmilchsau": something that may be indeed very useful, but does unfortunately not exist.

The work described in this manuscript targeted <u>not</u> the development of the most ambitious, most powerful or most efficient laser source based on coherently combined semiconductor emitters. In contrast, the focus lied on simple systems, where only a few optimized emitters are coherently combined and which can open new perspectives for high-power high-brightness semiconductor laser systems. My PhD-project was carried out at the Laboratoire Charles-Fabry (Palaiseau, France) in collaboration with the Ferdinand-Braun-Institut (Leibniz-Institut für Höchstfrequenztechnik, Berlin, Germany). It is also the continuation of previous research related to the PhD thesis of Guillaume Schimmel (2017). The content of the work is organized in the following chapters:

Chapter I covers the state of the art of high power semiconductor emitters in the near infrared spectral regime. The different types of emitters are compared to each other in terms of power, efficiency and brightness. After that, incoherent and coherent beam combining methods are introduced and specific requirements of coherent beam combining architectures are outlined. The state of the art of coherently combined semiconductor emitters is summarized. From that, conclusions for the design of a simple and robust architecture relying on a limited number of high-power high-brightness semiconductor emitters, in this case so-called tapered amplifiers, are made and the underlying experimental strategy of this work is defined.

Chapter II covers a detailed investigation of different designs of high-power high-brightness semiconductor emitters. The experimental investigations target to identify the best device design for the use in a coherent beam combining setup. Factors influencing the spatial properties of the laser beams and therefore influencing the brightness of the beams are investigated in detail.

Chapter III covers the basic experimental principles of coherent beam combining in the setups studied in this work. Coherent beam combining experiments in continuous wave operation are summarized and the effect of the used emitter design on power, efficiency and brightness of the whole setup are discussed. The usefulness of coherent beam combining for nonlinear frequency conversion is demonstrated. Furthermore, experimental challenges and problems concerning the stability and the efficiency of the experimental setup are pointed out and approaches to overcome these limitations are demonstrated. Finally the technical realization of a simple and modular experimental setup with excellent long term stability is described and analyzed.

Chapter IV covers coherent beam combining experiments with pulsed semiconductor emitters. The differences to operation in continuous wave operation are investigated. Coherent beam combining in the long-pulse regime, with pulse duration in the millisecond regime (also called quasi-continuous-wave operation) is demonstrated and compared to experiments described in chapter III. Additionally, perspectives for coherent beam combining with shorter pulses are outlined.

Chapter I

Fundamentals

Objectifs

This chapter covers the fundamentals relevant for this work. The first part is devoted to the basic principles of high brightness semiconductor lasers and amplifiers. Different architectures for high brightness diode lasers are discussed and compared regarding their intrinsic limitations of power and spatial properties of the output beam. In the second part of this chapter the basic principles of coherent beam combining (CBC) of semiconductor based laser systems are introduced and the state of the art in this field of research is discussed. The chapter ends with a description of the chosen strategy for brightness scaling in a simple coherent beam combining architecture.

Contents

1   High brightness diode lasers

Semiconductor light sources provide the optical energy for many applications in industry and research and benefit from their elevated electrical-to-optical efficiency and their potential for low-cost mass production, especially when compared to other sources of light. There are several types of semiconductor light sources to achieve high power [1] emission, coherent or incoherent, at many different wavelengths. Devices with coherent emission in the near infrared spectral region (NIR), especially with wavelengths from 900 nm to 1100 nm, are in the focus of this work. Here, III-V compound semiconductor materials, such as GaAs, with a forward biased p-n junction are used as the light emitting material. Such devices are fabricated by the growth of thin layers with slightly different characteristics on a substrate. Semiconductor laser sources can be roughly be divided two categories shown in Fig. I.1 : (a) Devices where the light is emitted perpendicular to the p-n junction are so called **surface-emitting** devices and (b) devices where the light is emitted parallel to the p-n junction are called **edge-emitting** devices. Only (electrically-pumped) edge-emitting devices will be discussed in this manuscript as most high-brightness semiconductor laser systems rely on them.
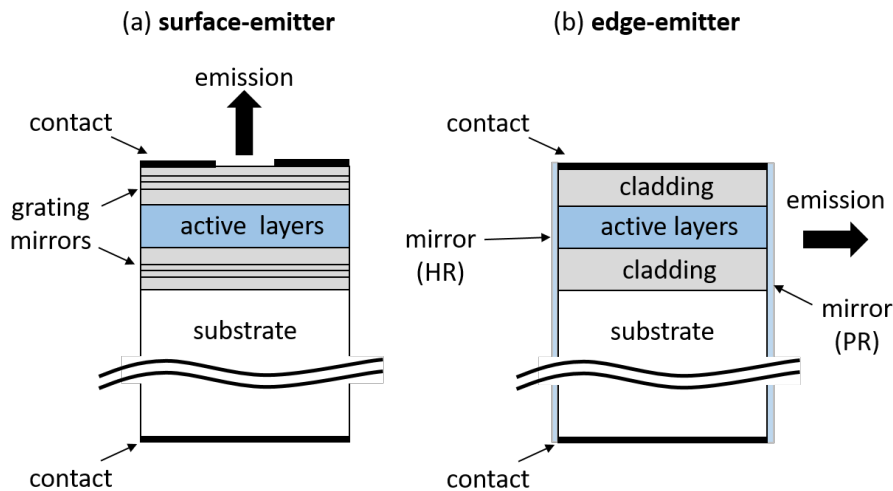
Figure I.1 – Simplified schematic of (a) a surface emitting and (b) an edge emitting smiconductor laser. HR: highly reflective, PR: partially reflective

Furthermore one can categorize coherent light sources in general in so-called laser-**oscillators** (usually short: lasers), where the coherent light is oscillating in a cavity containing the gain medium, and so-called laser-**amplifiers** (usually short: amplifiers), where the gain medium is used in single or multiple passes for the amplification of a low-power coherent seed signal. See Fig. I.2. Both oscillators and amplifiers will be discussed in this work, a large part is of this work is however dedicated to amplifiers. Note that the device architecture of semiconductor lasers and amplifiers is very similar, the only difference is that a semiconductor laser has dielectric mirror coatings with a higher reflectivity or integrated grating reflectors.

The device architecture of edge emitting laser and amplifiers consists of a vertical structure that is confining the field perpendicular to the active region of the device and a lateral structure confining both the field and the electronic carriers in a defined region parallel to the active layer [Epperlein 13a]. There are numerous degrees of freedom regarding the device design, such as the lateral dimensions of the waveguide, that influence the performance of the laser or amplifier regarding the achievable output power, the electrical-to-optical efficiency (also called PCE for power-conversion-efficiency and defined as η_e = PCE = optical output power / electrical power) and the beam quality. Unfortunately, there is no design that is optimal for all of these three aspects. For example, material damage thresholds of the facets limit the achievable output power. If one increases the dimensions of the waveguide to reduce the

---

[1]Emitters with $\geq$ 1 W optical power are considered as high-power devices in this work.

(a) laser-oscillator
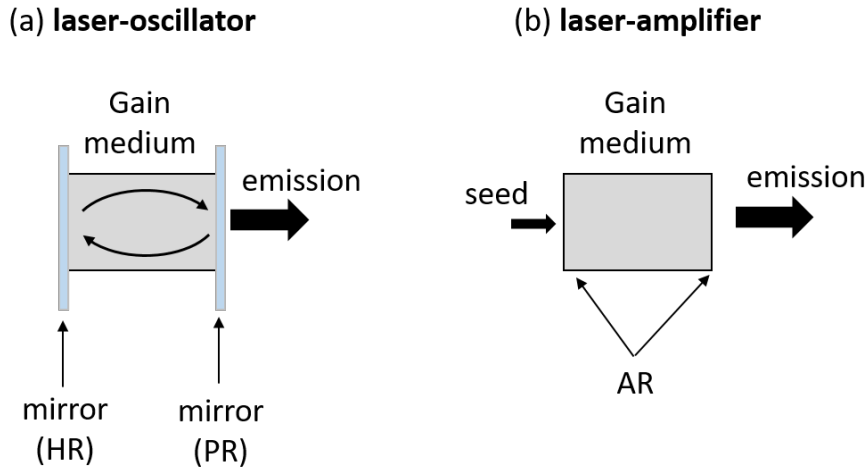
(b) laser-amplifier

Figure I.2 – Simplified schematic of (a) a laser-oscillator and (b) a laser-amplifier. HR: highly reflective, PR: partially reflective, AR: anti-reflection coating.

facet load in order to achieve higher powers, one degrades at the same time the achievable beam quality as the waveguide may guide higher order modes. The design of the actual device is therefore always a compromise between the limitations regarding output power, efficiency and beam quality. The most common architectures for high-power single emitters will be discussed in the following sections. A short introduction regarding the spatial properties, beam quality and brightness of laser beams is given in the paragraph below.

1.1 Spatial properties of laser beams

Laser beams have very distinct spatial properties that can be well described by using the theoretical model of the **Gaussian beam**, which describes the two dimensional electrical field propagating along the optical axis z as [Saleh 19]

$$E(x, y, z) = E_0 \frac{w_0}{w(z)} \exp\left(-\frac{x^2 + y^2}{w(z)^2}\right) \exp\left(-i\left(kz + k\frac{x^2 + y^2}{2R(z)} - \psi(z)\right)\right). \tag{I.1}$$

Where E_0 is the maximum field amplitude in the center of the focus plane, w is the beam radius[1], w_0 the minimum radius or waist, $k = 2\pi/\lambda$ is the wavenumber with the wavelength λ and $R(z)$ is the radius of curvature of the wavefront. The Gouy Phase $\psi(z)$ is also included for completeness but will be of no further interest in this work. A schematic of the spatial properties of such a Gaussian beam is shown in Fig. I.3. The beam radius is changing during propagation along the optical axis z by $w(z) = w_0\sqrt{(1 + (z/z_r)^2)}$. The Rayleigh length is defined as $z_r = (\pi w_0^2)/\lambda$ and stands for the distance from the waist-plane to the plane where the beam radius has increased by a factor of $\sqrt{2}$. The spatial evolution of the beam radius $w(z)$ approaches the linear relation $w(z) \approx w_0\frac{z}{z_r}$ when $z \gg z_r$. The divergence is consequently defined as $\Theta = w_0/z_r$. The beam parameter product is defined as $BPP = w_0\theta$ and is equal to λ/π for an ideal Gaussian beam. This work discusses mostly laser in the near infrared at a wavelength of about 1 μm, the BPP of a diffraction limited beam is 0.3 mm × mrad at this wavelength.

Such ideal propagation parameters are approximately achieved with purely single mode low power diode laser and amplifiers. The beams of high power high brightness lasers and amplifiers, such as tapered lasers, are however not ideally Gaussian. Their complex fields can be decomposed onto the orthogonal base of the Hermite-Gaussian modes. Any power content in higher order modes leads to

---

[1]This specifies the so-called $1/e^2$ beam radius, which is the distance from the optical axis to the point where the intensity has decreased to 13.5% of its maximum value.
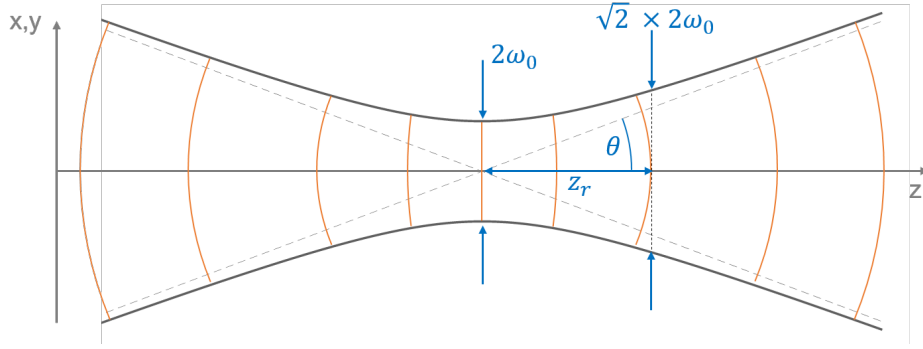
Figure I.3 – Simplified schematic of a Gaussian beam propagating along the optical axis z.

an increased BPP. The so-called **beam propagation factor** is defined as $M^2 = (BPP \times \pi)/\lambda$ and is a frequently used parameter to compare the beam propagation properties of laser beams (which have $M^2 \geq 1$) to the ideal Gaussian beam (which has $M^2 = 1$). Note that the beams from semiconductor lasers and amplifiers are (mostly) not circular and have different spatial properties in the transverse directions (x,y). The beam profile in vertical direction (perpendicular to the active layers) is more often than not close to a diffraction limited Gaussian beam. The beam quality in lateral direction (parallel to the active layers) depends on the lateral device structure and can be far from a diffraction limited ideal Gaussian beam in many configurations (see following sections). At the output of the device, the beam is usually diverging faster in vertical direction (therefore also called **f**ast **a**xis, **FA**) than in lateral direction (**s**low **a**xis, **SA**).

The term brightness is usually used as a synonym for the radiance of a laser beam which is defined as the power divided by the product of the mode area at waist and the solid angle in the far field [Shukla 15]. The brightness can be written as

$$B = \frac{P}{\pi w_0^2 \times \pi \Theta^2} = \frac{P}{\pi^2 \times BPP_x \times BPP_y} = \frac{P}{\lambda^2 \times M_x^2 M_y^2}, \tag{I.2}$$

where $M_{x,y}^2$ are the beam propagation factors in x and y direction respectively. To give an example, the brightness of an ideal Gaussian beam with 1 W optical power and $1\,\mu\text{m}$ wavelength is $100\,\text{MW cm}^{-2}\,\text{sr}^{-1}$.

1.2 Common architectures for high brightness edge emitting laser diodes

The light propagates parallel to the wafer substrate in edge emitting laser diodes and amplifiers. The lateral structure, which is confining the optical field and the carriers, can be roughly classified in three categories shown in simplified form in Fig I.4: (narrow-stripe) **single mode ridge waveguide** emitters, **broad-area** emitters and **tapered** emitters. The basic principles of these devices and the current state of the art for such devices are summarized in the following subsections with a focus on tapered lasers and amplifiers as these devices are used in this work. A compact summary and comparison of the different devices discussed in the following subsections is given at the end of the section in Table I.1 on page on page 18.

1.2.1 Single mode ridge waveguide lasers and amplifiers

Conventional single mode ridge waveguide lasers (RWL) and amplifiers consist of a narrow (typically $4\,\mu\text{m}$ or less in lateral direction an about $2\,\mu\text{m}$ in vertical direction) index-guided single mode waveguide. Power scaling of such devices is limited by power and beam steering instabilities [Achtenhagen 06] at high bias and finally by catastrophic optical damage (**COD**), induced by highly localized heating at the facets or in the bulk waveguide [Tomm 11]. Device designs for high power operation of single mode ridge waveguide emitters target therefore an increased mode size in lateral
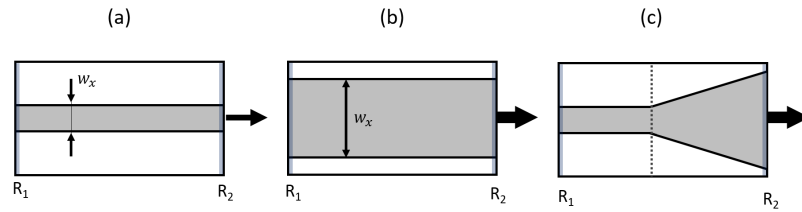
Figure I.4 – Simplified schematics (top view) of common lateral architectures for high brightness edge emitting laser diodes: (a) narrow stripe single mode ridge waveguide device, (b) broad area device, (c) tapered device consisting of a narrow stripe ridge waveguide followed by a tapered section. All three configurations exist both as lasers and amplifiers. For a laser, the coating R_1 is usually a HR-coating or a highly reflective DBR-grating and the coating R_2 a low (typically around 1%) reflectivity coating. High quality AR coatings with a nominal reflectivity in the order of 0.01% are used for R_1 and R_2 if the device is used as an amplifier.

and vertical direction, which has been achieved by a variety of different strategies [Epperlein 13b]. High power (> 1 W) operation has been demonstrated with **s**lab **c**oupled **o**ptical **w**aveguide **l**asers and **a**mplifiers (**SCOWL** and **SCOWA**) [Huang 03] that benefit from an almost circular mode with a diameter of typically $4\,\mu$m. Similar power levels have been achieved by increasing the mode size in vertical direction with a so-called **s**uper **l**arge **o**ptical **c**avity (**SLOC**) and in lateral direction with a slightly wider $w_x > (5\,\mu$m) leaky ridge waveguide [Wenzel 08]. A schematic cross-sectional view of such a device is shown in Fig I.5 (a). The beam quality of such devices is usually diffraction limited ($M_x^2 \approx 1$) at 1 W optical power and is only slightly degraded in horizontal at the maximum power of 1.5 - 2 W ($M_x^2 \leq 1.3$) as can bee seen from the beam profiles given in Fig. I.5 (b) and (c). The beam propagation factor in vertical direction is close to unity for all power levels ($M_y^2 \leq 1.1$). The PCE is below 50% at low bias and typically below 40% at high bias. The brightness reached with the two types of high power ridge waveguide lasers and amplifiers discussed above is in the order of 80 MW cm^{-2} sr^{-1} (cf. Table I.1).
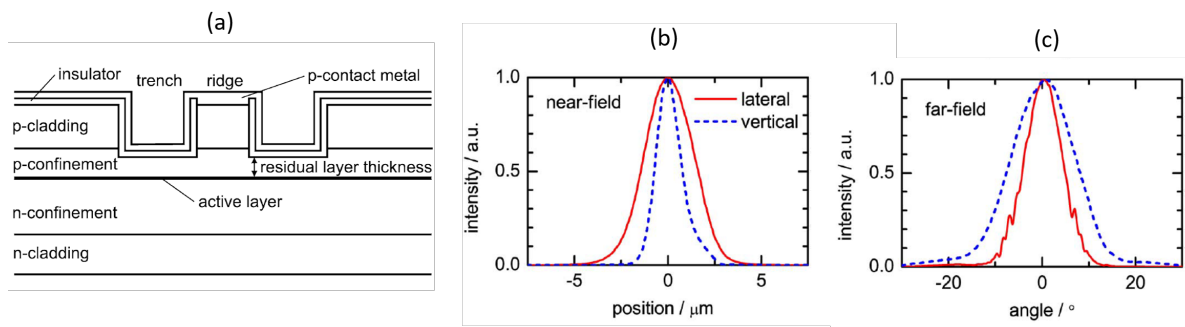
Figure I.5 – (a) Schematic cross-sectional view of a high power RW laser with a SLOC and a leaky ridge waveguide. (b) Near field and (c) far field intensity profiles for such a device with $5\,\mu$m wide ridge waveguide at 1.5 W optical output power. Taken from [Wenzel 08].

The recent development of so-called broad-ridge waveguide lasers [Wilkens 18], with an up to $w_x = 15\,\mu$m wide ridge waveguide, enable a significantly increased electrical-to-optical efficiency ($\eta_e > 60\%$ at 1 W single mode operation). The main challenge is however the onset of lasing of higher order modes at high bias. Very recently, single mode operation at 2.5 W ($\eta_e > 55\%$) has been achieved by implementing a transverse mode filter into the $15\,\mu$m wide ridge waveguide [Wilkens 19], corresponding to more than 200 MW cm^{-2} sr^{-1}. The extremely high efficiency (PCE = 67% at 1 W) is promising for potential future applications in high-brightness direct diode laser systems, where the efficiency is one of the most important criteria.

1.2.2 Broad area lasers and amplifiers

Broad **a**rea **l**asers (**BAL**) and amplifiers consist of a significantly larger (typically in the range of 90 μm) waveguide in lateral direction. The large number of modes guided in the multimode waveguide, allows to extract the energy more efficiently and makes high power near infrared broad area lasers the most efficient laser sources. Electrical-to-optical efficiencies as high as 85% at $-50\,°$C heatsink temperature and 76% percent at $10\,°$C have been reported at moderate power levels in the range of a few watts [Crump 06]. Broad area lasers can however reach much higher output powers (> 10 W) at the cost of a reduced efficiency at high powers. Recent improvements in device design enabled however operation at 14.5 W with $\eta_e > 60\%$ at $25\,°$C heatsink temperature and more than 21 W with $\eta_e > 60\%$ at $-50\,°$C [Crump 12].

While conventional broad area lasers have an about 90 μm wide lateral waveguide, there are also configurations where narrower waveguides are used. The brightest among these are devices with an about 30 μm wide lateral waveguide, so-called **n**arrow stripe **b**road **a**rea **l**asers (NBAL) [Decker 14]. The narrow waveguide leads to an approximately two-fold improvement of the beam quality. These emitters reach output powers >6 W at a BPP$_x$ of 1.8 mm-mrad in lateral direction. This corresponds to a brightness in the order of 125 MWcm^{-2}sr^{-1} and exceeds the brightness of conventional single-mode ridge waveguide lasers (cf. Table I.1.). The drawback however is the PCE, which is with approximately 40% not as high as for conventional broad area lasers.

Broad area amplifiers are less common than single mode amplifiers but do exist (e.g. [Goldberg 92]). Tapered amplifiers are however today the preferred alternative. But it is still quite common to use broad area emitters in a so-called V-shape configuration, shown in Fig I.6, as the amplifying medium for external cavity setups. The lateral structure of the broad area emitter is however not used as a waveguide in such configurations but only as the amplifying medium for an injected (in most cases single mode) seed beam. Some work on coherent beam combining of diode lasers and amplifiers relies on broad area emitters used in such V-shape configurations [Liu 08, Liu 10].
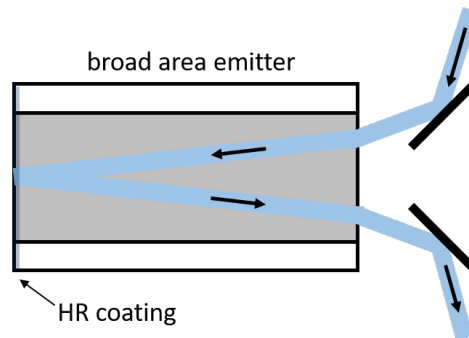
Figure I.6 – simplified schematic of a broad area emitter used in a V-shape configuration. The (in most cases single mode) beam is not guided by the lateral structure of the device.

1.2.3 Tapered lasers and amplifiers

Tapered lasers have, in contrast to single mode ridge waveguide and broad area lasers, at least two monolithically integrated sections with different properties. A simplified schematic of a tapered laser/amplifier is shown in Fig. I.7. The ridge waveguide (RW) is an index-guided narrow stripe single mode waveguide. The width w_1 of the RW is usually in the range from 2 to 5 μm and usually 1 to 2 mm long. The tapered section (also flared section) is usually a gain-guided section with no additional index waveguide. The tapered section has a full angle Θ_{TP} of usually around 6 °and is a few millimeters long. The field is confined in the vertical waveguide (FA) in the whole device but diverges in lateral direction (SA) in the tapered section. This leads to a significantly larger aperture w_2 in SA at the front facet, which dramatically reduces the facet load and enables high power operation without catastrophic optical damage of the output facet.
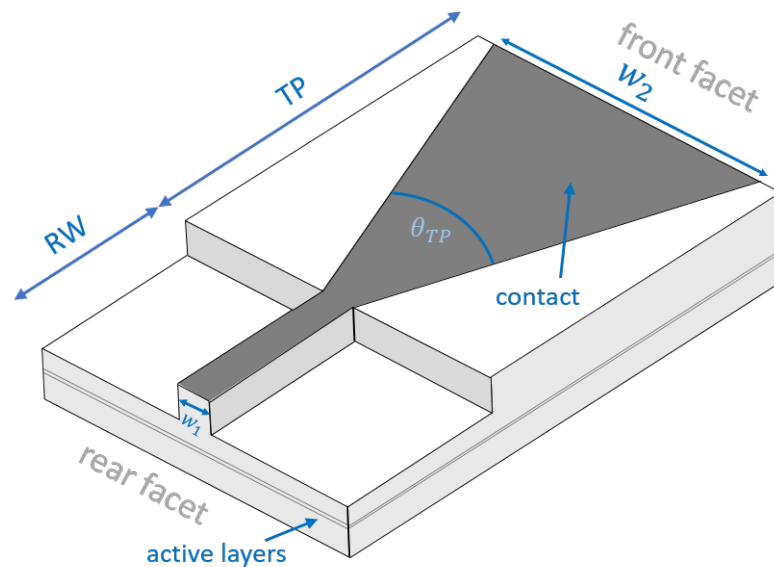
Figure I.7 – Simplified schematic of a tapered laser/amplifier. The electric contact is shown in dark gray. RW: ridge waveguide; TP: tapered section; QW: quantum-wells; w_1: width of ridge waveguide; w_2: maximum width of tapered section; Θ_{TP}: full taper angle.

The first tapered amplifiers were demonstrated in the early 90s [Bendelli 91]. The initial motivation was to develop semiconductor laser traveling wave amplifiers that require lower seed power levels compared to broad area traveling wave amplifiers [Goldberg 92]. Index-guided exponentially tapered, trumpet-like, sections were used in the first designs. The index-guided exponentially tapered section was soon abandoned and replaced by gain-guided linear tapered sections [Walpole 92]. Since then, high brightness tapered lasers and amplifiers have been developed over a wide coverage of different wavelengths and the performance has dramatically increased over the last 25 years. Today, tapered lasers and amplifiers are by far the brightest semiconductor lasers and amplifiers and are the workhorse for many applications requiring high brightness, such as nonlinear frequency conversion [Sumpf 18]. The challenges of tapered lasers are however to maintain good beam quality at high powers. In fact, the output beam of tapered lasers is slightly multimode. Only 60-80% of the power are considered to be in the fundamental mode (also referred as the central lobe) and the rest of the power is distributed in higher order modes (also referred as higher angle side lobes). This leads consequently to a significantly increased M^2 beam propagation parameter (usually in the range of 4 to 15). Furthermore, the power conversion efficiency is in the range of 30-45% at high powers and is significantly lower than for state of the art broad area lasers. More typical aspects of tapered lasers and amplifiers will be discussed in chapter 2.

The most common configurations of devices relying on the basic principles discussed above are summarized in Fig. I.8. Devices with the tapered section as part of the cavity are shown in the upper row (a)-(c) and are usually referred as tapered lasers. In amplifier configurations, shown in the second row (d)-(f), the tapered section is not part of the cavity and is used as a single pass amplifier only. The simplest concept are conventional **tap**ered **l**asers (**TPL**), as shown in Fig. I.8 (a). TPLs have a standard Fabry-Perot type cavity. Drawbacks of such devices are however the unstable spectrum and the poor beam quality at high bias [Lim 14]. Tapered lasers which are spectrally stabilized by a distributed Bragg reflector (DBR-TPL, Fig. I.8 (b)) maintain better beam quality at higher powers. Here, oscillation of higher order modes is at least partially suppressed by AR coatings at the rear facet. More than 5 W output power with 60-70% diffraction limited power content have been reported at many different wavelengths [Sumpf 18]. Particular high powers were so far achieved for wavelengths around 980 nm, which is also the wavelength range of the coherent beam combining experiments described in this manuscript. The electro-optic characteristics of a cutting edge 12 W DBR-TPL at

980 nm is shown in Fig. I.9 (a). The slow axis beam profiles at waist are shown in Fig. I.9 (b) and are typical for high-brightness tapered lasers.
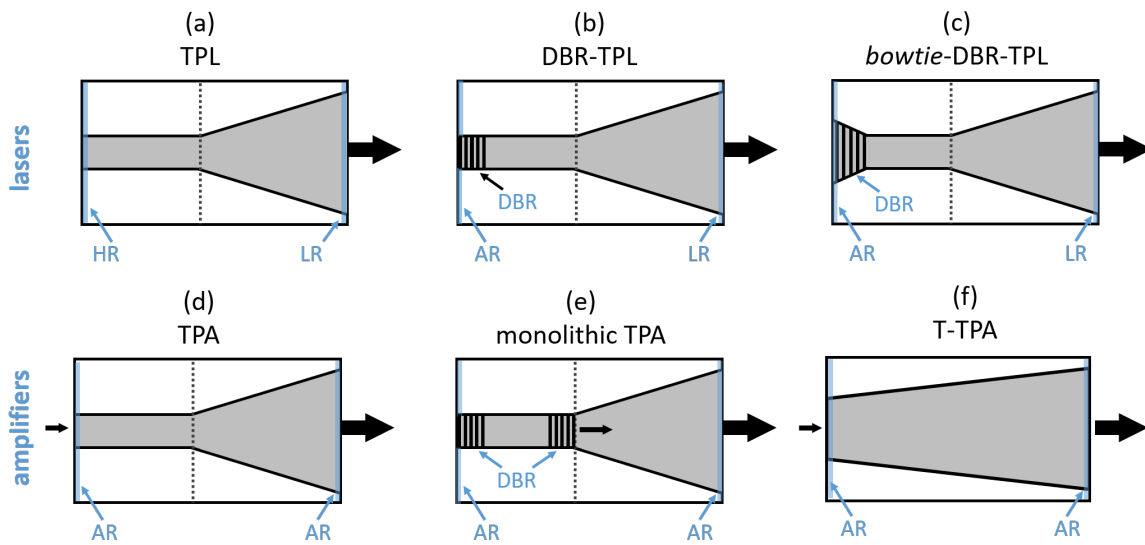
Figure I.8 – common configuration of tapered lasers and amplifiers. HR: high reflectivity coating, LR: low reflectivity coating; AR: anti reflection coating; DBR: distributed Bragg reflector.

Some tapered lasers make use of a bowtie-like structure by including a small additional tapered section at the rear facets. Record central lobe powers > 10 W were recently demonstrated by Müller et al. in a Bowtie-DBR-TPL configuration [Müller 17]. This device configuration enables an extremely high brightness of about 950 MWcm^{-2}sr^{-1}, which is roughly 10 times brighter than conventional single mode ridge waveguide lasers or conventional broad area lasers.
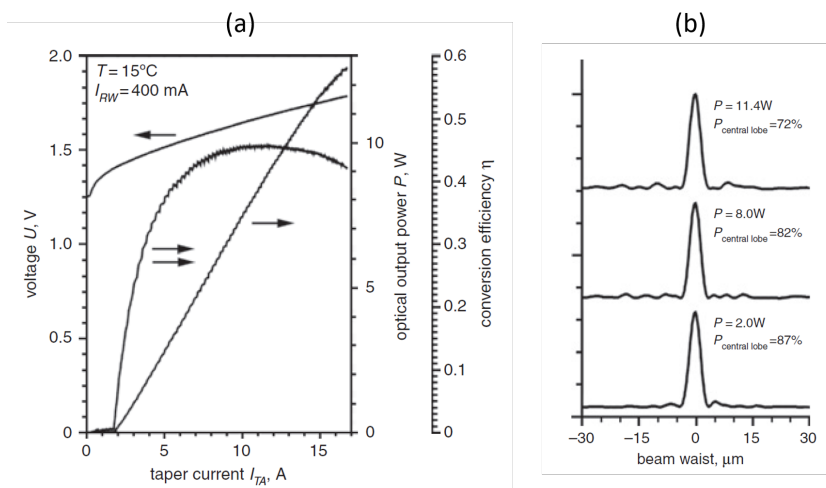
Figure I.9 – (a) CW power-voltage-current characteristics of a 6 mm long DBR-TPL. (b) SA beam waist profiles for three different output powers. Taken from [Fiebig 08].

The conventional **tap**ered **a**mplifier (**TPA**) is in principle similar to a conventional TPL but with AR coatings on both facets (see figure I.8 (d)). TPAs are most commonly used in single pass master oscillator power amplifier (MOPA) configuration, where the signal from a low power master oscillator is coupled into the RW. The RW acts as a mode filter and preamplifier for the large tapered section. TPAs are the standard concept for watt-level amplification of very-narrow line-width extended cavity laser diodes required for many applications in the field of quantum technology [Toptica 19]. Monolithic

TPAs carry the master oscillator directly on the chip [Welch 92]. The MO is usually realized in the form of stabilized cavity between two DBR gratings in the RW, as shown in figure I.8 (e). The tapered section is then used as a single pass amplifier. This concept enables more compact setups in comparison to conventional MOPA configurations. Power scaling is however limited by the onset of multi- cavity operation at high bias [Zink 19]. So-called **t**runcated **tap**ered **a**mplifiers (T-TPA) do not have a single-mode ridge waveguide and in contrast to all other configurations only one section as shown in figure I.8 (f). These devices can deliver up to 17 W of diffraction limited power in **q**uasi **c**ontinuous **w**ave (QCW) operation[1] and are with up to 1800 $\mathrm{MWcm^{-2}sr^{-1}}$ by far the brightest emitters available (cf. Table I.1).

---

[1]QCW operation specifies the pulsed operation of the devices. The pulse durations are in the millisecond range (0.1 - 10 ms) and the duty cycle (ratio of pulse duration over pulse period) is low (0.1 - 10%). The low duty cycle allows to test the devices at high bias as the thermal load in the device is dramatically reduced.

TABLE I.1 - Overview of the state of the art for high power semiconductor lasers and amplifiers (single emitters).

	type	power [W]	wavelength [nm]	M² in SA	estimated brightness [MW cm⁻² sr⁻¹]	PCE at specified power [%]	CW / QCW	heatsink temperature [°C]	reference
lasers	SCOWL	1.1	915	1.1*	89	not specified	CW	16	[Huang 03]
	RWL	1.5	1064	1.3	80#	≈ 37	CW	25	[Wenzel 08]
	broad RWL	2.5	970	1.1**	220#	> 60	CW	25	[Wilkens 19]
	BAL (400 µm)	60	940	88	75#	> 60	QCW	not specified	[Platz 14]
	BAL (90 µm)	14.5	940	≈ 20	≈ 77#	> 60	CW	25	[Crump 13a]
	BAL(90 µm)	21	940	≈ 20	≈ 110#	> 60	CW	-50	[Crump 13a]
	NBAL (30 µm)	6	970	≈ 5.2**	125#	40	CW	20	[Decker 15]
	commercial TPL	3	795 - 1010	1.7*	175-280#	not specified	CW	25	[Dilas 19]
	DBR-TPL	11.4	979	12.8	860##	44	CW	15	[Fiebig 08]
	Bowtie-DBR-TPL	15.5	1030	11	950##	46	CW	15	[Müller 17]
amplifiers	SCOWA	1.5	1060	1.1*	89	32	CW	25	[Smith 11]
	TPA	6.2	972	1.3*	520##	not specified	CW	15	[Tawfieq 17]
	commercial TPA	3	795 - 1010	1.7*	175-280#	not specified	CW	25	[Dilas 2019]
	monolithic- TPA	10	977	2*	620#	not specified	CW	15	[Wenzel 07]
	T-TPA	30	970	1.9*	1800##	> 40	QCW	20	[Wang 13]

* The specified M² value was calculated using the 1/e² beam diameters.
** The specified M² value was calculated using the 95 % power content beam diameters.
# The brightness was estimated from the published near and far field profiles.
The brightness was estimated from the specified diffraction limited power / power in the central lobe

1.2.4   Summary and conclusion

The state of the art of high power single emitter semiconductor lasers and amplifiers given in the previous subsection is summarized in Table I.1 with additional information. The comparison of the different specifications leads to the following conclusions:

- Broad area lasers are by far the most powerful and most efficient emitters. The high beam parameter product leads however to brightness levels in the range of 70-80 $\mathrm{MWcm^{-2}sr^{-1}}$ and only narrow stripe broad area lasers can provide more than 100 $\mathrm{MWcm^{-2}sr^{-1}}$ per emitter.

- Single mode ridge waveguide lasers have by far the best beam quality and are the only emitters that can provide diffraction limited beam quality. The power and efficiency is however limited. The brightness of conventional designs is the range of 80 $\mathrm{MWcm^{-2}sr^{-1}}$ Recent developments of ridge waveguide lasers with a 15 μm wide ridge waveguide enable more than 2 W with PCE > 60% and more than 200 $\mathrm{MWcm^{-2}sr^{-1}}$ for the first time.

- Tapered lasers and amplifiers are by far the brightest emitters with up to 900 $\mathrm{MWcm^{-2}sr^{-1}}$ in CW and up to 1800 $\mathrm{MWcm^{-2}sr^{-1}}$ in QCW. The power conversion efficiency is however significantly lower than for state of the art broad area lasers.

In other words, the ideal device fulfilling all three figures of merit (high power, diffraction limited beam quality, excellent power conversion efficiency) does not exist yet. Devices from each group (single mode ridge waveguide lasers, broad area lasers and tapered lasers) roughly fulfill only two of the three factors (see Fig. I.10).
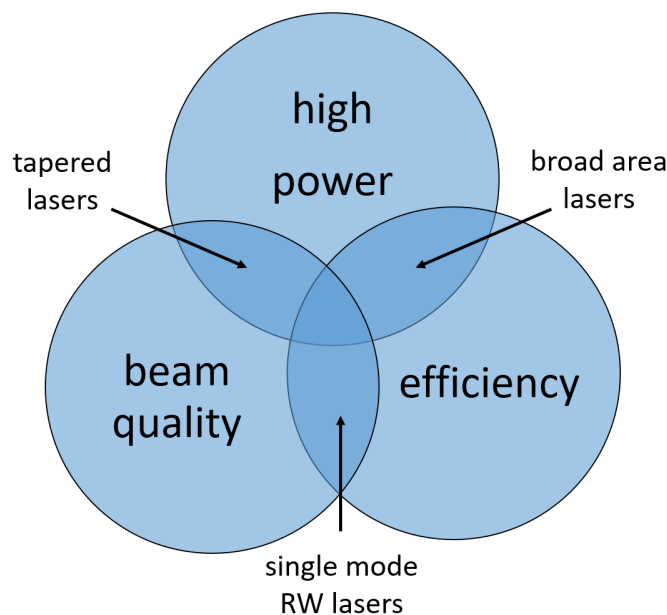
Figure I.10 – Simplified classification of the different single emitter concepts

1.3 Packaging of high power diode lasers

The packaging and cooling of the emitters is an essential parameter for the development of high brightness lasers sources. Semiconductor lasers and amplifiers are relatively efficient light sources especially when compared to other laser sources, but the heat load is concentrated in a highly confined area. Efficient heat extraction is essential to maintain a low temperature of the active zone, which is important for efficient and stable operation at high powers. The basic principles of the packaging and cooling of high power diode lasers are thoroughly described in [Loosen 00] and only some specific points relevant for this work are briefly mentioned below:

- Semiconductor lasers and amplifiers can be packaged as single emitters (one heatsink per emitter) or bars (10 or more emitters share a common substrate and heatsink). Bars with only few emitters (typically about 5 emitters) are usually referred as minibars. The heat extraction in single emitter based systems is usually more efficient and a low temperature in the active zone can be maintained at higher bias when compared to operation in a bar configuration.

- The carrier of the laser chip is usually made from an expansion matched material, such as CuW, AlN or diamond, to avoid temperature dependent mechanical stress and strain.

- There are different types of heat-sinks for single emitter lasers and amplifiers. The so-called c-mount is one of the most common mounts. C-mounts are small copper heat-sinks that carry the emitter without any protection for the emitter and the wire bonds. C-mounts are very compact heat-sinks and are the standard solution for systems where other optical components are located very closely to the emitter. The volume of the heatsink is however limited, which makes efficient heat-extraction at high powers challenging. An active temperature control with a Peltier-element is usually required.

- The emitters can be mounted with the epitaxial layers facing up (epi-side up) or facing the heatsink (epi-side down) as shown in Fig. I.11. Heat extraction is usually more efficient for mounting in epi-side down configuration as the thermal resistance of the substrate can be eliminated [Liu 04]. High power NIR diode lasers are most commonly grown on n-type doped substrates. It is therefore common to specify the orientation of the epi-layer as **p-side up/down**.
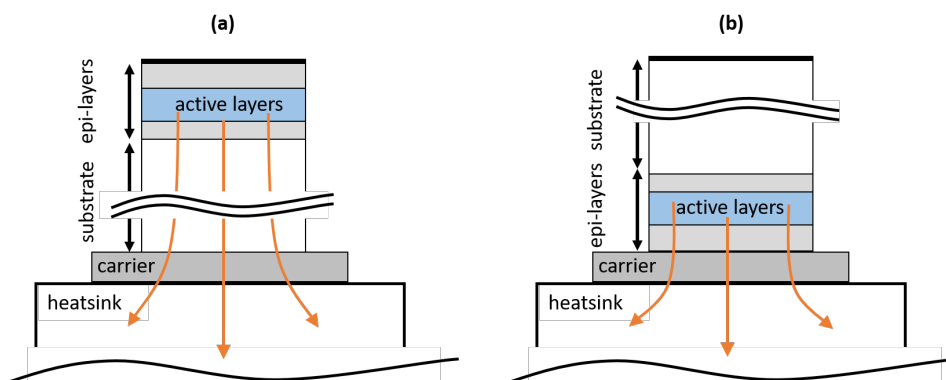
Figure I.11 – Schematic cross sectional view of (a) epi-side up and (b) epi-side down mounting. Approximate heat flow in orange.

.

1.4 Applications of high power edge-emitting diode lasers

Laser diodes are used as an efficient source of optical power in many industrial applications. Many applications require high power that can only by achieved by combining several diode lasers (the approaches for beam combining are discussed in section 2). One categorizes indirect and direct industrial applications.

Indirect applications   The optical power from diode lasers is used indirectly for pumping of other lasers sources, especially for solid-state-lasers (bulk crystal gain media and glass fiber gain media). Single emitters are used when comparably low pump powers are required, incoherently combined emitters are needed for high power pump modules. Broad area lasers are most commonly used for commercially available pump sources.

Direct applications   The optical power from diode lasers is used in many industrial applications in the field of material processing. Comparably low levels of brightness are sufficient for simple applications like laser-heating of laser-hardening. High(er) brightness is required for sheet metal cutting, laser-welding, laser-brazing and additive manufacturing based on selective laser melting. Power and brightness levels far beyond the performance of single emitters (cf. Table I.1) are necessary. This is achieved by spectral beam combining architectures (cf. section 2). Broad area emitters are used for direct applications, as the power conversion efficiency of the emitters is a very important factor for the overall cost of the material processing.

Even though tapered lasers reach significantly higher brightness than broad area lasers, they play a minor role in the applications listed above. There are however an important niche-product for a few applications discussed below, where the power conversion efficiency is less important.

1.4.1 Applications of tapered lasers and amplifiers

Tapered lasers and amplifiers are the workhorse for many applications requiring high power and high beam quality from a single emitter. These applications include but are not limited to:

Atom cooling, atom interferometry and quantum technology   Tapered amplifiers are used to amplify low-power narrow bandwidth signals from extended cavity diode lasers for atom cooling (e.g. for Potassium or Rubidium atom-physics experiments [Goldwin 02, Nyman 06]). Commercial modules of tapered amplifiers designed for such laboratory scale experiments are available [Toptica 19]. The high power from single amplifier enabled the design of ultra-compact modules for atom interferometry experiments on a sounding rocket [Schkolnik 16, Becker 18].

Atmospheric lidar   Pulsed tapered amplifiers are used in compact atmospheric micro-pulse differential absorption lidars for the amplification of low-power signals from extended cavity diode lasers. Especially wavelengths around 830 nm are used for water vapor and aerosol profiling in the troposphere [Nehrir 11, Nehrir 12].

Tapered lasers and amplifiers are in many cases cited above the only technology that can enable the required optical output power. An increase in the power, e.g. by the use of coherent beam combining architectures discussed in this work, may improve the performance in those fields in the future and may lead to new developments of applications requiring even higher power. The applications listed above use the light of tapered diode lasers at the emission wavelength directly. In many other cases however, it is necessary to use nonlinear frequency conversion to reach the desired wavelength. The role of tapered lasers and amplifiers in frequency converted semiconductor laser systems is discussed in the following subsection.

1.4.2   Visible laser sources based on frequency converted tapered lasers and amplifiers

High power high brightness visible laser sources are required for biomedical applications [Müller 13]. Semiconductor lasers emitting directly in the visible spectral range (VIS) are however not as bright as in the NIR. Furthermore, some wavelengths, e.g. in the yellow spectral range, are not directly accessible with semiconductor laser sources. Nonlinear frequency conversion, such as second harmonic generation (SHG) of high brightness NIR semiconductor laser sources is one standard approach for the development of high power visible laser sources. The textbook of Boyd is recommended for a complete overview of the underlying theory and principles of nonlinear frequency conversion [Boyd 03]. One main challenge is to achieve high conversion efficiencies, as the intensity of CW (or QCW) semiconductor lasers is not as high as in short-pulse solid-state lasers. Therefore, a high conversion efficiency with CW semiconductor lasers requires the use of long nonlinear crystals. This however requires a high beam quality and a high spectral purity of the used NIR pump laser, as the wavelength acceptance bandwidth scales inversely proportional to the crystal length ($\Delta\lambda \propto L^{-1}$). Quasi-phase matching in a periodically poled (PP) nonlinear crystal is the standard concept for nonlinear frequency conversion of semiconductor lasers. Periodically poled lithium niobate (PPLN) is often used, the high nonlinearity ($d_{33} = 28.4$ pm/V) enables conversion efficiencies up to 3.4%W^{-1} cm^{-1} [Jechow 10]. The wavelength acceptance bandwidth of PPLN is in the order of 150 pm cm, meaning that the use of a 6 cm long PPLN bulk crystal requires an optical spectrum with $\Delta\lambda_{FWHM} < 25$ pm corresponding to $\Delta\nu_{FWHM} < 7.5$ GHz (for $\lambda = 1\mu$m).

Tapered lasers and amplifiers are the preferred NIR pump source as they are by far the brightest emitters available. Typical setups for SHG of tapered lasers and amplifiers are shown in Fig. I.12.
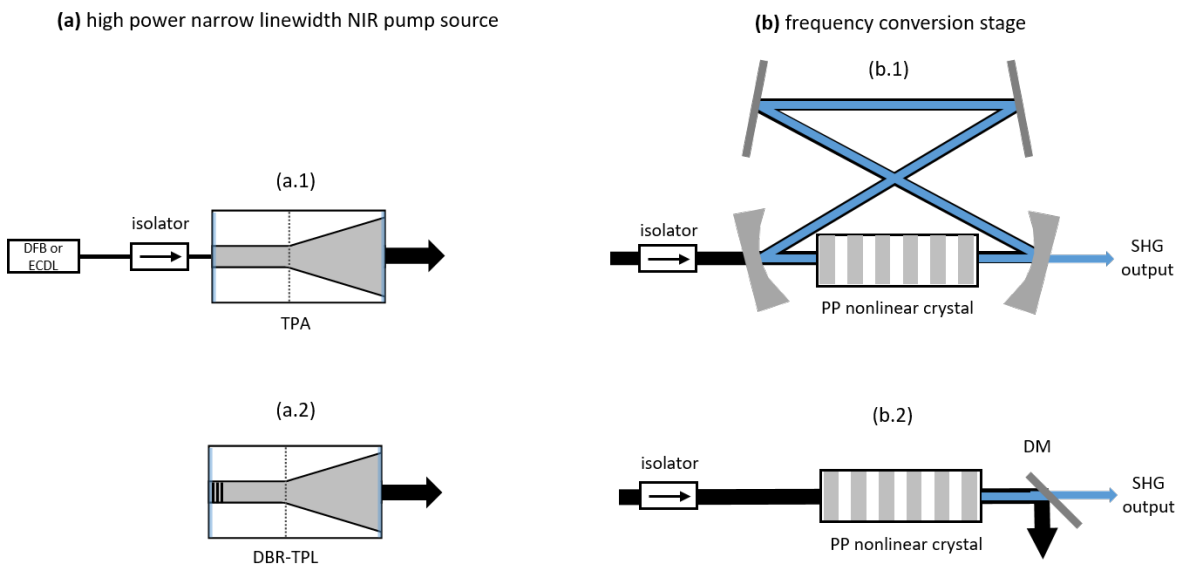
Figure I.12 – Simplified schematic of standard experimental setups for SHG of semiconductor lasers and amplifiers. (a) The NIR pump source is either a TPA in a MOPA setup, cf. (a.1) or a DBR-TPL. (b) The frequency conversion stage is either realized as a resonant ring-cavity, cf. (b.1) or a single pass setup, cf. (b.2).

The NIR pump source is either realized in a MOPA configuration or using a frequency stabilized DBR-TPL directly. The spectral purity in a MOPA configuration is essentially determined by the used MO: an ultra narrow spectrum can be achieved with extended cavity diode lasers ($\Delta\nu_{FWHM} < 100$ kHz for 5 μs) and the use of low power DFB lasers leads to a spectral width in the MHz range ($\Delta\nu_{FWHM} < 10$ MHz for 5 μs). A similar line-width can be reached with high power DBR-TPLs. There are however no rigorous measurements of the exact line-width at high powers published. The published data relies on measurements with optical spectrum analyzers (OSA) and confirms that the

line-width is below $\Delta\lambda_{FWHM} < 5$ pm, limited by the resolution of the OSA [Christensen 17]. Very high conversion efficiencies can be achieved in SHG setups using a resonant ring cavity (cf. Fig. I.12 (b.1)), but they require a high spectral purity and are usually realized with NIR pump sources in a MOPA setup. A more straightforward, but eventually less efficient, approach is a single pass SHG (cf. Fig. I.12 (b.2)), where the spectral line-width of high-power DBR-TPLs are sufficient.

Commercially available systems relying on a MOPA setup (MO: ECDL, PA: TPA) provide watt-level output powers by SHG in a resonant cavity [Toptica 19]. A very narrow spectral line-width below 500 kHz can be achieved in such systems. The setup is however costly and bulky. Recently, ultra-compact single pass SHG modules with 1.6 W output power at 576 nm have been developed by Sahm et al. with a spectral line-width of a few MHz [Sahm 18]. The NIR pump source was a miniaturized MOPA setup. The MO was a 1152 nm DBR-RW (100 mW output power) and was amplified in a high brightness tapered amplifier (more than 9 W output power with 70% power content in the central lobe). The second harmonic output power characteristics and the module are shown in Fig. I.13. The maximum SHG output power was 1.6 W corresponding to a single pass conversion efficiency of roughly 17%.
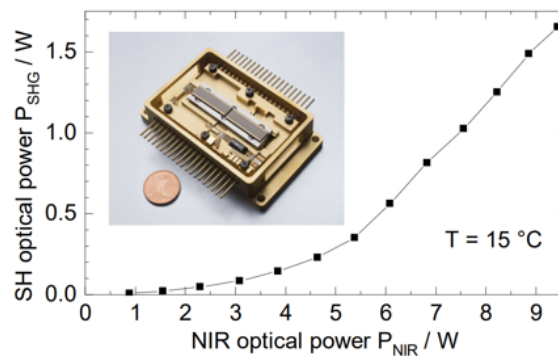
Figure I.13 – SH output power for different pump power levels. The inset shows the assembled ultra-compact module in a butterfly package with a volume of (47 x 76 x 15) mm^2 only. Taken from [Sahm 18].

An even simpler approach is the SHG of DBR-TPLs, which provide a narrow line-width high power output in a monolithic device. Up to 3.5 W SH power at 515 nm were achieved by Jensen et al. by SHG of a single high power DBR-TPL in a cascade of two nonlinear crystals [Jensen 17] as shown in Fig. I.14. The cascade of two crystals was used to avoid thermal effects in the nonlinear crystals and to increase the overall conversion efficiency which was 38.5%. The overall electrical-to-optical efficiency of the whole system was 7% and compares favorably to the efficiency of other laser sources in this spectral range.

Strategies for further power scaling of visible laser sources based on SHG of tapered lasers and amplifiers are discussed in [Jensen 14]. The ultimate limitation is however the available brightness from semiconductor based laser sources. It will be challenging to overcome the SH power barrier of 5 W using single emitters. The coherent beam combining architectures discussed in this manuscript are one potential pathway for future improvements in the field of high brightness visible laser sources and can potentially enable much higher output powers in the visible spectral range.
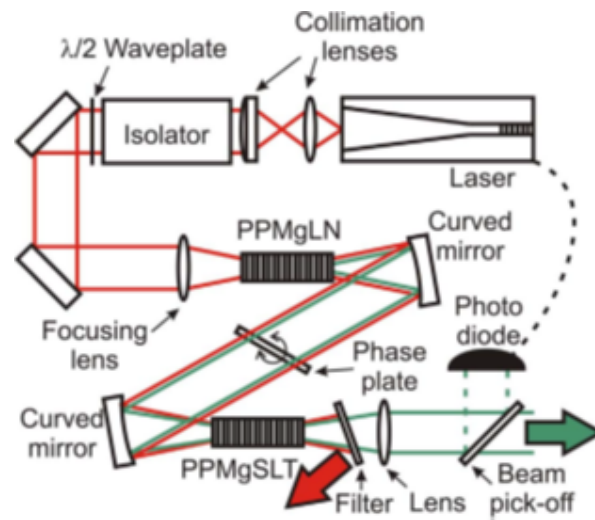
Figure I.14 – Sketch of the experimental setup for cascaded second harmonic generation of DBR-TPL. Taken from [Jensen 17].

2 Power and brightness scaling by beam combining techniques

Many technical applications require power and brightness levels that are not accessible with a single laser source. Beam combining of several emitters is therefore the key approach to develop systems with the required power and brightness levels. The most common approaches for beam combining will be discussed in this section. The focus lies on coherent beam combining. The state of the art for coherent beam combining of diode lasers is discussed and briefly put in relation with coherent beam combining of diode pumped solid state lasers.

2.1 Common beam combining techniques

Techniques used for combining N laser beams into one laser beam can be in principle divided into three categories: (a) incoherent beam combining, (b) spectral beam combining and (c) coherent beam combining. The basic principles of these three approaches are shown in figure I.15.
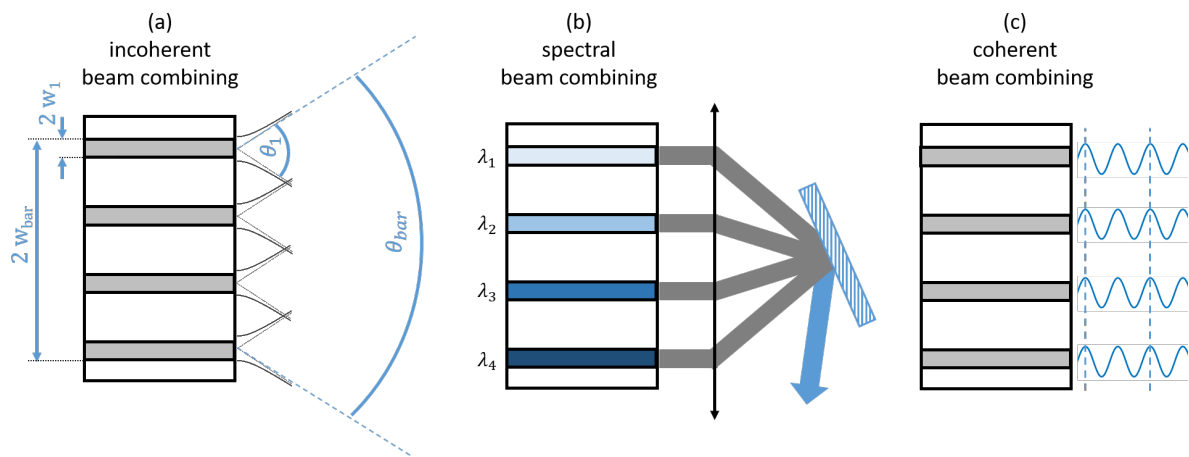
Figure I.15 – Simplified schematics of three common beam combining techniques: (a) incoherent side by side addition of N laser beams, (b) spectral beam combining of N lasers beams with slightly different wavelengths and (c) coherent beam combining of N coherent laser beams with stable phase relationship.

.

(a) Incoherent beam combining of N laser beams is probably the most straightforward concept as it does not require a fixed relationship of the spectra and phases of the individual beams. N incoherent beams with the radius w_1 at waist and the divergence Θ_1 are spatially stacked side by side leading to an N fold increase in power of the total beam. The increase in power does however not lead to an increase in brightness. Indeed the total emission radius w_{bar} is significantly increased but the angular divergence Θ_{bar} remains similar to the divergence of a single element. The BPP of the combined beam is therefore at least N times larger than for a single element and the brightness (cf. Eq. I.2), defined as power over BPP, is in fact lower (or in the ideal case) equal to the brightness of a single emitter. The most common methods for beam stacking and fiber coupling of diode laser bars are summarized in [Brauch 00]. Most high power semiconductor laser systems that are extensively used for both indirect (e.g. pumping of solid state lasers) and direct applications (e.g. low brightness material processing such as laser hardening) rely on incoherent beam combining.

(b) Spectral beam combining is the superposition of N laser beams with slightly different central wavelengths into one beam. This leads to a combined beam with N fold increased power but with a spectral width that is at least N times larger. The BPP of the final beam is equal or similar to the BPP of a single emitter which leads in the ideal case to an N fold increase in brightness. Spectrally selective components, such as diffraction gratings as shown in figure I.15 (b) are used for beam superposition.

Other spectrally selective components such as prisms or dichroic mirrors may also be used for spectral beam superposition. Configurations where spectral distance in between the different laser lines is in the range of a few tens of nanometers are usually considered as coarse wavelength multiplexing. A much narrower line-width and high wavelength stability of the individual emitters is required in so called dense wavelength division multiplexing configurations, where the laser lines are much closer to each other. Spectral beam combining is today an important building block for high brightness diode laser systems used for sheet metal cutting and other material processing application requiring a relatively high level of brightness. Commercial products in the kW regime with extremely high brightness of several GW cm^{-2} sr^{-1} are available [Fritsche 14].

(c) Coherent beam combining is more demanding than the previously mentioned techniques as it is based on constructive interference of N coherent and phase-locked electromagnetic fields. It requires identical spectral and spatial properties of each beam and a stable phase relationship [Fan 05]. The result is a single beam with N fold increased power that has the same spectral and spatial properties than a single beam and is therefore N times brighter. The two key requirements for coherent beam combining, **phase locking** and **beam superposition**, will be discussed in the following subsections. Coherent beam combining with diode lasers and amplifiers is still an exploratory field of current research and there are no commercial products available that make use of this technique. The state of the art of coherent beam combining with semiconductor lasers and amplifiers is summarized in section 2.5.

2.2   Requirements for coherent beam combining: phase locking

The gain medium is split in N parallel, in principle independent, parts in all coherent beam combining architectures. Some kind of electromagnetic signal has to be shared by the parallel emitters in order to achieve coherent phase locked emission. There are two approaches[1] to achieve phase-locking: (a) self-organization in an **extended cavity** or (b) the **parallel MOPA** configuration. The basic principles of these two approaches are shown in Figure I.16 .
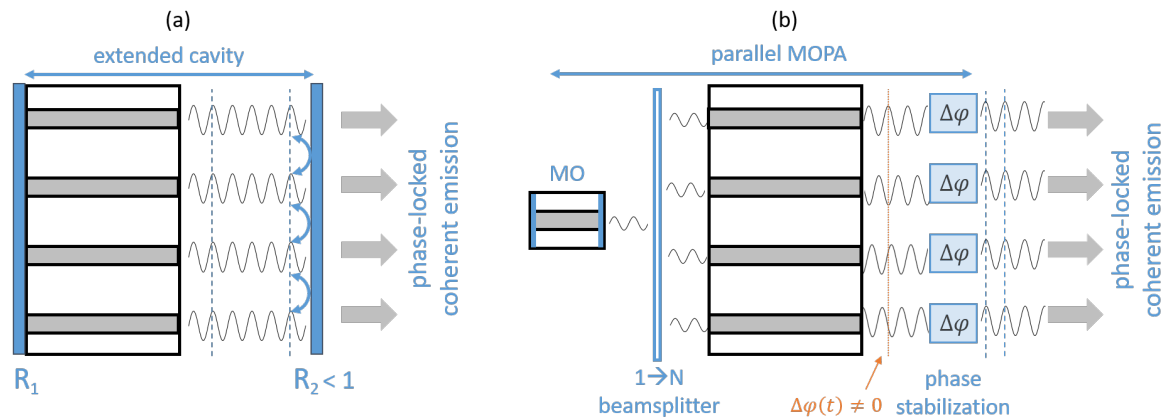
Figure I.16 – Simplified schematic of two approaches for phase-locking in coherent beam combining architectures: (a) extended cavity configuration and (b) parallel MOPA configuration.

(a)   The emitters are placed in a common extended cavity between two reflective elements R_1 and R_2. The role of the cavity is to ensure that the individual emitters share their emission and operate on one common so-called supermode. The modal theory of this approach is thoroughly summarized in [Khajavikhan 13]. Both external cavities based on beam superposition and parallel coupled cavities using some kind of spatial or angular filtering exist. Different concepts for fully self-organized external cavities and external cavities requiring some kind of active control have been extensively studied for coherent beam combining of diode lasers. The most significant work is summarized to a large part in [Schimmel 16, Lucas-Leclin 19]. The key challenge of this approach is to suppress individual and therefore incoherent operation of the different elements.

(b)   The emitters are used as individual amplifiers in the parallel MOPA configuration resulting in an interferometer setup. The beam from a stable master oscillator (MO) is split in N parts using some kind of beam splitters and injected into the amplifiers. Hence, the amplified beams are automatically coherent to each other. However, they may have a time dependent phase mismatch $\Delta\varphi(t) \neq 0$ due to thermal and acoustic noise. Active phase control in each arm is therefore necessary to ensure phase-locked coherent emission. The parallel MOPA approach is nevertheless a very straightforward concept and well suited for high power operation. In fact, incoherent self lasing can be omitted by high quality AR coatings on the emitters. The differences in the optical path lengths should be significantly smaller than the coherence length of the MO to ensure stable operation. A narrow line-width MO with a high coherence length, e.g a DFB or an ECDL, are commonly used for coherent beam combining of semiconductor amplifiers in parallel MOPA setups.

Active phase control   is necessary in most coherent beam combining setups to compensate for acoustic and thermal noise. The phase is controlled by some kind of adjustment of the optical path length in each arm. In setups using semiconductor lasers or amplifiers, this is most commonly done by variations

---

[1]One may also mention coupling via evanescent or leaky waves as a third approach, but this approach has little relevance for high power operation as the mutual coherence is usually not maintained at high bias [Botez 91]

of the current into the devices. This may however be unpractical in some cases and an external phase modulator has to be used (which is also the case for coherent beam combining of fiber lasers). The common elements used for phase modulation are: piezo mechanic actuators, acousto-optic-modulators, electro-optic-modulators and spatial light modulators [Fan 05, Brignon 13].

The common methods for active phase control include but are not limited to:

Hill climbing algorithms   The phase offsets in each arm are varied so that the combined power, measured at the output of the interferometer, is optimized. Hill climbing algorithms are straightforward to implement on embedded control units and require only a single detector. The simplest approach are sequential algorithms, but there are also more advanced hill climbing algorithms based on so-called stochastic parallel gradient descent (SPGD) algorithms [Vorontsov 98]. The convergence time increases linearly with N but is sufficient to phase-lock hundreds of semiconductor amplifiers [Redmond 13].

Synchronous multi-dither   This method is also referred as frequency-tagging (locking of optical coherence via single-detector electronic-frequency tagging - LOCSET) and consists in modulating the phase in each channel with a small dither at a proper frequency. The error signal for each channel can be retrieved by applying appropriate rapid frequency demodulation techniques of the recorded signal. Only one detector is necessary. This method was extensively investigated for coherent beam combining of high power fiber lasers [Flores 13, Klenke 18]. The scalability is limited by the number of available tagging frequencies but sufficient for roughly 100 channels.

Optical-heterodyne detection   A reference beam from the master oscillator is frequency shifted with an acousto-optic modulator and interferes with a low-power sample of each beam in the interferometer. The beat notes are recorded with one photodiode per channel. The error signal for each arm can be retrieved by signal processing of the recorded signals [Brignon 13]. The approach is highly scalable but also complex and of limited interest for coherent beam combining architectures with a limited number of channels.

Other techniques suitable for phase locking of a large number of channels are based on collective spatial interferometric measurements on a camera [Heilmann 18] or so called phase intensity mapping [Kabeya 15]. The choice of the elements and methods for the phase control is usually made after a detailed analysis of the phase-noise spectrum of the amplifiers. The bandwidth of the actuators and the speed of the optimization algorithm should be high enough to ensure phase matching with peak-to-valley fluctuations in the order of $\lambda/30$, which is regarded as a benchmark value for coherent superposition (cf. section 2.4).

2.3 Requirements for coherent beam combining: beam superposition

The coherent and phase locked beams have to be superposed in some way in order to interfere constructively. The different approaches can be classified in two categories: (a) tiled aperture far field superposition and (b) filled aperture near field superposition. The basic principles for coherent superposition of N coherent, phase locked and collimated beams are shown for both approaches in Fig. I.17.
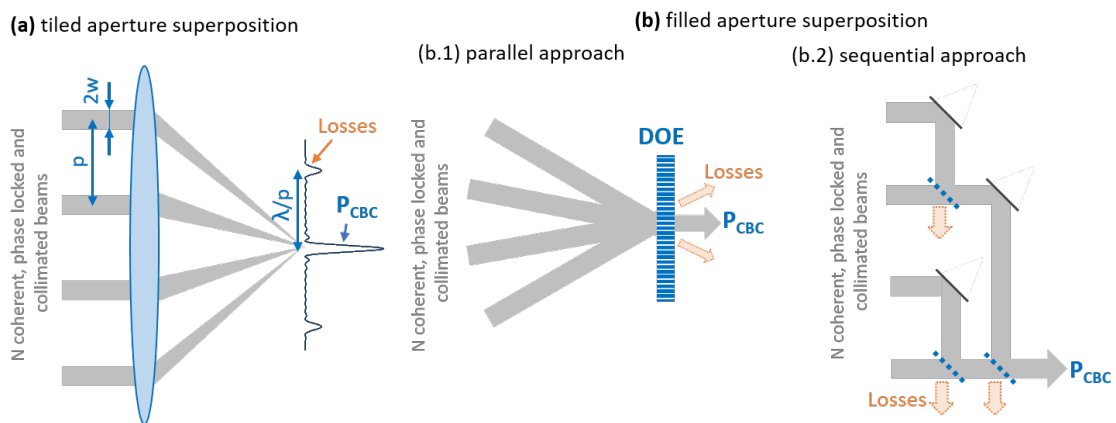
Figure I.17 – Simplified schematic for coherent beam superposition of an array of N coherent, phase locked and collimated beams: (a) tiled aperture superposition (b.1/2) parallel/sequential filled aperture superposition.

(a) Coherent **tiled aperture far field superposition** is the simplest approach. The N coherent, phase-locked and collimated beams with the diameter $D = 2w$ are arranged in an equally spaced array with the pitch p and form together a coherent near field. The combined beam can then be found in the far field, for example in the focal plane of a lens. The far field has contrasted fringes with an angular separation of λ/p and its central lobe is considered as the combined beam[1]. The number of fringes is related to the fill factor $FF = 2w/p$. The achievable combining efficiency is equal to the relative power content in the central lobe and is typically well below 100% for tiled aperture far field superposition. This approach has been mostly used for coherent beam combining closely-packed 2D fiber laser arrays [Yu 06, Bourderionnet 11, Heilmann 18]. Far field superposition is less common for coherent beam combining of semiconductor lasers and amplifiers, as it is challenging to achieve high fill factors with such devices. The few existing demonstrations typically reach poor combining efficiencies well below 10% only, as the far field consists of a high number of fringes [Redmond 11].

(b) Coherent **filled aperture near field superposition** can be done in parallel or sequential configurations. Only one optical element, usually a diffractive optical element (DOE), is used in a parallel configuration. The maximum achievable combining efficiency is limited by the diffraction efficiency of the used DOE (Leger et al. 1987). Sequential configurations make use of partially reflective optical elements as beam combiners. The combining efficiency can be theoretically 100%. Imperfections in the spatial overlap of the beams lead however typically to minor combining losses at each step. The simplest approach is a cascade of two-by-two beam superposition on non-polarizing 50:50 beam splitters (see Fig. I.17 (b.2)) and is particularly interesting for coherent superposition of a limited number of high power channels [Müller 18]. Segmented mirror splitters with zones of different reflectivity are

---

[1]The central lobe power content can be understood as a synonym for the combining efficiency in the context of tiled aperture superposition. This is not the case in this work where the technical term "central lobe power content" is used as a measure for the beam quality of slightly multimode beams.

a more advanced approach for sequential filled aperture superposition and are suitable for coherent superposition of larger numbers of channels [Klenke 18].

2.4   Combining efficiency

The combining efficiency is the ratio of the useful power in the coherently combined beam over the sum of the optical powers extracted from the emitters: $\eta_{CBC} = P_{CBC}/(\sum P_i)$. The achievable combining efficiency is influenced by the spatial overlap of the incident complex fields, besides other combining losses inherent to the approach chosen for coherent superposition (e.g. losses related to a poor fill factor in tiled aperture superposition or related to the diffraction efficiency of the DOE in filled aperture superposition). It is sufficient for the understanding of this work to express the combining efficiency for a very simple case, which is the interference of two beams on a 50:50 beam combiner (filled aperture near field superposition). Some fundamental aspects of this case are discussed below.

The complex field of a laser beam

$$\underline{E_j} = \sqrt{(I_j(x,y))} \times e^{i\varphi_j(x,y)}, \tag{I.3}$$

gets split in two parts of equal power on a 50:50 beam combiner. The transmitted part is $\underline{E_{j,t}} = \underline{E_j}/\sqrt{2}$ and the reflected part is $\underline{E_{j,r}} = i\underline{E_j}/\sqrt{2}$ (phase shift of $e^{i \times \pi/2} = i$ due to reflection). Figure I.18 (a) illustrates the interference of two coherent complex fields on a 50:50 beam combiner. The fields $\underline{E_1}$ and $\underline{E_2}$ are similar, but not necessarily identical. The fields interfere on both output paths of the 50:50 beam combiner and there is a $\pi/2$ phase-shift in between them. For a certain phase relationship of $\underline{E_1}$ and $\underline{E_2}$, one can achieve a mostly constructive interference in one pathway and a mostly destructive interference in the other pathway. In terms of power this means that most of the power, see Fig. I.18 (b) is transmitted in one pathway (P_{CBC}) and a small part is transmitted in the other pathway (Losses).
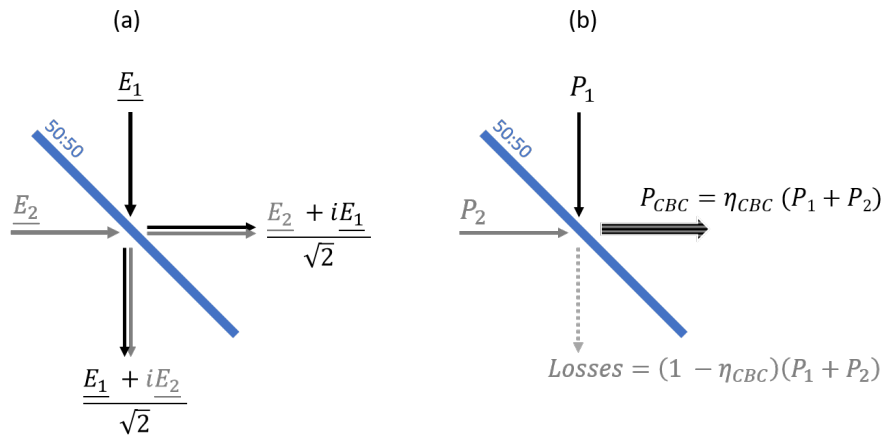
Figure I.18 – Simplified schematics of the interference of two coherent fields on a 50:50 beam combiner. (a) expressed as complex fields and (b) expressed in terms of optical power.

The combining efficiency η_{CBC} depends on the spatial overlap in amplitude and phase of the two incident fields and any spatial mismatch reduces the combining efficiency. Two exemplary cases are illustrated in Fig. I.19 (a) and (b).
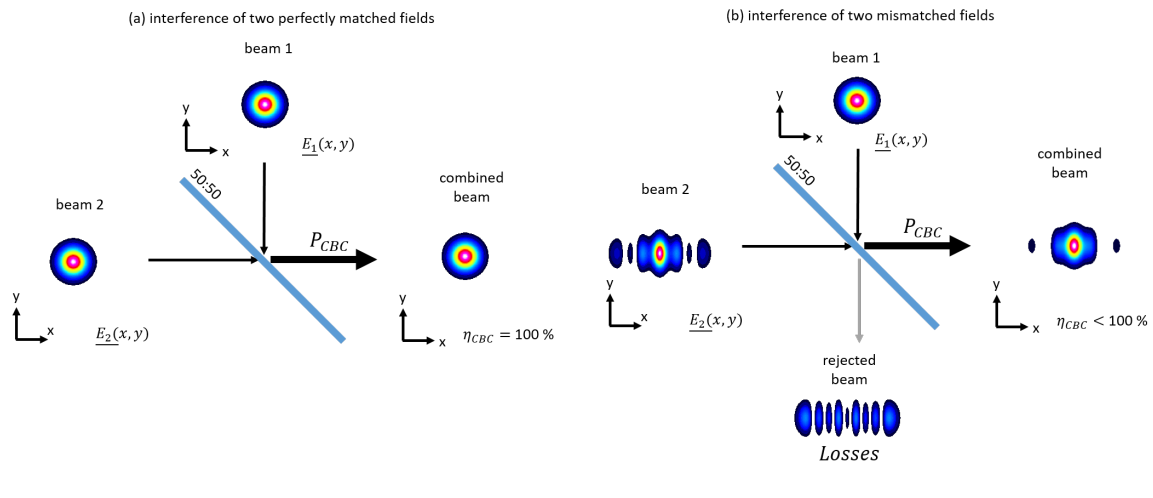
Figure I.19 – Simplified schematic of the interference of two complex fields on a 50:50 beam combiner. Beam profiles at waist are given in linear false color plots. (a) Interference of two identical Gaussian beams. (b) Interference of two mismatched fields: Beam 1 is an ideal Gaussian beam and beam 2 is slightly multimode (90% power content in the fundamental mode).

(a)   100% combining efficiency can be achieved for the trivial case of two perfectly coherent and **perfectly matched fields** (identical intensity profile, identical phase profile, identical power: $E_1(x, y) = E_2(x, y)$. All the power can be transferred to the output channel and the fields in the loss channel interfere completely destructively. The combined beam in the output channel and the input beams have identical spatial properties (waist, divergence, M^2).

(b)   The maximal achievable combining efficiency is below 100% for two **mismatched fields** (differences in intensity and/or phase profiles, power imbalances: $E_1(x, y) \neq E_2(x, y)$. The interference in the output channel can still be mainly constructive, but a small part of the power is always transferred to the loss channel. The spatial properties of the combined beam can be different to both input beams.

There are many different types of spatial mismatch, such as mismatches in: spot size, spot position, pointing, wavefronts, power or a different modal composition. The modal composition of the incident beams is different in the example given in Fig. I.19 (b). Beam 1 is an ideal Gaussian beam and beam 2 is an equally powerful but slightly multimode beam (90% of power in the fundamental mode and 10% of the power in higher order modes). The combined beam in the output channel is slightly multimode with a strong fundamental mode power content. The rejected beam in loss channel is highly multimode with almost no power content in the central lobe. This example results in a combining efficiency of 95%. These observations can be understood as a mode filter effect (spatial beam cleanup). In fact, the fundamental modes of both beams can interfere efficiently as they have an ideal spatial overlap. The higher order modes of beam 2 have however no counterpart in beam 1 and are therefore split in equal parts at the beamsplitter.

The maximal achievable combining efficiency for two coherent fields with any arbitrary kind of mismatch can be expressed with two simple equations. One can write, for the interference of two

fields, the local combining efficiency as [Goodno 10]

$$\eta'(x,y) = \frac{1}{2} \times \frac{\mid \sqrt{I_1(x,y)} \times e^{i\varphi_1(x,y)} \times \sqrt{I_2(x,y)} \times e^{i\varphi_2(x,y)} \mid^2}{\mid \sqrt{I_1(x,y)} \times e^{i\varphi(x,y)} \mid^2 + \mid \sqrt{I_2(x,y)} \times e^{i\varphi_2(x,y)} \mid^2}, \tag{I.4}$$

where $I_{1,2}(x,y)$ and $\varphi_{1,2}(x,y)$ are the intensity and phase profiles of the two incident complex fields. Any kind of mismatch in amplitude and phase at any position (x,y) reduces the local combining efficiency at this point. The total combining efficiency η_{CBC} can then be written as an intensity-weighted average of $\eta'(x,y)$ over the combining aperture

$$\eta_{CBC} = \frac{\iint \eta'(x,y)[I_1(x,y) + I_2(x,y)]dxdy}{\iint [I_1(x,y) + I_2(x,y)]dxdy}. \tag{I.5}$$

It is worth mentioning that the combining efficiency is relatively insensitive to power imbalances in the incident beams. The combining efficiency of two beams with $I_1(x,y) = 2 \times I_2(x,y)$ and perfectly matched phase profiles can still be as high as 97%. Different types of spatial mismatch, shown in Fig. I.20, were investigated in order to determine the necessary precision to achieve $\eta_{CBC} \geq 99\%$ for the coherent superposition of two coherent beams:
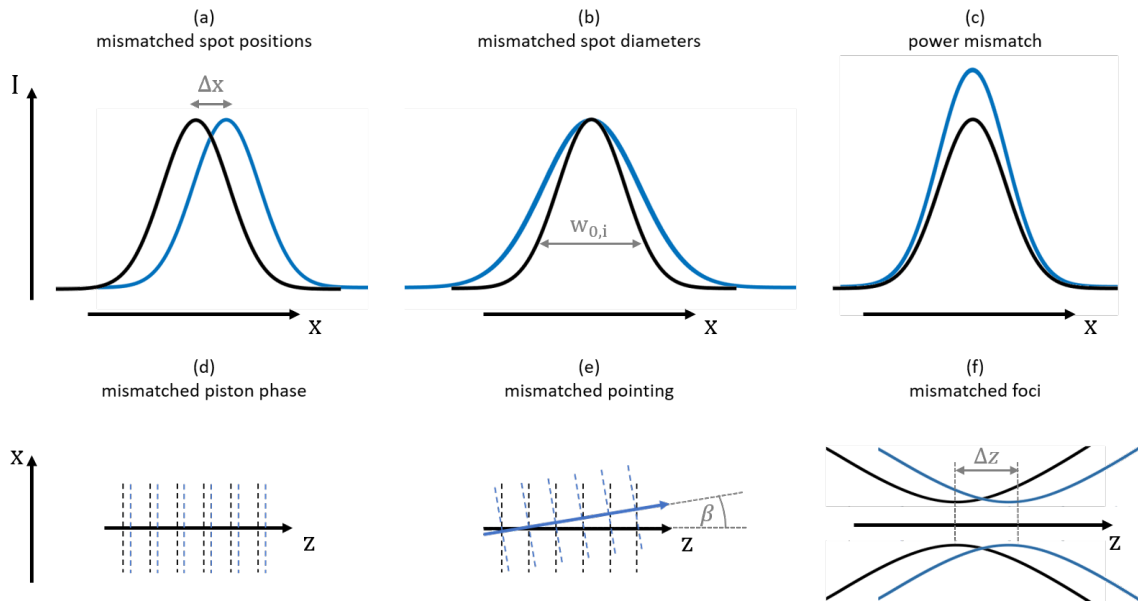
Figure I.20 – Simplified schematics of 6 different types of spatial mismatches.

(a) **Mismatched spot positions** of $\Delta x \approx 0.14 \times w_0$,
(b) **mismatched spot sizes** of $w_{0,2} \approx 1.22 \times w_{0,1}$,
(c) **power mismatches** of $P_2 \approx 1.5 \times P_1$,
(d) **mismatched piston phases** of $\Delta\varphi \approx 0.2$ rad,
(e) **mismatched pointing** of $\beta \approx 0.2 \times \theta$,
(f) **mismatched foci** with a distance of $\Delta z \approx 0.34 \times z_r$,

with P_i the optical power per beam, $w_{0,i}$ the beam radius at waist, θ the divergence angle and z_r the Rayleigh-length.

2.5 State of the art of coherent beam combining with semiconductor lasers and amplifiers

Coherent beam combining is not limited to edge emitting semiconductor lasers. It has also been demonstrated with other types of lasers relying on semiconductor gain media, such as VCSELS [Sanders 94], quantum-cascade-lasers [Zhou 19] and photonic crystal lasers [Zhu 17]. Of course, it has also been excessively studied with different types of solid-state lasers, see the textbook edited by Brignon for a broad overview [Brignon 13]. Some light is shed below on a few examples of work on coherent beam combining with edge emitting semiconductor lasers and amplifiers, that is the most relevant for the context of this manuscript.

Coherent beam combining with edge-emitting semiconductor lasers and amplifiers has been demonstrated in many configurations using all different types of emitters introduced before (single mode ridge waveguide lasers and amplifiers, broad area lasers and amplifiers[1], tapered lasers and amplifiers). Both external cavity and parallel MOPA configurations have been demonstrated. Coherent superposition was demonstrated in the far field and in the near-field. A review of the most relevant work can be found in [Lucas-Leclin 19]. The most successful and most promising demonstrations are briefly summarized in the following subsections.

2.5.1 Coherent beam combining of 47 slab coupled optical waveguide amplifiers

The work summarized below was part of a series of studies performed at MIT Lincoln Laboratory (Boston, MA, USA) on coherent beam combining of slab coupled optical waveguide amplifiers (SCOWAs). The SCOW concept [Walpole 02, Huang 03] (cf. section 1.2.1) is particularly well suited for coherent beam combining architectures as the optical mode is comparably large, nearly circular and nearly diffraction limited in both axis. The experimental setup of the most successful experimental demonstration of coherent beam combining of SCOWAs is shown in Fig. I.21. The MO, a 1064 nm DFB laser diode, was pre-amplified in an ytterbium-doped fiber amplifier (YDFA). The seed beam was split using a series of one $1\rightarrow6$ fiber splitter and six $1\rightarrow8$ beam and injected into a 1x47 SCOWA array. Each element of the array was individually addressable. The 47 beams were superposed in a filled aperture approach on one high efficiency DOE. Phase locking was achieved by adjusting the current into the amplifiers. The phase matching method was based on a SPGD hill climbing algorithm. The combined power was 40 W with an excellent combining efficiency of 87% [Creedon 12]. This is, to date, by far the highest coherently combined power from semiconductor-based lasers or amplifiers.

The impact of this work on further developments of high-power diode laser systems and their application was however limited. The reason for that may be the complexity of the experimental setup. An YDFA is necessary to provide the required seed power for the large array. The mounting and individual addressing of the large number of elements is complex and requires high technical expertise. The combined power per element P_{CBC}/N is 0.85 W and strongly limited by the single mode SCOWA.

2.5.2 Coherent beam combining of a mini-array of tapered amplifiers

The work summarized below was part of a series of studies performed at the Laboratoire Charles Fabry (Palaiseau, France) on coherent beam combining of high power diode lasers in the framework of the doctoral thesis of Guillaume Schimmel [Schimmel 16]. The amplifiers were developed and fabricated by the Ferdinand-Braun-Institut (Leibniz-Institut für Höchstfrequenztechnik, Berlin, Germany) and packaged into an individually addressable mini-array at the Fraunhofer Institut für Lasertechnik (Aachen, Germany) in the framework of the European research project BRIDLE [Unger 13]. The experimental setup is shown in Figure 13. Both coherent beam combining in (a) an external cavity configuration and (b) parallel MOPA configuration was demonstrated [Schimmel 17].

---

[1]Coherent beam combining architectures using broad area emitters are using a V-shape amplifier configuration as shown in Fig. I.6. In this configuration one can achieve almost single mode emission even though a broad area emitter is used.
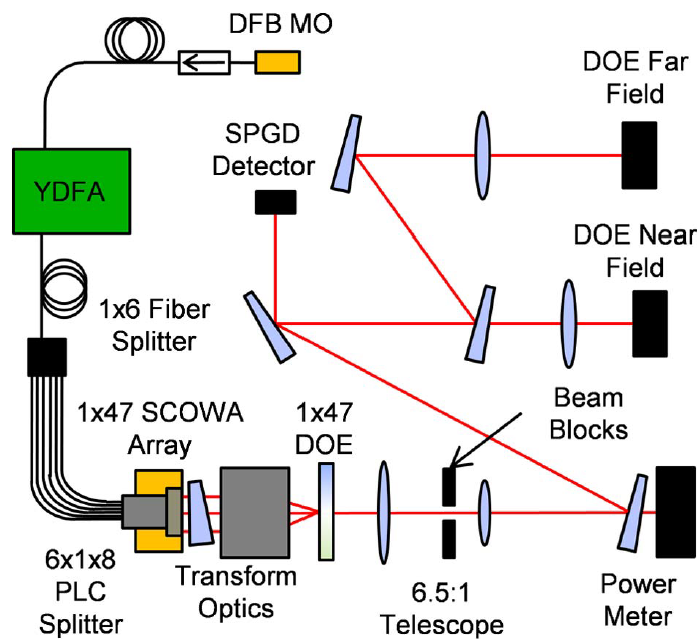
Figure I.21 – Experimental setup for the coherent combining of an array of 47 slab-coupled amplifiers (SCOWA). A single-frequency source is amplified in an Yb-doped fiber and split into 48 beams, which are butt-coupled to the array. The SCOWA output beams are combined using a single Fourier lens and DOE, and the output is sent to diagnostics. Only three SCOWA beams are shown for clarity. Taken from [Creedon 12].

(a) The **extended cavity** configuration makes use of a rear side interferometric cavity approach for phase locking, which has proven to be particular effective for coherent beam combining of tapered lasers [Schimmel 17]. DOEs are used for beam splitting and combining on both sides. Fine adjustments of the currents into the emitters were required to operate the cavity in a stable coherent supermode. Up to 12 W of coherent emission were extracted from the mini-array, of which 7.5 W were coherently combined into a nearly diffraction limited beam (>80% central lobe power content). This is, to date, the highest coherently combined power from semiconductor lasers in an extended cavity configuration. The combining efficiency was 62% percent.

(b) A 976 nm DFB MO was used in the **parallel MOPA configuration**. The DOEs used for beam splitting and combining were identical to those used in the extended cavity configuration. Phase matching was achieved with a sequential hill-climbing algorithm. The combined power was higher than for the extended cavity configuration and reached 11.5 W, which was until recently the highest coherently combined power from tapered amplifiers. The combining efficiency was significantly better than in the extended cavity configuration and was 78% at the highest power. The beam quality of the final beam was nearly diffraction limited (> 80% central lobe power content).

The results lead to the following conclusions:

- The same mini-array performed significantly better in the parallel MOPA approach than in extended cavity configuration. In fact, the drive current was limited by the onset of independent and therefore incoherent lasing of the individual emitters in the extended cavity configuration. Further power scaling appears therefore to be more straightforward in parallel MOPA configurations.

- The combined power per element was with 2.3 W significantly higher than for comparable work

(a) external cavity configuration

(b) parallel MOPA configuration
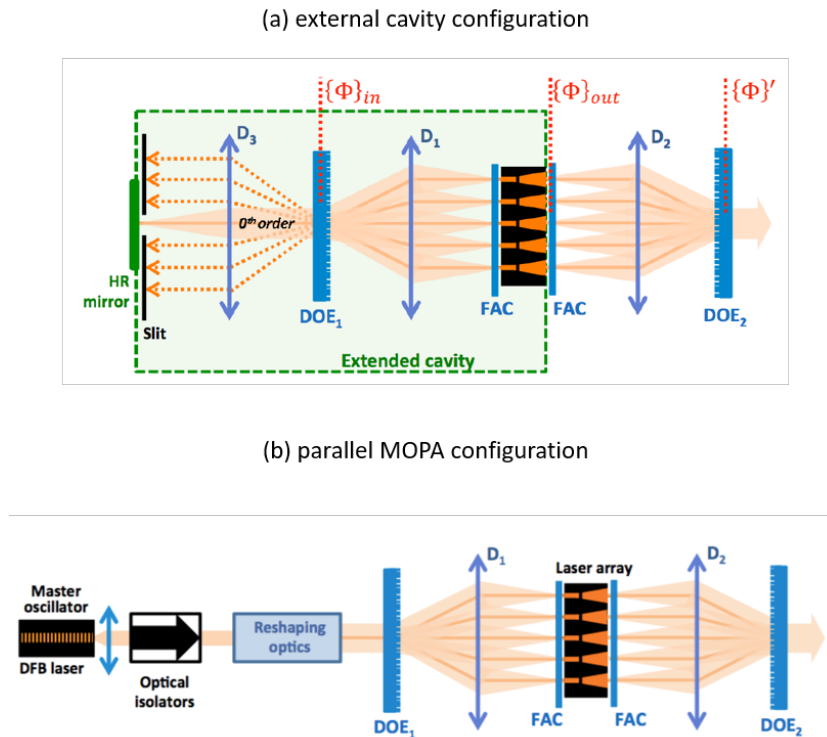
Figure I.22 – Simplified schematic of the experimental setup for the coherent beam combining of an array of 5 tapered amplifiers in (a) an extended cavity configuration and (b) a parallel MOPA configuration. FAC: 0.6 mm fast axis cylindrical collimator; DOE: diffractive optical element used as beamsplitter and combiner; $D_{1,2,3}$: 80 mm doublet. Taken from [Schimmel 17].

with single mode SCOWA amplifiers.

- The combined power per element was still well below the achievable output power from high power tapered amplifiers (cf. Table I.1) as the thermal management of the mini-bar was challenging and collective thermal effects lead to an early thermal rollover of the devices. One can expect a roughly two fold increase in power per emitter for optimized thermal management.

- The mounting of the mini-bar was quite compact but the overall dimensions of the optical setup were quite bulky (The diameter (2") and focal length (80 mm) of the optics required for beam splitting and combining with the DOEs was quite large).

- The performance of a minibar was limited by its weakest element. The whole bar had to be replaced in case of failure of a single element. The mounting and individual addressing was complex.

2.5.3 Overview of work on coherent beam combining with semiconductor lasers and amplifiers

Coherent beam combining with semiconductor lasers and amplifiers has been demonstrated in many configurations in the last 25 years. The most important work is summarized regarding the power level and the number of emitters in Fig. I.23. Work with a demonstration of coherent superposition into a single nearly diffraction limited beam is represented by filled circles (extended cavity configurations) and filled squares (parallel MOPA configurations). Demonstrations of phase locked and coherent emission without coherent superposition into a single diffraction limited beam (empty symbols) are also given for completeness, although not directly comparable to the other results. Each data-point is linked to a row in Table I.2 (see lowercase letters a-n), where a more detailed description of the corresponding

experiment is given. The graph shows that significantly different approaches have been chosen (using 4 to 900 emitters) with very different output powers.

The overview of the state of the art leads to the following conclusions:

- Coherent beam combining in parallel MOPA configuration appears to be more adapted for high power operation.

- Phase locking in a parallel MOPA configuration was demonstrated with > 100 emitters and appears to be more scalable than phase locking in an extended cavity configuration.

- Coherent beam combining in extended cavity configuration with successful demonstration of coherent superposition into one diffraction limited beam lead typically to output powers in the range of a few watts only. These power levels are not competitive to high power single emitter tapered lasers, capable of > 10 W single mode emission.

- Tapered lasers and amplifiers are the only architecture that has proven to provide output powers in the range of 10 watts in a simple setup using a limited number of amplifiers.

- SCOWA and SCOWLs enable coherent beam combining with > 80% combining efficiency but are limited to operation below 1 W per emitter.
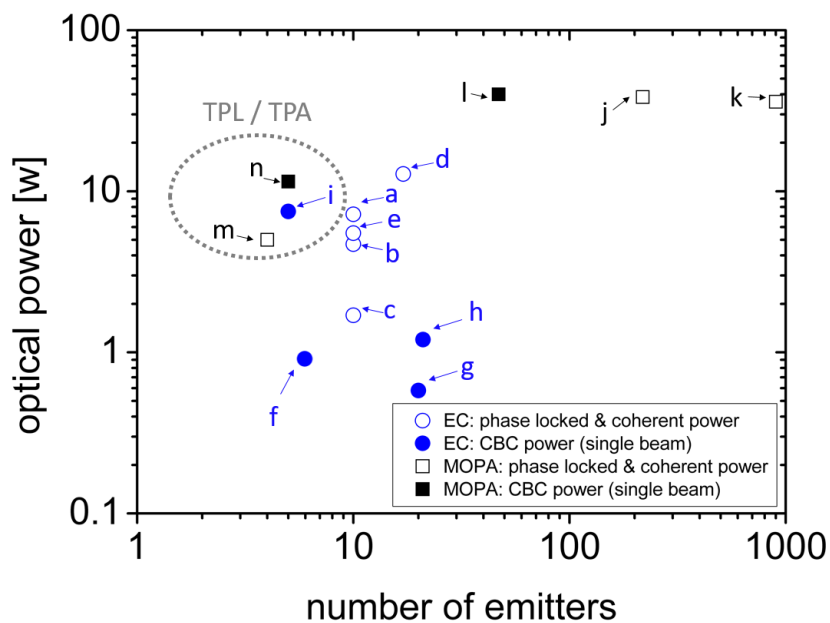
Figure I.23 – Overview of state of the art for coherent beam combining with edge emitting NIR semiconductor lasers. Configurations in extended-cavity (EC – blue symbols) and parallel MOPA configuration (black symbols). The filled symbols represent work, were coherent superposition into a single nearly diffraction limited beam was demonstrated. Additional information about the different experiments is provided in Table I.2 (see lower-case letters a-n).

TABLE I.2 - Overview of the state of the art for coherently combined edge-emitting semiconductor lasers and amplifiers in the NIR.

	number of emitters	power [W]	single beam at output?	combining efficiency	emitter type	reference
a	10	7.2	no	-	SCOWL	[Huang 09]
b	10	1.7	no	-	tapered lasers	[Pabœuf 08]
c	10	4.7	no	-	broad area lasers	[Liu 13]
d	17	12.8	no	-	broad area lasers	[Liu 10]
e	10	5.5	no	-	broad area lasers	[Liu 18]
f	6	0.97	yes	-	tapered lasers	[Pabœuf 11]
g	20	0.58	yes	-	conventional RW	[Barthelemy 92]
h	21	1.2	yes	81 %	SCOWL	[Montoya 12]
i	5	7.5	yes	62 %	tapered lasers	[Schimmel 17]
j	218	38.5**	no	-	SCOWA	[Redmond 13]
k	47	40	yes	87 %	SCOWA	[Creedon 12]
l	900	36**	no	-	conventional RW	[Levy 95]
m	4	5*	no	-	tapered amplifiers	[Osinski 95]
n	5	11.5	yes	72 %	tapered amplifiers	[Schimmel 17]

(Rows a–i grouped as "extended cavity"; rows j–l grouped as "parallel MOPA")

* QCW operation
** coherent power measured in the far field integrated over numerous side lobes

3   Conclusions for the experimental strategy of this work

The goal of this work is to develop simple high-power high-brightness systems. The architectures should be based on a limited number of emitters and standard optical elements in a compact setup. The following choices were made in consideration of the basic principles and the state of the art of high brightness single emitters and of coherent beam combining discussed before:

- Tapered lasers and amplifiers are by far the brightest emitters available and are the preferred building block for simple high-brightness systems based on coherent beam combining. The NIR around 980 nm was chosen as the spectral range, as high-brightness tapered amplifiers are widely available in this spectral range.

- Architectures based on single emitters were chosen to benefit from the full power potential of the emitters as the performance per emitter is more limited by thermal effects for arrays of emitters. Furthermore, this allows very simple individual electrical addressing and individual collimation of each emitter.

- Phase-locking in a parallel MOPA configuration was chosen as this has proven to be the preferred solution for high power operation. Narrow line-width master oscillators were used for potential application in experiments requiring a high spectral purity. Hill climbing algorithms are sufficiently fast for phase control of a limited number of emitters.

- Sequential filled aperture coherent superposition with standard off the shelf non-polarizing beamsplitters was chosen to achieve high combining efficiencies in a simple and compact setup.

- The focus lies on operation in the continuous wave regime. Further power scaling in the quasi-continuous-wave regime and operation in the ns regime is investigated.
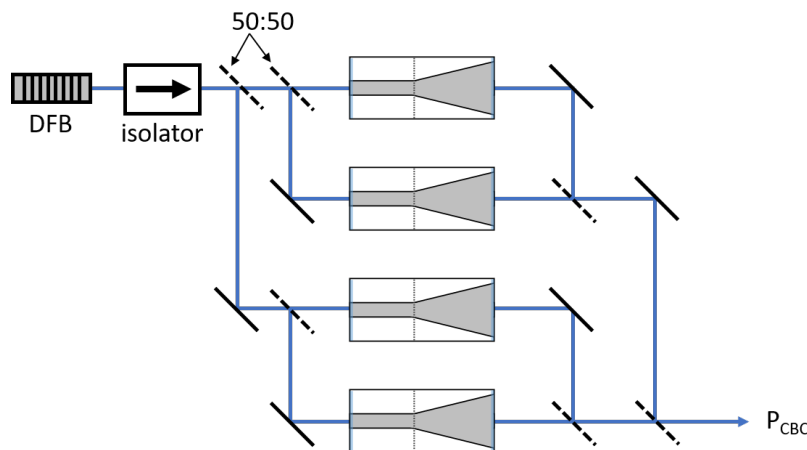
Figure I.24 – Simplified schematic of the coherent beam combining architectures investigated in this work.

Figure I.24 shows the typical architecture of the coherent beam combining architectures investigated in this work. The experimental work was realized in a collaboration of the Laser research group at Laboratoire Charles Fabry (Institut d'Optique Graduate School, CNRS, Université Paris-Saclay, Palaiseau, France) and the high power diode laser research group at Ferdinand-Braun-Institut (Leibniz-Institut für Höchstfrequenztechnik, Berlin, Germany).

Chapter II

Investigation of tapered lasers and amplifiers

Objectifs

This chapter covers a more detailed investigation of the properties of tapered lasers and amplifiers. Methods for the characterization of the beam quality are discussed in the first section. Preliminary experiments with tapered lasers having different epitaxial layer designs are discussed in the second section. One vertical design is chosen for further more detailed studies of different lateral amplifier designs. The focus lies on the analysis and understanding of beam quality degradation effects. Intensity and phase noise measurements are also discussed.

Contents

1   Spatial beam properties of tapered amplifiers

The understanding of the spatial beam properties of tapered lasers and amplifiers is important for the development of coherent beam combining architectures. Several physical effects influence the spatial beam properties of such devices and lead to beams that are highly astigmatic and slightly multimode in the lateral (SA) direction. Figure II.1 illustrates in a simplified view the evolution of the spatial beam properties in a tapered amplifier (first row: top view on SA; second row: side view on FA). DFB laser diodes with diffraction limited beam quality are most commonly used as the master oscillator. The beam from the master oscillator is collimated with an aspherical lens (L_1) with a high numerical aperture (NA). Eventually, additional elements for beam shaping, optical isolation and for control of the polarization[1] may be placed in the collimated beam. The beam is then coupled into the ridge waveguide of the TPA with a high NA aspherical lens (L_2). The beam is index-guided in FA in the whole amplifier by a single mode waveguide and is collimated in SA with a high NA aspherical lens (L_3). In SA however, the beam is index-guided only in the single mode ridge waveguide and diverges in the gain-guided tapered section. This affects the spatial properties of the beam in two ways:
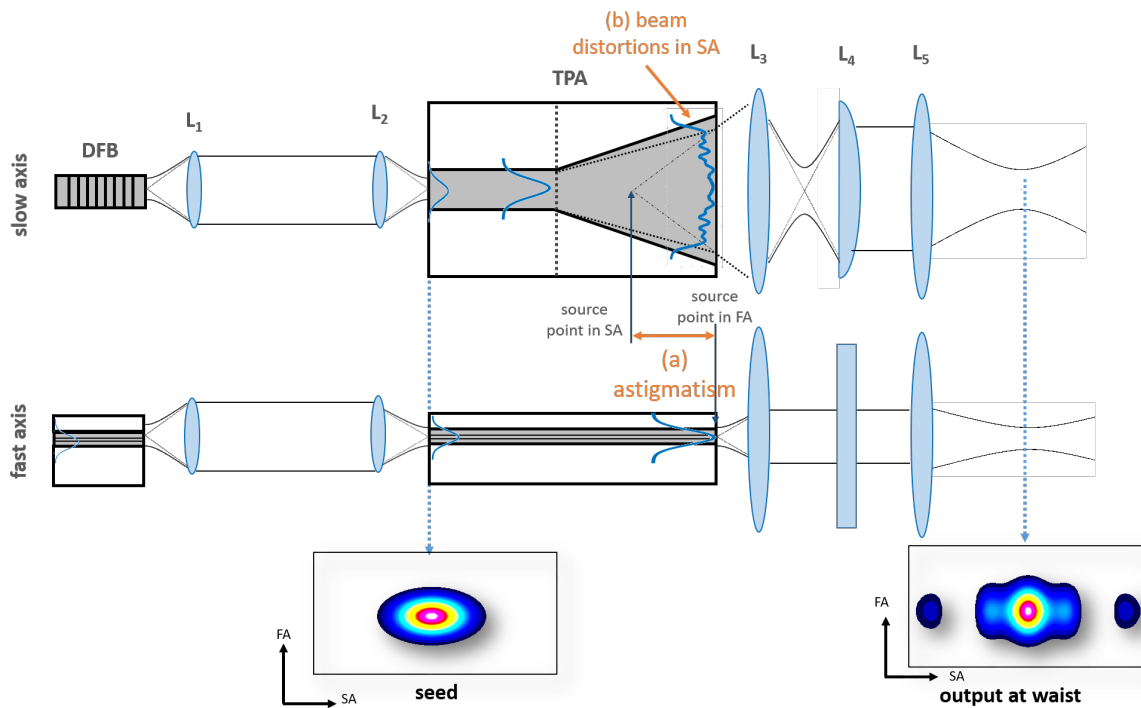
Figure II.1 – Simplified schematic of a typical MOPA setup using a tapered amplifier. The first row shows a the evolution of the beam profiles in slow axis, the second row shows the evolution of the beam profiles in fast axis.

(a)   The beam is consequently highly **astigmatic** at the output as the virtual source point in SA is not in the same plane as the virtual source point in FA [Kelemen 04]. The virtual point source is located at about L/n_{eff} distance to the output facet, where L is the length of the tapered section and n_{eff} is the effective refractive index of the waveguide. This distance depends on the current into the tapered section and the temperature of the device as the effective refractive index changes with temperature and carrier density. The astigmatism is corrected by a cylindrical lens (L_4) used for collimation in SA (cf. Fig II.1).

---

[1]The beams from edge emitting semiconductor lasers and amplifiers are usually linearly polarized in lateral direction.

(b)   The beam is **slightly multimode** in SA. There is no mode-filtering in the gain-guided tapered section and the beam quality is deteriorated by gain saturation in the center, carrier lensing, thermal lensing, filamentation and other effects [Lim 14]. The beam profile in SA is therefore far from Gaussian at the output facet of the amplifier. In fact, a top-hat-like intensity profile with filament-like intensity modulations is usually measured at the output-facet (cf. Fig II.1).

The output beam shape at waist (astigmatism corrected) consists typically of a clearly pronounced central lobe and some higher-angle side lobes in SA (cf. Fig II.1). The beam quality is considerably deteriorated in SA. While single-mode laser beams maintain the same intensity distribution during propagation, this is not the case for multimode beams from tapered lasers and amplifiers as shown in Fig. II.2 (a-c). The figure shows three beam shapes from a typical TPA measured with a CCD camera at three different positions along the caustic (at waist and three Rayleigh lengths z_r before and after the waist)[1]. The beam shape consists of a clear central lobe only at waist (b) and is far from Gaussian in SA in the other planes (a,c). The beam profiles in SA are varying considerably during propagation, which indicates a significantly deteriorated beam quality in this direction. The beam profiles in FA are however nearly Gaussian in all planes, which indicates a nearly diffraction limited beam quality in FA.
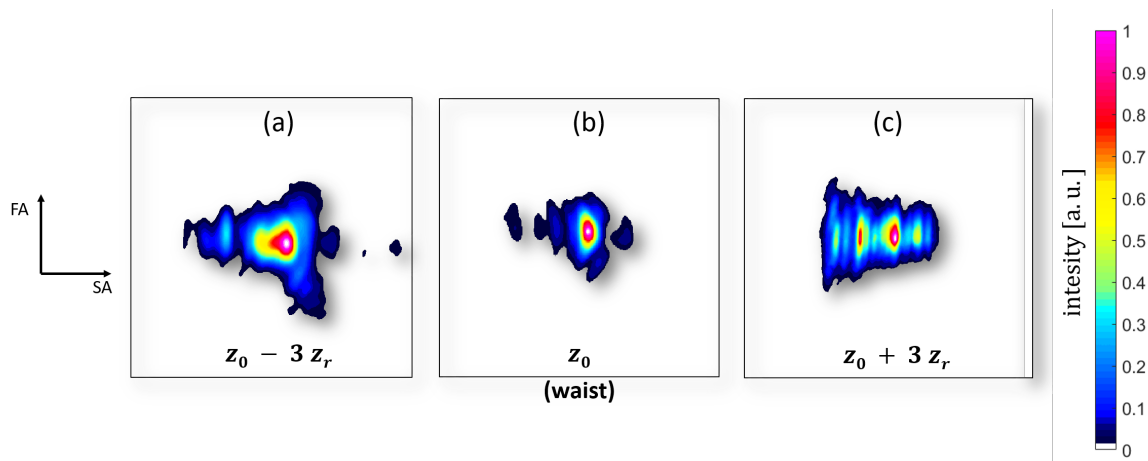
Figure II.2 – Measured beam shapes in false color plots of a tapered amplifier at waist ($z = z_0$) and at $\pm 3 z_r$ distance to waist. Each image was normalized on independently the give false-color scale.

While it is quite straightforward to describe the spatial properties of an ideal Gaussian beam, one has to pay special attention to apply the right criteria to evaluate:

- the **beam radius** and **divergence** of slightly multimode laser beams. Several definitions are commonly used leading to significantly different values. See subsection 1.2.

- the **beam propagation parameter** M^2 allowing to compare the spatial properties of slightly multimode laser beams to those of ideal Gaussian beams. See subsection 1.3.

- the so-called **central lobe power content**. This is a commonly used term to evaluate the relative diffraction-limited power content of a slightly multimode laser beam. See subsection 1.4.

In order to define the right criteria for the evaluation of these spatial properties, an analytic expression of a slightly multimode beam is investigated below.

1.1   Modal content of slightly multimode beams

The model of the Gaussian beam introduced in the previous chapter is not sufficient for the description of laser beams similar to the beam shown in Fig II.2. In fact, the Gaussian beam is only the fundamental

---

[1]The design of the amplifier used for this visualization will be characterized in detail in section 3.

mode of a complete orthogonal set of modes, the so-called Hermite-Gaussian modes E_{nm} that can be used to compose or decompose any arbitrary field distribution [Saleh 19][1]. The complex electrical field distribution E_{nm} (also transverse electromagnetic mode TEM_{nm}) is essentially described by the product of the Gaussian function with a Hermite polynomial in x and y direction respectively:

$$E_{nm}(x,y,z) = E_0 \frac{w_0}{w(z)} \cdot H_n(\sqrt{2}\frac{x}{w(z)}) \cdot \exp(-\frac{x^2}{w(z)^2}) \cdot H_m(\sqrt{2}\frac{y}{w(z)}) \cdot \exp(-\frac{y^2}{w(z)^2})$$
$$\cdot \exp -i\Big[kz - (1+n+m)\arctan\frac{z}{zr} + \frac{k(x^2+y^2)}{2R(z)}\Big], \tag{II.1}$$

where $H_{n,m}$ is the Hermite polynomial of order n, m used to determine the shape of the field in x, y direction respectively. The functions for the beam radius $w(z)$ and for the radius of curvature $R(z)$ are as described for the fundamental Gaussian beam in chapter one. The intensity distribution of the first Hermite-Gaussian modes are visualized in Fig. II.3.
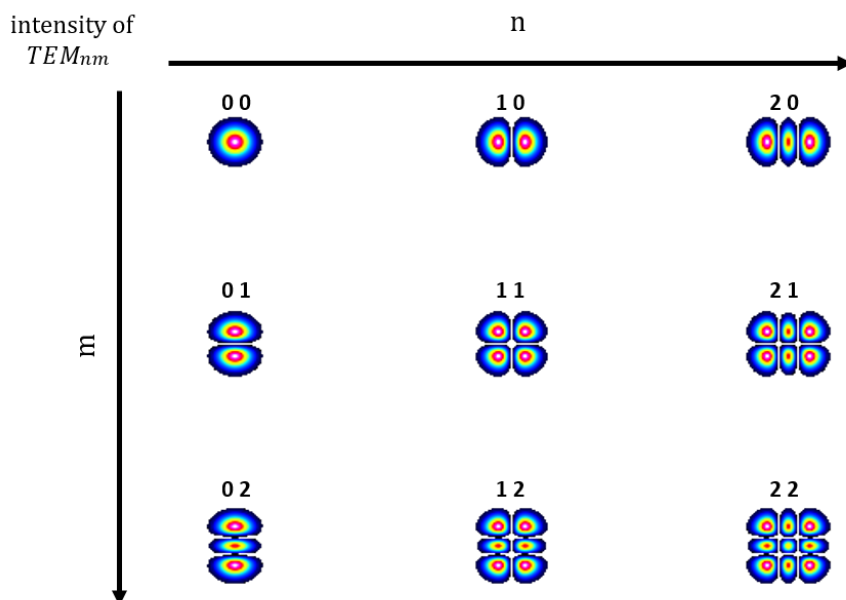
Figure II.3 – Intensity distribution of a few Hermite-Gaussian modes

One can construct arbitrary optical fields as a sum of these modes

$$E(x,y,z) = \sum_n \sum_m c_{nm} \cdot E_{nm}(x,y,z), \tag{II.2}$$

where the complex expansion coefficient c_{nm} defines the relatives amplitudes and phases of the different modal contributions.

The power content in each mode writes as $P_{nm} = |c_{nm}|^2 / \Big(\sum_n \sum_m |c_{nm}|^2 \Big)$. Equations II.1 and II.2 were used to construct two exemplary fields shown in Fig. II.4 that will be used to demonstrate the different definitions for the beam diameter and the divergence. Both exemplary fields (a) and (b) have a strong power content in the fundamental mode (91% and 71% respectively). The rest of the power is distributed onto higher order modes in horizontal direction. The resulting intensity distribution at waist is somewhat similar to what is usually observed with tapered lasers and amplifiers (cf Fig. II.2 (b)), as the intensity profile at waist consists of a clearly visible central lobe and some side lobes at lower intensity. Furthermore, the intensity profiles of the two examples are varying during propagation (see

---

[1]Another orthogonal base of modes are the Laguerre-Gaussian modes. This base is commonly used for optical fields expressed in cylindrical coordinates.

beam profiles at $z_0 + z_r$ and $z_0 + 2z_r$ in Fig. II.4). The two exemplary fields (a) and (b) will be used in the following subsection for visualization of the different definitions for the beam radius, divergence and beam propagation parameter.
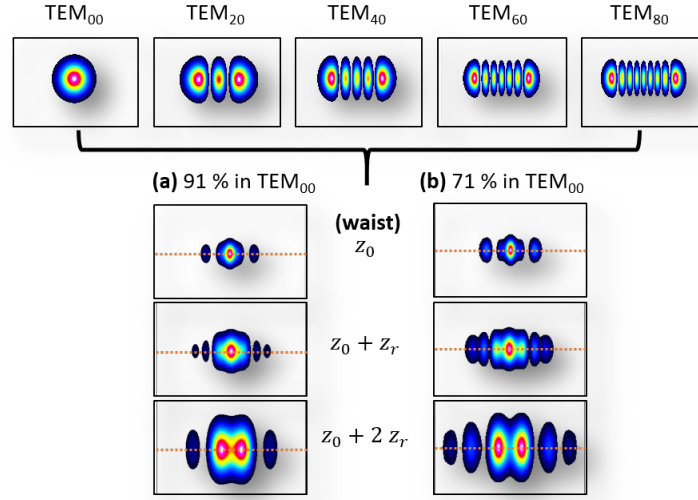
Figure II.4 – Intensity distribution of two exemplary slightly multimode fields constructed as a superposition of a few higher order Hermite-Gauss modes. Beam (a) and (b) have a relative power content of 91% and 71% in the fundamental mode respectively. The rest of the power is similarly distributed on higher order modes in x-direction. Only even mode-numbers were used to achieve a symmetric beam profile at waist. Real expansion coefficients c_{nm} were used for all modes (same phase for all modes). The $1/e^2$ radius of the fundamental mode was $100\,\mu\text{m}$. The exact modal compositions are (in terms of power per mode): (a) 91% TEM$_{00}$ + 2.25% TEM$_{40}$ + 2.25% TEM$_{60}$ + 4.5% TEM$_{80}$ and (b) 71% TEM$_{00}$ + 7.25% TEM$_{40}$ + 7.25% TEM$_{60}$ + 14.5% TEM$_{80}$.

1.2 Beam width and divergence of slightly multimode laser beams

Different definitions are commonly used to define the beam radius w (or diameter $D = 2w$) of a laser beam. A straightforward method is the so-called clip-level method, where the beam radius is defined as the distance from the optical axis to the point where the intensity is equal to a certain clip-level. The clip levels area commonly chosen at 50% of the peak intensity (full width half maximum - FWHM - diameter) or at $1/e^2 = 13.5\%$ of the peak intensity ($1/e^2$ beam diameter). Clip-level beam widths are easy to measure but neglect the power content below the clip-level intensity completely. Less common but also useful is the method to define the beam width as the size of an aperture containing 95% of the optical power. Here, only 5% of the power is neglected for the determination of the beam width. The spatial distribution of the optical power within the aperture has however no influence on the 95%-power content beam width.

The only method to determine the beam width that takes into account the whole beam and the spatial distribution of the power within the beam is the so-called second-moment beam width

$$w_{2nd} = 2\sqrt{\frac{\iint I(x,y) \cdot (x - \bar{x})^2 \, dx \, dy}{\iint I(x,y) \, dx \, dy}}, \tag{II.3}$$

with the beam centroid $\bar{x}$ in x-direction

$$\bar{x} = \frac{\iint I(x,y) \cdot x \, dx \, dy}{\iint I(x,y) \, dx \, dy}. \tag{II.4}$$

The second-moment beam width in y-direction is calculated accordingly. The root-term in Eq. II.3 is in fact the standard deviation σ of the intensity and one therefore also refers to the second moment beam diameter as $D_{4\sigma}$ beam diameter (because one considers four times σ as the diameter). For a Gaussian beam profile, the second-moment beam diameter is equal to the $1/e^2$ beam diameter. In contrast, the second moment beam diameter is usually significantly larger for beam profiles with a clear Gaussian central lobe and low-intensity side-lobes. The disadvantage of this definition is however that it requires numerical calculations and that noise in measurement data can considerably increase the measured beam width.

The different definitions of the beam widths are now applied to the exemplary slightly multimode fields (a) and (b) defined earlier in Fig. II.4. The SA beam profiles (horizontal x-direction) are shown as solid blue lines in Fig. II.5 (a) and (b). The three different beam diameters are highly different for the exemplary field (a). The side-lobes are well below the $1/e^2$ clipping-level, leading to a small D_{1/e^2} beam diameter of $188\,\mu$m. The $D_{95\%}$ beam diameter is in this example very large as the two side-lobes contain more than 5% of the total energy[1]. The second-moment beam diameter lies in this case in between the two other diameters. The situation is very different for the second example shown in Fig II.5 (b), where the differences in between the different diameters are in the range of $10\,\mu$m only. These two examples illustrate the problems in using methods other than the second-moment method, as the full beam and the power distribution within the beam has to be taken into account for the definition of a meaningful beam width.
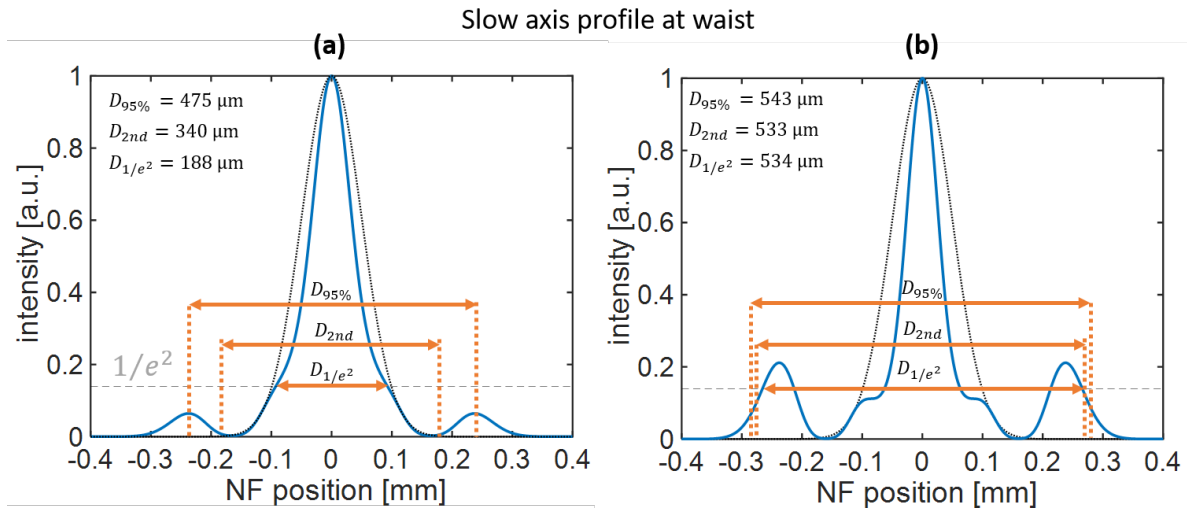
Figure II.5 – Slow axis (x-direction) beam profiles (blue solid line) of the two exemplary fields (a) and (b) introduced earlier in Fig. II.4. The different beam diameters using 13.5% clip-level method D_{1/e^2}, the 95% power content method $D_{95\%}$ and the second moment method D_{2nd} are given. The dashed black line represents the profile of the TEM_{00} component ($D = 200\,\mu$m) .

Similar to the different definitions of the beam widths one can also define the far field **divergence** angle with a clip-level method (e.g. Θ_{1/e^2}), a relative power content (e.g. $\Theta_{95\%}$) or the second moment method (Θ_{2nd}). The two far field profiles shown in Fig. II.6 (a) and (b) are the far field profiles of the two exemplary fields (a) and (b) discussed earlier. Example (a) shows significantly different values of the divergence for the different methods, similar to the differences for beam widths at waist. The values are again very close to each other for example (b). As stated above for the beam width, one also should consider the full beam profile in the far field and the angular power-distribution withing the profile to determine a meaningful divergence angle. The 95% divergence angle is however very commonly used for the specifications of diode lasers, as this parameter is useful for the design of the optical setup.

---

[1]It may be confusing on the first glance that the side-lodes contain this much energy for a 91% power content of the fundamental mode. Interference effects within the different mode lead in this case to an increased intensity in the side-lobes and a reduced central lobe power content (See dashed black line and blue line in Fig. II.5 (a))
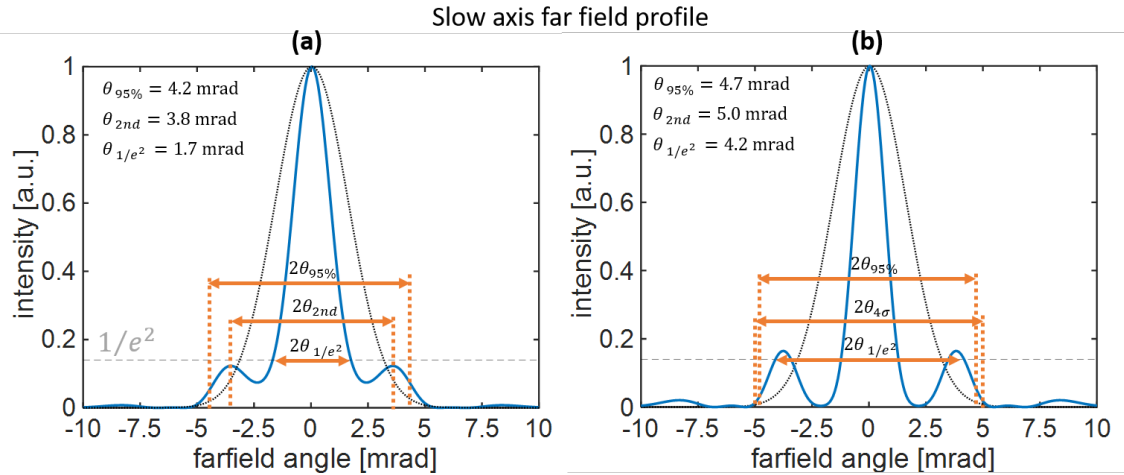
Figure II.6 – Slow axis far field beam profiles (blue solid line) of the two exemplary fields (a) and (b) introduced earlier in Fig. II.4. The far field divergence is given using using 13.5% clip-level method Θ_{1/e^2}, the 95% power content method $\Theta_{95\%}$ and the second moment method Θ_{2nd} are given. The dashed black line represents the far field profile of the TEM_{00} component ($\Theta = 3.2$ mrad).

1.3   Beam propagation factor

The beam propagation factor M^2 is used to compare the beam propagation properties of a laser beam to an ideal Gaussian Beam [Siegman 98]. The M^2-factor can be simply calculated by $M^2 = \frac{BPP \times \pi}{\lambda}$, where the BPP is the product of beam radius at waist and far field divergence angle. As there are different definitions for the measurement of these parameters, the M^2-values appear unfortunately in the literature in different ways and one usually writes M^2_{1/e^2} if the parameters were measured by the 13.5% clip level method, $M^2_{95\%}$, if the parameters were measured by the 95% method and M^2_{2nd} or $M^2_{4\sigma}$ when the parameters were measured with the second-moment method. The question however is, if expressing the M^2 - factor with anything other than the second-moment method is actually meaningful?

Exemplary slightly-multimode fields were again investigated to answer this question. The TEM_{00} power content was varied from 100% to 50% in steps of 1% and the remaining power was distributed onto some higher order modes in horizontal direction (in this example: 25% on TEM_{40}, 25% on TEM_{60} and 50% on TEM_{80}). The exemplary fields (a) and (b) introduced earlier in Fig. II.4 are included in this series of samples for a TEM_{00} power content of (a) 91% and (b) 71% respectively. The radius at waist and the far field divergence were calculated in horizontal SA-direction for each sample and the SA beam propagation factor was determined using the different definitions for beam width and divergence. The results plotted in Fig. II.7 show that the evaluated beam propagation factors by the different methods are in fact highly different for almost any slightly-multimode beam. One might expect that the beam propagation factor is a slowly varying monotonic function of the power content in the fundamental mode, which is clearly not the case if beam width and divergence are determined by the $1/e^2$ method. The $1/e^2$-method underestimates the M^2 value and also leads to beam propagation factors below unity in some cases (cf. Fig II.7), which does not make sense. The values calculated for the 95% method are also significantly different to the second-moment method and there are some cases where (a) $M^2_{95\%} > M^2_{2nd}$ and where (b) $M^2_{95\%} < M^2_{2nd}$. The $M^2_{95\%}$ increases monotonically but somewhat irregularly with decreasing fundamental mode power content. Only the M^2_{2nd} method leads to a meaningful result, which is a (in this example linearly) increasing beam propagation factor with decreasing fundamental mode power content. There is however no direct connection of the power content in the fundamental model and the M^2 factor as its value depends on the distribution of the remaining power on the higher order modes[1].

---

[1]In other words, the slope of the M^2_{2nd}-line in Fig. II.7 would for example be significantly shallower if the power would be shared by the fundamental mode and TEM_{10} with no power content of other higher order modes.
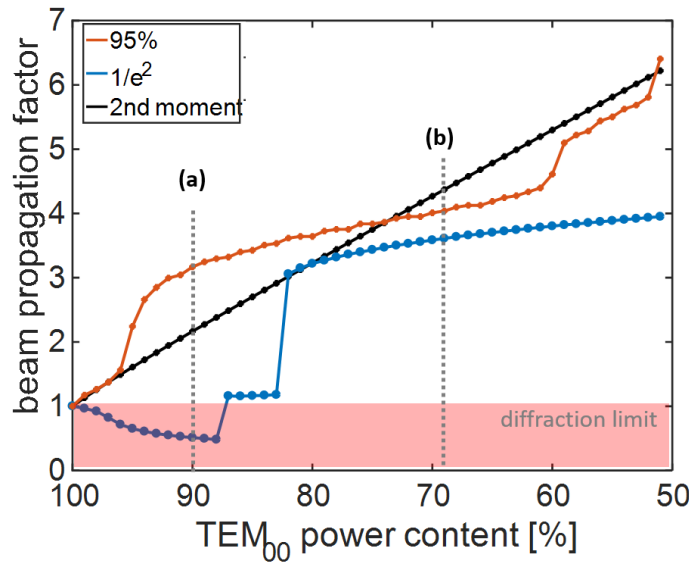
Figure II.7 – Calculated SA (horizontal x-direction) beam propagation factors for exemplary multimode fields at different TEM_{00} power content. The remaining power was distributed onto some higher order modes in horizontal direction. The fields (a) and (b) are identical to the fields described earlier in Fig. II.4

.

Nevertheless, it is very common to specify the M^2_{1/e^2} parameter on data-sheets of commercially available tapered lasers and amplifiers [DILAS 19] and also in scientific publications (see references within Table I.1 in chapter I). One should however keep in mind that a specification of a M^2_{1/e^2}-factor close to unity does not necessarily mean that the laser beam is close to an ideal Gaussian beam.

Furthermore one has to pay attention when using the M^2-factor for calculation of the beam size at distance z to the waist by

$$w(z)^2 = w_0^2\Big(1 + \frac{z^2}{z_r^2}\Big) = w_0^2 + \big(M^2\big)^2\Big(\frac{\lambda}{\pi w_0}\Big)^2 z^2, \qquad \text{(II.5)}$$

where w_0 is radius at waist. This only holds true when the second-moment definition of beam width and M^2 are used. In fact, the evolution of the $1/e^2$ or 95% beam radius of a slightly multimode beam during propagation does not follow the typical caustic-shape of a Gaussian beam as one can see in Fig. II.8. In fact, only the second-moment beam radius follows for any arbitrary beam (coherent or incoherent, single or multiple-transverse mode) the relation given in Eq. II.5. One can observe multiple minima or waists along the axis (cf. 95% beam radius in Fig II.8), plateau-like areas of almost constant beam radius (cf. $1/e^2$ beam radius in Fig II.8)) and in some cases discontinuous jumps along the axis [Siegman 98].

The preferred choice in this work is to follow the ISO 11146 standard and to specify always the M^2_{2nd} beam parameter. One common way to determine the M^2 value is to measure the beam profile with a CCD sensor in several planes along the caustic and to fit Eq. II.5 to the measured beam widths. Adequate camera settings, noise reduction and baseline-subtraction are necessary to limit measurement errors and it often leads to quite high values even for high power content in the fundamental mode (cf. II.7). The industrial standard for many applications are M^2 values close to unity, which encourages in some cases researches and engineers to specify a close to unity M^2_{1/e^2} value, even if this is of limited physical significance.
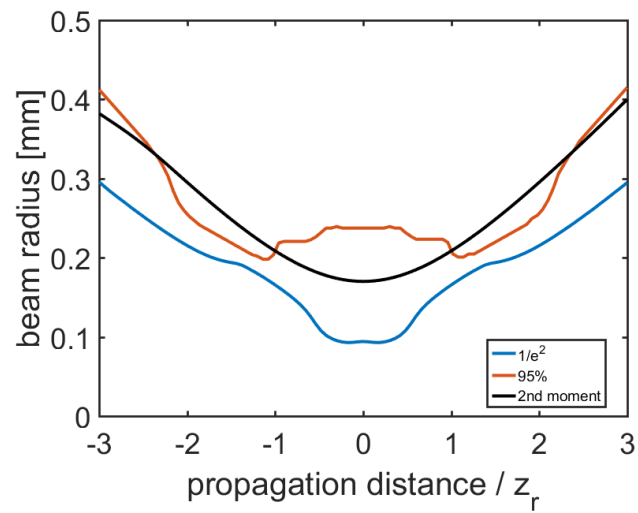
Figure II.8 – Calculated SA (horizontal x-direction) caustic for the exemplary multimode field (a) introduced Fig. II.4. Second moment beam radius in black, 95% beam radius in orange and $1/e^2$ beam radius in blue.

1.4 Central lobe power content

Another useful measure for the determination of the beam quality of a slightly multimode beam is the so-called central lobe power content. This measure is particular relevant for tapered lasers and amplifiers, where the slightly-multimode beams have a strong power content in the fundamental transverse mode and therefore show a clear central lobe around the waist (cf. Fig II.2). The central lobe power content is often specified in the literature as an estimation of the diffraction-limited power and as an additional measure for the overall beam quality of tapered lasers and amplifiers. The definition, the measurement method and the physical meaning of the central lobe power content are discussed below.

Definition The central lobe power content η_{cl} is defined in the context of this work as the relative power content of an ideal Gaussian beam $I_{fit}(x, y)$ fitted to the central lobe of the intensity profile at waist of a slightly multimode beam $I_m(x, y)$:

$$\eta_{cl} = \frac{\iint I_{fit}(x, y)\, dx\, dy}{\iint I_m(x, y)\, dx\, dy}. \tag{II.6}$$

The central lobe of the intensity profile at waist of the two exemplary multimode fields (a) and (b) introduced earlier is shown in Fig. II.9 and the central lobe power content is given in percent.
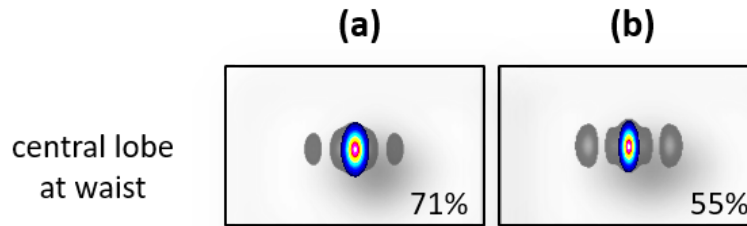
Figure II.9 – Central lobe (false color plot) and central lobe power content for two exemplary beam profiles (gray scale plot). The fields (a) and (b) are identical to the fields described earlier in Fig. II.4 at z_0.

Measurement The central lobe power was measured in this work as visualized in Fig II.10 (a-c). The beam profile used in this example is in fact the beam profile at waist shown earlier in Fig II.2 (b). The intensity profile at waist (astigmatism corrected) was measured with a CCD sensor with high resolution and signal to noise ratio. The data was then imported as a 16-bit image into Matlab and the central lobe power content was evaluated numerically following equation II.6. The power not included in the central lobe leads to higher angle side lobes around the waist (see gray-mesh plot in of Fig. II.10 (a)). Most of the side-lobe power is indeed contained in side lobes along the slow axis (see (b)), there are however also some minor pedestals in fast axis that contribute to the reduced central lobe power content (see (c)).

Physical meaning The central lobe power content is often used in the literature as a synonym for the diffraction limited power content of beams from tapered amplifiers [Sumpf 18, Müller 17, Wang 13]. The question however is, whether if this central lobe power is rigorously equal to the fundamental-mode power content of a slightly multimode beam. The central lobe content of the exemplary multi-mode fields with varying TEM$_{00}$-content investigated earlier in II.7 was calculated by the numerical method introduced above. A comparison of the evaluated central lobe content and the actual TEM$_{00}$ content is shown in II.11. In this example, the evaluated central lobe content is lower than the actual power content in the fundamental mode. The exemplary field (a) has a central lobe power content of
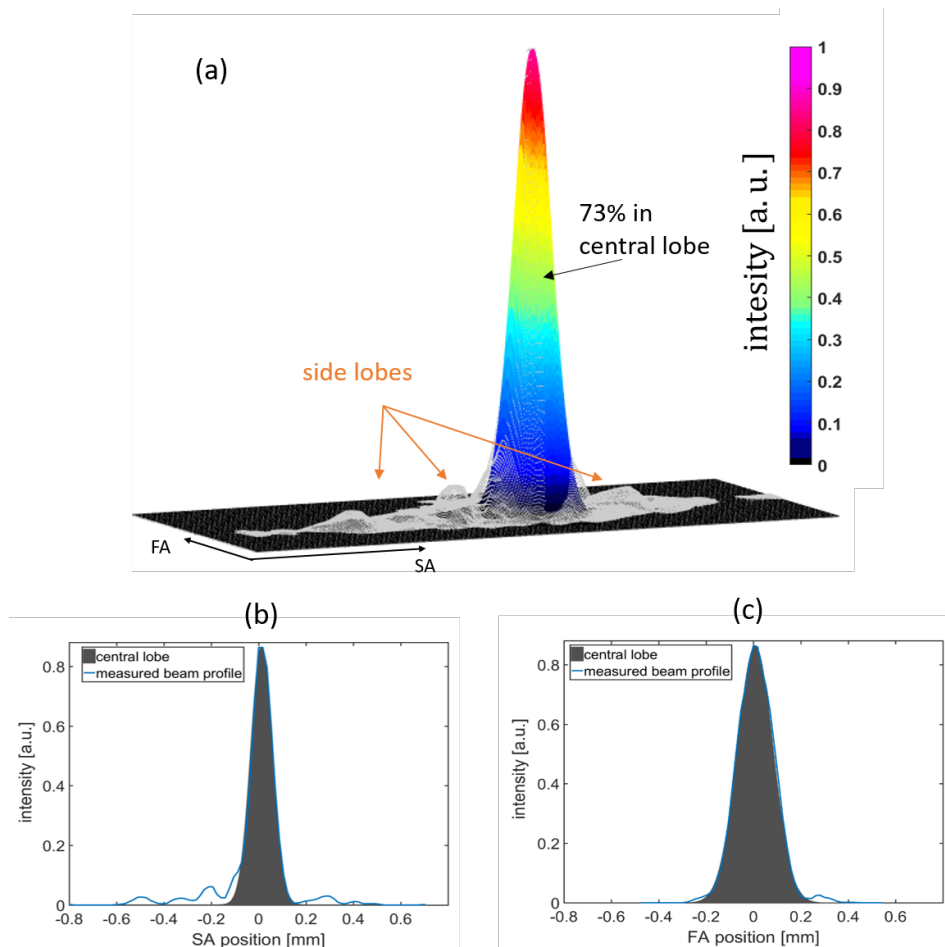
Figure II.10 – Visualization of the applied numerical investigation of the central lobe power content. (a) is a 3D-mesh-visualization of the original beam (gray mesh) and the fitted central lobe (false-color mesh); (b) shows the SA profiles and (c) the FA profiles through the beam centroid. The evaluated central lobe power content is 73%.

73% (for 91% in the fundamental mode) and field (b) has a central lobe power content of 55% (for 71% in the fundamental mode). The quite significant difference is caused by interference effects of the different modes leading to a central lobe at waist that is somewhat spatially compressed in this particular example (see Fig. II.5). This may not be the case in other examples or in actual beams from tapered lasers and amplifiers, but this example shows nevertheless that the central lobe power content is not rigorously equal to the power content in the fundamental mode. Furthermore, the assumption that if one observes a nicely shaped almost Gaussian-Intensity profile at several positions along the caustic, one therefore has a nearly ideal TEM$_{00}$ beam with M^2 close to unity, can be wrong. In a very particular case of an incoherent superposition of a few higher-order Laguerre-Gaussian[1] one can achieve a "nongaussian-Gaussian" beam that has in fact an almost perfect Gaussian beam profile in any plane but absolutely no power content in the fundamental mode [Siegman 98]. Figure II.12 shows such a nongaussian-Gaussian beam compared to an ideal TEM$_{00}$ beam. The central lobe power content of such a beam, evaluated with the methods described earlier, is close to 100% but the M^2-factor is significantly increased. The comparison with an ideal Gaussian beam shows that the nongaussian-Gaussian beam is in fact diverging about 3 times faster even though an almost perfect Gaussian beam profile is preserved during propagation. Even if this particular case is not relevant for this work, it is a warning example showing that the central-lobe-power is by no means always equal or less than the power in the fundamental mode. The central lobe power content is nevertheless a good measure for the beam

---

[1]To be precise: 41% on TEM$_{01}$, 17% on TEM$_{10}$, 19% on TEM$_{11}$, 11% on TEM$_{20}$ and 6% on TEM$_{21}$.
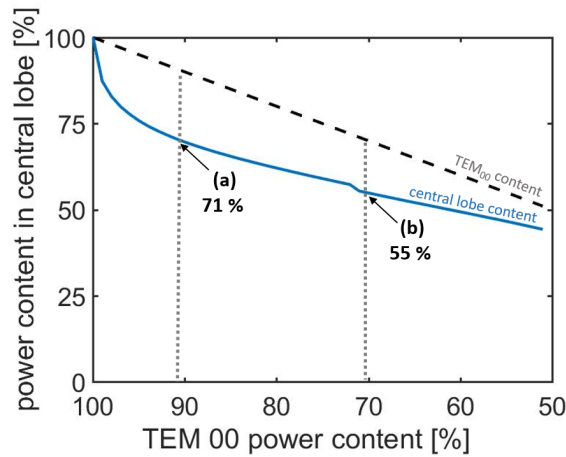
Figure II.11 – Calculated central lobe power content for exemplary multimode fields at different TEM_{00} power content. The remaining power was distributed onto some higher order modes in horizontal direction (in the same way than previously described for II.7). The fields (a) and (b) are identical to the fields described earlier in Fig. II.4.

quality of tapered laser and amplifiers (cf. Fig. II.11), but should not be used as a synonym for the diffraction limited power content.
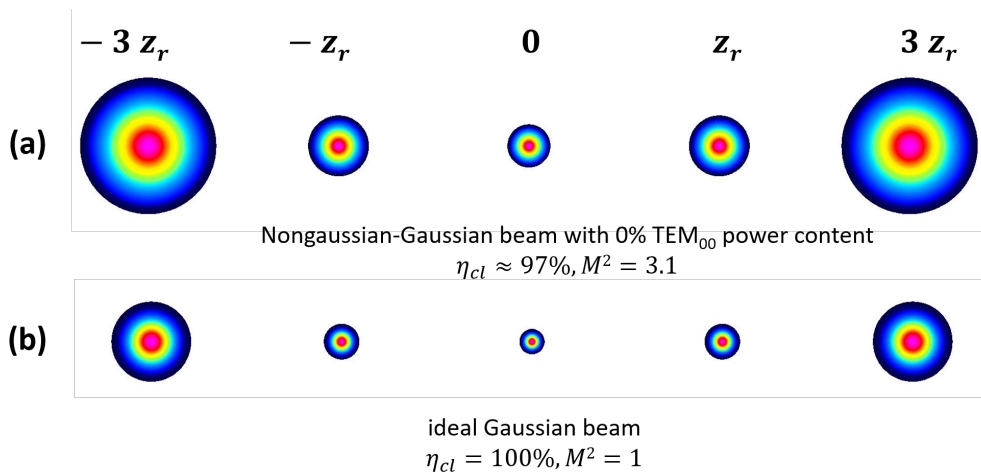
Figure II.12 – Beam profiles along caustic for (a) a nongaussian-Gaussian beam with absolutely no power content in the fundamental mode compared to (b) an ideal Gaussian TEM_{00} beam.

Theoretically, one could also measure intensity and phase of the beam at waist and calculate the TEM_{00} power content by projection on the Hermite-Gauss base. This is however not practical as phase measurements with a standard wavefront sensor are not straightforward for beams with irregular intensity patterns. The intensity of the side-lobes is quite low, which leads to highly noise related measurement errors. Furthermore the projection on the Hermite-Gauss base is highly dependent on the choice of beam centroid and the waist diameter.

1.5 Conclusion

Anthony E. Siegman wrote in the conclusion of his article "*How to (Maybe) Measure Laser Beam Quality*" (1998) that "*the term 'beam quality' at this point remains a handy buzz word, but is not yet a solidly defined technical term - and very likely never will be*" [Siegman 98]. To date, more than

twenty years later, this statement still hits the nail on the head. Some kind of classification for the beam quality is however required for this work, as a nearly diffraction limited beam quality is required for efficient coherent beam combining. The M^2_{2nd}-factor, the central lobe power content and the beam profile at waist will be used in the framework of this work to specify the beam quality. These three points together still do not tell the full story but are nevertheless a consistent method to characterize and compare the beam quality of tapered lasers and amplifiers.

2   Investigation of different epitaxial designs for high brightness tapered lasers and amplifiers

In this work, three different vertical epitaxial designs developed and grown by MOVPE techniques at the Ferdinand-Braun-Institut were investigated experimentally in order to choose the most promising vertical layer design for further detailed investigations. These preliminary characterizations were performed with DBR-TPLs instead of tapered amplifiers for the sake of simplicity and for better control of the test conditions. The lateral design and the mounting are shown in Fig. II.13 (a). The DBR-TPL had a 6 mm long optical resonator with a 3 mm long ridge waveguide followed by a 3 mm long 6° taper. The facets were passivated and coated with dielectric layers. The front facet reflectivity was 0.3% and the nominal rear facet reflectivity was below 0.01%. The reflection at the rear facet was provided by a 1 mm long 6th order surface grating (DBR) located at the rear facet (approx. 35% reflectivity). The devices were mounted p-side up on expansion matched CuW-submounts and c-mounts. A 3 mm long CuW-sandwich was used as an additional heat-spreader on the p-side of the tapered section. The devices had independent electrical contacts for the current I_{rw} into the ridge waveguide and the current I_{tp} into the tapered section. The following vertical layer designs were investigated:

Reference design   The so-called Reference design was taken from a process for the development of high-power DBR-tapered lasers for single-path second harmonic generation [Fiebig 09a]. The vertical layer structure is shown schematically in Fig. II.13 (b). It consists of an asymmetric $4.8\,\mu\mathrm{m}$ wide waveguide, also called super large optical cavity (SLOC). The active region consisted of two $8\,\mathrm{nm}$ thick InGaAs quantum wells separated by GaAsP barrier lasers.

New-TPL   The so called New-TPL design targeted an increased power conversion efficiency by a reduced electrical resistance. The resistance was reduced as compared to the Reference design by a very low aluminum content in the layers. Additionally a much narrower $2.4\,\mu\mathrm{m}$-wide vertical waveguide with a conventional double quantum well was used to achieve a higher gain in the device [Crump 15].

ELoD2   The so called ELoD2 designed was developed to achieve an **e**xtremely **lo**w vertical **d**ivergence. This was achieved by a $4.8\,\mu\mathrm{m}$ wide waveguide (SLOC) and three quantum wells separated by low index quantum barriers [Crump 13b]. This design was developed in the framework of the BRIDLE project and has proven to maintain good beam quality achieved by the suppression of filamentation effects. [Crump 15].

2.1   Optical power and power conversion efficiency

Fundamentals   The vertical layer design influences the electro-optical characteristics. The output power of a diode laser can be described in a very simplified form as shown in Fig. II.14. The optical output power at a current I above the threshold current I_{th} is

$$P_{opt} = \frac{hc}{e\lambda} \times \eta_d \times (I - I_{th}), \tag{II.7}$$

where h is the Planck constant, e is the electron charge , c is the speed of light, λ is the laser wavelength and η_d is the external differential quantum efficiency. The required electrical power is $P_{el} = U(I) \times I = (U_0 + R_s I) \times I$, where U_0 is the extrapolated voltage at $I = 0$ and R_s is the series resistance. The power conversion efficiency (PCE) is defined as $\eta_e = P_{opt}/P_{el}$.

Influence of the epitaxial design on I_{th} The variation of I_{th} with design changes can be extrapolated with the following parametric equation

$$I_{th} = N_{QW} J_{tr} \times A \times \exp\left[\frac{\alpha_i + \alpha_m}{N_{QW}\Gamma_{QW}g_0}\right], \tag{II.8}$$
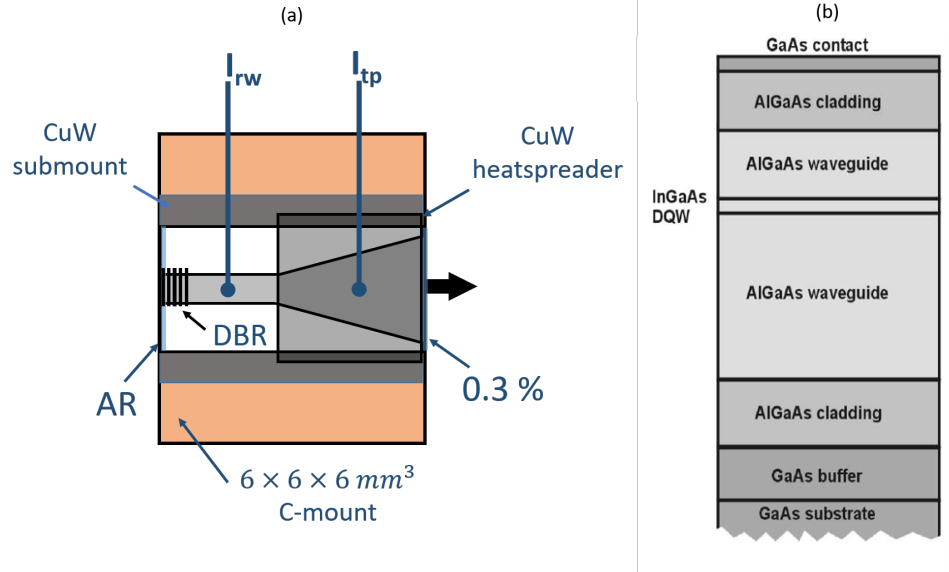
Figure II.13 – (a) Simplified schematic of the mounting plan for the DRB-TPLs investigated in this section. (b) Vertical layer structure of the Reference design. Taken from [Fiebig 09a].
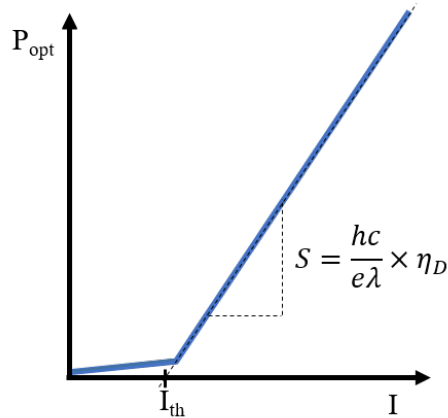
Figure II.14 – Simplified representation of the optical output power P_{opt} for different drive currents I. I_{th}: threshold current, S: slope of power-current curve, η_D: slope efficiency.

where N_{QW} is the number of the quantum wells, J_{tr} is the transparency current density, A is the lateral in-plane surface area of the waveguide, α_i are internal losses, $\alpha_m = \frac{1}{2L} \ln(R_1 R_2)$ are mirror losses, Γ_{QW} is the confinement factor per quantum well[1] and g_0 the gain parameter. Consequently, a number of parameters that are defined by the design of the vertical layer structure influence the threshold current. Although a nominally ideal device has a threshold current close to zero, in some cases however it may be beneficial for the overall performance of the device to accept an increased threshold current to achieve other beneficial properties, such as an improved beam quality enabled by low confinement factors Γ_{QW}.

Influence of the epitaxial design on η_e   The PCE efficiency η_e can be written as

$$\eta_e(I) = \frac{hc}{e\lambda U(I)} \times \eta_d \times \frac{I - I_{th}}{I}, \tag{II.9}$$

---

[1]As a side-note, the confinement factor is not exactly the same per well. Here one should understand Γ_{QW} as the average confinement factor per quantum-well.

which can be seen as the product of three efficiencies $\eta_e = \eta_u \times \eta_d \times \eta_{th}$ representing the influence of a non-ideal voltage (η_u), a non-ideal slope (η_d) and a non-ideal threshold current η_{th} [Crump 13a]. The design of the vertical structure influences the maximal achievable efficiency therefore in several ways, for example via the series resistance (leading to a reduced η_u) or via a certain threshold current (leading to a reduced η_{th}).

Experimental investigation   The optical power was measured for each design in quasi continuous wave operation (QCW - $\Delta t = 1$ ms, 1% duty cycle). QCW operation was chosen in order to compare the performance of the device without major influences of thermal effects in the devices. The electro-optic performance characteristics are shown in Fig. II.15 (a) and (b). The reference design (black) reached about 7 W optical power at 10 A with a maximal PCE of 34%. The NewTPL design (blue) showed indeed a very low threshold current, reduced series resistance, evidenced by a lower slope of $U(I)$ and therefore significantly improved PCE (max. 48%). The optical power was > 8 W. The ELoD2 design (orange) had the lowest optical output power of about > 5.5 W, mainly caused by a high threshold current. This can be attributed to the low confinement factor. The maximal PCE was below 30%, mainly limited by high threshold current.

A similar experimental investigation of these three different epitaxial layer structures was previously published by Crump et al. [Crump 15]. The mounting was however different (p-side down with a single electrical contact) and both broad area lasers and tapered lasers were investigated.
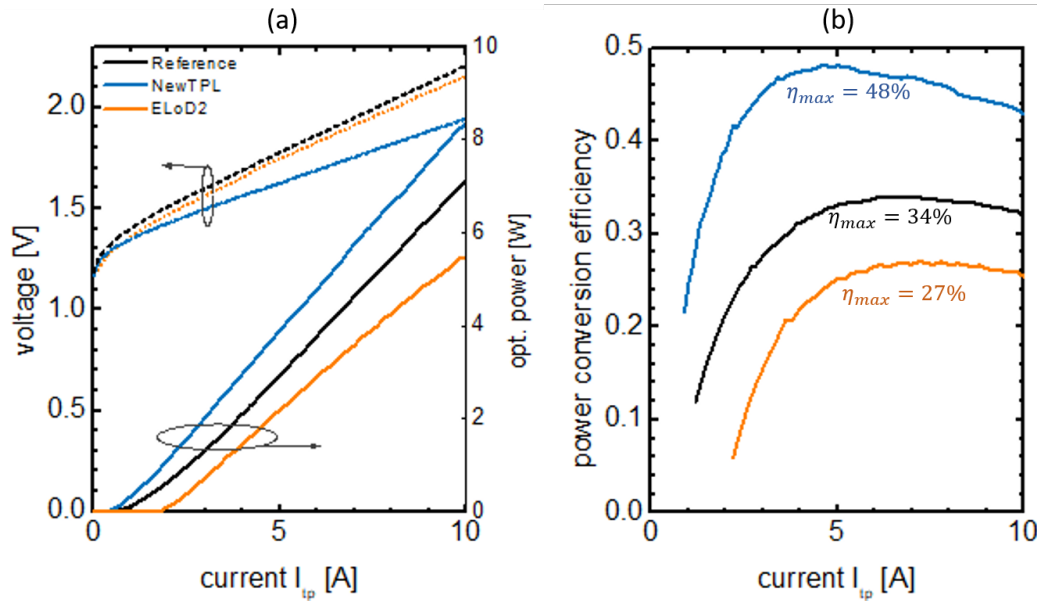
Figure II.15 – (a) Optical output power and voltage for different currents into the tapered section. (b) Corresponding power conversion efficiency. The current into the ridge section was 400 mA. 20°C heatsink temperature.

2.2 Lateral beam quality

The vertical layer design influences the spatial properties (divergence, M^2) in both vertical and lateral direction. Differences in vertical direction were however limited to a slightly different divergence and the beam quality was nearly diffraction limited ($M^2 < 1.3$) for all three investigated designs. The lowest vertical divergence was achieved with the ELoD2 design (full angle $2\theta < 26°$). More important for the context of this work are however the differences in the lateral beam quality discussed below.

Several physical effects influence the beam quality in lateral direction. One effect, particularly relevant for the design of the vertical layer structure is the formation and growth of filaments in the
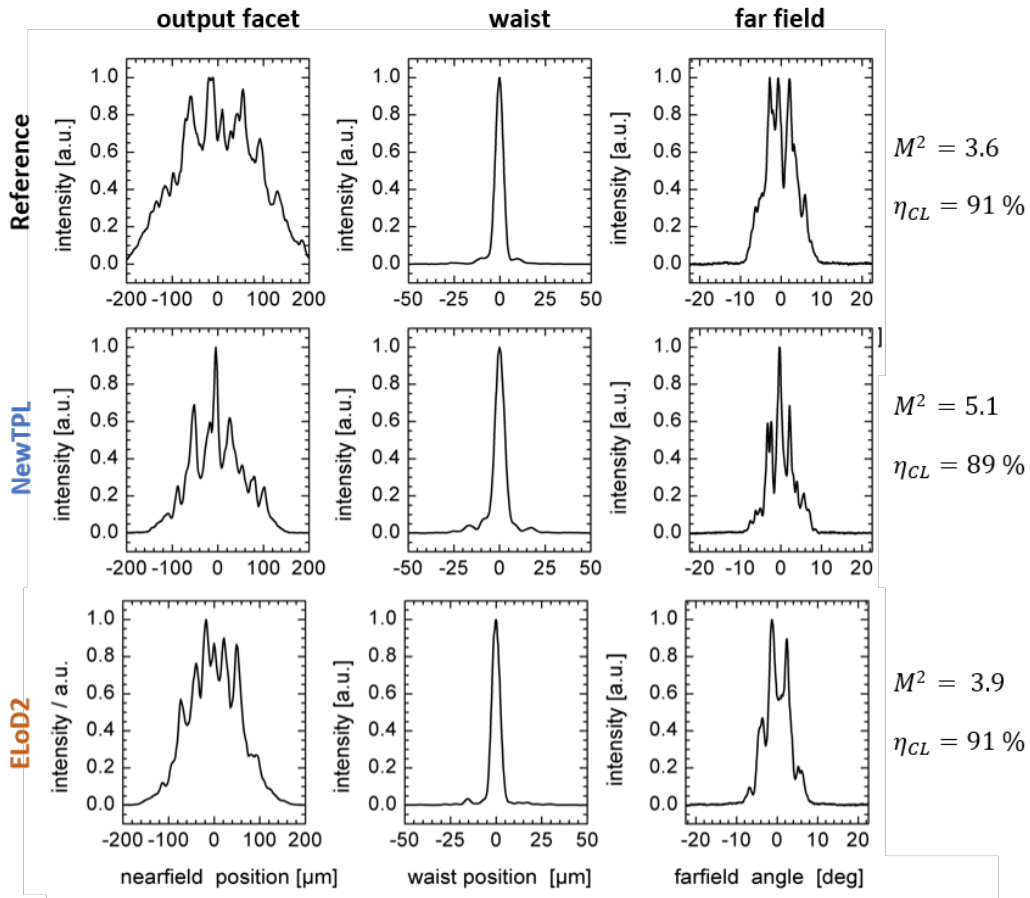
Figure II.16 – Beam quality measurements of DBR-TPL at 1 W output power with three different vertical layer designs. The first column shows the intensity profile measured at the output facet, the second column shows the intensity profile at waist and the third column shows the angular far field profile. The near-field profile at the output facet for the Reference device appears slightly larger, as a device with a 4 mm long TP section was used for this measurement for practical reasons.

gain-guided tapered section. Filamentation is attributed to self focusing effects induced by a carrier-dependent refractive index [Thompson 72]. Filamentation results to highly contrasted modulations in the intensity, so called filaments, at the output facet of the laser. This leads to a degraded beam quality, notably to strong side-lobes in the intensity profile at waist [Goldberg 93]. The formation and growth of filaments happens usually at high bias (several times above the threshold current). Filamentation can be caused by local perturbations, local heat hot-spots and spontaneous emission [Sujecki 03] but is also related to the modal gain ($\Gamma g - \alpha_i$) in the device. Wang et al. observed experimentally for tapered amplifiers that lateral designs with extremely low confinement factors Γ and hence low modal gain are substantially more resistant to the formation and growth of filaments than comparable vertical designs with higher modal gain [Wang 12]. Similar observations were made for broad area lasers [Winterfeldt 14]. The three vertical layer designs investigated here have different confinement factors (NewTPL: highest confinement, EloD2: lowest confinement) and one can therefore expect a different behavior regarding formation and growth of filaments. Furthermore, the low-index-quantum-barriers used in the ELoD2 design suppress the impact of changes in the refractive index in the active region on the beam propagation [Crump 13b, Crump 15].

The lateral beam quality of the lasers was investigated by measurements of the intensity profile at three different positions. The intensity profile at the output facet (near field) was measured in order to determine if filamentation occurs in the tapered section. The intensity profiles at waist and in the far field were measured to determine the power content in the central lobe and the M^2 beam propa-
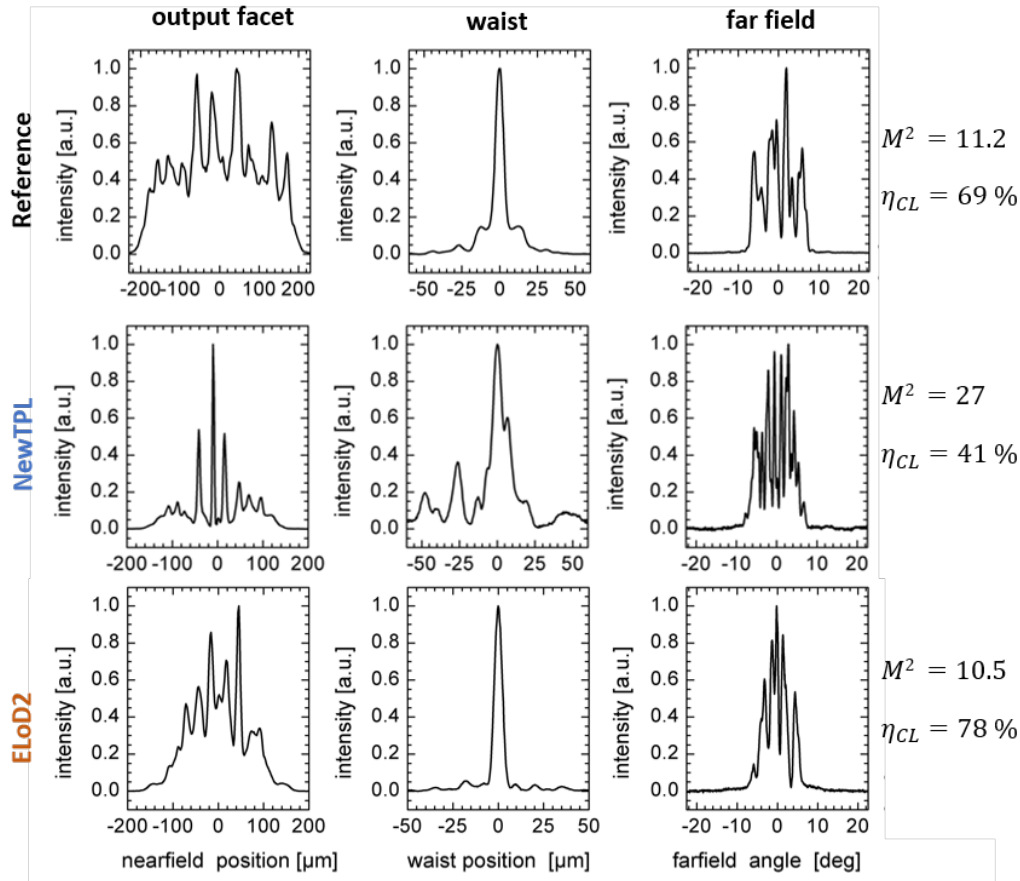
Figure II.17 – Beam quality measurements of DBR-TPL at 6 W output power with three different vertical layer designs. The first column shows the intensity profile measured at the output facet, the second column shows the intensity profile at waist and the third column shows the angular far field profile. The near-field profile at the output facet for the Reference device appears slightly larger, as a device with a 4 mm long TP section was used for this measurement for practical reasons.

gation factor. The measurements were done with a moving-slit beam profiler used for standard laser diode characterization at FBH. The operation conditions were identical to the power characterization discussed above (QCW operation[1], $400\,\text{mA}$ into the RW) and are summarized for 1 W optical power in Fig. II.16 and for 6 W optical power in Fig. II.17. The M^2-factor and the evaluated power content in the central lobe η_{cl} are given for each device.

The measurements at 1 W output power in Fig. II.16 show that the behavior of the devices is very similar at low bias. The central lobe at waist is clearly visible in all cases and contains 89 - 91% of the power. The M^2-factor varies between 3.6 for the Reference design and 5.1 for the NewTPL design. The measurements prove that all device behave normally and as expected at low bias.

The measurement at 6 W output power, shown in Fig II.17, indicate in contrast strong differences in the performance of the devices. The worst beam quality was observed for the NewTPL design with a near field that indicates significant filamentation processes, evidenced by highly contrasted and narrow peaks in the near field profile. In consequence, a highly distorted and far from Gaussian beam profile was measured at waist leading to a poor M^2-factor and poor central lobe power content. Similar beam quality degradation was observed with two other chips of this design, which allows the conclusion that the significant beam quality degradation at high bias is inherent to the device design and not a single-chip failure. The beam quality of the laser with the Reference design remained reasonably good. The beam profile at waist consists of a clear central lobe and some side lobes. Values typical for DBR-

---

[1]It was experimentally verified that the beam quality in QCW and CW mode operation was roughly identical.

TPLs at high bias were measured for η_{cl} and M^2. The ELoD2 design showed the best beam quality at high bias, with a beam-profile at waist almost identical to the measurements at low bias. The power content in the central lobe was excellent and compares favorably to the reference design. Overall, the ELoD2 designs showed the best beam quality at high bias. While contrasted filaments were observed for devices with the New-TPL design, devices with the ELoD2 and Reference design were found to be resistant against filamentation processes.

2.3 Conclusion

The results of the experimental investigations of the three designs are briefly summarized in Table II.1 below. The results lead to the general conclusions discussed below.

The power-current-voltage characteristics of the NewTPL design compared favorably (lowest threshold current, lowest series resistance, therefore best efficiency and highest total power) to the other designs but very strong filamentation-related beam quality degradation was observed. This design was not further considered for the context of this work, as a good beam quality at high bias is required for coherent beam combining.

The Reference design appears to provide a good compromise in terms of beam quality, output power and PCE. The ELoD2 design is particularly resistant against beam quality degradation processes and shows clearly the best beam quality, but suffers from a significantly reduced PCE. Calculating the effective PCE for the central lobe power content, one finds however that the ELoD2 design is effectively almost as efficient as the Reference design.

The ELoD2 design was chosen for further investigations of different lateral device designs which are discussed in the following section. Coherent beam combining experiments using tapered amplifiers with the Reference design and the ELoD2 design are described and compared in chapter III.

Table II.1 – Summary of the investigation of three different vertical layer designs

	Reference	**NewTPL**	**ELoD2**
Thickness of vertical waveguide [µm]	4.8	2.4	4.8
Number of QW	2	2	3
Vertical divergence, full angle [deg]	30	>50	26
Threshold current I_{tp} [A]	1.2	0.5	2.0
Optical power [W] at I_{tp} = 10 A	7.1	8.3	5.5
M^2 at P_{opt} = 6 W	11.2	27	10.5
η_{CL} [%] at P_{opt} = 6 W	69	41	78
Maximal PCE [%]	34	48	27
Eff. PCE for central lobe [%]	25	20	21

3 Investigation of lateral designs for tapered amplifiers

The influence of the lateral device design of tapered amplifiers on optical power, power conversion efficiency, beam quality and noise properties is investigated in this section. The focus lies however on the investigation of beam quality degradation processes. The target of this study was to investigate the following hypotheses, illustrated in Fig. II.18, concerning the degradation of the beam quality of tapered amplifiers at high bias:

(a) The beam quality degradation is mainly driven by a dysfunction of the mode filtering in the ridge waveguide. The absorbing region next to the ridge waveguide gets bleached by back-reflections from the output facet, which favors the transmission of higher order modes in the ridge section. The higher order modes may be excited by imperfect coupling of the seed laser or by residual reflections of the back-coupled light on the AR coating at the back facet. The higher order modes entering the tapered section then lead to significant beam distortions. This hypothesis is supported by numerical simulations of beam quality degradation processes in tapered lasers [Helal 17, Larkins 19] and experimental investigations of tapered diode lasers with reverse bias absorber sections beside the ridge waveguide [Fiebig 09b].

(b) The beam quality degradation is mainly driven by gain-dependent effects in the tapered section. High gain may favor the growth of filaments in the tapered section that lead to significant beam distortions. This hypothesis is supported by experimental investigations of truncated tapered amplifiers with extremely low confinement factors (low gain) that enabled a significantly improved beam quality when compared to similar designs with higher confinement [Wang 12] (cf. section 2.2). Here a modification in the lateral device design that may prevent the growth of filaments is investigated.
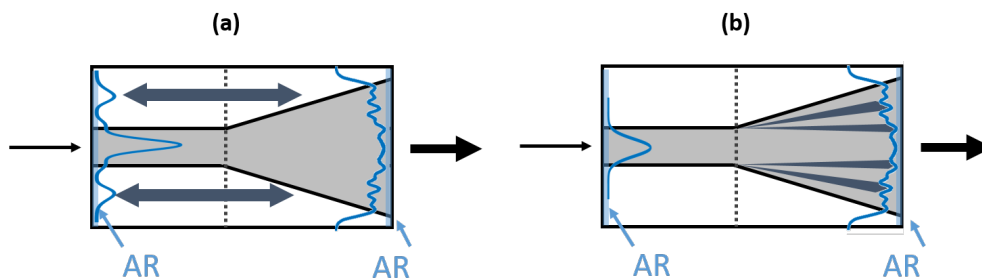
Figure II.18 – Simplified visualization of two hypotheses for the cause of beam quality degradation in the tapered section

3.1 Design description

All investigated chips were designed, developed, grown, fabricated and packaged at FBH using the ELoD2 epitaxial design in the same fabrication process. The facets were passivated and coated with dielectric layers. The nominal reflectivity of the rear facet was below 0.01% and below 0.3% for the front facet (at 976 nm). The reflectivity of the front facet was slightly higher as these devices have also been used in extended cavity configurations where minor reflections at the front-facet were required [Schimmel 16]. The devices were mounted p-side up on C-mounts es described for the DBR-TPLs in Fig. II.13, the only difference is the use of 5 mm long devices instead of 6 mm long devices. Note that the mounting was not optimized for a low thermal resistance (both p-side up mounting and the use of C-mounts make efficient heat extraction challenging) but was instead selected for easy handling of the devices in compact amplifier setups.

The investigated lateral designs are shown in Fig II.19 (a-e). The designs were taken from a fabrication process of ELoD2 DBR-TPLs [Crump 15] and the DBR grating was cleaved off. The so-called

baseline design is given in Fig. II.19 (a) and consists of a 2 mm long $4\,\mu$m wide ridge waveguide and a 3 mm long $6\,°$ tapered section. The other designs are variations of this baseline design. Ridge width, taper-angle and coatings are however identical for all designs. The varied parameters are highlighted in orange in Figure II.19. Design (b) includes a **Ge-absorber** region around the ridge waveguide. The concept relies on higher-order lateral mode suppression by a resonant anti-guiding Ge-layer with a high refractive index[1] (anti-waveguide layer - AWL) [Wenzel 13]. The fundamental transverse mode in the RW is in principle only weakly affected by the Ge-layer but any higher order modes couple strongly to the Ge-layer, where they get absorbed. The purpose of this design is to assess hypothesis (a) discussed above.

The other designs, see Fig. II.19 (c-e), target a modification of the gain in the taper. Design (c), referred as the **4 mm taper** design, has a 4 mm long tapered section and a 1 mm long ridge waveguide. The carrier density and gain in the tapered section are therefore significantly different at a given drive current, as the surface of the tapered section is roughly 1.75 times larger when compared to the baseline design (but as a side-effect, the design has also a shorter RW). Design (d), referred as the **50% stripes** design, has also 4 mm long tapered section but with a stripe patterned electrical contact (50 μm wide contact stripes). Consequently only 50% of the tapered section are electrically pumped and 50% remain un-pumped with no gain. Design (e) is similar to (e) but with 70% un-pumped area in the tapered section and is referred as the **70% stripes** design.
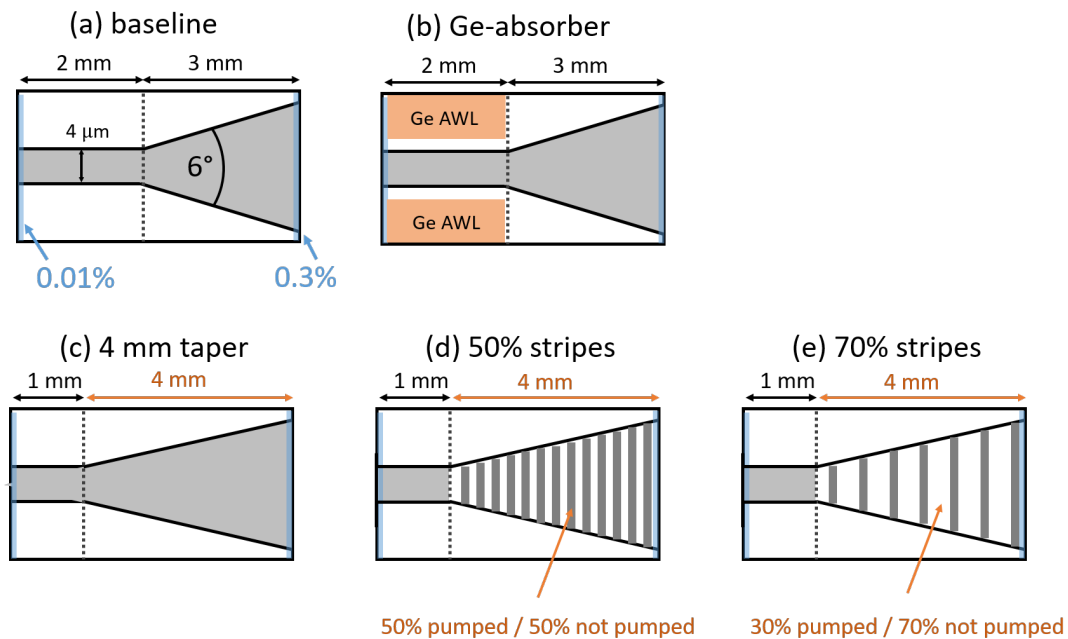
Figure II.19 – Simplified schematics of the investigated lateral device designs. (a) baseline, (b) Ge-absorber, (c) 4 mm taper, (d) 50% stripes, (e) 70% stripes. RW width, taper angle and facet coatings were identical for all designs.

3.2   Comparative experimental study

The comparative experimental study of the different device designs was split in two parts. First, a standard characterization of power and beam quality was performed with 2-3 chips per design. After that, relative intensity noise and phase noise was measured with a few devices for further analysis. The seed source was a narrow line-width (< 10 MHz) DFB laser at 976 nm isolated by a double stage

---

[1]The refractive index af Ge is approximately 5, which is significantly higher than the refractive index of GaAs in the order of 3.5.

Faraday optical isolator (-60 dB isolation). If not specified differently, the seed power at the entrance facet of the ridge waveguide was $30\,\mathrm{mW}$. The spatial profile of the seed laser beam was measured at waist (corresponding to the focal spot after L_2 in Fig. II.1) and is shown in Fig. II.20. The measured beam diameters were almost identical to the dimensions of the fundamental mode guided by the RW (theoretically: 5.4 μm in SA and approximately 3.8 μm is FA). The beam quality of the seed laser beam was nearly diffraction limited ($M^2 < 1.3$) in both directions.
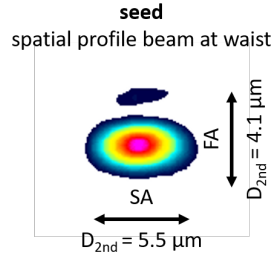
Figure II.20 – Measured beam profile and diameters of the seed laser at waist.

3.2.1 Power characteristics

The CW and QCW-power characteristics of the different lateral designs were investigated at a current of $I_{rw} = 350$ mA into the ridge waveguide and for different currents I_{tp} into the tapered section. The results are shown in Figs. II.21 and II.22. Each figure has three sub-figures (a-c) addressing the following fundamental questions regarding the lateral device design:

   (a) How does the Ge-absorber layer influence the electro-optic characteristics of the amplifier?

   (b) How does the length L of the taper influence the electro-optic characteristics of the amplifier?

   (c) How does the periodic gain modulation generated by the stripe patterned electrical contact of the tapered section influence the electro-optic characteristics of the amplifier?

CW power characteristics   The results in CW operation are shown in Fig. II.21 (a-c) and lead to the following answers to the three questions given above.

   (a) The Ge-absorber layer had a negative impact on the electro-optic characteristics. The output power of the baseline design and the Ge-absorber design were both limited by a thermal rollover at high bias, the onset of the rollover was however at lower bias for chips with Ge-absorber layers. One possible explanation for this effect is that the Ge-layer added minor losses to the RW favoring an early rollover. The maximum output power measured for the baseline design was 4.4 W and about 20% higher than for the Ge-absorber design. There was no significant influence of the Ge-absorber layer on the maximal PCE, which was similar to previous measurements of ELoD2 DBR-TPLs with the same lateral design (cf. Fig. II.15).

   (b) The design with a 4 mm long tapered section compares favorably to the baseline design that has only a 3 mm long tapered section. The increased area of the tapered section makes the device more resistant against the thermal rollover as the thermal resistance R_{th} is reduced. R_{th} scales approximately with $R_{th} \propto 1/A$, where $A \approx 0.5 \times L^2 \tan(\theta/2)$ is the surface area of the tapered section. The thermal resistance of the 4 mm taper design is therefore reduced by 44% when compared to the baseline design. The maximum output power was 6.6 W at 12 A and there was no indication for an onset of a thermal rollover. The larger surface area of the taper also reduces the electrical resistance leading to a slightly lower voltage at high currents. But, the increased surface area of the tapered section also increases the threshold current leading to a slightly reduced maximal PCE when compared to the baseline design.

   (c) The designs with a stripe patterned contact of the tapered section were limited by an onset of the thermal rollover at about 8 A leading to 15-20% lower output power when compared to the design without a stripe patterned contact. This can be attributed to a spatial concentration of the heat load in the pumped regions favoring an earlier thermal rollover. The stripe patterned contacts have a higher

electrical resistance leading to a slightly increased voltage at high currents.

The most favorable power-voltage-current characteristics was achieved with the 4 mm taper design, which was the only design not limited by a thermal rollover. This was attributed to the reduced thermal resistance of the tapered section and the reduced heat load density in the large homogeneously pumped tapered section.

QCW power characteristics The QCW output power was also measured for comparison of the device designs with significantly reduced average heat load. The bias conditions (current into RW, seed power, heatsink temperature) were identical to the measurements in CW mode. The pulse duration Δt_{qcw} was 1 ms and the duty cycle was 10%. Note that only the current into the tapered section was pulsed as the current into the RW is not relevant for the overall heat-load into the device (approx. 1 W dissipated heat in RW). The results are shown in Fig. II.22 (a-c).

(a) The baseline design, which was limited by a thermal rollover in continuous wave operation, showed a linear increase in output power up to 18 A with a maximum power of 9.5 W. The power of the amplifier with the Ge-absorber layers however plateaued at about 13 A and was about 25% lower than for the baseline design. This effect was attributed to a reduced efficiency of the RW section (losses linked to Ge-absorber), leading to a not-saturated power-amplifier at high bias. The measured maximal PCEs were similar to the measurements in CW mode.

(b) The design with a 4 mm long tapered section compared again favorably to the baseline design as the maximal output power was approximately 30% higher. The slope efficiency of the 4 mm long taper design was with $0.8\,\mathrm{W/A}$ significantly higher than the slope efficiency of $0.55\,\mathrm{W/A}$ for the baseline design. The maximum PCE of the 4 mm taper was significantly improved when compared to CW operation.

(c) The designs with stripe patterned electrical contacts of the tapered section behaved similarly to the 4 mm taper design. The differences observed in CW were related to thermal effects, which are less critical in QCW operation. Minor differences in the PCE related to increasing electrical resistance of the stripe patterned contacts were observed.

The most favorable power-voltage-current characteristics in QCW operation was achieved with the 4 mm taper design. The designs with stripe-patterned electrical contacts performed similar to the 4 mm taper design. The Ge-absorber layer influences the output power characteristics of the amplifiers negatively even under QCW operation. Overall, the results in QCW operation show that the maximal output power in CW of all designs is mainly limited by thermal effects. Improved packaging of the amplifiers may help to improve the CW output power in future experiments.

(a)
Ge-absorber

baseline:

$P_{max} = 4.4$ W
$\eta_{max} = 32\%$

Ge-absorber:

$P_{max} = 3.7$ W
$\eta_{max} = 32\%$

(b)
taper length

baseline:

$P_{max} = 4.4$ W
$\eta_{max} = 32\%$

4 mm taper:

$P_{max} = 6.6$ W
$\eta_{max} = 29\%$

(c)
stripes

4 mm taper:

$P_{max} = 6.6$ W
$\eta_{max} = 29\%$

50% stripes:

$P_{max} = 5.3$ W
$\eta_{max} = 27\%$

70% stripes:

$P_{max} = 5.1$ W
$\eta_{max} = 26\%$
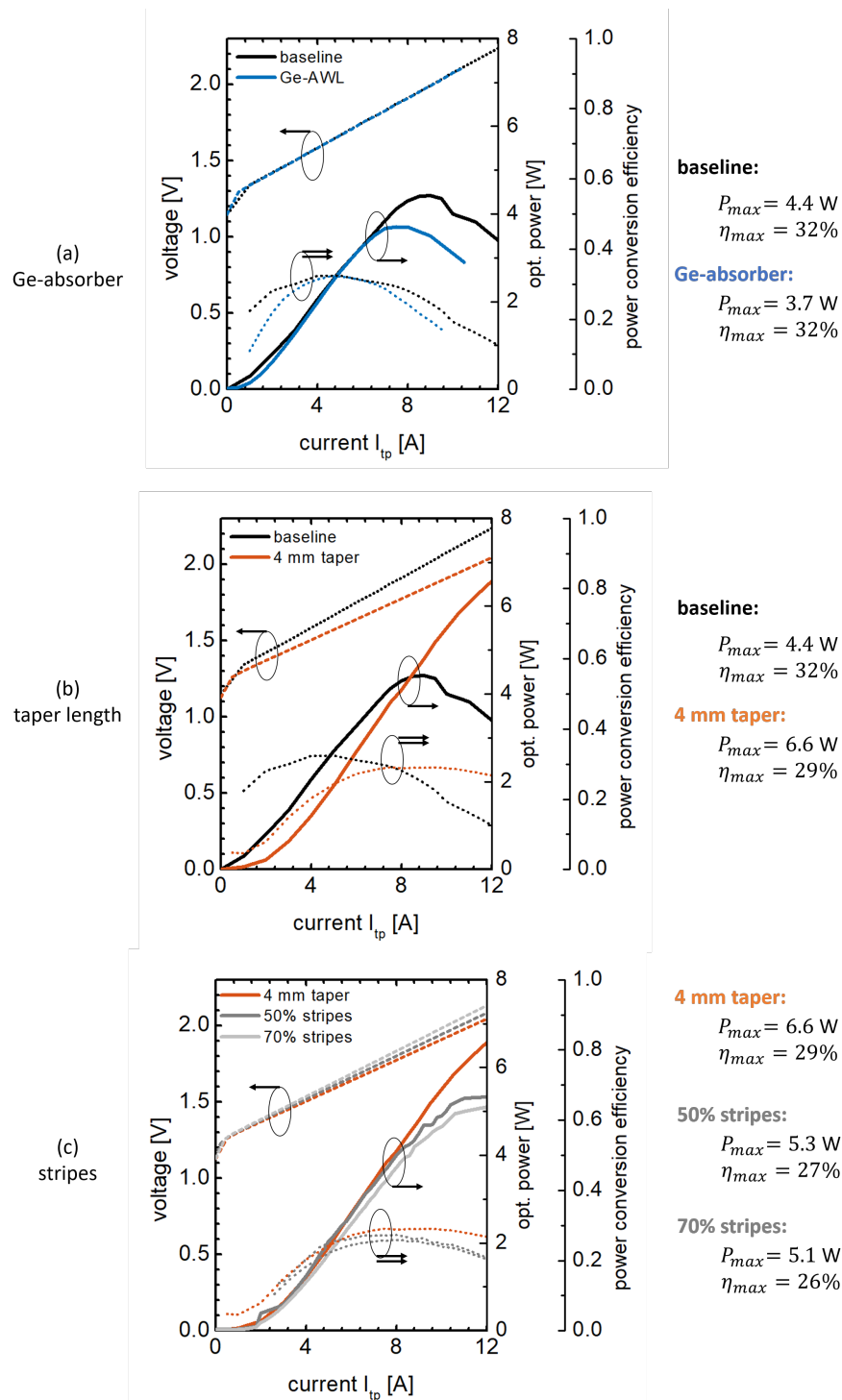
Figure II.21 – CW power-voltage-current characteristics for the different device configurations. The current through the RW was $I_{rw} = 350$ mA, the seed power into the RW was $P_{in} = 30$ mW and the heatsink temperature was $20\,°C$. (a) Comparison of the baseline design with and without Ge-absorber layers. (b) Comparison of the baseline design with the 4 mm taper design. (c) Comparison of the 4 mm long taper design with the 50 and 70% stripes design.

(a)
Ge-absorber

baseline:

$P_{max}= 9.5$ W
$\eta_{max} = 32\%$

Ge-absorber:

$P_{max}= 7.2$ W
$\eta_{max} = 35\%$

(b)
taper length

baseline:

$P_{max}= 9.5$ W
$\eta_{max} = 32\%$

4 mm taper:

$P_{max}= 12.5$ W
$\eta_{max} = 36\%$

(c)
stripes

4 mm taper:

$P_{max}= 12.5$ W
$\eta_{max} = 36\%$

50% stripes:

$P_{max}= 12.3$ W
$\eta_{max} = 34\%$

70% stripes:

$P_{max}= 11.7$ W
$\eta_{max} = 32\%$
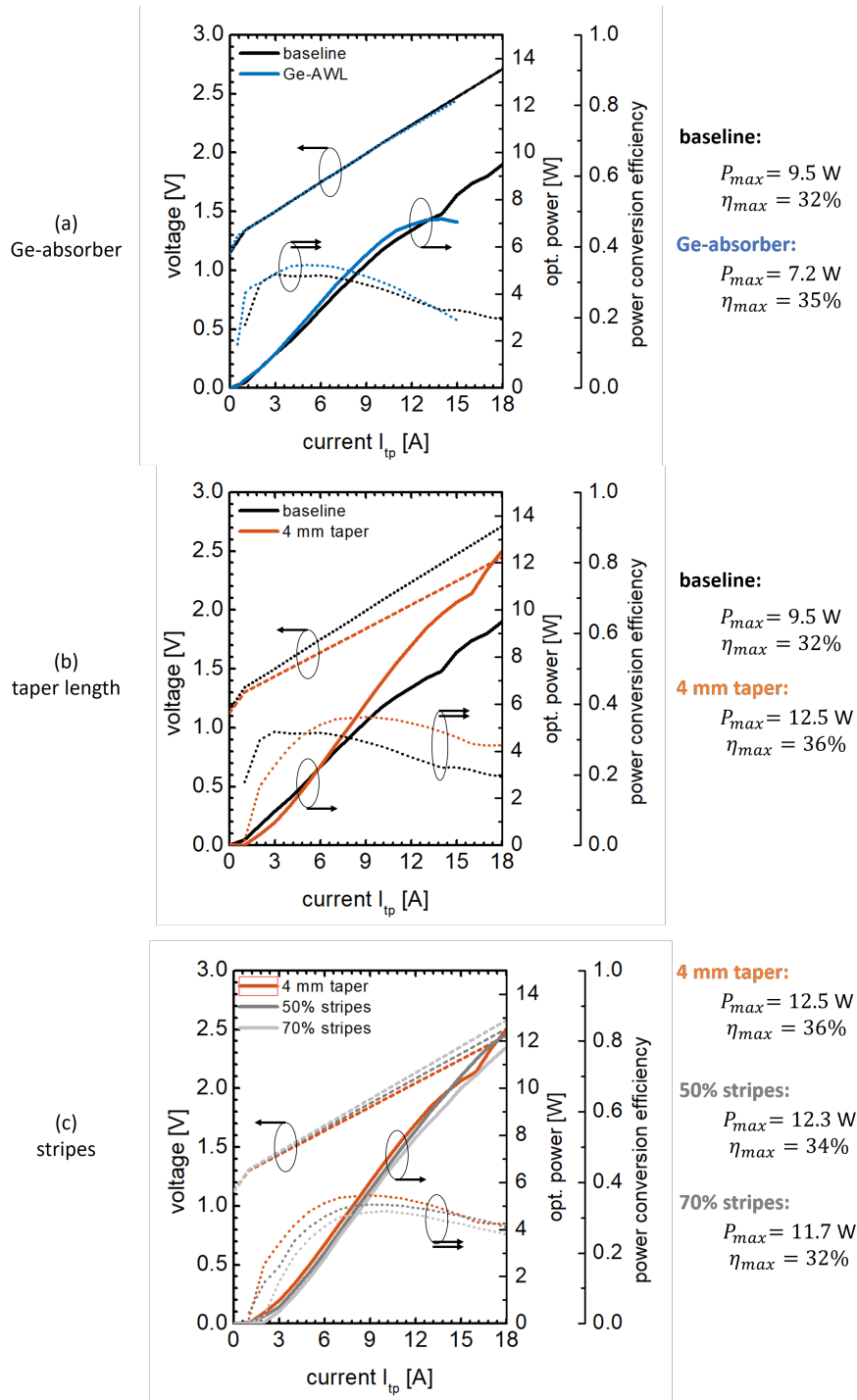
Figure II.22 – QCW power-voltage-current characteristics for the different device configurations. The current through the RW was $I_{rw} = 350$ mA, the seed power into the RW was $P_{in} = 30$ mW and the heatsink temperature was $20\,^{\circ}$C. Measurements for $\Delta t_{qcw} = 1$ ms and 10% duty cycle. (a) Comparison of the baseline design with and without Ge-absorber layers. (b) Comparison of the baseline design with the 4 mm taper design. (c) Comparison of the 4 mm long taper design with the 50 and 70% stripes design.

3.2.2 Beam quality

Central lobe power content The beam quality of the different lateral designs (all with ELoD2 epitaxial design) was investigated in CW operation at different bias points. The measurement of the central lobe power content, following the methods discussed earlier (cf. section 1.4), is a particularly straightforward method for the determination of the beam quality and well adapted for the comparison of a large number of samples. The central lobe power content was measured for a few different bias points for all amplifier designs as summarized in Fig. II.23. The measurements show a slight, approximately linear, decrease of the central lobe power content for increasing currents I_{tp} into the tapered section. The highest central lobe power contents were measured for the baseline design (95% at 1 A and 84% at 9 A), enabling a focal spot at waist with a very clearly pronounced almost circular central lobe and only minor side lobes in SA (see waist beam profiles at 1-9 A given in Fig. II.23). The central lobe power content measured with the 4 mm taper design (93% at 1 A and 82% ar 9 A) was nearly as high as for the baseline design. Nevertheless, the focal spot at waist[1] consists of more higher order side-lobes when compared to the baseline design even if the total energy content in the side-lobes is very similar. The other designs incorporating a stripe patterned contact of the tapered section or a Ge-absorber layer had significantly lower central lobe power contents when compared to the more conventional designs (baseline and 4 mm taper). An exemplary beam shape at waist is given for the 50% stripes design at 7 A with a central lobe power content of 76% in Fig. II.23, showing that the intensity in the higher order side lobes is increased when compared to the other designs. The central lobe power content of the Ge-absorber and the 70% stripes design was with < 70% at 7 A significantly lower than for the other designs[2]. For that reason, these two designs were not investigated in details.

Beam propagation factor As an additional measure for the beam quality, the M^2 beam propagation factors were measured in SA at moderate bias. The M^2 measurement was done by a caustic measurement (60 samples within $\pm 3z_r$) with a CCD camera on an automated translation stage (Dataray Inc. WinCamD camera and 40 mm translation stage). Figure II.24 shows the measurement for the baseline amplifier at 5 A as an example. The Gaussian fit was obtained numerically. The most robust fitting results are achieved if a strong weight is applied to the data points within one Rayleigh length of the waist. More results are summarized in Table II.2. Approximate measurement tolerances are specified. The baseline design had the lowest M^2-factor (3.5 ± 0.3) followed by the 4 mm taper design (4.5 ± 0.4) and the 50% stripes design (5.5 ± 0.5). The M^2 factor increased with decreasing central lobe power content, which confirms that both measures are useful for beam quality measurements of tapered amplifiers. The M^2 factor in FA was close to unity (1.3 ± 0.3) for all designs.

Conclusions Overall, the beam quality of the ELoD2 amplifiers with the baseline design, the 4 mm taper design and the 50% are good and sufficient for coherent beam combining experiments, which will be discussed for this design in chapter 3. The best beam quality was observed for the baseline design, which may be attributed to a better pre-amplification of the single mode seed laser in the 2 mm long RW when compared to designs with a shorter RW section. The Ge-absorber layers did not lead to any improvement regarding the beam quality. Together with the poor electro-optic characteristics discussed previously, this may indicate that the Ge-absorber layers influence the RW section negatively and lead to additional losses in the device that are not fully understood to this point. The designs with the stripe patterned contacts did not show an improved beam quality when compared to the other designs. The initial idea for this design was that the stripe pattern may prevent the growth of filaments (by re-absorption and low carrier density in the un-pumped region). There is undoubtedly experimental evidence in the literature [Goldberg 93, Sujecki 03] and in the results discussed in section

---

[1]The focal spot of all designs with a 4 mm long tapered section appear slightly elliptical when compared to the baseline design. The used optics were optimized for the baseline design and led to a slightly elliptical beam for devices with a 4 mm long tapered section.

[2]The amplifiers with Ge-absorber layer design and the 70% stripes design were investigated in a slightly different experimental setup but under comparable operating conditions.
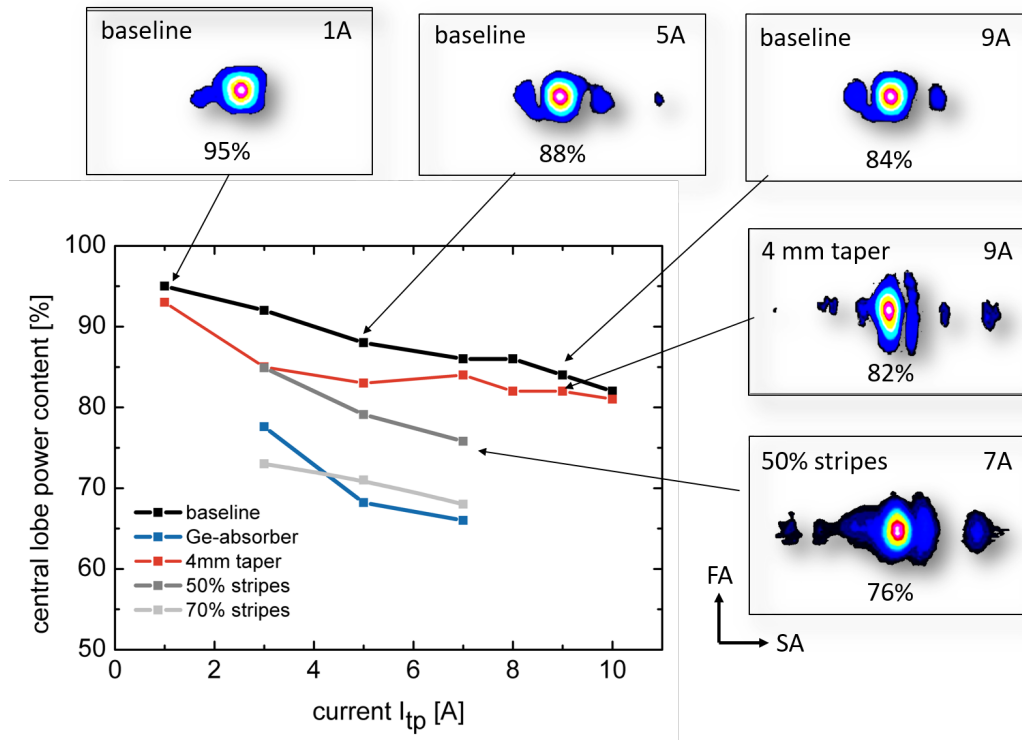
Figure II.23 – Measured central lobe power content for the different lateral amplifier designs as a function of the current I_{tp} into the tapered section. The bias conditions for all measurements were $I_{rw} = 400$ mA, $P_{in} = 10$ mW, 20°C heatsink temperature. A few exemplary beam-profiles at waist (astigmatism corrected) are given.
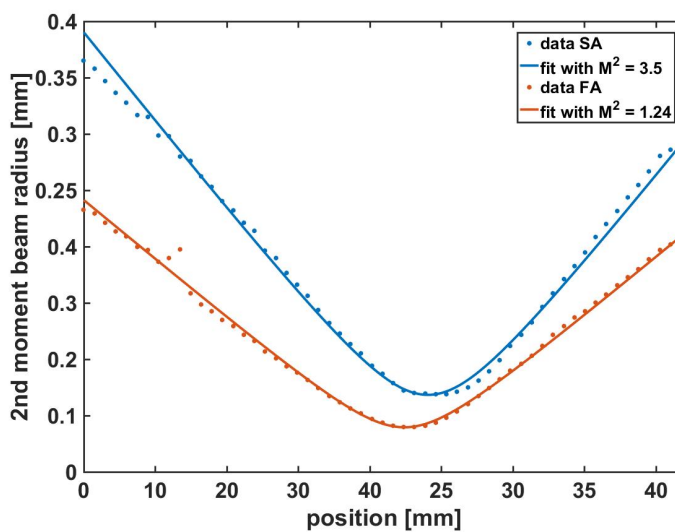
Figure II.24 – Measured and fitted caustic in SA (blue) and FA (orange) for the baseline ELoD2 tapered amplifier at $I_{tp} = 5$ A).

Table II.2 – Measures for beam quality. The uncertainty of the M^2 values was evaluated by repeated caustic measurements under identical test conditions.

design	η_{cl} at 5 A	M^2 at 5 A in SA
baseline	88%	3.5 ± 0.3
4 mm taper	85%	4.5 ± 0.4
50 % stripes	79%	5.5 ± 0.5

2.2 that filamentation in the tapered section degrades the beam quality significantly and that filamentation is especially critical in device designs with high local gain [Wan 12]. The results presented in this section indicate however that the stripe patterned electrical contacts are probably not an adequate approach to prevent the formation and growth of filaments by a modulated gain in the tapered section. The stripe pattern however also increases as a side-effect the local gain and the average carrier density in the pumped-regions, which may counter-balance any possible beneficial effect of the un-pumped regions. Furthermore, effects related to carrier-accumulation at the edges of the tapered section that favor beam quality degradation processes in tapered lasers [Lim 09], are not suppressed by the chosen stripe pattern. Numerical investigations of other more complex stripe patterns have shown that patterns targeting a reduced carrier density at the edges of the tapered section may improve the output beam quality of such devices [Borruel 04]. Such stripe patterns have however not yet been investigated experimentally. Further studies of stripe patterned electrical contacts for amplifiers with epitaxial designs highly limited by filamentation processes (e.g. the NewTPL design, cf. Fig. II.17) may be useful to clarify definitely if gain variation using stripe patterned electrical contracts are capable of limiting the growth of filaments.

3.2.3   Relation of ridge waveguide bias conditions and beam quality tapered amplifiers

The influence of the vertical and lateral chip design on the beam quality was discussed in the previous subsections. This is however not yet the full story, as the beam quality also depends on the bias conditions of the ridge waveguide section itself. The EloD2 4mm taper design was chosen for further more detailed experimental investigations.

The role of the ridge waveguide in a tapered amplifier consists in both **pre-amplification** of the low-power input signal in order to extract the energy in the tapered section efficiently and in **mode filtering** to extract the energy mainly in the fundamental transverse mode. The bias conditions of the ridge section (seed power coupled into the RW and current into the RW) therefore determine both power and beam quality at the output of the tapered amplifier.

Pre-amplification   The power-RW-current characteristic shown in Fig. II.25 for three different seed power levels shows a clear regime of saturation. The optical output power changes only in the order of 5% for 300 mA $< I_{rw} <$ 400 mA. The output power also saturates with increasing seed power ($P_{in} >$ 10 mW is required).

Mode filtering   The bias conditions of the RW have however an influence on the beam quality even in the saturation regime. The beam profile at waist was measured for three different currents into the tapered section (8, 10 and 12 A) at a current of 300, 350 and 400 mA into the ridge waveguide. The seed power coupled into the ridge waveguide was 20 mW for all measurements. Figure II.26 shows the measured beam shapes for a few different operating points. The measured central lobe power content is given for each case. The central lobe power content was > 80% even at the highest current into the tapered section for $I_{rw} = 400$ mA. It decreased however only 55% for $I_{tp} = 12$ A and a low current $I_{rw} = 300$ mA into the RW. This trend was observed in a similar way for lower currents into the tapered section but was less dramatic. The decreasing central lobe power content with decreasing
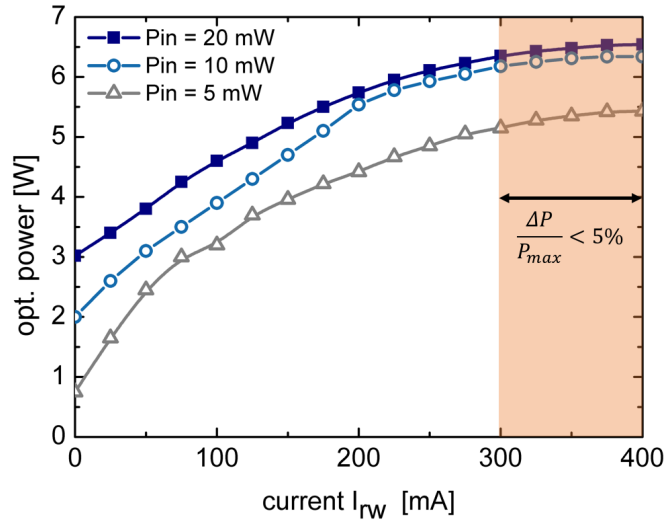
Figure II.25 – Measured optical output power for a tapered amplifier (ELoD2 4mm taper design) at $I_tp = 12$ A for different currents I_{rw} into the RW and different levels of seed power P_{in} coupled into the RW.

current I_{rw} means that the optical power is somehow transferred from the fundamental mode to higher order modes, which has only minor effects on the total power (cf. Fig. II.25).

The beam profiles at waist were investigated in a similar way for three different levels of seed power and three different currents into the RW for $I_{tp} = 12$ A. The measurements for the different operating points are summarized in Fig. II.27. The trend of a decreasing central lobe power content for decreasing currents into the ridge waveguide was observed for all seed power levels. But this trend was less surprisingly dramatic for a comparably low seed power of $P_{in} = 5$ mW. Here, the difference in the central lobe power content was only 9% (see first row) while the difference was 28% for high seed power levels (see third row). This observation is somewhat contra-intuitive, as one usually expects a better beam quality for higher seed power levels. The question arising from that observation is, why does the beam quality degrade significantly more for high seed power than it does for low seed power level? One possible explanation for this effect is a so-called bleaching of the ridge waveguide filter. Bleaching means that the absorbing region next to the ridge waveguide gets optically pumped to transparency by stray light. The bleached waveguide is then no longer a proper mode filter and may excite higher order modes in the tapered section. This effect has previously been observed in simulations of DBR-TPLs [Larkins 19]. The hypothesis in the case studied here is that a high seed power level is contributing to the bleaching of the ridge waveguide filter (for example by residual light that is not properly coupled into the RW and by evanescent field components).

Analysis of the optical feedback   It is not straightforward to verify this hypothesis by experimental investigation as the possibilities to measure the processes in ridge waveguide section of amplifier itself are quite limited. One source of information is however the optical feedback of the amplifier, which is mainly caused by backward propagating signal. The forward propagating signal beam gets in fact partially reflected at the output facet (AR coating with R = 0.3%) and amplified when counter-propagating. Contributions of amplified spontaneous emission (ASE) to the optical feedback are minor.

A simple experimental setup shown in Fig II.28 (a) was used to measure the spatial distribution of the optical feedback. The optical feedback from the amplifier was separated from the seed laser beam with a 50:50 beam-splitter. A CCD sensor was placed in an image plane of the rear facet. At the same time power and beam quality of the output beam were also measured on the front side. Figure II.28 (b) shows a simplified schematic of the rear facet of a tapered amplifier. The expected spatial distribution
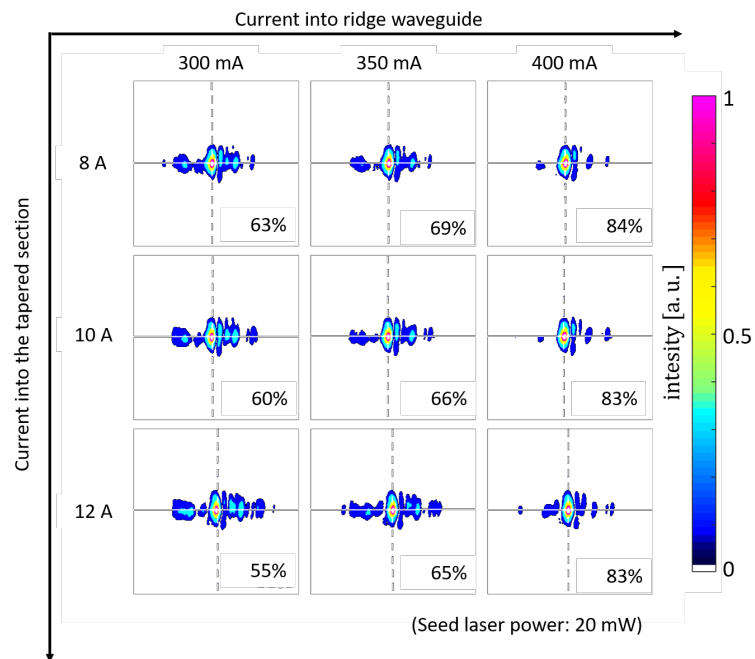
Figure II.26 – Measured beam profiles at waist (astigmatism corrected) for different currents into the tapered and ridge section. All measurements were done with an EloD2 4 mm taper amplifier. The seed power at the entrance of the ridge section was 20 mW.
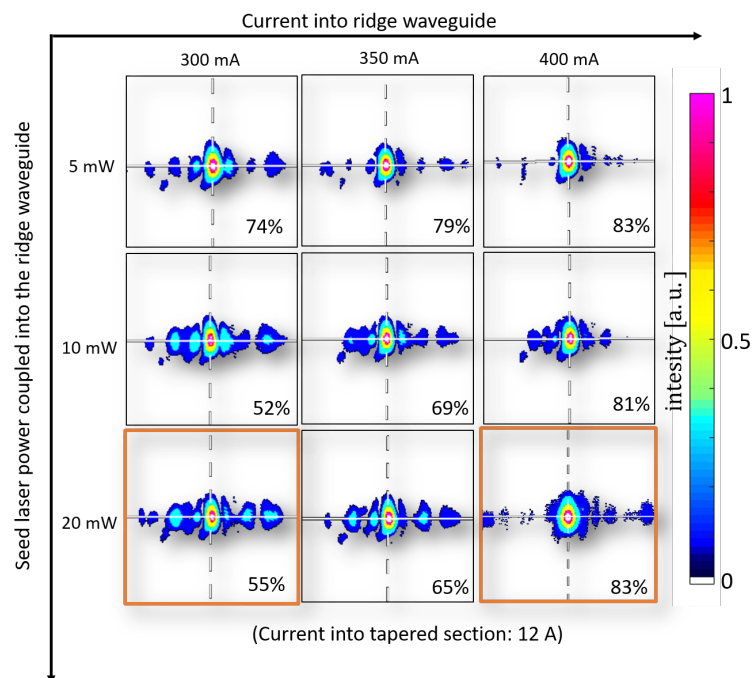
Figure II.27 – Measured beam profiles at waist (astigmatism corrected) for different currents into the RW and three different levels of seed power coupled into the RW . All measurements were done with an EloD2 4 mm taper amplifier. The current into the tapered section was 12 A. The two beam profiles marked by orange boxes will be analyzed regarding the optical feedback in Fig. II.29.

of the optical feedback is a single Gaussian spot corresponding to the fundamental mode guided by the ridge waveguide. The electrically un-pumped regions on both sides of the ridge waveguide are absorbing and in the ideal case completely nontransparent for any higher order mode feedback from the tapered amplifier.
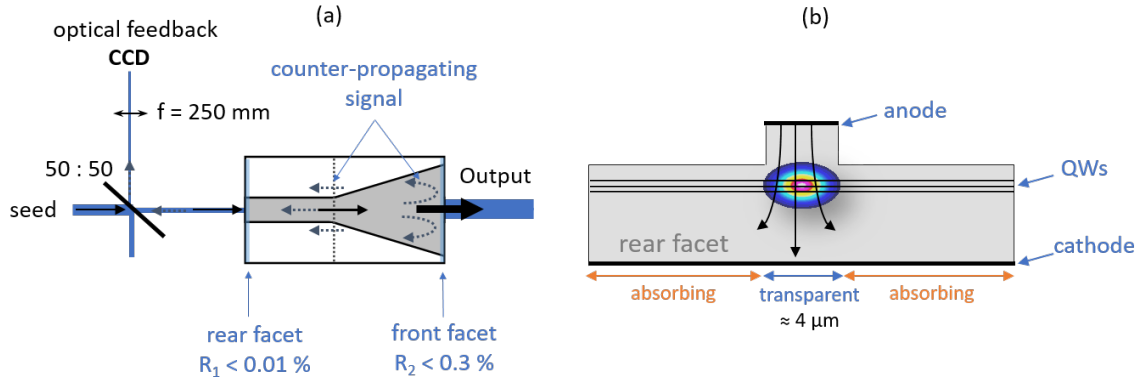
Figure II.28 – (a) Simplified schematic of the experimental setup for the investigation the amplifier feedback. (b) Simplified schematic of the rear facet of a tapered amplifier.

Two exemplary measurements of the optical feedback and the corresponding output beams at waist are shown in Fig. II.29 (a) and (b). The two cases correspond to the beam profiles marked with orange boxes in Fig. II.27 and have a very different beam quality even though the current into the tapered section was in both cases $I_{tp} = 12$ A. The feedback measured for case (a) at $I_{rw} = 400$ mA shows an about $4 \, \mu$m wide nearly Gaussian spot at the position of the ridge waveguide. Almost no intensity was measured around the ridge waveguide, showing that it works efficiently as a mode filter. The output beam quality at this operating point was good (83% central lobe power content). The spatial distribution of the feedback was significantly different for case (b), where a large amount of the optical feedback is actually transmitted in several tens of micrometer wide areas on both sides of the ridge waveguide. The ridge waveguide filters the higher order modal content of the feedback and the un-pumped regions next to the ridge waveguide do not absorb the optical feedback. The corresponding output beam quality was poor with only 55% central lobe power content. This experimental observation indicates a correlation of a dysfunction of the ridge waveguide mode filter and a degraded beam quality of the amplified beam. But, it leads at the same time to a *hen-egg-dilemma*, as it remains unclear to this point if the observed feedback pattern is the cause or the effect of the beam quality degradation.
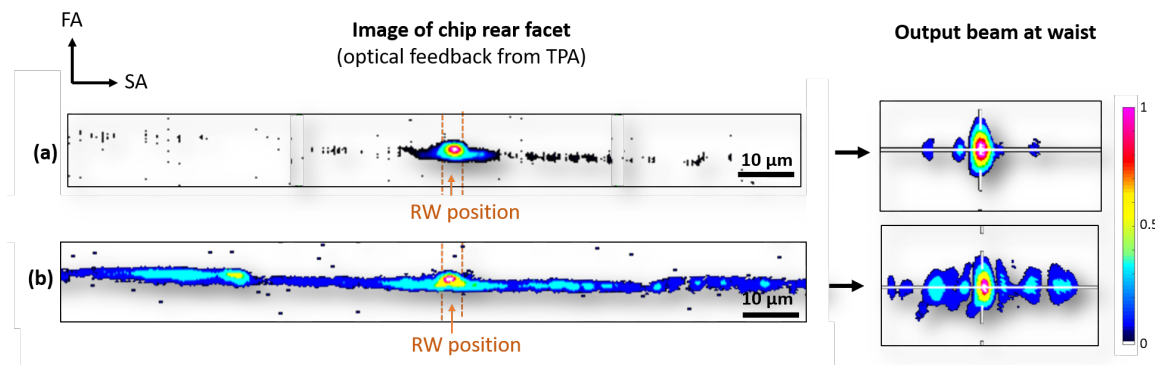
Figure II.29 – Measured optical feedback and corresponding output beam at waist (astigmatism corrected) for (a) $I_{tp} = 12$ A and $I_{rw} = 400$ mA and for (b) $I_{tp} = 12$ A and $I_{rw} = 300$ mA. The 4 mm taper design was used and the seed power was $P_{in} = 20$ mW.

Analysis of backward ASE   The measured optical feedback for the different lateral amplifier designs was compared experimentally for further understanding. Three different designs were chosen: (a) The Ge-absorber design (2 mm long RW with Ge-absorber layers) that was expected to show the best mode-filtering in the ridge waveguide section, (b) the baseline design that has a 2 mm long conventional RW and (c) the 4 mm taper design that has only a 1 mm long RW and has therefore the least effective mode filter. It is however not straightforward to compare these designs as the output powers at high bias are highly different (see Figs. II.21 and II.22). It was therefore chosen to compare the amplified spontaneous emission (ASE, no injection into the amplifier $P_{in} = 0$) for an un-pumped ridge section ($I_{rw} = 0$ mA) and a moderate current through the tapered section ($I_{tp} = 8$ A). In other words, the experimental setup was similar to Fig. II.28 but without the seed beam. The camera consequently measured the backward traveling ASE from the pumped tapered section that was filtered by the ridge waveguide.

The spatial distribution of the ASE is shown in Fig. II.30 (a-c) in false-color plots. The amplifier design with the Ge-absorber layers showed clearly the best filtering of the ASE. The Ge-absorber layers were located at $15\,\mu$m distance to the ridge section. The measurement of the ASE shown in Fig. II.30 confirms that the Ge-absorber layer does indeed absorb the backward traveling ASE. The closer surroundings of the ridge waveguide ($\pm\,15\,\mu$m from center) are however bleached by the backward traveling ASE. The backward traveling ASE of the baseline design (see Fig. II.30 (b)) was spread over a larger area when compared to Ge-absorber design. The 4 mm taper design showed the strongest backward traveling ASE, which was attributed to the shorter ridge waveguide and the large gain volume. The measurements show that the ridge waveguide sections of the different lateral designs were indeed filtering the backward traveling light differently. The point however is that the design with the Ge-layers did not show an improved output beam quality (cf. Fig. II.23)) even though it was shown that the Ge-absorber layers were functional and were in fact effectively absorbing backward traveling components. The Ge-absorber layer did however not improve the mode filter of the 4 μm wide RW section. In fact, within the distance $\pm\,15\,\mu$m from center of the RW, there was no significant difference for the Ge-absorber design and the baseline design (cf. Fig. II.30 (a) and (b)). Furthermore, both the baseline design and the 4 mm taper design showed a very similar output beam quality for different lengths of the ridge waveguide filter. It is therefore questionable if the hypothesis that the beam quality degradation of tapered lasers and amplifiers is mainly driven by a bleached ridge-waveguide filter, is true. It is likely that the back-coupled light, transmitted through the absorbing region of the ridge waveguide filter is not the cause but only the effect of beam quality degradation processes in the taper.
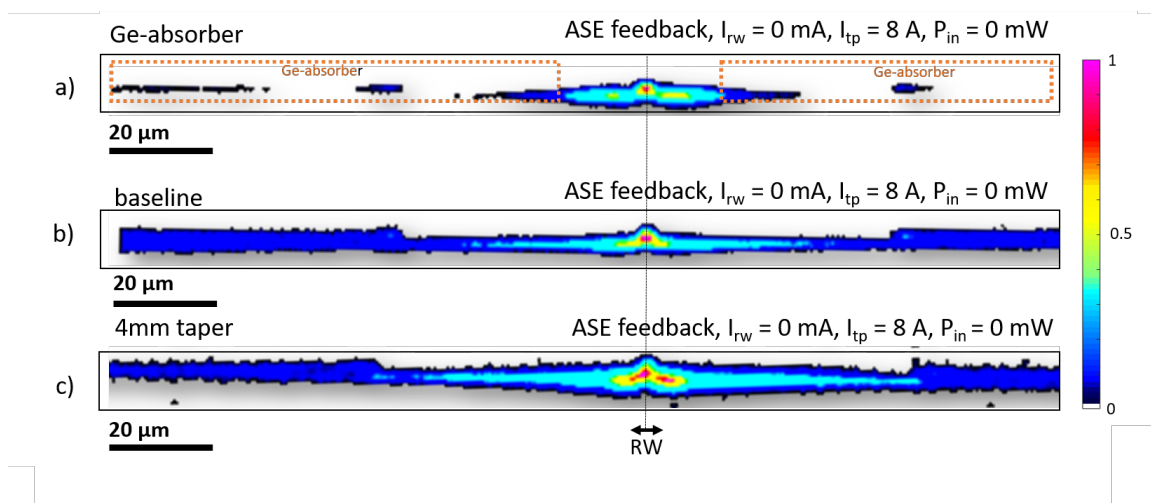
Figure II.30 – Measured ASE at rear facet ($P_{in} = 0$ mW, $I_{tp} = 8$ A and $I_{rw} = 0$ mA for three different lateral designs: (a) Ge-absorber (b) baseline and (c) 4 mm taper. The color scale of the three sub-figures is identical. The measurements were taken with the same integration time and gain on the camera.

Conclusions   The experiments presented in this section do however clearly point out that the bias conditions of the ridge wave guide have a significant effect on the output beam quality. The total output power of the amplifier may saturate for a range of different bias conditions (cf. Fig. II.25) but power in the central lobe may vary significantly.

After all, it can be seen that the beam quality degradation processes in tapered lasers and amplifiers are still not completely understood and that detailed numerical simulations and more experiments are needed for further understanding. The Laser research group at Laboratoire Charles Fabry is currently cooperating with Prof. Eric Larkins (University of Nottingham, Photonic and Radio Frequency Engineering Laboratory) in order to develop a full numerical model for ELoD2 tapered amplifiers with different geometries for future studies.

3.2.4 Phase noise

A low phase noise in the amplifier is besides high beam quality and high output power the most important requirement for coherent beam combining. Relative piston phase differences lead to a reduced combining efficiency (cf. section 2.4 in chapter I). A piston mismatch of $\Delta\varphi_{rad} = 0.2$ rad leads to losses in the order of 1% for the coherent superposition of two beams. It is often more graspable to express the relative piston mismatch in waves: $\Delta\varphi_\lambda = \Delta\varphi_{rad}/2\pi$. A piston phase mismatch of 0.2 rad corresponds for example to roughly $\lambda/30$. A spectral analysis of the phase fluctuations is required to determine the required bandwidth of the phase control to ensure correction of the piston phase mismatches with sufficient precision.

The phase noise of tapered amplifiers with different lateral designs was investigated in order to verify if a specific amplifier design shows beneficial noise properties. The signal accumulates a time dependent phase $\varphi(t)$ in the amplifier that can be written as

$$\varphi(t) = \bar{\varphi} + \delta\varphi(t), \tag{II.10}$$

where $\bar{\varphi}$ is the average value of the accumulated phase and $\delta\varphi(t)$ specifies any time dependent fluctuations. Such fluctuations can be caused by thermal, electric and acoustic noise. Another potential reason for phase fluctuations is the gain-phase coupling related to the Kramers-Kronig relations [Saleh 19]. This effect is however not relevant in the context of this work, as the gain, which is related to the carrier density, can be considered as constant.
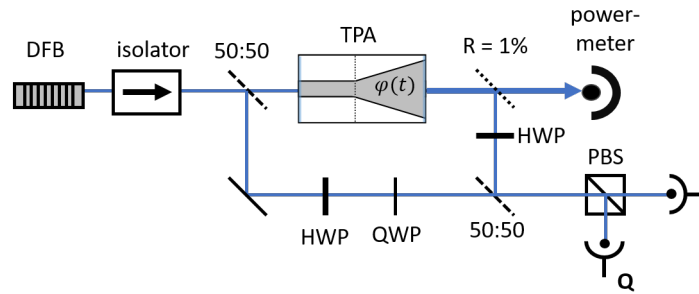
Figure II.31 – Simplified schematic of the experimental setup used for phase noise measurements. QWP: quarter-wave-plate, HWP: half-wave-plate, PBS: polarizing beam splitter, I: in-phase signal component, Q: quadrature signal component

The experimental setup, shown in Fig II.31, was a simple Mach-Zehnder interferometer. The beam of a narrow-line-width linearly polarized DFB laser was split by non-polarizing 50:50 beam splitter in two parts. The tapered amplifier was located in one of the arms of the interferometer and the second arm was used as a reference beam in free space. A small part of the amplified beam (1%) was taken for interference with the reference beam. The fluctuations in the interference were used to investigate the phase noise in the interferometer. The optical path length in each arm of the amplifier was in the range of 50 ± 1 cm. A quarter-wave-plate (QWP) was used to measure in-phase (I) and quadrature (Q) signal components with two fast Si-photodiodes after a polarizing beamsplitter (PBS) [Huang 09]. Half wave plates (HWP) were used in both arms of the interferometer to achieve approximately the same signal contrast for the I and Q components. A linear phase-drift in the active arm of the amplifier was applied (by a linear increase of the current into the ridge section) to calibrate the experimental setup. Figure II.32 shows the obtained signals for I and Q components, which are in this case (linear phase drift) sinusoidal functions with a $\pi/2$ phase shift.

The I and Q signal components were then recorded with different tapered amplifiers at a few different operation points. The measurement time was 40 s and the sample rate of $f_{max} = 25$ kHz. The change in phase $\varphi(t)$ in the active arm of the interferometer can be directly calculated by the relation

$$\varphi(t) = -\arctan\frac{Q(t)}{I(t)}. \tag{II.11}$$
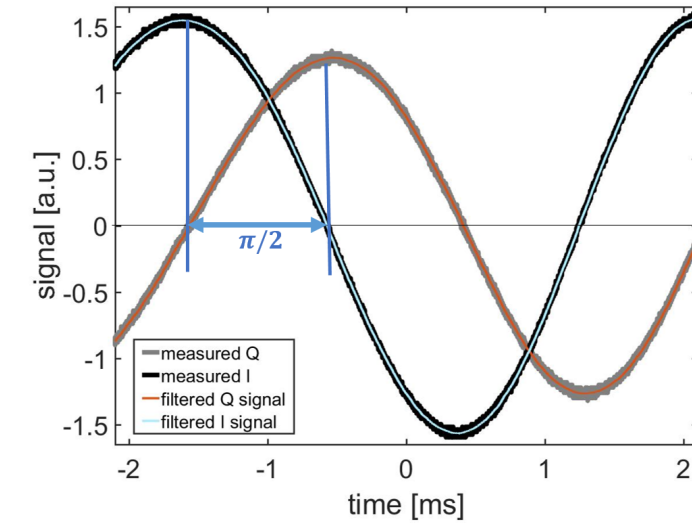
Figure II.32 – Quadrature calibration signals for phase noise measurement. The (approximately) linear phase drift was generated by a linear increase of I_{rw}

An exemplary measurement of the phase drift $\varphi(t)$ (for an ELoD2 TPA with the 50% stripes at $I_{tp} = 10$ A) is shown in Fig. II.33 (a). The measured phase drift (see blue line) is slow and the total amplitude of the variations are in the range of $\pm\lambda/20$ only. The detection limit (background noise of detectors and oscilloscope) is shown in black for comparison. The one sided power spectral density (PSD)

$$S_\varphi(f) = 2 \int_0^{f_{max}} \left[\delta\varphi(t)\delta\varphi(t+\tau) \right] e^{(i2\pi f\tau)} d\tau \qquad \text{(II.12)}$$

is shown in Fig. II.33 (a). A moving average filter was applied to the PSD for $f \in [1 \text{ Hz}, f_{max}]$ for better visibility. The unfiltered PSD is shown in gray for completeness. Frequencies below 100 Hz are clearly dominating the noise spectrum and the PSD is close to a $1/f^2$-noise. The detection at higher frequencies is limited by the (white) background noise floor at about 10^{-8} rad^2/Hz. The integrated phase noise

$$S_{int}(f) = \sqrt{\int_f^{f_{max}} S_\varphi(f) df} \qquad \text{(II.13)}$$

is shown in Fig. II.33 (c) and was $S_{int}(1 \text{ Hz}) = 0.02$ rad $\approx \lambda/300$. This means that a simple phase control loop, correcting the phase fluctuations only once per second is would be sufficient to achieve excellent phase matching. Also free-running operation without any active correction on the order of 10 s seems feasible as the integrated phase noise at 0.1 Hz is still very low.

This measurement showed an excellent phase stability of the interferometer. The question however is, if the measured phase drift is actually dominated by noise in the tapered amplifier or dominated by noise in the optical setup itself. The amplifier in the experimental setup (cf. Fig. II.31)) was removed and the phase noise in the interferometer itself was characterized under identical conditions. A comparison of the phase noise with and without the amplifier is shown in Fig. II.34 (a) and (b), showing that the observed phase noise is indeed dominated by fluctuations in the amplifier. The contribution of the amplifier can be estimated by subtraction of the two lines in Fig. II.34 (b), which leads to an estimate of the integrated phase noise in the amplifier itself of $S_{int,TPA}(0.1 \text{ Hz}) \approx \lambda/100$ which was six times more than the contribution of the interferometer itself $S_{int,rest}(0.1 \text{ Hz}) \approx \lambda/600$. Note that these measurements were done in a laboratory environment well protected from external noise sources. The interferometer was isolated from external mechanical vibrations and inside a closed box. All acoustic noise sources in the laboratory were eliminated. The noise contribution from the interferometer itself
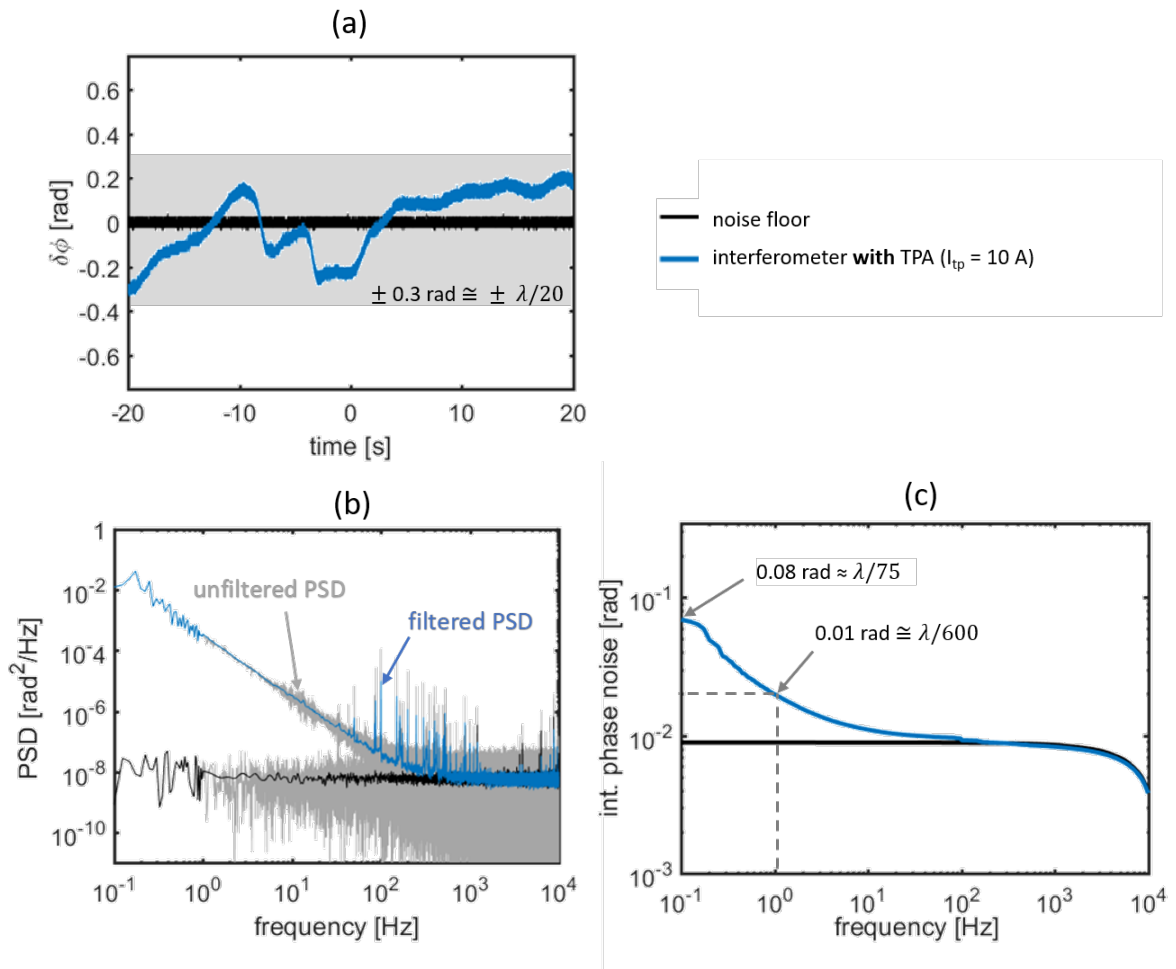
Figure II.33 – Phase noise characterization for the active arm of the interferometer with an EloD2 TPA amplifier (50% stripes design, $I_{tp} = 10$ A, $I_{rw} = 350$ mA, $P_{in} = 30$ mW, measured data in blue, noise floor level in black). (a) measured phase drift, (b) PSD, (c) integrated phase noise.
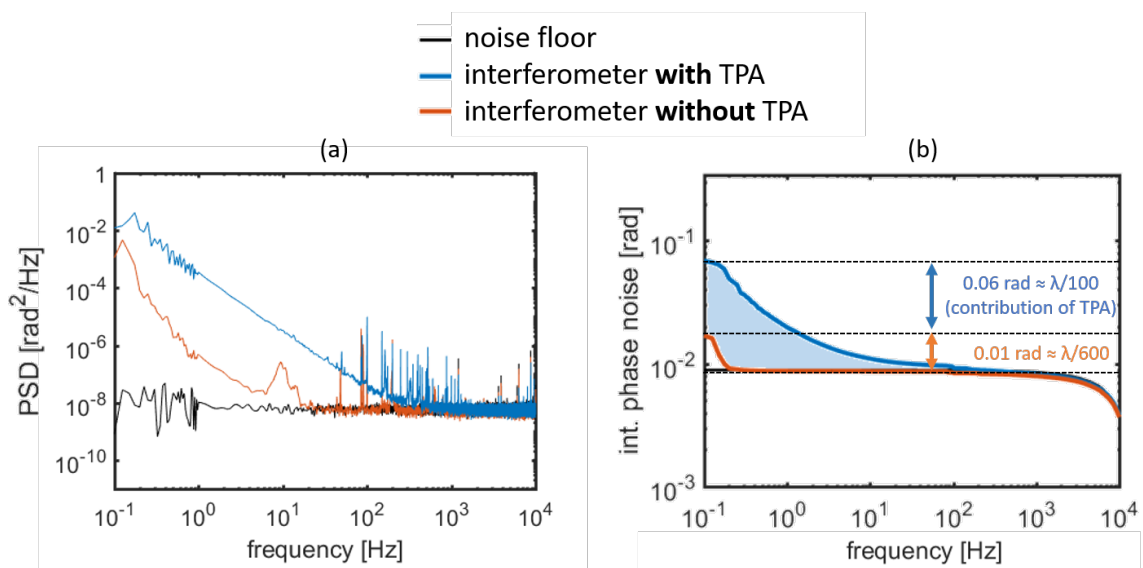
Figure II.34 – Phase noise characterization for the active arm of the interferometer with and without EloD2 TPA amplifier (50% stripes design, $I_{tp} = 10$ A, measured data with TPA in blue, without TPA in orange, noise floor in black). (a) filtered PSD, (b) integrated phase noise.

can be much higher in a more realistic environment, e.g. in the presence of acoustical noise or air flow from an air-conditioning system. In fact, the noise in the experimental setup was clearly dominated by the noise of the interferometer itself if the box, protecting the interferometer from air convection, was opened. In other words, a comparison of the phase noise of amplifiers with different lateral design has to be performed carefully and with the best possible protection from external noise sources.

For completeness, it was chosen to compare the noise properties of tapered amplifiers with and without a stripe patterned electrical contact. The observed phase drift in a device of the 4 mm taper design and a device of the 50% stripes design was almost identical as shown in Fig II.35. The relative differences in the integrated phase noise were only in the range of $\lambda/600$ and in the order of the repeatability precision of the noise measurements. A technical challenge is the temperature stability of the setup and the precision of the used active temperature control. An integrated phase noise in a 5 mm long tapered amplifier in the range of $S_{int,TPA}(0.1\text{ Hz}) \approx \lambda/100$ means that the optical path length in the amplifier is changing in the order of 10 nm only. The refractive index of the waveguide approximately 3.4 and $dn/dT = 2\times10^{-4}$ [Gehrsitz 00], which leads to a required temperature stability better than ±0.005 K to achieve a stability of the optical path in the order of ±10 nm. The used temperature controller (Arroyo Instruments, 5305 TEC Source) had a specified temperature stability of ±0.01 K, meaning that the observed phase drift in the amplifier can be attributed to a slowly fluctuating temperature in the device. It is therefore questionable if a comparison of the low frequency noise components (thermal noise) of different amplifier designs makes sense, as the observed phase noise is most probably dominated by thermal noise from the TEC controller.

There was no experimental evidence for an effect of the lateral design on the phase noise. The conclusion of these experiments was that the phase-noise in the amplifier is very low and hardly detectable. A comparison of the phase noise of different device designs was not possible, but is also not required as phase noise in the amplifier is very low and not critical for coherent beam combining.
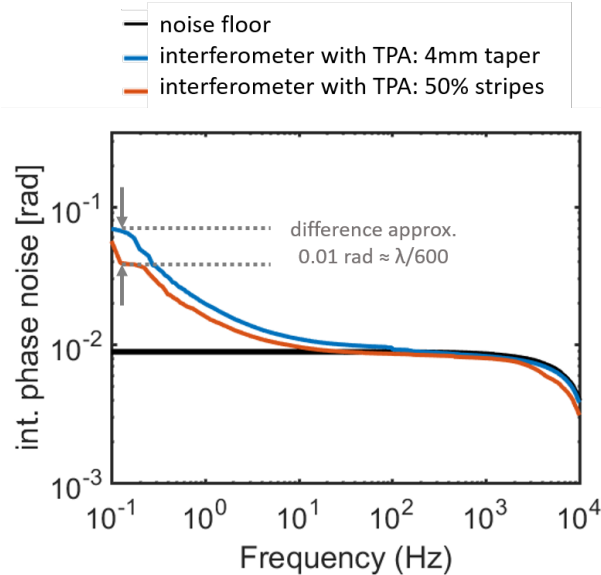
Figure II.35 – Phase noise characterization for two different amplifier designs: 50% stripes design in orange, 4 mm taper design in blue $I_{tp} = 10$ A, noise floor in black.

3.2.5 Phase control

Active phase control is required for coherent beam combining to correct the small phase drift in the amplifiers. A straightforward concept is to use an active feedback on the current into the ridge waveguide for phase control. This can be done with limited impact on the optical output power within the saturation regime in the range of $300\text{ mA} < I_{rw} < 400\text{ mA}$ (cf. Fig. II.25). Note that there may how-

ever be a considerable influence on the central lobe power as the beam quality is sensitive to the bias conditions of the ridge section (cf. section 3.2.3). The effective optical path in the amplifier is almost linear to the current into the ridge section with $dI_{rw}/d\varphi = 35$ mA $/\pi$ [Schimmel 16, Albrodt 18b].
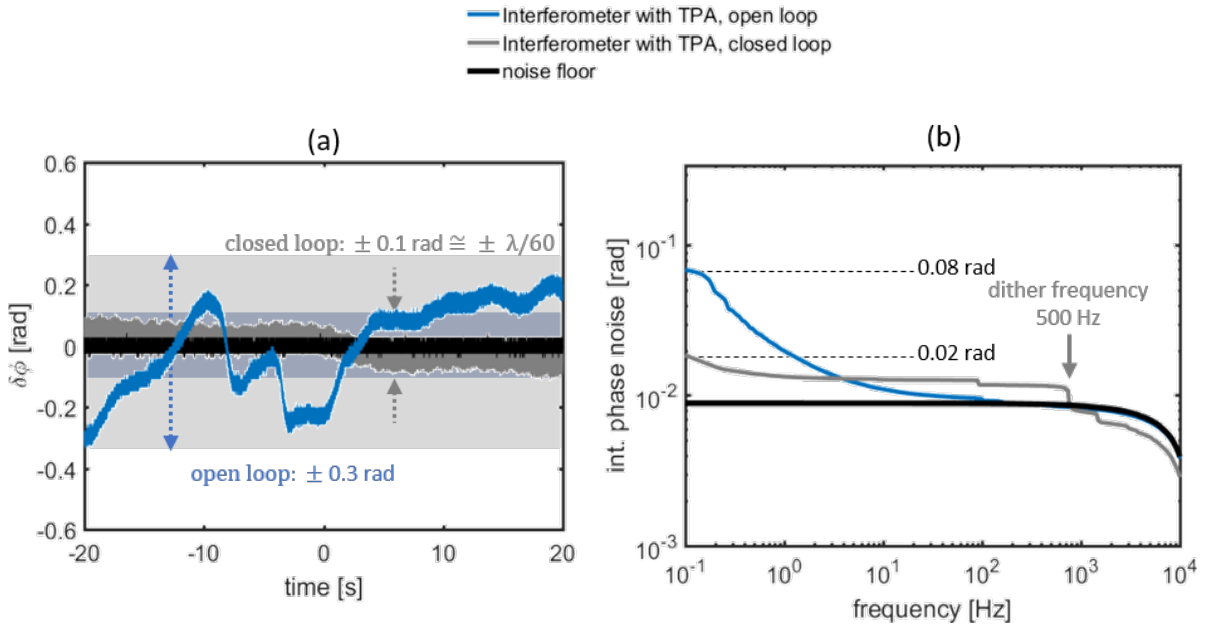
Figure II.36 – Phase noise characterization of the interferometer without phase control (open loop, blue line) and with phase control (closed loop, gray line). ELoD2 TPA (50% stripes design), $I_{tp} = 10$ A, noise floor in black.

A simple hill-climbing algorithm, implemented on a micro controller, was used to maximize the in phase signal component (cf. experimental setup Fig. II.31). The used algorithm was based on a small periodical dither at a frequency of 500 Hz and an adaptive hill-climbing step calculated as a function of the dither signal. The algorithm is described in details in the annex of this manuscript (see page 2.3). The residual phase noise with the active phase control was characterized under identical bias conditions as for the previously discussed measurements. The measured residual phase drift was close to the detection limit as shown in Fig. II.36 (a) with an integrated phase noise of $S_{int}(0.1 \text{ Hz}) \approx \lambda/300$ (cf Fig. II.36 (a)). The dither of the hill-climbing algorithm leads to a slightly increased phase noise around 500 Hz. The low frequency components of the phase noise are however effectively corrected and the achieved precision is largely sufficient. The difference between the recorded signal with and without phase control may seem small in this example, this is however due to the low level of noise in the interferometer itself.

Sequential correction of a several tens of channels is also possible as the achievable bandwidth of a simple micro-controller based hill climbing algorithm is in the MHz range, and the bandwidth for an active current control with commercial laser diode drivers is in the kHz regime. One can therefore easily sequentially correct the phase fluctuations, dominated by very low frequencies (cf. Fig. II.33) in the different arms of the interferometer.

3.2.6   Relative intensity noise

The standard specification for optical power fluctuations of laser sources is the **r**elative **i**ntensity **n**oise (RIN). The optical power of a laser source can be written as

$$P(t) = \bar{P} + \delta P(t), \tag{II.14}$$

with the average optical power $\bar{P}$ and time dependent fluctuations $\delta P(t)$. The power fluctuations can be statistically described with a PSD and its integrated form in the same way as previously discussed

for the phase noise (cf. equations II.12 and II.13). The RIN was measured with a fast photodiode and a low-noise analog amplifier was used to amplify the signal fluctuations (40 dB gain for f > 100 Hz). The measured RIN is shown in Fig. II.37 ((a) PSD, (b) integrated RIN) for three different device designs (4 mm taper, 50% stripes and 70% stripes). Minor differences were observed for frequencies from 25 kHz to 100 kHz, where amplifiers with a stripe patterned electrical contact showed multiple discrete noise peaks. The most conventional design, the 4 mm taper design, showed the lowest intensity noise. The differences to the device design with stripe patterned contact were small but the measurements indicate that the RIN is slightly increased by the modulated gain in the tapered section. The integrated RIN was below 0.02% rms (1 Hz - 200 kHz) for all amplifier designs, which is comparable to commercial low-noise diode laser modules relying on tapered amplifiers (e.g. Toptica Photonics, BoosTA pro product line [Toptica 19]).
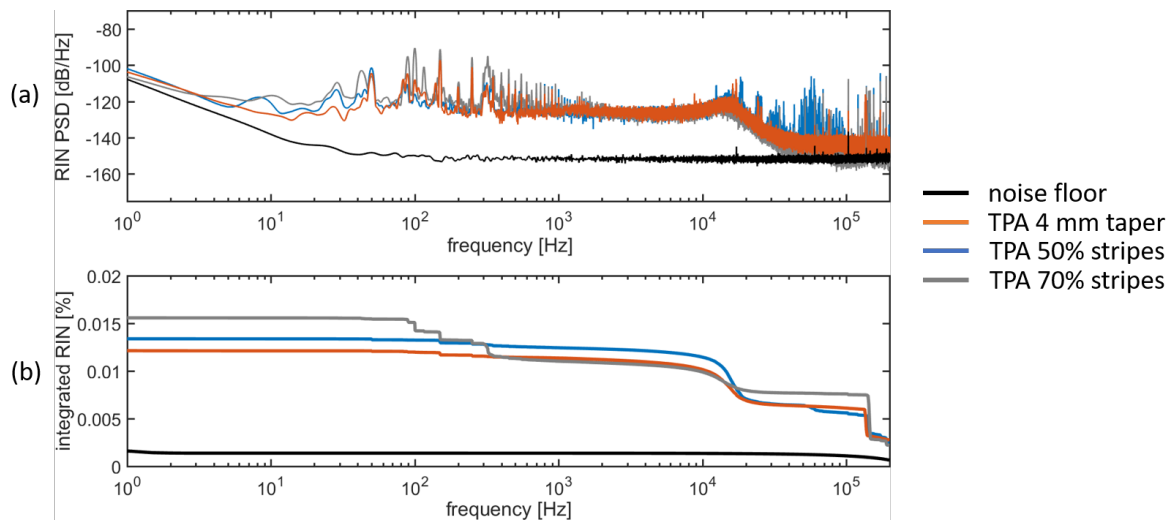
Figure II.37 – RIN measurements for three different lateral amplifier designs (orange: 4 mm taper, blue: 50% stripes, gray: 70% stripes). The optical power was 5 W for all measurements. The same current supply was used.

3.3 Conclusions for the lateral design of tapered amplifiers

Optical power, power conversion efficiency, beam quality, intensity and phase noise properties of five different lateral designs of ELoD2 tapered amplifiers have been investigated and the results were discussed in the previous sections. The most relevant results are summarized in Table II.3 including a few generalized comments on the designs. Three designs with particular good characteristics (baseline, 4 mm taper and 50% stripes), were chosen for CBC experiments that will be discussed in Chapter 3 and 4 of this manuscript. The aim of this comparative experimental study was to investigate if advanced lateral designs, incorporating absorber layers for an enhanced mode filtering or stripe-patterned electrical contacts of the tapered section, help to improve the properties of tapered amplifiers. The summarized results however show that the more conventional designs (baseline, 4 mm taper), performed significantly better than the other designs. The results lead to the following conclusions:

Ge-absorber layers in the ridge waveguide section do not improve the beam quality of tapered amplifiers. The Ge-absorber layers were located at $15\,\mu m$ distance to the ridge waveguide. It has been shown that the Ge-absorber layers are functional and absorb back-coupled light, they do however not enhance the filtering of the close surroundings of the ridge waveguide. Furthermore a decrease in performance in terms of output power has been observed in CW and QCW operation, which was attributed to slight additional losses in the device related to the modified ridge waveguide structure. As there was overall no benefit from the Ge-absorber layers next to the ridge waveguide, it is questionable if parasitic oscillation of back coupled higher order modes plays a significant role in beam quality degradation processes in tapered amplifiers. Further investigations by numerical simulations are in progress.

Stripe patterned electrical contacts of the tapered section do not improve the beam quality and the noise properties of tapered amplifiers. The idea behind this design variant was that alternating pumped and un-pumped regions in the tapered section may prevent the growth of filaments and improve the performance of tapered amplifiers. There was however no experimental evidence showing that the stripe patterned electrical contact improves the performance of tapered amplifiers. It is questionable if a stripe patterned contact is actually helpful to prevent the growth of filaments as the average gain is lowered at the cost of an alternating structure of regions with very high gain and regions with no gain. Stripe patterned electrical contacts may however still be useful in configurations where one common electrical contact is used for tapered section and ridge waveguide section [Crump 19].

The phase noise in high power tapered amplifiers is not a key-challenge regarding coherent beam combining. It has been shown that the phase noise in tapered amplifiers is low (in the order of 0.1 rad rms (0.1 Hz - 10 kHz)) and dominated by very low frequencies. Standard sequential hill-climbing algorithms are the most straightforward technique for the phase control in coherent beam combining architectures. There was no evidence for an influence of the lateral design of the amplifier on the phase noise. Most of the phase fluctuations were attributed to slow temperature fluctuations within the temperature tolerance of the used TEC controllers.

Table II.3 – Summary of the experimental results for the different lateral designs

	baseline	Ge-absorber	4 mm taper	50% stripes	70% stripes
P_{max} (CW)	4.4 W	3.7 W	6.6 W	5.3 W	5.1 W
PCE_{max} (CW)	32%	32%	29%	27%	26%
P_{max} (QCW)	9.5 W	7.2 W	12.5 W	12.3 W	11.7 W
PCE_{max} (QCW)	32%	35%	36%	34%	32%
η_{CL} at 8 A	88%	66%	85%	79%	68%
Phase noise	< 0.06 rad RMS ≈ λ/100 (0.1 Hz – 10 kHz) mainly caused by a slowly varying device temperature. No measurable differences within the different device designs.				
Intensity noise	RIN < 0.02 % RMS (1 Hz – 200 kHz). Minor differences in the frequency range of (25-100 kHz) were observed for devices with a stripe patterned electrical contact.				
Used for CBC experiments	Yes	No	Yes	No	No
Comment	Critical thermal rollover, Best beam quality.	Poor output power, poor beam quality. Ge-absorber works but is not improving the beam quality and is possibly causing other problems in the RW.	Highest power, decent beam quality. **Preferred device design for high-power experiments**	Acceptable power and beam quality. There was however no evidence for a benefit from the stripe-patterned contact (tapered section).	Acceptable power, poor beam quality. There was no evidence for a benefit from a stripe patterned electrical contact (tapered section).

Chapter III

Continuous wave coherent beam combining

Objectifs

This chapter covers continuous wave coherent beam combining experiments. The experimental principles, which are essentially identical for all experiments, are discussed in the first section. The second section is about a preliminary experimental setup for coherent beam combining of three tapered amplifiers using the reference epitaxial design. This experiment was used to demonstrate the effect of the scaled brightness for nonlinear frequency conversion. Different lateral designs of the ELoD2 epitaxial design are investigated in the third section and a clear improvement of the achievable combining efficiency was demonstrated. In the last section, a simple pathway for the development of coherent beam combining modules based on commercially available tapered amplifiers and standard off-the-shelf optical elements is demonstrated.

Contents

1 Experimental principles of coherent superposition

Several experiments on coherent beam combining will be discussed in this chapter. The difference in between the experiments described in the sections 2-4. are the type and the number of the used amplifiers, but the experimental setup and the general principles discussed below are very similar.

1.1 Typical experimental setup and optimization of the combining efficiency

The typical setup for coherent superposition of two tapered amplifiers is shown in Fig. III.1 (a). The MO was for all experiments discussed in this manuscript a DFB laser at 976 nm with a spectral linewidth below 20 MHz. An aspherical lens with a high numerical aperture (L_1, NA = 0.55, f = 8 mm) was used for collimation. A double stage optical isolator ($2\times$ Thorlabs IO-5-NIR-LP ensuring an optical isolation > 55 dB) was used. Two folding mirrors were used for alignment of the seed into the first TPA (A_1). The 50:50 plate beam-splitter and a third mirror were used for coupling into the second TPA (A_2). A high NA aspherical lens (L_2, NA = 0.55, f = 8 mm) was used for coupling into the RW section and glued to the heatsink of the amplifier. The tapered amplifiers, mounted on C-mounts, were fixed on a large copper heatsink. We used active thermoelectric cooling with a Peltier-element mounted on a large water-cooled aluminum radiator for each amplifier.

Note that the optimization of the coupling into the RW is very critical regarding the output beam quality of the tapered amplifiers. The coupling was optimized to achieve the highest power in the central lobe at high bias. The total optical output power of a tapered amplifier is less sensitive to misalignment of the seed laser beam as the power in the central lobe. It is therefore required to measure the power and the beam profile at waist simultaneously during the optimization of the setup.
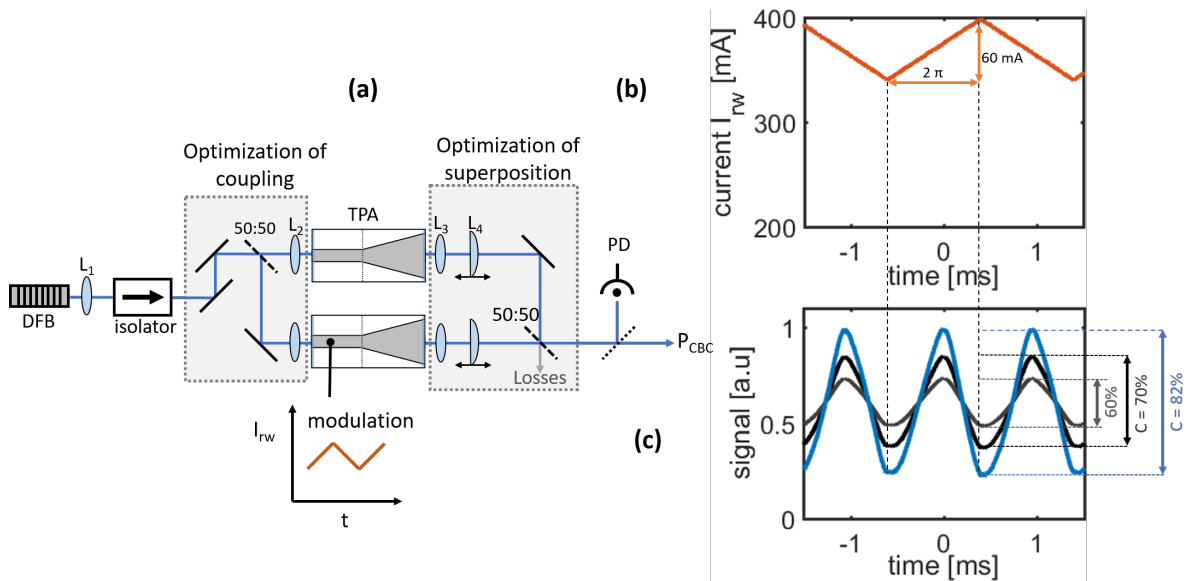
Figure III.1 – Simplified schematic of (a) the typical coherent beam combining architecture used in this work; (b) Modulated current I_{rw} to achieve a phase shift in the interferometer; (c) Recorded alignment signals with three different levels of contrast.

The beam was collimated with a high NA aspherical lens glued to the heatsink at the output of the amplifier (L_3, NA = 0.55, f = 2.3 mm). A cylindrical lens (L_4, f = 19 mm) mounted on a linear translation stage was used to correct the astigmatism of each amplifier. The astigmatism of a tapered amplifier depends in fact on the current into the tapered section (also called *wandering astigmatism*) [Kelemen 04, Larkins 19] and was corrected individually at each investigated bias point. A pair of mirror and beam splitter allowed to overlap the beams in near and far-field with minimal displacement and pointing errors, cf. Fig III.1 (a).

Both the coupling into the amplifier and the superposition have to be optimized to achieve the best

possible combining efficiency at the output of the interferometer. For that reason, the interference signal of two beams is optimized, while the piston phase in one arm of the interferometer is modulated. A periodic linear modulation of the current I_{rw} into the RW of one amplifier leads to an approximately linear phase-modulation $\Delta\varphi_{mod}(t)$ (cf. Fig. III.1 (b) and (c)). The beams interfere on a 50:50 beam combiner and the optical power in the output pathway was measured with a photodiode[1] (PD). The field in one of the output pathways of the beamsplitter is

$$E_{CBC}(x,y,t) = \frac{\underline{E_1}(x,y) + i\underline{E_2}(x,y)e^{i\Delta\varphi_{mod}(t)}}{\sqrt{2}}. \tag{III.1}$$

The photodiode signal is proportional to the optical power $P_{CBC}(t)$, which can be written as

$$P_{CBC}(t) = \frac{1}{2}\Big(P_1 + P_2 + 2\sqrt{P_1 P_2} \times C \times \cos(\Delta\varphi_{mod}(t))\Big), \tag{III.2}$$

where $\Delta\Phi_{mod}(t)$ is the piston phase induced by the modulated ridge current and C is the overlap factor of the two complex fields

$$C = \frac{|\iint \underline{E_1}(x,y)\underline{E_2}^*(x,y)dxdy|^2}{\iint I_1(x,y)dxdy \iint I_2(x,y)dxdy}. \tag{III.3}$$

The induced linear phase shift $\Delta\varphi(t)$ leads consequently to a sinusoidal oscillation of the output power $P_{CBC}(t)$. For two perfectly coherent fields and $C = 1$, one would detect a modulation with 100% contrast. The fields from the tapered amplifiers are however slightly mismatched ($C < 1$), which leads in our case to a modulation with limited contrast. The expected maximal combining efficiency of the setup can be calculated from the recorded signal by the simple relation

$$\eta_{CBC} = \frac{P_{CBC}}{P_1 + P_2} = \frac{P_{CBC}}{P_{CBC} + Losses} = \frac{S_{max}}{S_{max} + S_{min}}, \tag{III.4}$$

where S_{max} and S_{min} are the maximal and minimal value of the modulated signal shown in Fig III.1 (c). The combining efficiency can be put in relation to the overlap by $C = 2(\eta_{CBC} - 0.5)$. The photodiode signal was used for the optimization of overlap and combining efficiency. Three exemplary signals for 60, 70 and 80% combining efficiency are shown in Fig III.1 (c). The maximal achieved combining efficiencies for the interference of two beams were in the range of 80-90% (cf. following sections), mostly limited by the slightly degraded beam quality of the tapered amplifiers. Mismatches related to spot displacement or pointing errors were not significant. This experimental procedure was applied for the optimization of the experimental setups described in the following section. The optimization of larger setups with for example four amplifiers, as shown in Fig. III.2 can be done in a similar way by series of two-by-two optimization steps as indicated in Fig. III.2.

1.2 Stabilization and operating conditions

The phase control was achieved by an active control of the optical path in the arms of the interferometer. Active control on the currents into the ridge waveguide was used for phase control in the experiments described in section 2 and 3 and piezoelectric actuators were used in the experiments described in section 4, where phase control via the currents was not possible. The general principle of the phase control and the used hill climbing algorithm were however identical. One arm of the interferometer was always used as the *reference* (free running - no active control), and the piston phases in the other arms were actively controlled to achieve phase matching. A sequential hill-climbing algorithm was used. The phase matching of the first arm with respect to the *reference* was optimized, after that the phase matching of the other arms in sequential order before starting again with the first arm. The duration of one optimization step was in the order of a few milliseconds only, so that the phases in the other

---

[1]The beam was focused on the photodiode to average over the full aperture.
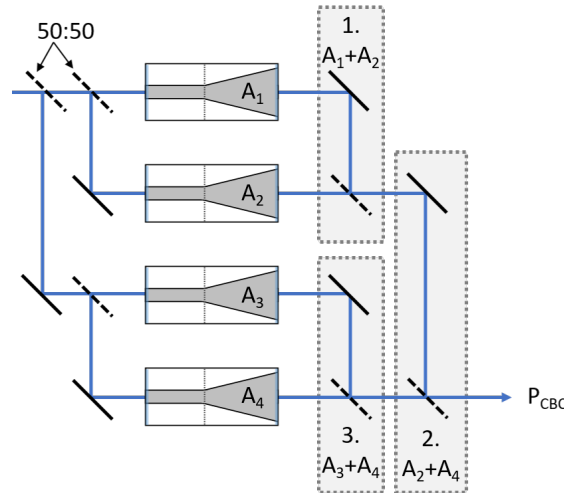
Figure III.2 – Simplified schematic of the optimization procedure for a CBC setup with four amplifiers.

arms of the interferometer can be considered as constant during the optimization (cf. II.3.2.4). The general principle of the used hill climbing algorithm is shown in Fig. III.3. A small dither was applied to the current into the RW, which corresponds to a small dither in the relative piston-phase differences. The dither allows to measure the local slope of $P_{CBC}(I_{rw})$. The hill-climbing step is calculated as a function of the measured slope. The dither amplitude is reduced once the maximum is reached. If the current I_{rw} approaches the defined minimum and maximum values, a large current step ΔI_{jump} approximately corresponding to 2π phase-shift is used to *jump* to the next local maximum. The difference $I_{max} - I_{min}$ has to be larger than ΔI_{jump} to avoid instabilities. A change of approximately ± 70 mA corresponded to a 2π phase shift in the experiments described in this work and currents from 250 mA to 400 mA were allowed for I_{rw}. A detailed flowchart of the hill-climbing algorithm implemented on a micro controller is given in the annex(see page 145) of this manuscript. The bandwidth of the used phase control mechanism was in the order of 1 kHz, which was limited by the modulation bandwidth of the laser diode drivers and not by the speed of the algorithm. This was however largely sufficient as the phase noise in the interferometer is dominated by low frequencies far below 100 Hz (cf. II.3).
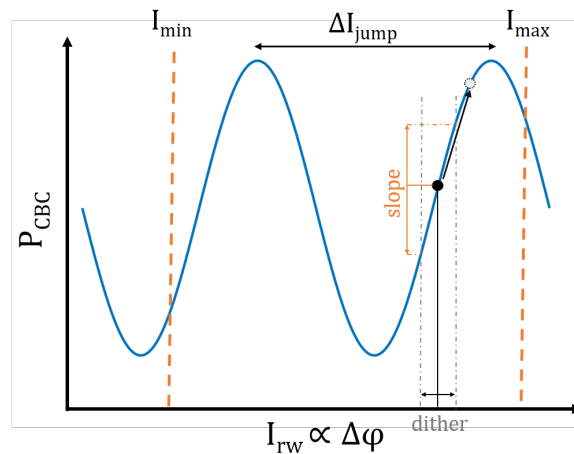
Figure III.3 – Simplified schematic of the phase control.

2   Coherent beam combining using the reference epitaxial design

Preliminary experiments with tapered amplifiers using the reference epitaxial design (cf. section 2 in chapter II) are discussed in this section. The amplifiers used in this work were recycled from previous experiments in the framework of the BRIDLE project and the PhD-thesis of Guillaume Schimmel [Schimmel 16].

The coherently combined beam (976 nm) was used as the NIR pump source for nonlinear frequency conversion to 488 nm in order to demonstrate the usefulness of coherent beam combining for the development of high power visible laser sources based on semiconductor emitters only.

2.1   Experimental setup

The experimental setup was a simple three arm interferometer shown in Fig. III.4. The setup was originally designed for two amplifiers only and then extended for three amplifiers in total. This is the reason why it may seem imbalanced and slightly asymmetric at the first glance. The idea was however to investigate if a cascade of combining steps is practical and beneficial for nonlinear frequency conversion and to investigate how the beam quality is evolving. The setup was easily adaptable to use the beam from coherent superposition of A_1 and A_2 only by removing the second combining element (C_2 in Fig. III.4). Similar to that, the beam from A_2 only can be used by removing both combiners (C_1 and C_2 in Fig. III.4).

The optical elements used for splitting and combining were standard 50:50 beamsplitters. This leads obviously to imbalanced seed powers (seed power for A_3 is lower), which is however not critical as long as all amplifiers are saturated. Furthermore, this leads also to power mismatches during coherent superposition causing however combining losses 3% only (see section I.2.4). The optical path-length in the interferometer was not balanced for practical reasons. In fact, the path length of the arm with A_3 was about 30 cm longer than the optical path in the other arms.
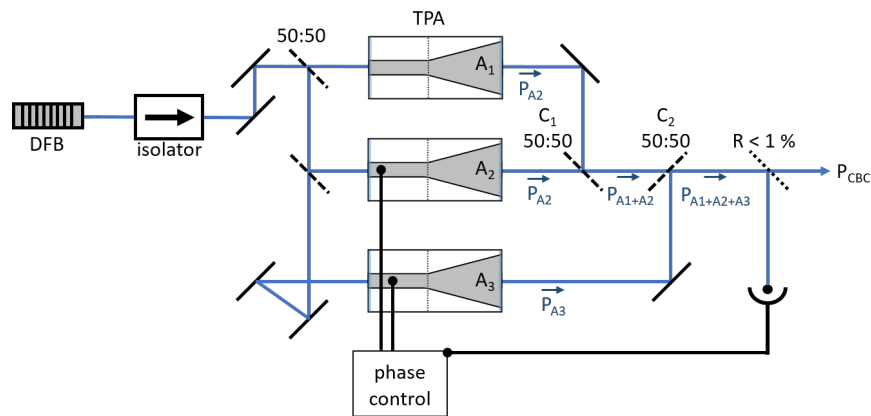
Figure III.4 – Simplified schematic of the experimental setup. Lenses for collimation and coupling are omitted for simplicity. Non-polarizing 50:50 beamsplitters were used for separating and combining the beams. A double stage optical isolator with > 55 dB isolation was used.

The amplifiers were 6 mm long and mounted p-side down in CuW-submounts and C-mounts. The RW was 2 mm long and 4 μm wide for A_1 and A_2. A similar device with a 4.5 μm wide RW was used as A_3, limited by the availability of the amplifiers. The tapered section was 4 mm long (6° taper angle). The facets of the amplifiers were passivated and AR coated (R < 0.1%). The output power characteristics of the amplifiers are shown in Fig. III.5 (a). The maximal power was > 6 W at the maximum current I_{tp} = 10 A. Figure III.5 (b) shows the output power of A_1 as a function of the current into the RW and the seed power at constant current into the tapered section. The results show that > 10 mW of seed power is sufficient to saturate the amplifier. The seed power for the coherent beam combining experiments was approximately 20 mW for A_1 and A_2 and 10 mW for A_3, so that all

amplifiers were saturated.
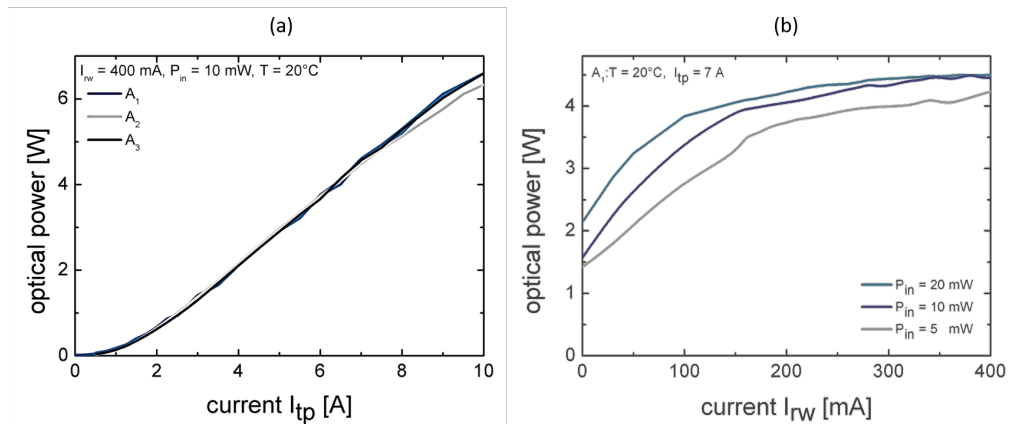
Figure III.5 – (a) Output power characteristics $P_{out}(I_{tp})$ for the three used tapered amplifiers. (b) Output power characteristics $P_{out}(I_{rw}, P_{in})$ of A$_1$ at $I_{tp} = 7$ A.

2.2 Coherent beam combining results

Stability The stability of the setup was investigated by recording the signal from the photodiode at the output of the interferometer, which was also used as the input signal for the phase control loop (cf. III.4). The currents into the RW of A$_2$ and A$_3$ were also recorded. Figure III.6 shows an exemplary measurement with excellent stability of the power over about one hour. The rise time of the hill-climbing algorithm was below 1 s. The standard deviation in the stabilized level was below 0.6% (rms). The recorded signal for currents into the RW shows that the phase of the whole setup is quite stable with a slow derivation of $\Delta\varphi < \pi$ over 30 min only. The average value of the applied currents evolved very slowly, however the amplitude of the recorded signal shows that continuous phase control was required to correct for small fluctuations. Some spontaneous large scale variations in the ridge currents corresponding approximately to a π-phase shift were occasionally observed, as clearly visible for the ridge current of A2 at t = 20 min (30 mA jump), but were not fully understood. However, overall the active phase control is capable of controlling the output power with more than sufficient stability [Albrodt 18b]. The power drops slightly at the end of the measurement (see 55 min < t < 60 min), which was related to the comparably low current into the RW of the amplifiers 2 and 3 (cf. Fig. III.6).
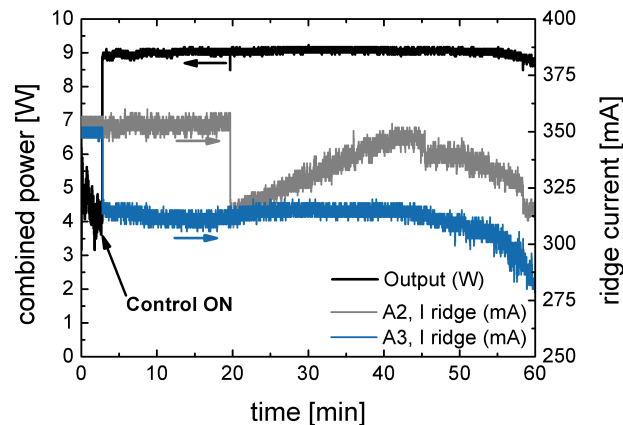
Figure III.6 – Power stability for coherent beam combining of three amplifiers at $I_{tp} = 7$ A. The power was measured with a calibrated Si-photodiode. This signal was also used as the error signal for the phase control. The actively currents into the RW are also plotted for A$_2$ (gray) and A$_3$ (blue).

The stability of the power at the output of the interferometer with and without any phase control was compared for better understanding. An exemplary measurement at moderate current into the amplifiers is given in Fig. III.7. The data shows that the interferometer is quite stable without any active control. The power fluctuations were only slightly higher ($\sigma_p < 1.6\%$) without any phase control for the first 5 min. After that, the phase-matching was however lost by some spontaneous fast variations (see pos. 1 and 2 in Fig. III.7). These variations were probably related to perturbations of the master oscillator discussed later in section 2.3.
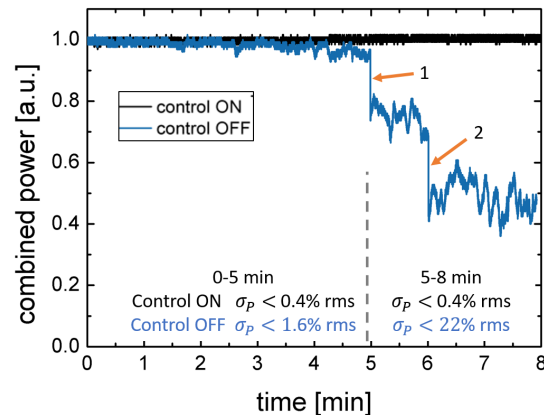
Figure III.7 – Power stability for coherent beam combining of three amplifiers at $I_{tp} = 5$ A with and without phase control.

Power and combining efficiency   Combined power and combining efficiency were evaluated for the use of only two amplifiers and all three amplifiers separately. The combining efficiency η_{CBC} is defined for the use of two amplifiers as $P_{A1+A2}/(P_{A1} + P_{A2})$, and for the use of all three amplifiers as $P_{A1+A2+A3}/(P_{A1} + P_{A2} + P_{A3})$ (cf. Fig. III.4). The results are summarized in Fig. III.8. The power of one individual amplifier is also given for completeness.
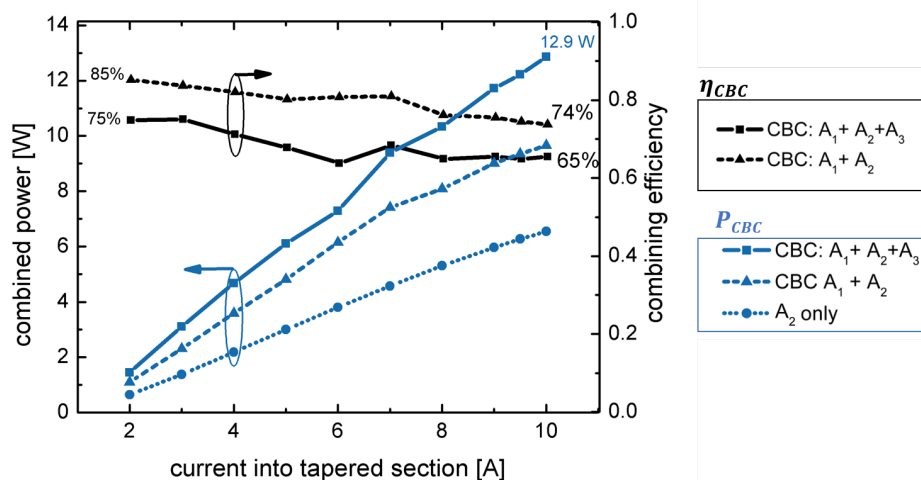
Figure III.8 – Measured coherently combined power (P_{CBC}) and combining efficiency η_{CBC} for different currents into the tapered section. The currents into the RW were actively controlled in the range of 250 to 400 mA, the heatsink temperature was T = 20°C. The astigmatism was corrected at each operating current. Reference design TPAs were used.

Coherent beam combining of all three amplifiers resulted in 12.9 W at the output of the interferometer. This compares favorably to previous studies in the framework of the PhD-thesis of Guillaume Schimmel where 12 W were achieved in a more complex setup using a mini-bar of five tapered amplifiers [Schimmel 17]. The main benefit from the single emitter approach (each amplifier has its own heatsink) in this work is that the amplifiers can be operated at higher bias when compared to similar emitters on a bar (where the amplifiers share a heatsink).

Operation at high bias comes however at the price of a degraded beam quality of the individual beams, as beam quality degradation processes in the devices become more severe. This is problematic as beams with a degraded beam quality are likely to have higher spatial mismatches in amplitude and phase profile and mismatched fields have a reduced overlap which leads to a reduced combining efficiency. The overall combining efficiency was found to be $> 65\%$ at the highest power. Furthermore, it was found that the combining efficiency was decreasing with increasing current into the tapered section, both for coherent superposition of two and three amplifiers. This observation underlines that the intrinsic beam quality of the beams influences the combining efficiency. The combining efficiency was slightly better for coherent superposition of only two amplifiers: 74% were measured at high bias and $> 85\%$ at low bias, which was consistent to previous experiments in the framework of the PhD-thesis of Guillaume Schimmel [Schimmel 16]. Factors limiting the combining efficiency in this configuration are investigated in details below.

Beam clean-up   The not-ideal combining efficiency is mostly related to a clean-up of the beam profile inherent to the combining process. This effect is visualized in Fig. III.9, where the beam profile at waist is shown for all different steps from the seed laser (diffraction limited beam quality), the individual amplifiers (significantly degraded beam quality) to the final beam (nearly diffraction limited beam quality). This detailed analysis was done at a moderate drive current (7 A). The beam profiles given for the individual amplifiers make clear that mismatches in the intensity profiles are quite significant. Especially the intensity distribution in the side lobes varies from amplifier to amplifier. In some cases, side lobes were also observed in FA (e.g. for A_2). The beam quality of the beams from the individual amplifiers was moderate, the typical M^2 factor in FA and SA and the central lobe power content η_{cl} are given in Fig. III.9. The beam profiles for the coherently combined beams show a step-wise improved beam quality. The central lobe power content of the final beam was $> 83\%$ and the M^2 factor was below 1.1 in FA and below 3.5 in SA. The reason for the improved beam quality is that the central lobes interfere efficiently with each other while the mismatched power content in the side lobes exhibits high combining losses and gets consequently filtered.

The beam quality of the beam at the output of the interferometer was also very good at the highest power (12.9 W at 10 A) as evidenced in the measurement of the beam shape at waist given in Fig. III.10 (a). Central lobe power content and the M^2 factor were comparable to the previously discussed results at lower currents. The more detailed investigations of the beam-clean up effect were done at a moderate drive current (7 A) as the stability of the setup was problematic at the highest power, which is investigated in section 2.3.

The beam profiles of the rejected beams were also measured and the rejected beam at the first combining step is shown in Fig. III.10 (b). The rejected beam has almost no central lobe power content and is clearly dominated by numerous side-lobes. One can identify certain intensity patterns in the side lobes that come indeed from far angle side lobes of the individual beams (see marked regions). This measurement shows that the power losses (the rejected beam) at the combining steps are dominated by power content in higher order modes, which is useless for many applications anyway. Only a small part of the *useful* central lobe power is found in the rejected beam. The results shown above in Fig. III.9 show however that the beam quality is still improving significantly during the second combining step, as the power content in the higher order modes does not get filtered completely in one combining step. Assuming totally mismatched power content in the side lobes, one can roughly estimate that the side lobe intensity gets weakened by 50% at each combining step.
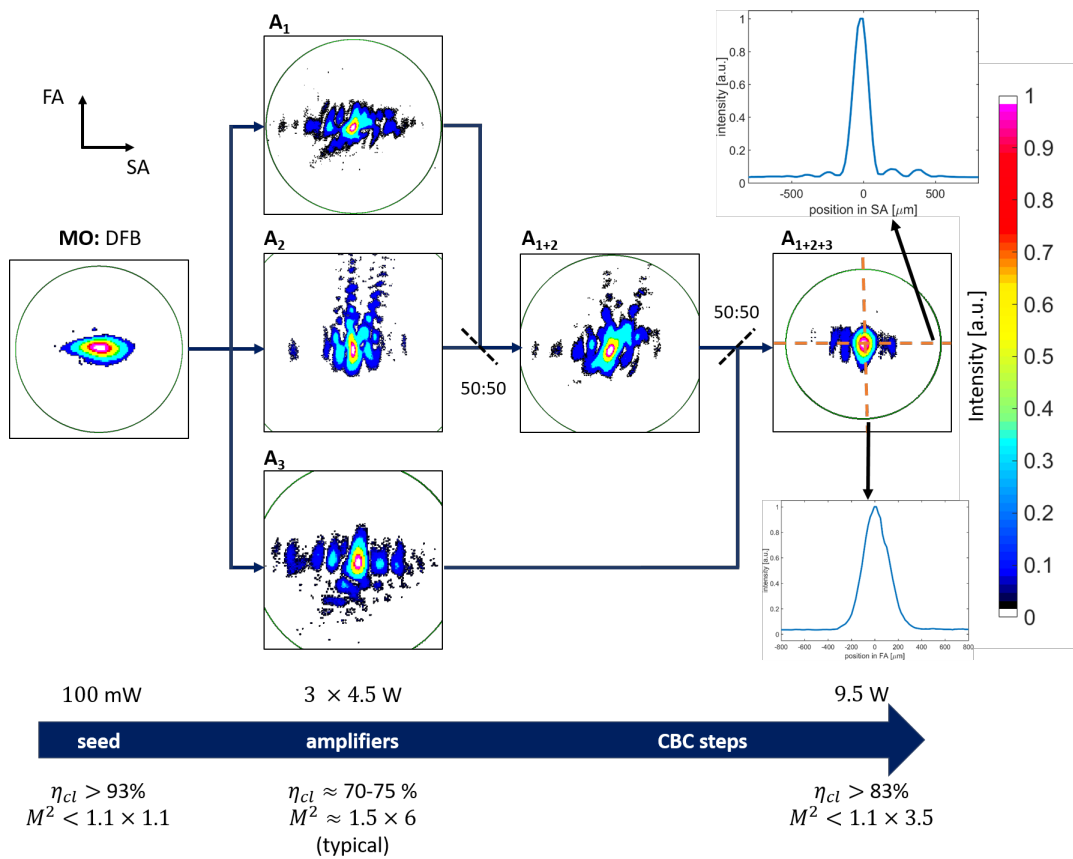
Figure III.9 – Simplified schematic of the beam clean-up effect. The waist beam profile (astigmatism corrected) is given for each step. Below, the power level, power content in the central lobe η_{cl} and the M^2 factor is specified for the seed laser, the individual amplifiers and the final beam.
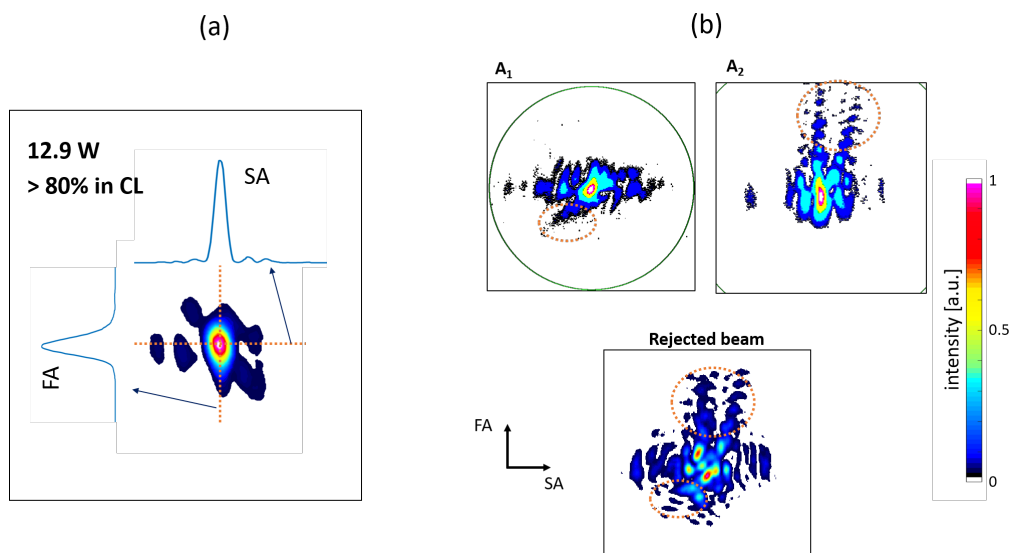
Figure III.10 – (a) Beam profile at waist (astigmatism corrected) of the combined beam at the highest power 12.9 W at $I_{tp} = 10$ A. (b) Beam profile at waist (astigmatism corrected) of A_1 and A_2 and the rejected beam (losses at C_1 in Fig. III.4. Each image was normalized and plotted on a false color scale separately. The camera settings were also different (longer exposure time) for the measurement of the rejected beam for better visibility. The dimensions are however identical. Measurement for $I_{tp} = 7$ A.

2.3   Challenges and problems

Limitations to the combining efficiency   Coherent superposition in filled aperture configurations usually enables high combining efficiencies. In the literature, excellent combining efficiencies > 87% has been reported for the coherent superposition of 47 single-mode slab-coupled optical waveguide amplifiers [Creedon 12] using a diffractive optical element. Combining efficiencies above 98% were reported for coherent superposition of fiber amplifiers using a similar two-by-two combining approach with beamsplitters [Müller 18]. The combining efficiency was significantly lower than that in the experiments discussed in this section. The physical reason for the reduced combining efficiency were investigated using wavefront and intensity measurements of the different beams. The data from the wavefront sensor allows to calculate the overlap factor of the different fields which determines the maximal achievable combining efficiency (cf. chapter I section 2.4).
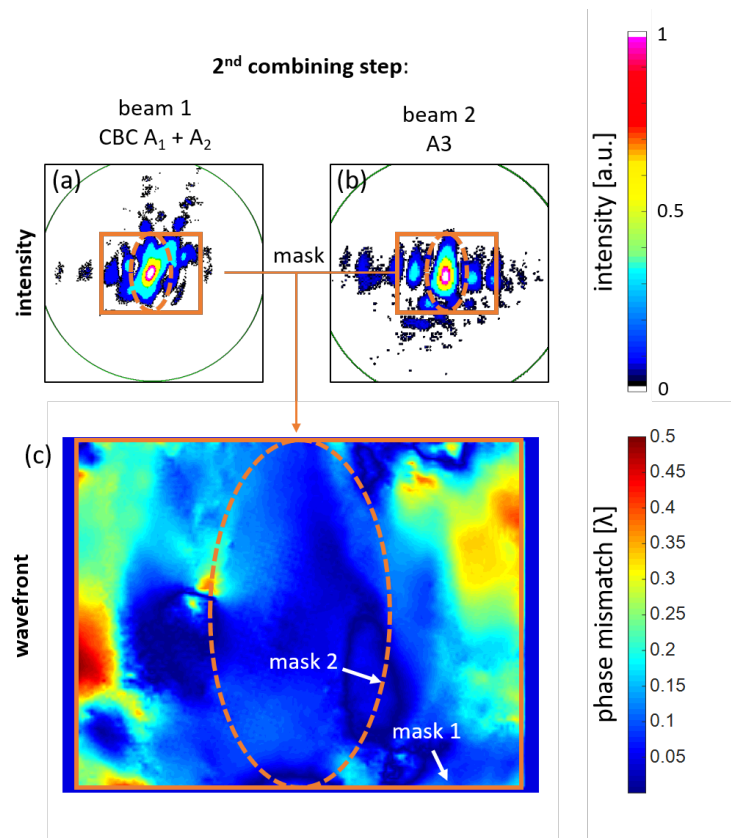
Figure III.11 – Investigation of limitations to the combining efficiency. Measurement of intensity mismatches (a) and (b) and mismatches in the wavefront (c) for the second combining step (cf. C_2 in Fig. III.4). The measurement plane was at waist (astigmatism corrected) of the beams. Two masks were chosen for the calculation of the measured overlap factor. Mask 1 is significantly larger than the central lobe, mask 2 corresponds roughly to the central lobe. Measurement for $I_{tp} = 7$ A. The given wavefront measurement represents an average wavefront mismatch as 10 measurements (10 ms integration time) were averaged.

An investigation of the second combining step (superposition on C_2 in Fig. III.4) is shown in Fig. III.11, where the intensity profiles and the relative wavefront differences $\varphi_1(x, y) - \varphi_2(x, y)$ are shown. Two different masks were chosen, the rectangular mask 1 contained the central lobe and a few side-lobes and mask 2 corresponded approximately to the central lobe. The 2D intensity and wavefront profiles were measured with a commercially available wavefront sensor based on quadri-wave lateral shearing interferometry (Phasics SID4). The measurements of the relative wavefront mismatches showed that the wavefronts were almost identical within mask 2. The wavefront mismatches were however quite significant for the side lobes (cf. Fig. III.11). The data from the wavefront sensor was

then used to calculate the *theoretical* combining efficiency of the two fields following Eq. I.5. The evaluated combining efficiency was 87% for mask 1 (rectangular aperture with $\approx$ 95% power content) and 93% for the central lobe (mask 2). The experimentally measured combining efficiency of the second combining step, taking into account the full beam including the components outside mask 1, was 81%. This indicates that the mismatches within the central lobe power content in the different beams is well overlapped and interferes efficiently. Furthermore, it was experimentally observed by several consecutive measurements that the wavefronts in the side lobes were de-correlated from the flat wavefront in the central lobe, as there were significant differences in the wavefront mismatch from measurement to measurement. The data shown in Fig. III.11 represents only an averaged wavefront mismatch evaluated by where several consecutive measurements of the wavefront sensor. Slight differences in the FA collimation slightly reduced the combining efficiency of the central lobe, which was nevertheless far above the average value considering the full beam.

The main limitation to the combining efficiency in this setup was therefore the initial intrinsic beam quality of the single tapered amplifiers. One can expect that amplifiers with an improved beam quality and a higher power content in the central lobe enable coherent beam combining with improved efficiency.

Stability problems at high bias   The stability of the setup was excellent for moderate bias conditions (such as $I_{tp} = 7$ A as shown earlier in Fig. III.6). At high bias however ($I_{tp} > 9$ A), there were however quite significant stability problems that appeared at some moment during the experiments and got worse and worse during the full experimental characterization of the setup. An exemplary measurement of the instabilities is shown in Fig. III.12. There were multiple spontaneous perturbations of the combined power. It was possible to correct them in most cases rapidly with the active phase control but the overall stability of the power was significantly degraded. These problems occurred only if the third amplifier A_3 was used and it seemed that the relative piston phase between the third arm of the interferometer and the other arms was unstable. The stability of the coherent superposition of the other two amplifiers was excellent even at high bias.
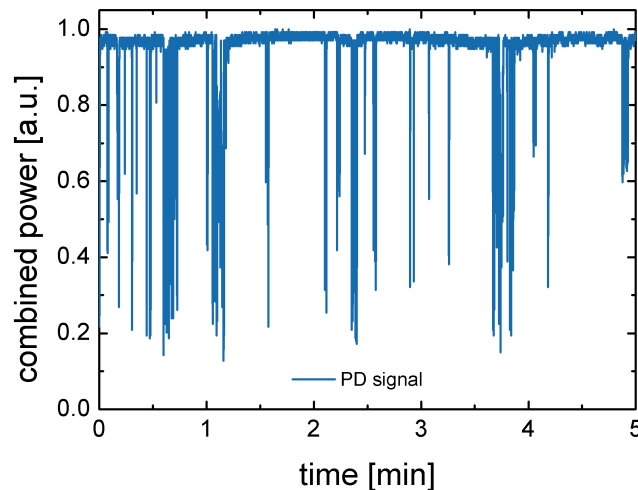
Figure III.12 – Power at the output of the interferometer for coherent beam combining of all three tapered amplifiers at $I_{tp} = 9$ A.

The interference signal of the first arm of the interferometer (with A_1) and the third arm of the interferometer (with A_3) was investigated in order to understand the stability problems evidenced in Fig. III.12. A linear modulation of the current into the RW of A_3 was applied as previously discussed in section 1.1. The interference signal of A_1 and A_3 was as expected quasi-sinusoidal at moderate currents (below 7 A) into the tapered section, as shown on the left in Fig. III.13. In contrast to that,

there were multiple discontinuous jumps of the signal for $I_{tp} > 9$ A. The amplitude of the phase-jumps roughly correspond to $\pi/2$ for the measurement shown in Fig. III.13 (b) and indicate that the current-phase relationship of the third arm of the interferometer was not normal, which explains the instabilities shown in Fig. III.12. It was experimentally verified that this was not a device-specific effect, as similar observations were made with several other devices in the same way. The conclusion was that the observed phase jumps were due to the interferometer itself.
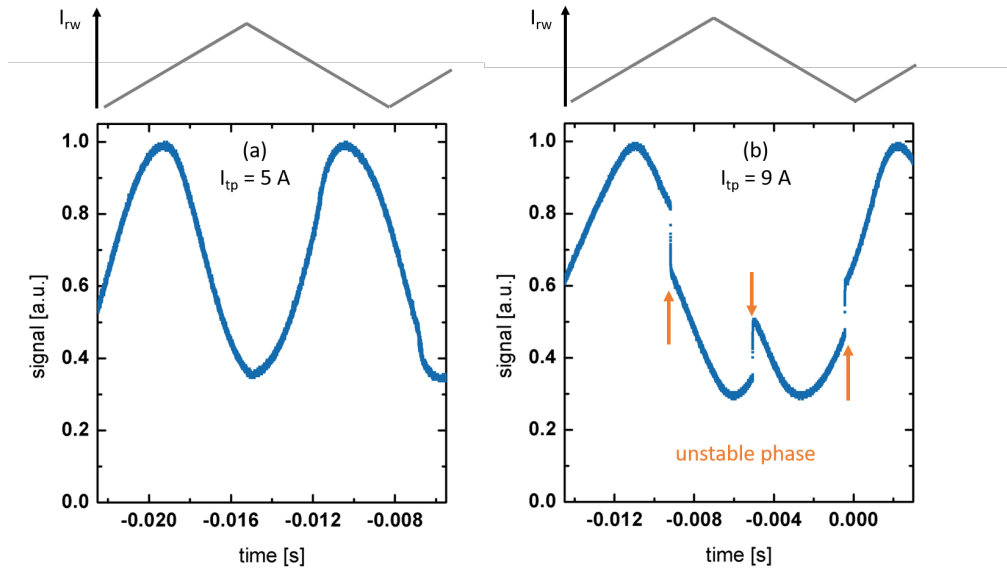
Figure III.13 – Interference beat signal of A$_1$ with A$_3$ at (a) $I_{tp} = 5$ A and (b) $I_{tp} = 9$ A.

It was found that the instabilities discussed above were in fact related to slight perturbations of the master oscillator laser and a difference in the optical path of the third arm in the interferometer (cf. Fig. III.4). Theoretical aspects of the effect of external optical feedback on a DFB laser is briefly summarized below and then put in relation with the experimental observations in this experiment.

Effect of external optical feedback on a DFB laser   It is well known that optical feedback for an external reflector may perturb the lasing process in a DFB laser and may cause a wide variety of different effects that depend of the level of feedback ($P_{feedback}/P_{DFB}$) and the distance L to the reflector [Coldren 95, Lang 80]. Optical feedback comes in principle from any optical interface (e.g. lenses or polarizing beam splitter cubes) in the experimental setups, the highest level of feedback is however generated by the tapered amplifier as illustrated in Fig. III.14. The amplified signal in the amplifier gets partially reflected at the AR coating of the front facet and amplified when propagating backwards. This leads to a significant amount of light that is in fact mostly coherent to the seed source and that is propagating backwards towards the MO, as already analyzed in chapter II in the context of section 3.2.3 and Fig. II.29. The DFB laser is protected against this feedback by the optical isolator, but a small amount of the light is nevertheless transmitted through the isolator and coupled back into the DFB laser. Additionally, there are in fact multiple sources of such optical feedback as there is more than one tapered amplifier in the experimental setups investigated in this work. The exact phase of the feedback depends on the length of the optical pathway and is also influenced by the phase-noise of the interferometer (cf. chapter II section 3.2.4). In other words, there are quite a few different factors that influence the optical feedback in the coherent beam combining setups investigated here. It is nevertheless sufficient to regard this problem in a simplified equivalent configuration, where the optical feedback is caused by a passive external reflector with unknown reflectivity R_e at a large distance L (cf. Fig. III.14).

The influence of an external reflector on the spectrum of a DFB laser has been extensively studied in different context. Tkach classified the effects of optical feedback in different regimes by numerical
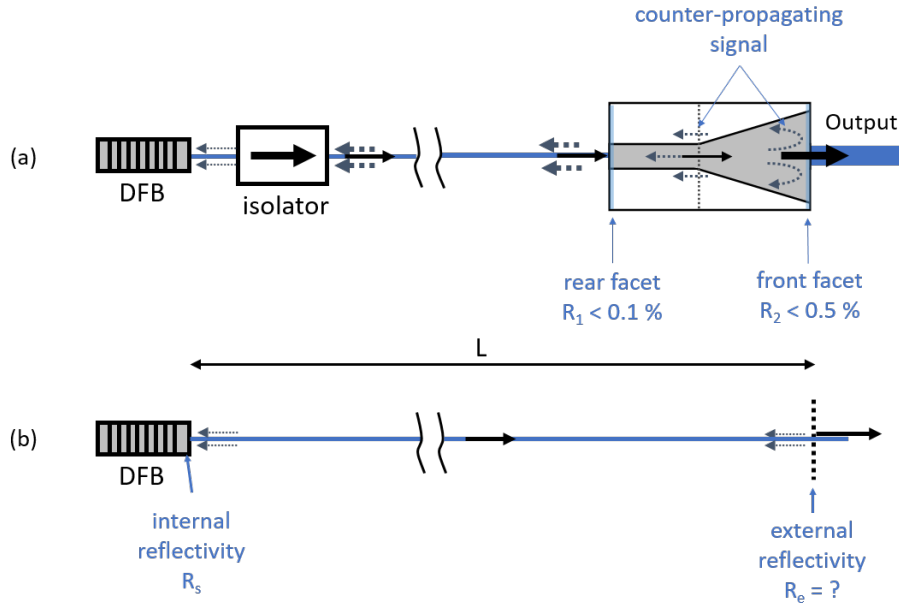
Figure III.14 – (a) Simplified schematic the optical feedback coming from a tapered amplifier. (b) Equivalent representation for a system where the optical feedback comes from a passive external reflector with reflectivity R_e at the distance L.

analysis of a few simple equations briefly outlined below [Tkach 86].

The analysis of the feedback effects proceeds from a modified Van der Pol equation for the electric field of the laser with an additional source term representing the external optical feedback:

$$\frac{dE}{dt} = \left(-i2\pi\nu_0 + \frac{\Delta G}{2}(1 - i\alpha) \right) E(t) + \kappa E(t - \tau_e), \tag{III.5}$$

where ν_0 is the free running laser frequency, ΔG is the gain change due to optical feedback, α is the so-called line-width enhancement factor, τ_e is the external round trip delay time and κ is a coupling coefficient which specifies the level of the optical feedback. The coupling coefficient can be written as

$$\kappa = \frac{1}{\tau_s} \frac{1 - R_s}{\sqrt{R_s}} \sqrt{R_e}, \tag{III.6}$$

with the internal round trip time τ_s in the DFB laser, R_s the effective facet power reflectivity of the DFB laser and R_e the external power reflection coefficient. From that, one can derive simple equations for the change in steady-state gain, the oscillation frequency and the laser line-width. The change in the oscillation frequency, which is the most relevant effect for the context of this work, can be written as

$$\Delta\nu \equiv \nu - \nu_0 = -\frac{\kappa}{2\pi} \left(\sin(2\pi\nu\tau_e) + \alpha \cos(2\pi\nu\tau_e) \right). \tag{III.7}$$

Different effects of the feedback can be identified by numerical analysis of the equations listed above for different coupling coefficients κ and different relative phases of the optical feedback represented by the term $2\pi\nu_0\tau_e$. At the lowest levels of feedback, the laser frequency is only changing slightly (cf. Eq. III.7) and the laser line-width is slightly broadened or narrowed depending on the phase [Tkach 86]. For slightly higher levels of feedback, one can find multiple solutions of Eq. III.7[1], and mode-hopping of the DFB laser may occur. This is in particular relevant for feedback coming from a reflector at a large distance in the order of 1 m or higher, as it is also the case in the experiments discussed in this manuscript.

---

[1]Multiple solutions exist if $\sqrt{1 + \alpha^2}\kappa\tau_e > 1$

The presence of mode-hopping of the DFB laser line was evidenced by measurements with a confocal Fabry-Perot interferometer, which was placed in the third arm of the interferometer (instead of A_3) shown earlier in Fig. III.4. The spectrum of the DFB laser was analyzed when all amplifiers were turned off (no relevant optical feedback) and if A_2 was operated at $I_{tp} = 7$ A. The free spectral range (FSR) of the used interferometer was 10 GHz and the finesse was experimentally determined to be in the order of 70 as shown in the scanning trace signal given in Fig. III.15 (a). The scanning interferometer was then biased at a constant voltage and the frequency of the DFB laser was fine-tuned by changing the temperature to achieve 50% transmission through the interferometer. The transmission signal was recorded for 10 s. This signal was then converted to the equivalent DFB frequency drift $\Delta\nu(t) = \nu(0) - \nu(t)$ by numerical analyze of the scanning trace. The calculated frequency signal is shown in Fig. III.15 (b) for a measurement where the amplifiers were turned off (black) and for a measurement with one amplifier turned on (blue). Even though the double stage Faraday isolator with about 55 dB optical isolation protected the DFB laser against optical feedback from the amplifier, multiple jumps in the laser frequency with an amplitude of about 80 MHz were observed if the amplifier was turned on. The amplitude of the frequency jumps increased with increasing feedback levels (cf. Eq. III.7) and one can extrapolate that the operation of three tapered amplifiers in the experimental setup given in Fig. III.4 may cause spontaneous instabilities (jumps) of the laser frequency higher than 100 MHz.

These jumps were caused a piston phase difference in between the arms of the interferometer as the optical path lengths of the third arm of the interferometer was roughly $\Delta L = 30$ cm longer for practical reasons. The relative phase change $\Delta\varphi = 2\pi\Delta L/c \times \Delta\nu$ in between the third arm and the other arms of the interferometer was in the order of $0.2\,\pi$ for a 100 MHz frequency jump. This explains the abnormal current-phase relationship evidenced in the measurement shown in Fig. III.13 and the instabilities of the coherently combined power at high bias (cf. Fig. III.12).

The conclusion of these investigations is that even higher optical isolation should be used in further experiments and that differences in the optical path lengths in the arms of the interferometer should be minimized in order to avoid stability problems at high bias.
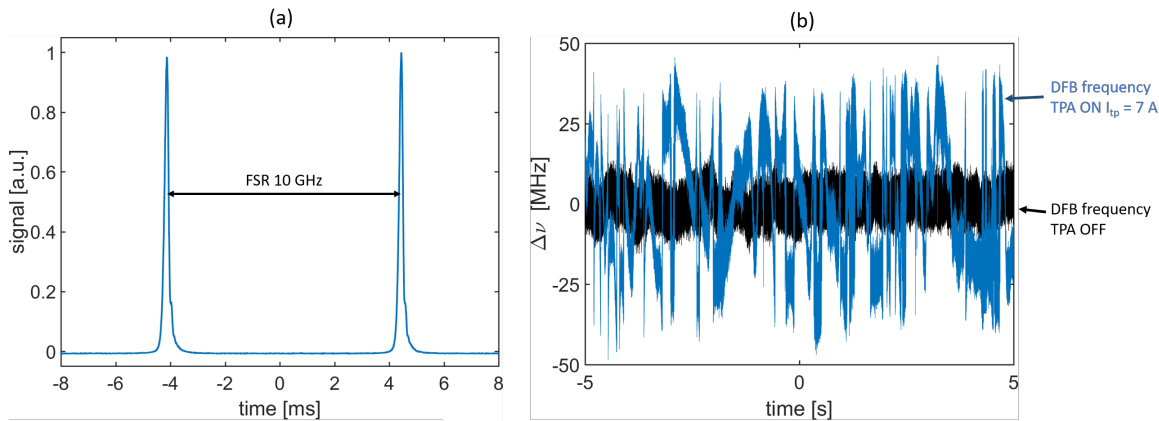
Figure III.15 – (a) Measured signal of the DFB laser spectrum with a scanning Fabry-Perot interferometer (Thorlabs SA210-8B). (b) Measured frequency drift of the DFB laser if the TPA was turned off (black) or operated at $I_{tp} = 7$ A (blue).

2.4   Second harmonic generation

One aspect of the work presented in this manuscript was the development of simple systems that are actually useful for applications and go beyond proof-of-principle laboratory scale coherent beam combining demonstrations. Nonlinear frequency conversion enabling high power laser emission based on semiconductor emitters only was chosen as a first simple experiment to demonstrate the usefulness of the systems developed in this work. The results summarized below were obtained in collaboration with the "Diode Lasers and LED Systems Group" at DTU Fotonik (Roskilde, Denmark) and were published recently in a joined-article in Optics Express [Albrodt 19a].

2.4.1   Experimental setup

The output of the CBC-interferometer was used for single pass SHG as shown in Fig. III.16. During the SHG experiments all three amplifiers were operated at constant current into the tapered section[1] and the power used for SHG was adjusted by turning the polarization before the first polarizing beam splitter (PBS). The optical isolation between the CBC interferometer and the SHG experiment was > 25 dB. After reshaping optics (two cylindrical lenses with f = 50 mm and f = 100 mm) for beam size adjustment and astigmatism correction, another half-wave plate was used to align the polarization of the NIR beam with the crystallographic z-axis of the nonlinear crystal. The beam was then focused with a lens (f = 150 mm) into the 40 mm long periodically poled bulk $MgO:LiNbO_3$ (PPLN). PPLN is the most widely available quasi-phase-matching crystal and has a large effective non-linearity ($d_{eff} \approx 16$ pm/V). Quasi-phase-matching in a simple single pass configurations enables therefore high conversion efficiencies. The $1/e^2$ waist diameter of the focused beam inside the crystal was measured to be 95 μm, which was experimentally verified to be the optimum focusing condition at the highest input power. The focusing conditions are in fact critical regarding the achievable combining efficiency [Boyd 68]. Furthermore, the beam quality of the used pump beam also influences the conversion efficiency, as evidenced in the experiments described below.

The PPLN crystal was mounted into a temperature-controlled closed-top oven. The temperature was measured with a temperature sensor in the oven and corresponds to an average temperature of the PPLN. The spectral components were separated by a dichroic mirror (DM).
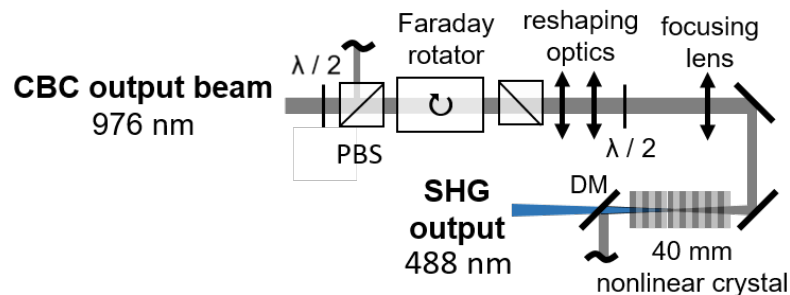
Figure III.16 – Simplified schematic of the single pass SHG setup. The beam at the output of the CBC interferometer was used as the NIR pump beam. DM: dichroic mirror.

2.4.2   Experimental results

The SHG power was measured for three source configurations: a single amplifier (A_2), coherent beam combining of two (A_{1+2}) and three amplifiers (A_{1+2+3}). Note that the experimental characterization for coherent superposition of all three amplifiers was challenging as the stability problems discussed above appeared during the experiments. The optical path differences in the interferometer were slightly

---

[1] $I_{tp} = 9$ A for A_1 and A_2 and $I_{tp} = 8$ A for A_3

reduced and A_3 was operated at a slightly lower current which was sufficient to achieve acceptable stability.

Conversion efficiency using different levels of brightness The SHG output power ($P_{2\omega}$) was measured at different pump power P_ω levels. The equation

$$P_{2\omega} = P_\omega \tanh^2(\sqrt{\eta_{nl} P_\omega}),$$ (III.8)

where η_{nl} is the nonlinear conversion efficiency, describes the evolution of the SH power taking pump-depletion effects into account, was fitted to the experimental results (see. Fig. III.17). The temperature of the PPLN crystal was optimized at each pump power level to achieve the highest output power level.

The results clearly show that the beam with the highest central lobe power content (CBC A_{1+2+3}) enabled the highest nonlinear efficiency. In this case coherent beam combining enabled a fourfold increase in SHG output power and a nonlinear efficiency increased by a factor of 1.7 when compared to SHG with a single amplifier. The deviation to the theoretical fit for pump powers $P_\omega > 6$ W was attributed to thermal dephasing caused by blue-light absorption, which is discussed in details below. The SHG output power therefore plateaued at 2.1 W and the maximal conversion efficiency $\hat{\eta}$ was 24%. Without thermal dephasing, one can expect to achieve SHG output powers > 3 W and a conversion efficiency above 30%, which would be excellent results for SHG in a simple single pass configuration [Jensen 14]. This is a promising approach the development of multi-watt visible laser sources based on semiconductor emitters only.
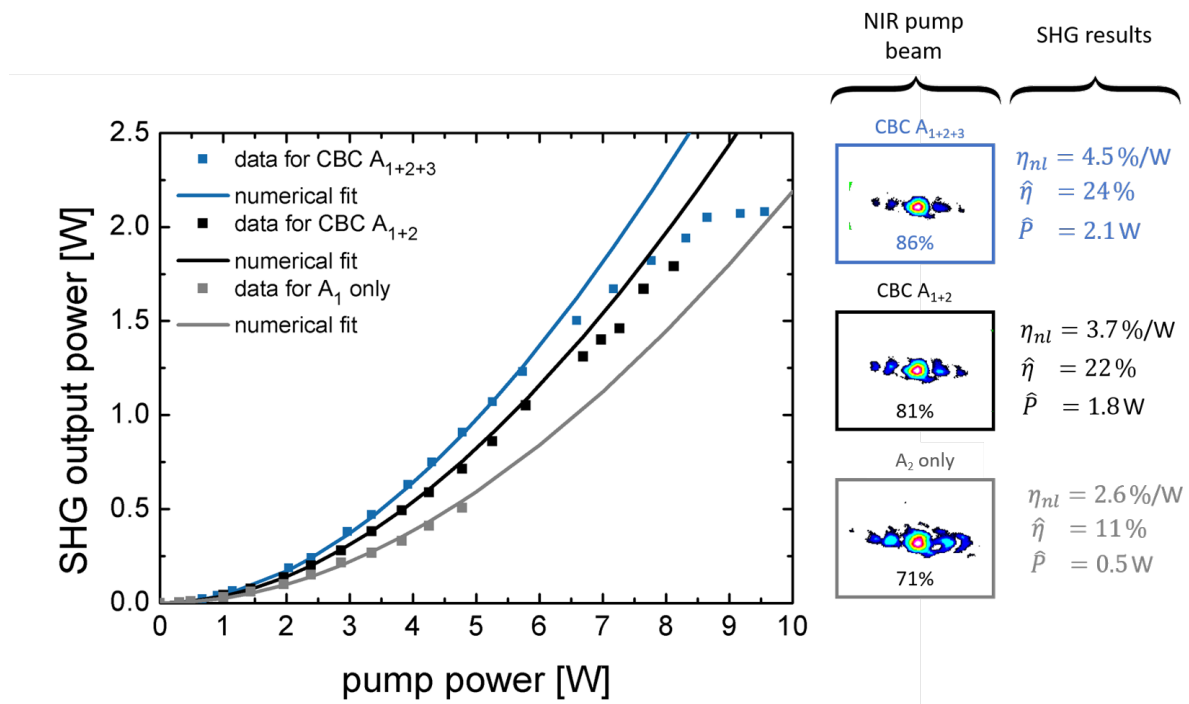
Figure III.17 – Measured SHG output power using three different NIR pump beams with different levels of brightness. The beam profile at waist of the corresponding NIR pump beam is given on the right for the three different cases. The central lobe power content is given in percent. The evaluated nonlinear efficiency η_{nl}, maximal conversion efficiency $\hat{\eta} = P_{2\omega}/P_\omega$ and the maximal SHG power $\hat{P}$ are specified for each data series.

Investigation of thermal effects in the nonlinear crystal It is well known that thermal dephasing in periodically poled nonlinear crystals leads to a reduced conversion efficiency at high power and can cause power instabilities [Sabouri 13]. A MgO doped PPLN crystal was used in this case for practical

reasons. Unfortunately this material absorbs visible light especially in the blue spectral range. The absorbed light leads to a local temperature variation, which makes it difficult to maintain identical quasi-phase-matching conditions over the whole interaction length. This effect is in particular critical for high average powers. Operation in QCW mode is a work-around to prevent the crystal from heating locally, which reduces the negative effect of thermal dephasing.

A mechanical chopper was placed in the pump beam to reduce the average power in the crystal and to limit the effects related to thermal dephasing. The duty cycle of the chopping was 50%. The chopper was operated at the lowest possible frequency (≈ 0.7 Hz). The intensity of the SH power was measured with a photodiode at the output of the setup. The recorded signals are shown in Fig. III.18 for 1 W (a) and 7 W (b) pump power. The signal was nearly rectangular for low pump powers, which indicated that the crystal temperature is constant during the pulses (see Fig. III.18 (a)). This is however not the case for high pump power levels, where a clear decrease in power was measured during the pulses (see Fig. III.18 (b)). This was attributed to a locally increasing temperature induced by blue-light absorption. The crystal temperature was set to achieve maximal peak power at the start of the pulses in Fig. III.18 (b). This power corresponds approximately to the power theoretically achievable under the absence of any thermally related dephasing effects.
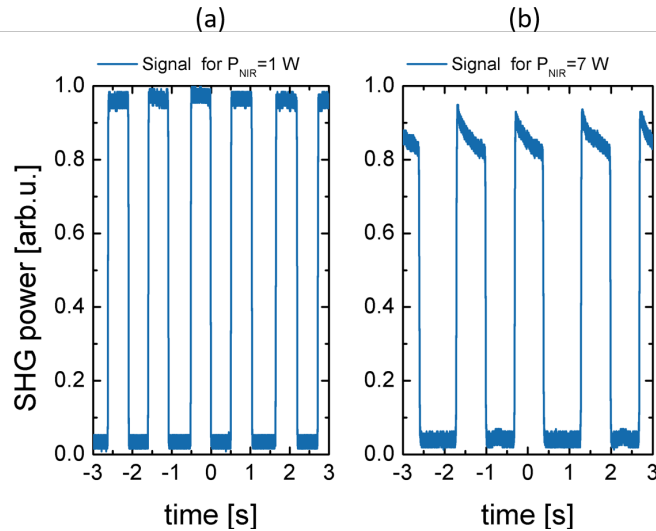
Figure III.18 – Photodiode measurements of the SHG output power with chopped pump beam for two different power levels: (a) 1 W pump power, (b) 7 W pump power.

The SHG peak power for a chopped pump beam was measured and compared to the fit function given in Eq. III.8 as shown in Fig. III.19 (a). The measured peak power data points (see data points in blue) are in excellent agreement with the fit function (dashed black line). This confirms that the observed differences of experimental data for $P_w > 6$ W and the theoretically expected evolution (Eq. III.8) are indeed caused by thermal dephasing.

The crystal temperature acceptance bandwidth was measured for different pump powers for further investigation of the thermal effects. Theoretically, one expects a sinc^2 shape dependence of the SHG output power for a varying crystal temperature and one specifies the FWHM of the main lobe as the temperature acceptance bandwidth. The measured SHG output power for different temperatures of the crystal are shown in Fig. III.19 (b) for 1 W pump power (black) and 7 W pump power (blue). The secondary maxima of the sinc^2 function are in both cases not visible, which is attributed to a non uniform temperature in the nonlinear crystal, but one clearly observes the main lobe. The FWHM bandwidth was about 0.7°C for 1 W pump power and 0.6°C at 7 W pump power. Furthermore a shift of 0.4°C was observed as the pump power was increased. The shift and the slightly reduced temperature acceptance bandwidth indicate the overheating of the crystal at high powers. Additionally, one can see that the slope of the temperature tuning curve for $P_w = 7$ W pump power is more important on the low

temperature side when compared to the high temperature side, which leads to a slightly asymmetric main lobe, which is another typical indication for thermal dephasing [Liao 04, Kumar 09].
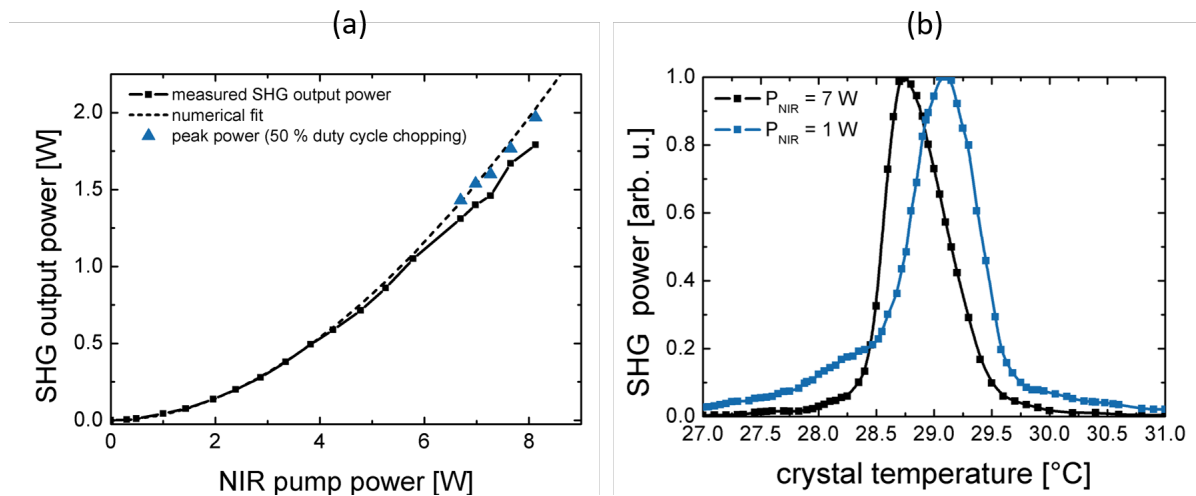
Figure III.19 – (a) SHG output power in CW and SHG peak power in QCW operation (by mechanical chopping with 50% duty cycle). The used pump beam was generated by CBC of A_{1+2}. (b) Normalized SHG power vs crystal temperature at 1 W pump power (blue) and 7 W pump power (black).

The achieved results are however encouraging as the achievable maximal conversion efficiency was limited by thermal effects and not by the beam quality of the pump source. Technical solutions to circumvent thermal dephasing include the use of a cascade of nonlinear crystals with different materials, which allows to adapt the focusing conditions and the nonlinear material in the second crystal to avoid SH absorption [Kumar 11]. NIR pump sources based on coherently combined high power tapered lasers and SHG architectures adapted for high visible powers may enable > 5 W emission in the visible spectral range in future work.

Stability and beam quality   The power stability of the SHG setup was investigated using CBC of A_{1+2} as the pump beam. The power was measured over one hour with 1 Hz sample rate (see Fig. III.20 (a)). The average blue power at maximum NIR pump power was 1.72 W with a stability of 0.8% rms, which was comparable to the power stability of the NIR beam. Further improvement of the power stability seems achievable by eliminating the thermal effects in the nonlinear crystal and by further improvement of the CBC setup. The results demonstrate however that coherent beam combining of tapered lasers in a simple and robust MOPA configuration can indeed provide reliable high power output for high brightness applications.

The beam quality of the SH beam was nearly diffraction limited. The caustic measurement given in Fig. III.20 (b) shows that the M^2 beam propagation factors were in the order of 1.1 ± 0.1 in FA and 1.2 ± 0.1 in SA. The improved beam quality when compared to the pump beam is related to the so-called nonlinear beam-cleanup and a typical observation for SHG with tapered lasers and amplifiers [Jechow 10].
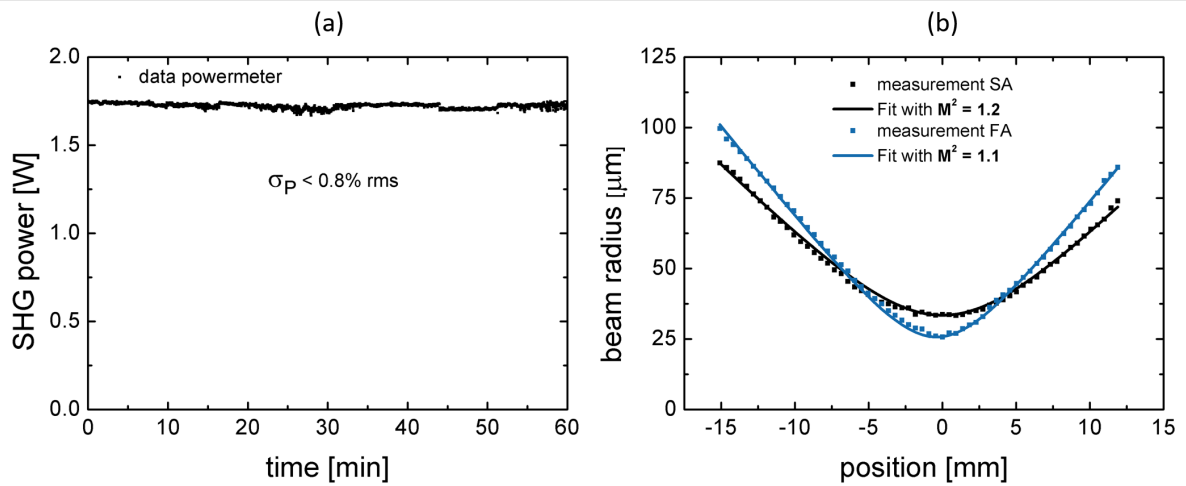
Figure III.20 – (a) Measured SH power. Sample rate 1 Hz, 60 min measurement time. Measured and fitted caustic (2nd moment) of the SH beam at 1.7 W output power. CBC of A_{1+2} was used as the NIR pump beam in both cases.

3   Coherent beam combining using the EloD2 epitaxial design

The coherent beam combining experiments using tapered amplifiers with the reference epitaxial design (cf. section 2) clearly indicated that the combining efficiency was limited by the intrinsic beam quality of the tapered amplifiers. The ELoD2 epitaxial design enables an improved beam quality, evidenced by a high central lobe power content (cf. chapter 2) and is therefore a promising amplifier design for efficient coherent superposition.

Coherent beam combining of three different lateral ELoD2 amplifier designs (so-called "baseline", "4 mm taper" and "50% stripes" - see chapter II section 3) was investigated and the results were compared to similar experiments with reference-design tapered amplifiers described earlier in section 2.

Experimental setup   The experimental setup of the interferometer (see Fig. III.21) was similar to the setup used in the experiments described in section 2 and only a few points were improved:

- **optical isolation** - a triple stage optical isolator for the DFB seed laser was used with a total optical isolation better than 73 dB[1]

- **optical path lengths** - the total optical path length in each arm of the interferometer was identical. Furthermore, the optical path from the first beam splitter to the input of the amplifier and the optical path from the output to the amplifier to the beamsplitters were identical for each arm of the amplifier. This way, beam mismatches on the beamsplitters related to different optical pathways are minimized.
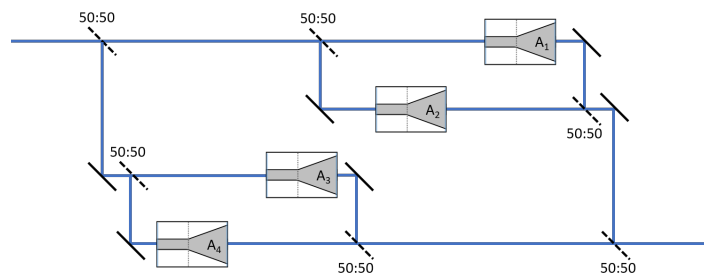
Figure III.21 – Simplified schematic of the experimental setup used for the comparative study of CBC with different amplifier designs.

3.1   Comparison of different lateral amplifier designs for coherent beam combining of two amplifiers

The experimental setup was used to compare the different lateral amplifier designs in a simple coherent beam combining setup. Two amplifiers per design were used, e.g. the baseline design was used for A_{1+2} and the 4 mm taper design was used for A_{3+4}. The combined power and the combining efficiency were measured for both subsystems (2 amplifiers each) and then compared to each other. The results are summarized in Fig. III.22 for the baseline design (black), the 4 mm taper design (orange) and the 50% stripes design. The baseline design enabled the highest power at comparably low drive currents ($I_{tp} < 8$ A), the power then however plateaued as this amplifier design was limited by an early thermal rollover (cf. chapter 2 section 3). The coherently combined power did not plateau for the other two designs (no thermal rollover of the amplifiers) and the highest power was reached with the 4 mm taper design (10.2 W). There was no evidence for any benefit of a stripe patterned electrical contact (50% stripes design) of the tapered section for the use in coherent beam combining experiments. The

---

[1]This corresponds to a transmitted power below 50 nW for a potential optical feedback in the order of 1 W.

combining efficiencies were similar and above 84% for all designs at 8 A. Combining efficiencies close to 100% were measured at low currents. The slight differences in the evaluated combining efficiency should not be over-interpreted. The typical systematic relative error of power measurements is $\pm 1\%$, which transfers to the combining efficiency defined as $\eta_{CBC} = P_{CBC}/(P_1 + P_2)$ as a relative error of $\pm 2\%$. An additional random error inherent to the coherent beam combining process (alignment precision during optimization) can be estimated in the order of $\pm 1\%$. Within this error range, one can consider the measured combining efficiencies of the three different lateral designs as identical (error bars have been omitted in Fig. III.22 for clarity). The preferred choice is however clearly the 4 mm taper design enabling the highest output power.

baseline

$\hat{P}_{CBC} = 7.0$ W
η_{CBC} (8 A) = 87%

4 mm taper

$\hat{P}_{CBC} = 10.2$ W
η_{CBC} (8 A) = 89%

50% stripes

$\hat{P}_{CBC} = 7.9$ W
η_{CBC} (8 A) = 84%
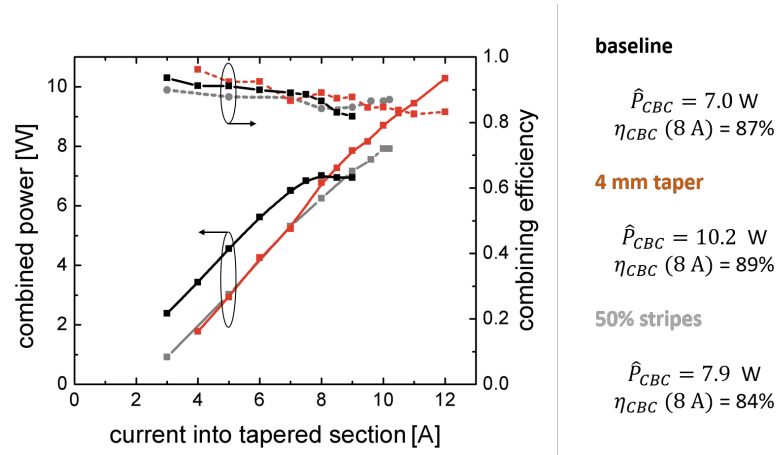
Figure III.22 – Measured coherently combined power P_{CBC} and corresponding combining efficiency η_{CBC} for CBC of two ELoD2 amplifiers with three different lateral designs: baseline (black), 4 mm taper (orange) and 50% stripes (gray).

The results of the ELoD2 4 mm taper design are compared to the results for the reference amplifier design (data taken from section 2) in Fig. III.23. The advantage of the ELoD2 design in terms of combining efficiency is clear. The disadvantage of the ELoD2 design remains however the high threshold, which is of course also visible in the coherently combined power. The maximum power for coherent beam combining of two amplifiers was similar, the ELoD2 design was however up to higher currents.

The overall system efficiency taking into account the power conversion efficiency of the amplifiers and the combining efficiency is however higher for the reference design. The PCE of the ELoD2 design is currently the main drawback of this approach and should be in the focus of future device development for coherent beam combining architectures. An additional option is an improved packaging to avoid the early thermal rollover of the ELoD2 baseline amplifier design, which was in terms of threshold the closest to the reference design but not suitable for high power operation.

The reason for the higher combining efficiency of the ELoD2 tapered amplifiers is undoubtedly the improved beam quality, in particular the high central lobe power content. The central lobe power content η_{cl} and the combining efficiency η_{CBC} are clearly correlated as shown in Fig. III.24. Identical combining efficiency was measured for beams with (almost) identical central lobe power content (cf. Fig. III.24 ELoD2 at 2 A and Reference at 10 A). The ELoD2 design however enables emission at high bias (I_{tp} = 10-12 A) with similar central lobe power content than the reference design at low bias. The combining efficiency was in all cases slightly higher than the central lobe power content, as some of the power content in the side lobes is nevertheless transferred to the combined beam. One should also keep in mind that the power content in the central lobe is also not transferred with close to 100% efficiency as a few imperfections in the experimental setup have been identified and discussed before (cf. section 2.3).

This stated, one has however to consider one slight relativization of the results given in Fig. III.24: the central lobe power content depends always at least slightly on the current into the RW section of the amplifiers, as analyzed in detail in chapter II. The current into the RW is however used for phase
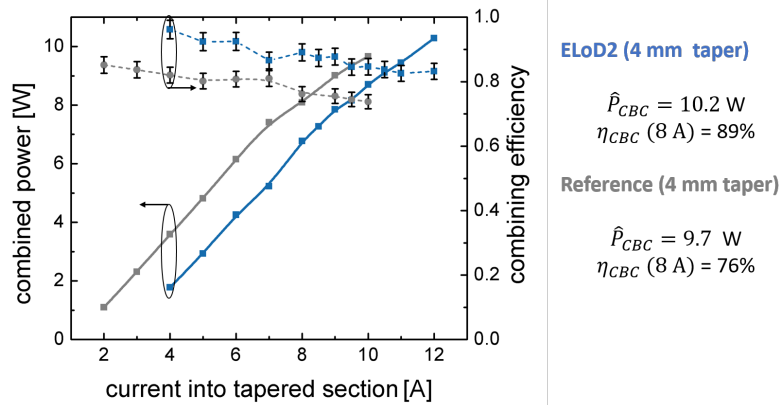
Figure III.23 – Measured coherently combined power P_{CBC} and corresponding combining efficiency η_{CBC} for CBC of two 4 mm taper ELoD2 amplifiers (blue) compared to results obtained with the reference epitaxial design (gray).

control and was not the same for all data points given in Fig. III.24, where the measured central lobe power content for $I_{rw} = 400$ mA was used for plotting the data. It is nevertheless clear that the central lobe power content and the combining efficiency are correlated.
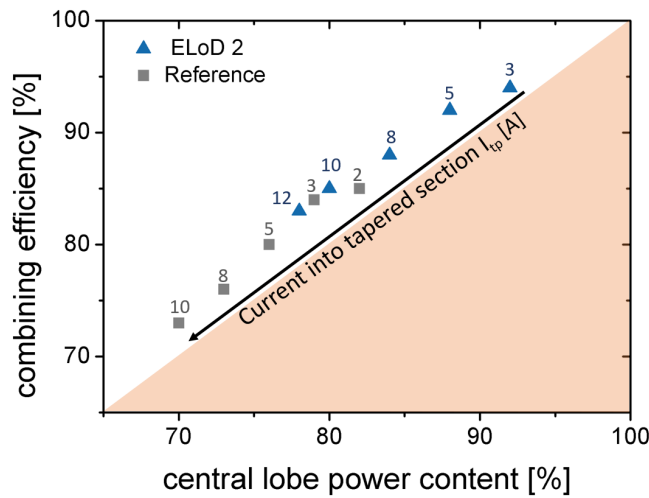
Figure III.24 – Measured combining efficiency η_{CBC} as a function of the power content in the central lobe η_{cl} for CBC of two TPAs with the ELoD2 4 mm taper design (blue) and the reference design (gray). The corresponding drive current into the tapered section is given in Ampere for each data point.

3.2 High power coherent beam combining of four ELoD2 amplifiers with optimized design

The ELoD2 4 mm taper design enabled, as discussed above, the highest power and the best beam quality and was therefore chosen for the demonstration of high power coherent beam combining of four identical amplifiers in the experimental setup given in Fig. III.21.

Power and combining efficiency The coherently combined power P_{CBC}, the combining efficiency η_{CBC} and the central lobe power content of the coherently combined beam η_{cl} were measured for a few bias points as summarized in Table III.1. The maximum power was 17.0 W of which 92%, corresponding to 15.6 W, were contained in the central lobe of the final beam. These values are the highest coherently combined power from tapered lasers or amplifiers in continuous wave regime and compare favorably to the coherent beam combining experiments described in section 2 (CBC of 3 TPAs resulted in 12.9 W with 83% in central lobe). The achieved central lobe power compares also favorably to the state of the art of high-brightness DBR-TPLs with optimized grating structures (e.g. [Müller 17]: 10 W central lobe power in CW - cf. chapter I section 1). The overall combining efficiency was 71% ($\pm 1\%$) and almost identical for the different bias points. The combining efficiency for the two subsystems consisting of A_{1+2} and A_{3+4} was $> 80\%$ (cf. Fig. III.23). The combining efficiency of the final combining step, where the beams from the two subsystems are combined, was in the order of 90%. These two values together lead to the overall combining efficiency in the order of 71%, which was significantly higher than for the experiments described in section 2. The combining efficiency considering the central lobe power contents in the individual beams and the final beam only was even higher than that and $> 81\%$ for the whole system. Mismatches in the FA collimation were identified as the most critical parameter regarding the combining efficiency of the central lobe. The stability of the setup was excellent with residual power fluctuations below 1% rms for drive currents $I_{tp} \leq 10$ A. At the highest powers, there were some instabilities which are investigated below.

Table III.1 – Experimental results for CBC of four ELoD2 (4 mm taper) amplifiers. P_i: power of one individual tapered amplifier, P_{CBC}: coherently combined power, η_{CBC}: combining efficiency, η_{CL}: power content in central lobe

I_{tp} [A]	P_i [W] (typical)	P_{CBC} [W]	η_{CBC} [%]	η_{CL} [%]
8	3.75	10.8	72	95
9	4.44	12.9	72	93
10	5.05	14.4	72	92
11	5.66	16.2*	72	92
12.3	5.96	17.0*	71	92

* The stability of the coherent superposition was limited.

Beam quality The beam quality of the final beam was investigated by a caustic measurement shown in Fig. III.25. The M^2 beam propagation factors obtained by numerical fitting were 1.2 ± 0.1 in FA and 4 ± 0.4 SA. The value in SA may appear surprisingly high given the fact that the central lobe power content was $> 92\%$, but the low intensity side lobes at waist (see beam profile 4) still increase the second moment beam diameter significantly. Furthermore one can see that some data points close to the waist are slightly off the fit to the caustic. It is indeed challenging to measure the beam shapes close to waist accurately as the intensity in the side lobes is very close to the noise level of the camera. The beam profiles at larger distance to waist also show that the almost Gaussian beam shape at waist is not maintained during propagation. The beam shapes also indicate that higher order spherical aberration is contributing to the increased M^2 value. The asymmetry in the beam shapes on both sides of the

caustic (eg. beam profile 1 compared to 7 or 2 compared to 6) is typical for laser beams with spherical aberration [Siegman 93, Albrodt 18a]. Preliminary numerical simulations of beam quality degradation processes in tapered lasers indicate that these aberrations are caused by perturbations of the refractive index in the tapered section [Larkins 19]. One should therefore be careful by using the central lobe power content as a synonym for the diffraction limited power.

The observed beam quality is nevertheless excellent when compared to the typical beam quality of high power tapered lasers or amplifiers. An estimation of the beam propagation factor using the $1/e^2$ beam radius leads to 1.0 is SA and 1.2 in FA, but is as discussed in chapter 2 of limited physical significance.
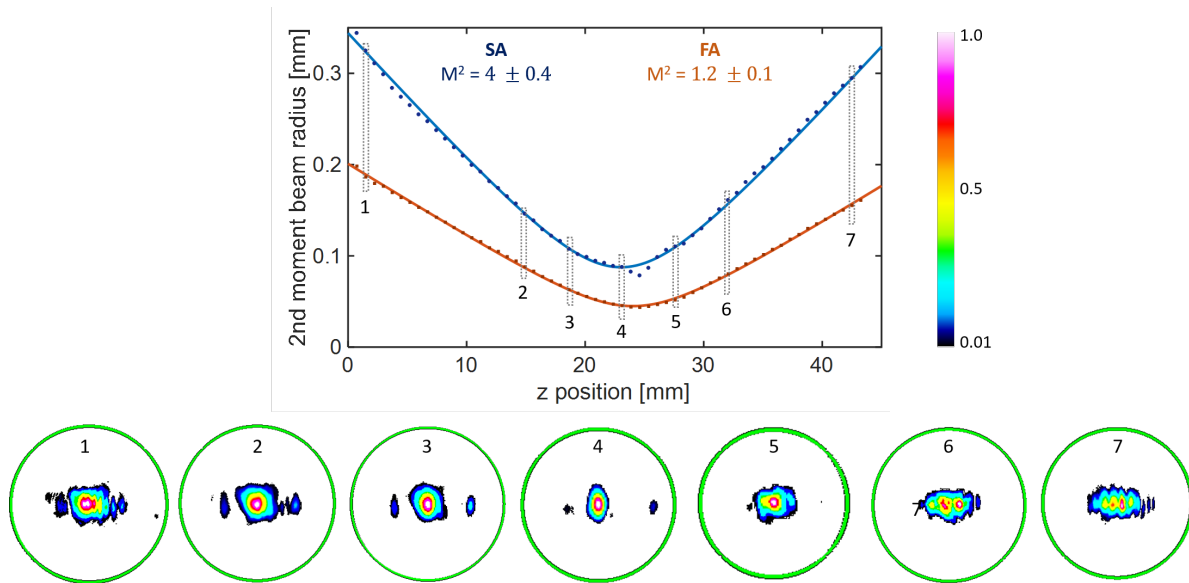
Figure III.25 – Measured beam caustic of the coherently combined beam (SA in blue, FA in orange). Seven false color plots of the beam at different positions along the caustic are given (see pos. 1-7). The beam profiles are not to scale and are given with approximately the same beam size in FA for better visibility. The optical power was 17 W, the current into the tapered section of the amplifiers was 12.3 A.

Stability The problems with the stability of the coherently combined power discussed earlier in the context of the experiments described in section 2 were related to a perturbation of the master oscillator. In this setup, no perturbation of the MO seed laser line was measurable even at high powers. Nevertheless, the stability of the setup was not optimal at the highest powers as shown in Fig. III.26 (a). The power fluctuations in the stabilized level were in the order of 1.3% rms over 10 min, which was slightly worse than for the experiments described earlier in section 2. Furthermore long-term operation without any significant perturbations for more than 10 min was not possible (cf. instabilities in Fig. III.26 (a)).

The reason for the residual power fluctuations in the stabilized level were identified in the strong dependence of the central lobe power content, which determines η_{CBC} and influences therefore P_{CBC}, and the current into the RW section, which is used for phase control. This effect was already previously discussed in the context of section 3 in chapter II. The central lobe power content of the beam from A_3 was investigated under the same operating conditions as for the measurement given in Fig. III.26 (a). Figure III.26 (b) shows clearly that the central lobe power content is varying in the order of 20% for a change in current into the RW needed for a phase-shift of 2π whereas the total optical power is almost constant. This explains the residual fluctuations of the power in the stabilized level, where the control of the RW current leads to slight changes in the combining efficiency and hence destabilize the power. At least at this very high operating current one can say that the control of the phase via the electrical currents is not decoupled from an influence of the relevant optical power. This effect is however much

less relevant at lower current levels (cf. Fig. II.26 in chapter II), where the stability of the setup was excellent.

The unstable power in the second half of the measurement Fig. III.26 (a) was attributed to the used hill-climbing algorithm, which needs to be improved. The residual fluctuations of the power in the stabilized level distort the functionality of the algorithm which is based an evaluation of the slope of $P_{CBC}(I_{RW})$.
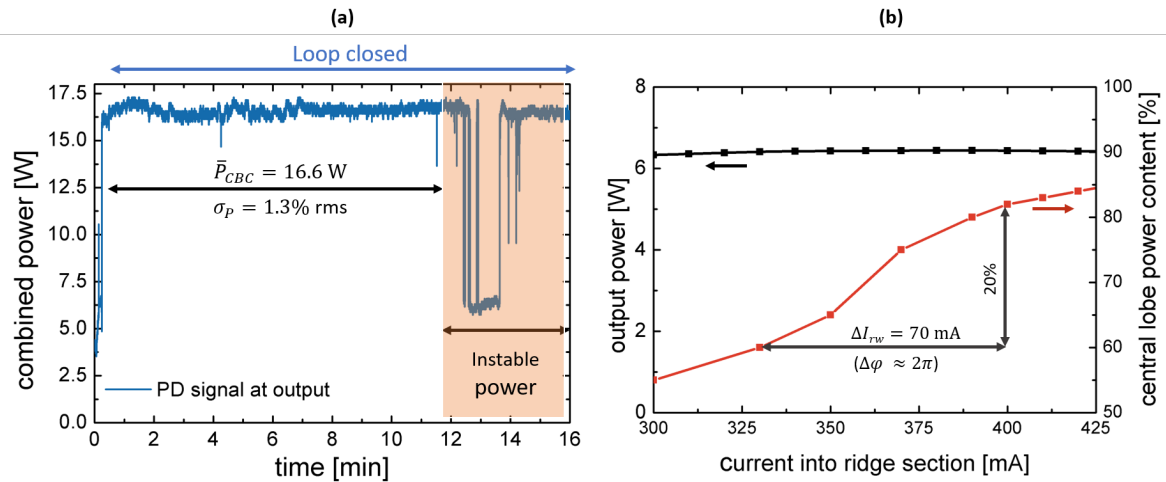
Figure III.26 – (a) Photodiode signal at the output of the CBC interferometer at high power. Average power and rms stability is specified for period without stability problems. The current into the tapered section of the amplifiers was 12 A. (b) Measured output power and central lobe power content for A_3 at $I_{tp} = 12$ A for different current into the RW.

The hill-climbing algorithm is however working extremely well at moderate bias conditions (here 9 A) as evidenced in Fig. III.27. The control loop was turned off to investigate the free-running stability of the setup without active phase control. The phase matching was lost without active phase control after approximately 10 s. The observed power fluctuations without active phase control were significant but slow. After closing the loop again, the combined power reached quickly (rise time < 1 s) the stabilized level.

These observations lead to the conclusion that active phase control via the current into the RW is critical at very high currents into the tapered section. Active phase control with external elements was investigated in the experiment described in the following section. The sequential hill combining algorithm was sufficient for phase control but needs to be improved to ensure long term stability at the highest powers.
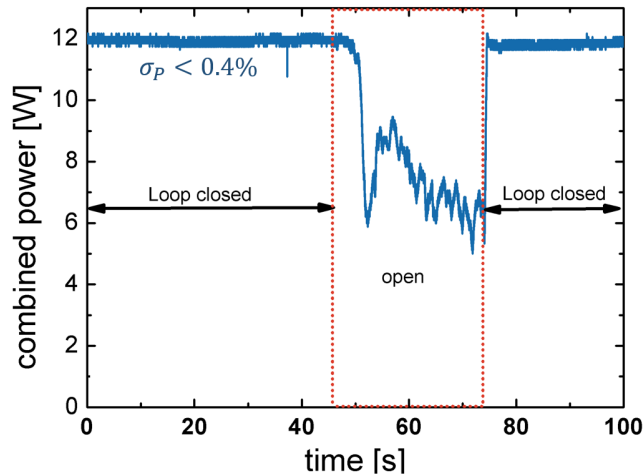
Figure III.27 – Measured power at the output of the CBC interferometer. The current into the tapered section of the four amplifiers was $I_{tp} = 9$ A. The control loop was opened for approx. 30 s to investigate the free running stability of the setup.

4   Compact coherent beam combining module using commercially available amplifiers

The coherent beam combining experiments described in the previous sections relied on custom-built amplifiers developed and fabricated by the Ferdinand-Braun-Institut in Berlin. The motivation for the work described in this section was to develop a compact and simple coherent beam combining module consisting of off-the-shelf commercially available elements only. Commercially available tapered amplifiers come usually with one common electrical contact for the current only, so that the current into the RW can not be independently controlled. The concept for the phase control was therefore different in this work, the hill-climbing algorithm was however identical. The wavelength was still 976 nm, but a transfer to any other wavelength in the range of 765-1060 nm would be straightforward as only the MO and the amplifiers have to be changed.

The module was mounted and characterized with the help of Jonas Hamperl, who was a master-level intern at Laboratoire Charles Fabry for one year [Hamperl 19].

4.1   Experimental setup

The experimental setup was again a typical four arm Mach-Zehnder interferometer (see. Fig. III.28) with one 5 mm long tapered amplifier (DILAS TA-0976-3000) in each arm. The MO oscillator was a narrow line-width DBR laser diode (Photodigm PH976280TO, λ = 976 nm) delivering up to 281 mW in a free space single mode beam. A double stage isolator (> 50 dB isolation) was used. The beam was split and recombined by a series of standard non-polarizing 50:50 plate beamsplitters. Each amplifier was seeded with approximately 30 mW. The amplifiers were mounted p-side down in a so-called DHP-inset package, which is larger than a standard c-mount and ensures efficient heat removal. The maximum output power from each amplifier was 3 W at 5 A. The setup was optimized for operation at the maximum current. The beam propagation factor M^2 of the PA (at I = 5 A) ranged from 2.1 to 2.7 in fast axis (FA) and from 5.0 to 6.5 in slow axis (SA).

Figure III.29 (a) shows a drawing of the integrated mechanical setup of the CBC interferometer. The total lateral dimension of the base plate including electronic contacts was in the order of an A4 page. The footprint of the experiments presented before was significantly larger than that, in the order of 1 m × 2 m, for practical reasons. The base-plate was a machined aluminum plate on which all mechanical
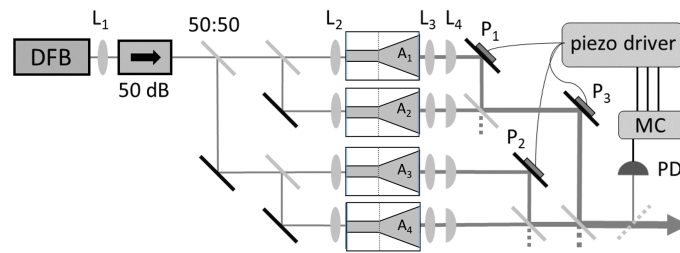
Figure III.28 – Simplified schematic of the integrated experimental setup: L_1 - aspherical lens (f = 8 mm, NA = 0.5), L_2 - aspherical lens (f = 4.51 mm, NA = 0.55), L_3 - cylindrical lens lens (f = 15 mm), P_i - mirror glued on piezoelectric chip, PD - photodiode, MC - micro-controller.

components were fixed. Two heat-pipes were pressed into notches for efficient heat transport from the amplifiers to the external radiators. The amplifiers were mounted in groups of two on a sub-module (see Fig. III.29 (b)). Each sub-module consisted of a gold-plated copper base plate and the temperature of each base plate was actively controlled by a Peltier element. Two amplifiers were mounted on each sub-module and the optics for coupling into the RW, FA and SA collimated were glued on the sub-module with UV curing adhesive. The correction of the astigmatism of each amplifier was optimized for the maximum current 5 A.

Phase control was achieved by folding mirrors glued on a small half-inch piezoelectric chip (see Fig. III.28 P_{1-3}). The frequency bandwidth of the piezo-mirror arrangement was experimentally evaluated to 6.6 kHz, which is far above the typically required bandwidth for phase control of tapered amplifiers. A voltage change of approximately ± 20 V corresponded to a piston-phase shift of π in one arm of the interferometer. The micro controller (MC) delivered at the output of the digital-to-analog converters (DAC) a voltage of 0-5 V and a piezo driver converted these signals to the drive voltage range 0-50 V.
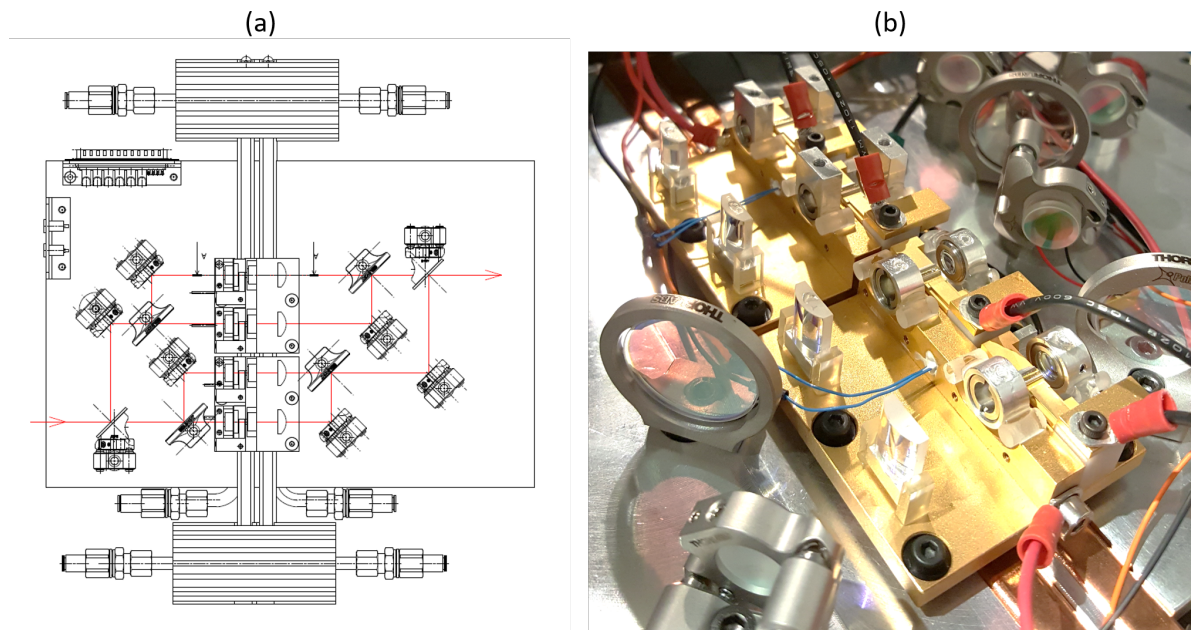
Figure III.29 –   (a) CAD drawing of the integrated CBC interferometer, (b) photograph of the two sub-modules.
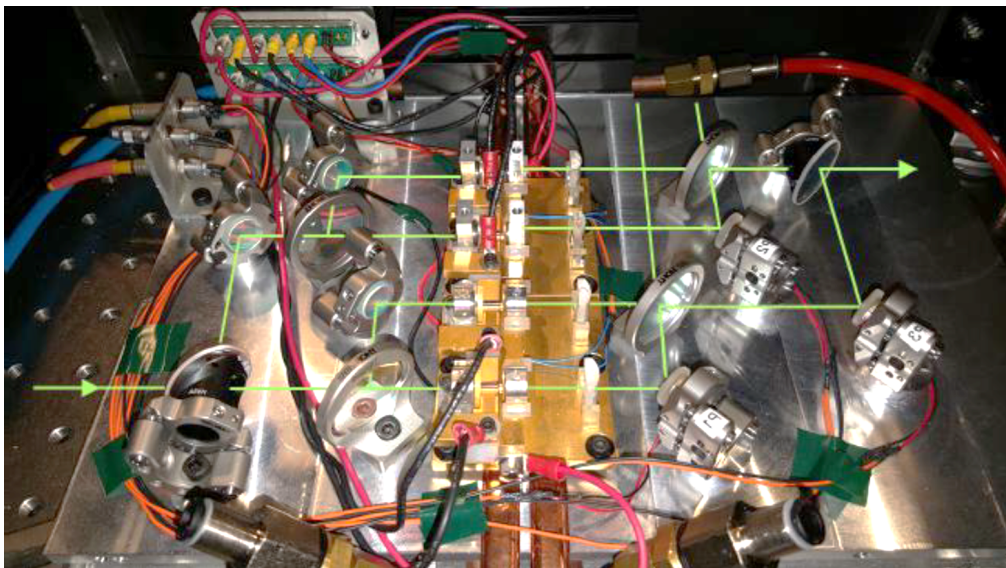
Figure III.30 –   Photograph of the mounted CBC interferometer with schematic indication of the laser beam line.

4.2   Experimental results

Power and combining efficiency   Coherent superposition of the four beams at 5 A resulted in 9.5 W at the output of the interferometer with excellent stability as shown in Fig. III.31 (a). The residual power fluctuations over 160 min were below 0.6% rms. The signals sent from the micro controller to the piezo driver are shown in III.31 (a) and indicate an excellent stability of the experimental setup. The peak-to-valley fluctuations of the signal sent for controlling the displacement of the actuators P_1 and P_2 correspond to a peak-to-valley phase fluctuations of $\pi/2$ over 160 min only. This means that the residual phase fluctuations of two amplifiers closely packaged on a common temperature stabilized base-plate are minimal and can easily be corrected. The actuator P_3 correcting the residual phase fluctuations in between the two sub-modules was slightly more active with a peak-to-valley amplitude of π over 160 min. The extremely slow phase fluctuations were far below the phase fluctuations in the previous significantly larger experiments. This demonstrates that coherent beam combining of four tapered amplifiers in a simple and compact small footprint can be very straightforward with minimal complexity regarding the required phase control, as the stability of the interferometer is improved.

The combining efficiency of the individual combining steps are given in the schematic overview in Fig. III.32 and were in the order of 80%. This led to a total combining efficiency of 66% for the full system, which was mostly limited by the beam quality of the tapered amplifiers as evidenced by the strongly increasing central lobe power content. The combining efficiency of the central lobe power content was however excellent, approximately in the range of 90%-95% at each combining step and in the order of 86% for the full setup.
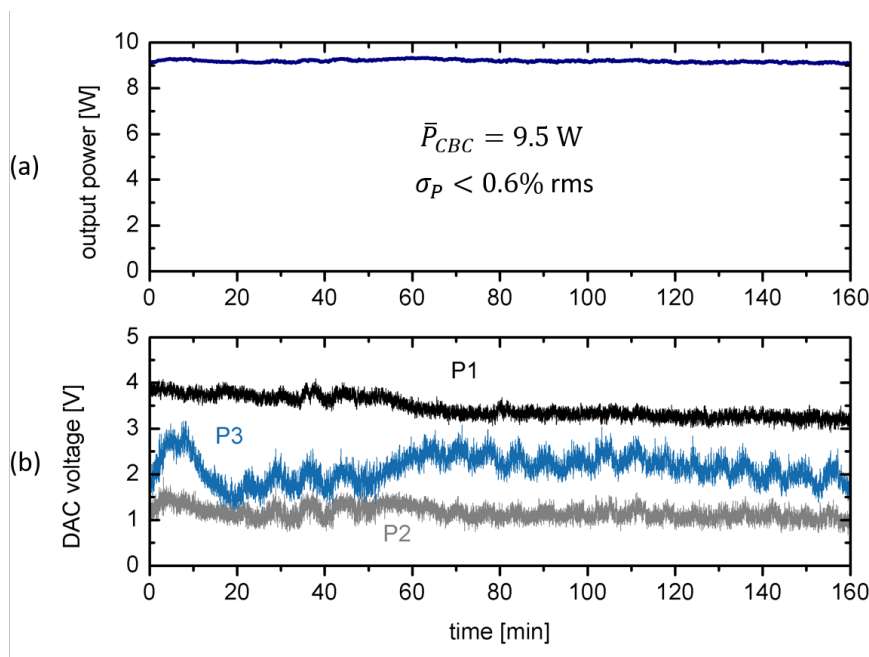
Figure III.31 – (a) Stability test of the coherently combined power over 160 min (1 Hz sample rate). (b) Corresponding output signals of the DAC sent to the voltage-drivers of the piezoelectric chips for phase control. Bias conditions: $I = 5$ A, $P_{in} = 30$ mW and T = 20°C

Beam quality   The beam quality was investigated by measurements of the M^2 beam propagation factors and the central lobe power content at the different steps. The beam quality of the individual amplifiers was not as good as for the amplifiers used in the previous experiments. The central lobe power content was typically in the order of 70% at 5 A. The M^2 beam propagation ranged from 2.1 to 2.7 in fast axis (FA) and from 5.0 to 6.5 on slow axis (SA).

The beam quality was significantly improved by the beam clean-up inherent to the coherent beam combining process and resulted in a final beam with $> 85\%$ central lobe power content and an M^2 of

1.8 ± 0.2 in FA and 2.7 ± 0.3 in SA.
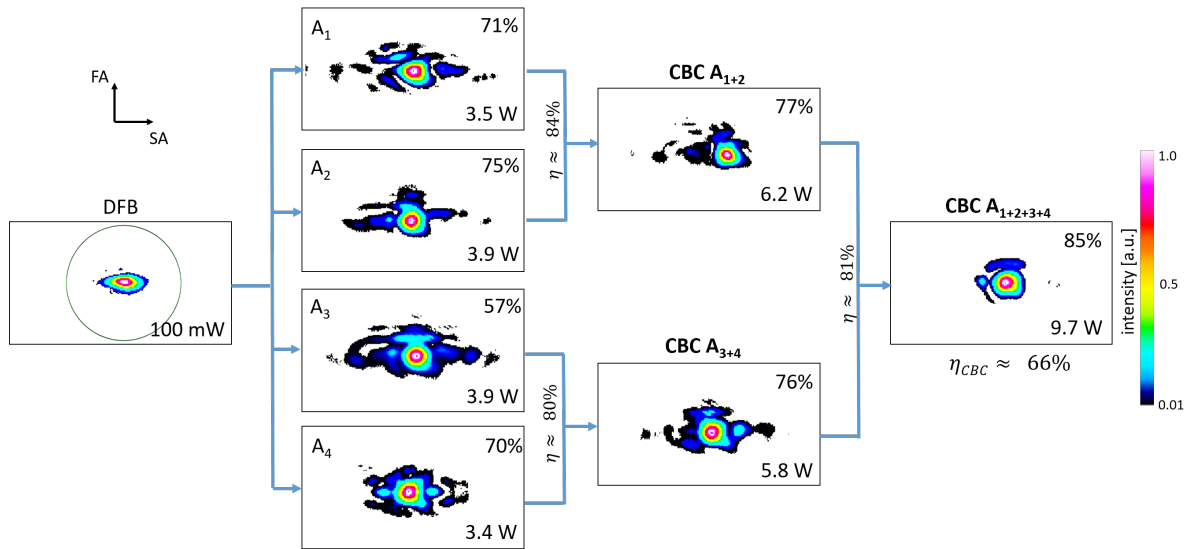
Figure III.32 – Measured beam profiles at waist (astigmatism corrected) of the beams from the amplifiers (A_{1-4}) and the beams after coherent superposition of two beams (A_{1+2} and A_{3+4}) and at the output of the CBC interferometer $A_{1+2+3+4}$. The power and central lobe power content is given at each step. The combining efficiency η at each step and the combining efficiency of the whole setup η_{CBC} are also given in percent. The current into the amplifiers was $I = 5$ A and the seed power per amplifier was $P_{in} = 25$ mW.

Conclusions   The development of small footprint modules of coherently combined tapered amplifiers based on off-the-shelf elements only was described. The setup is particular simple and can easily be transferred to other wavelengths. Such modules could significantly improve the performance of laser systems relying on tapered amplifiers for applications such as spectroscopy or atom cooling. Furthermore, coherent beam combining modules might also be an excellent high brightness pump source for solid-state lasers or nonlinear frequency conversion. Further increase in the power is feasible by adding more amplifiers to the setup. Additionally one could combine several of such modules incoherently by polarization coupling or spectral beam combining to reach powers far above 10 W in a close to diffraction limited beam.

Chapter IV

Pulsed mode coherent beam combining

Objectifs

This chapter covers coherent beam combining experiments in pulsed mode. As a first approach, quasi-continuous-wave (QCW) operation is thoroughly investigated regarding dynamic effects in the amplifiers as the devices are turned on. The demonstration of QCW coherent beam combining of four over-driven tapered amplifiers is described and the results are compared to the CW regime. Preliminary investigations for transferring the experiments to the short pulse regime are briefly discussed in the second section.

Contents

1   Quasi continuous wave operation

Quasi continuous wave (QCW) operation is a common method for peak-power scaling of diode laser systems. It consists in pumping the emitters electrically only for certain time intervals, which are short enough to reduce the thermal load in the device, but still long enough that the device is optically in a steady state ($dP_{opt}/dt \approx 0$). The typical pulse duration (Δt_{QCW}) is in the order of 1 ms and the duty cycle, which is the ratio of the pulse duration and the pulse period $D = \Delta t_{QCW}/T$, is typically in the order of a few percent (see Fig. IV.1). This significantly reduces the average thermal load, which is related to the not-ideal power conversion efficiency, and allows to operate the devices at higher currents when compared to normal CW operation. Coherent beam combining in QCW mode is therefore a promising approach to scale the coherently combined power beyond limitations linked to the thermal rollover of the amplifiers. The extracted average power is however significantly lower and depends on the duty cycle $\bar{P} = D \times P_{QCW}$. It is common to specify the optical power P_{QCW} during the pulses and not the average power for QCW diode laser systems.
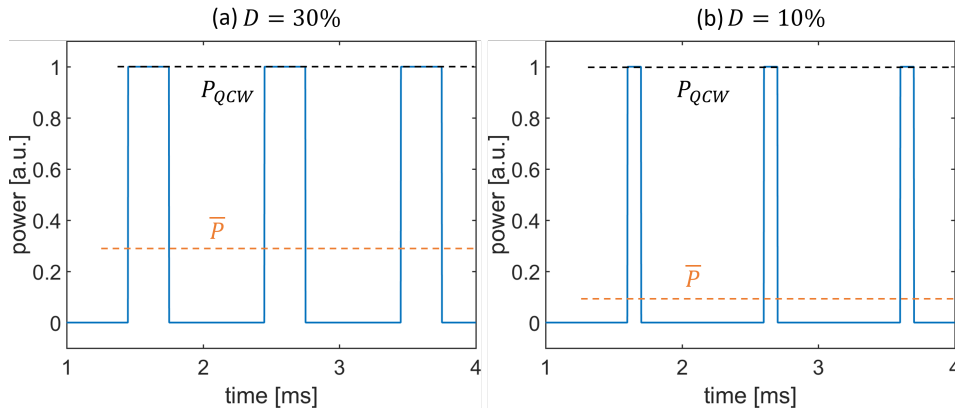
Figure IV.1 – Principle of QCW operation with QCW peak power P_{QCW} and average power $\bar{P}$ for (a) 30% duty cycle (b) 10% duty cycle.

Coherent beam combining with diode lasers was demonstrated in CW mostly [Lucas-Leclin 19] and there are only few demonstrations of pulsed phase-coupled semiconductor optical amplifiers [Osinski 95]. Operating a coherently combined systems in QCW operation is not as straightforward as it may seem at the first glance. The devices are indeed optically and electrically in quasi-steady state during the QCW pulses, but they may exhibit significant thermal dynamics during the pulses. These temperature changes have to be taken into account regarding the phase matching and the coherent superposition. Coherent beam combining of fiber amplifiers has been demonstrated in the long pulse regime (100 ns to a few μs) [Lombard 13], where similar to the case investigated here, several non-trivial effects concerning phase and gain during the pulse were observed.

The so-called turn-on dynamics of tapered amplifiers in QCW operation will be discussed in section 1.2.2. Three different amplifier designs (ELoD2: baseline, 4 mm taper, 50% stripes) were used for the investigations of the turn-on dynamics. The focus lied however on the ELoD2 4 mm taper design which was chosen for the final QCW coherent beam combining demonstration.

Parts of the content of this section were recently published in Optics Express [Albrodt 19b]. The content of this paper is summarized below and put in relation with additional experimental data.

1.1 Experimental setup

The experimental setup for coherent beam combining in QCW mode (see Fig. IV.2) was similar to the experimental setup used in the experiments described earlier (cf. section 3 in chapter III). The laser diode drivers (Arroyo 4320-QCW) delivering the currents into the tapered section of each amplifier were operated in QCW mode and synchronized by an external function generator (Keysight Technologies 33210A). The function generator also triggered the micro-controller on which a simplified version of the previously discussed hill-climbing algorithm was implemented. The phase matching approach will be discussed in section 1.4. Phase matching was achieved by active feedback on the currents into the RW. The seed laser and the current into the RW were operated in CW mode and only the currents into the tapered section were modulated. This had no negative impact on the contrast as the signal from seed laser and RW were almost completely absorbed when the tapered section was unbiased. Furthermore, the heat load of the RW is in the order of 1 W only and is negligible compared to the heat-load generated in the tapered section (in the order of 30 W at high bias). The system was operated with a pulse duration from 1-5 ms at a duty cycle of 10%.
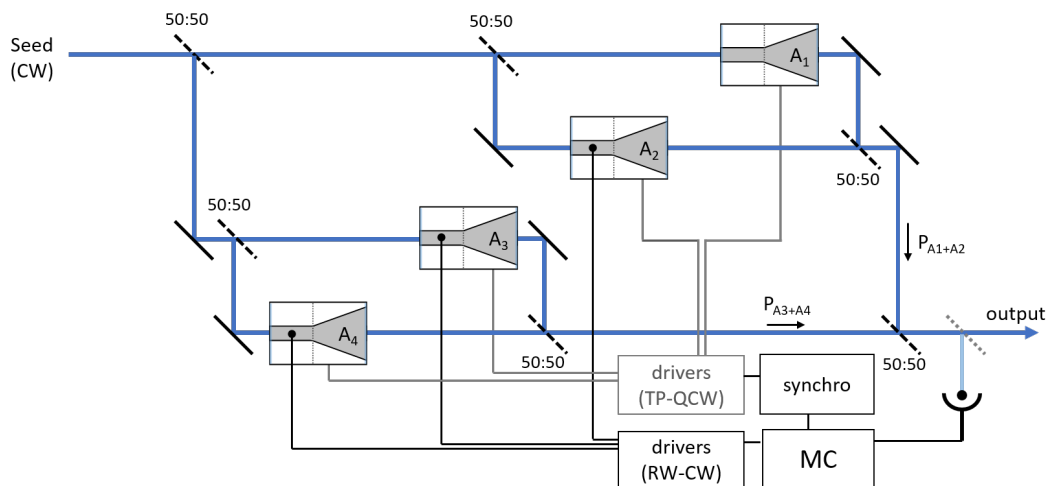
Figure IV.2 – Simplified schematic of the experimental setup for QCW coherent beam combining of four tapered amplifiers. The currents into the RW were actively controlled for $A_{2\text{-}4}$. An external synchro TTL signal was used to trigger the QCW laser drivers for the current into the tapered sections and to trigger the phase control loop implemented on a micro-controller (MC). The basic optical setup of the interferometer was identical to the experiments described in chapter III section 3.

1.2 Characterization of tapered amplifiers in QCW operation

1.2.1 Power and beam quality

The QCW output power was measured individually for the four tapered amplifiers used in the final coherent beam combining experiments and compared to measurements in CW operation. The influence of the reduced heat load on the optical output power is clearly visible as shown in the Fig. IV.3, showing the average of the four devices. While there was an onset of the thermal rollover at about 10 A in CW mode (black line), this was not the case for QCW operation (blue line). The slope efficiency remained constant at approximately 0.7 W/A resulting in a typical output power of 9.3 W at 16 A, which is roughly 3 W higher than the typical CW output power. In principle one could operate the devices at even higher currents, this was however not useful for coherent beam combining experiments regarding multiple effects discussed below concerning the beam quality and pulse stability. The QCW power characteristics of the other ELoD2 designs, which were used during the investigation of the turn-on dynamics, can be found in Fig. II.22 on page 64.
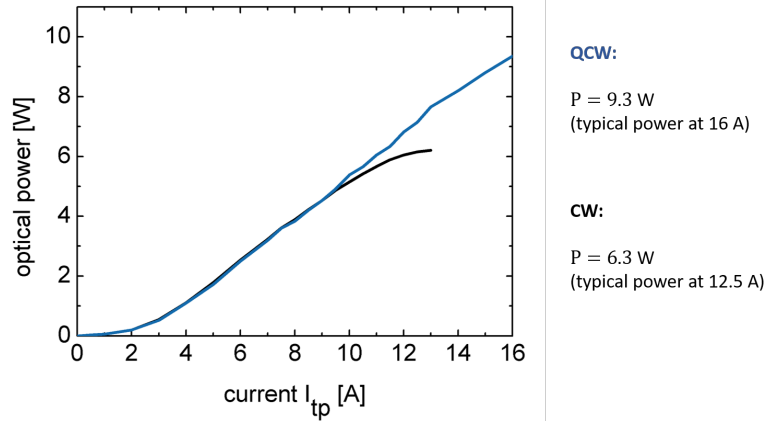
Figure IV.3 – Measured output power in QCW and CW operation (ELoD2 - 4 mm taper). Four of such amplifiers were used in the experiments described in section 1.4 (QCW, 1 ms, 10% duty cycle, $I_{rw} = 400$ mA, $P_{in} = 20$ mW).
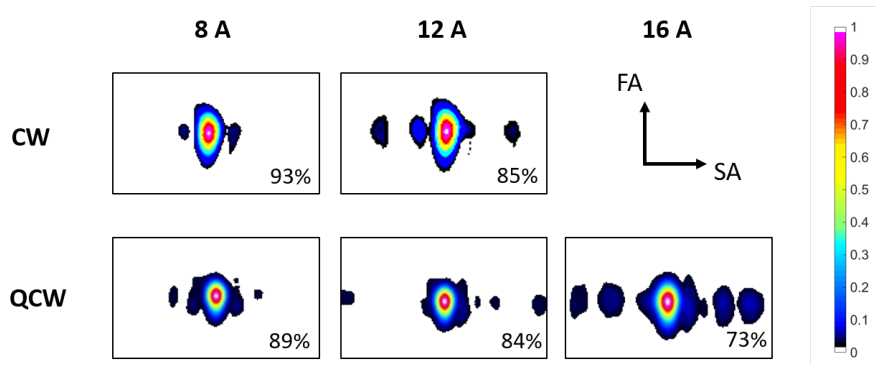
Figure IV.4 – Measured beam shaped at waist (astigmatism corrected) for CW and QCW operation at different current levels. The central lobe power content is given for each beam (QCW, 1 ms, 10% duty cycle, $I_{rw} = 400$ mA, $P_{in} = 20$ mW, an ELoD2 4 mm taper amplifier was used). The measurements in QCW mode where done 0.8 ms after the start of the pulse with an integration time of 50 μs in order to eliminate any effect from a dynamic change in the beam shape (cf. Fig. IV.5).

The beam shape at waist (astigmatism corrected) was measured at different bias points and compared to CW operation as shown in Fig. IV.4. The differences in the beam shapes between CW and QCW operation were minor at moderate currents. The evaluated central lobe power content was only slightly lower for QCW operation and a slightly different intensity distribution of the side-lobes was observed. The central lobe power content decreased however rapidly for currents higher than 12 A and was in the order of 73% at 16 A. The beam profiles of the four amplifiers were similar with minor differences in the central lobe power content at equal bias conditions ($\pm$ 5%). As it has been shown before that the combining efficiency is related to the central lobe power content (cf. Fig. III.24) in chapter III), it is therefore not useful to operate the devices at even higher currents.

Note that the measurements of the beam shape in QCW mode represent however only a snapshot-like measurement of the beam profile at waist. There is in fact a dynamic change in the beam propagation in the tapered section during the QCW pulses, which will be discussed below.

1.2.2 Turn-on-dynamics

Beam propagation   It is well known that the astigmatism of a tapered laser or amplifier depends on the bias condition of the device (cf. section 1 in chapter II) [Kelemen 04]. The virtual point sources in SA is located approximately L/n_{eff}, where L is the length of the gain-guided tapered section and n_{eff}
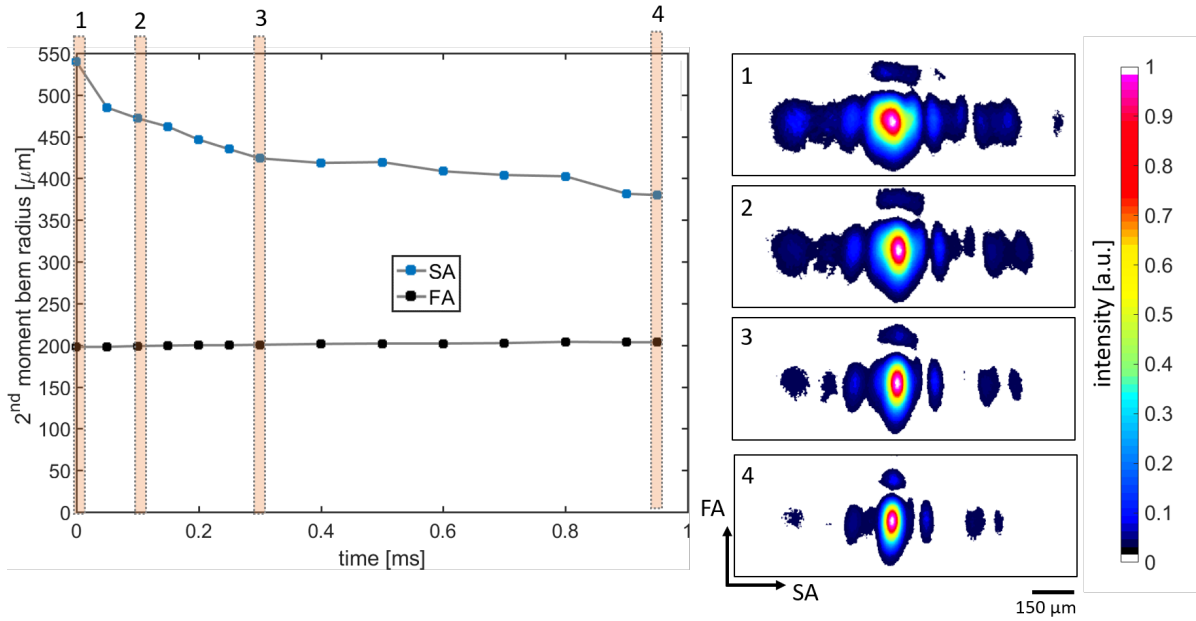
Figure IV.5 – Measured second moment beam radius in SA (blue) and fast axis (black) at the measurement plane (see CCD sensor position in Fig. IV.6). Four exemplary beam profiles (see pos. 1-4) are shown on the right. Each image was measured with 50 μs integration time. $I_{tp} = 12$ A (QCW, 1 ms, 10% duty cycle), $I_{rw} = 400$ mA, $P_{in} = 20$ mW. A 5 mm long ELoD2 (50% stripes) tapered amplifier was used.

is the effective refractive index of the waveguide, behind the front facet of the device. The refractive index however depends on the temperature and the carrier density at the given bias conditions. Furthermore, a transverse thermal lens in the tapered section may influence how the beam is propagating in the tapered section and the location of the virtual point source. These effects together lead to a so-called wandering astigmatism [Sujecki 03]. The question however is, what happens if one operates tapered amplifiers at high bias in quasi continuous wave operation? During each pulse, the device exhibits changes in the average temperature, the carrier density is rapidly varied at the beginning of the pulse and the thermal lens may be varying during the pulse. A CCD camera was placed in a measurement plane corresponding to the beam waist (astigmatism corrected) in CW mode. The amplifier was then operated in QCW mode ($\Delta t = 1$ ms) and the camera measured the beam profile at different instances during the pulse. Figure IV.5 shows how the second moment beam diameters are changing during the pulse. The SA beam radius is changing significantly, especially during the first 250 μs of the pulse. The beam radius at the beginning of the pulse (cf. pos. 1 in Figure IV.5) was roughly $\sqrt{2}$ times larger than at the end of the pulse (cf. pos. 4 in Figure IV.5). There was no significant change in the beam shape after 1 ms if longer pulse durations were used. The FA beam radius was constant during the pulse duration. This means that only the z-position of the virtual point source in SA is changing during the pulse as shown in Figure IV.5, which also leads to a displacement of the beam waist after the focusing lens L$_3$ and consequently causes the varying SA beam radius as shown in Fig. IV.6. Note that the absolute z-position of the SA beam waist after the focusing lens depends on the optical setup and may vary significantly even for a minor displacement of the SA virtual point source in the tapered section. In the case discussed above, an absolute displacement of the SA beam waist of 20 mm was observed which corresponded approximately to a displacement of the virtual point source of 50 μm in the tapered section. The measurement presented here was done with the ELoD2 50% stripes design, the effect was however very similar for the 4 mm taper design.

This dynamic change has to be taken into account for the coherent superposition of the beams, as the spatial overlap of the fields on the combining elements defines the achievable combining efficiency
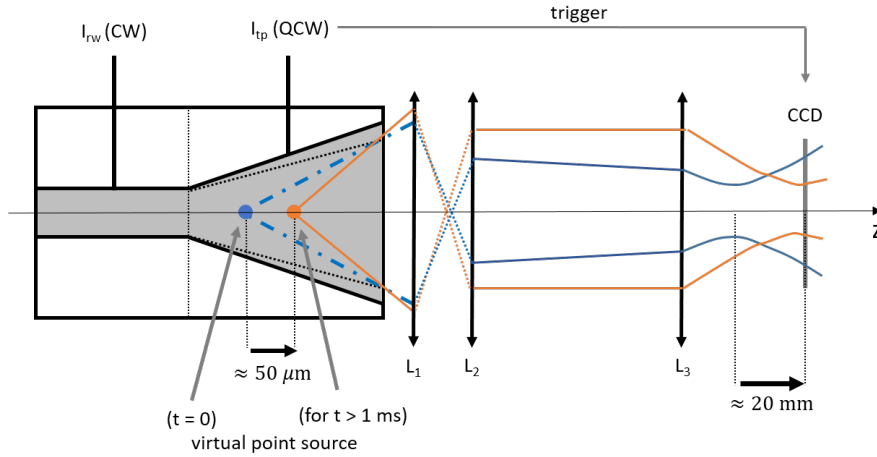
Figure IV.6 – Simplified schematic of the dynamic change in the beam propagation in SA during a QCW pulse. L_1: f = 2.75 mm NA = 0.55, L2: f = 19 mm, L_3: f = 150 mm.

(cf. section 1 in chapter III). The effect is however deterministic and depends on the bias conditions. Furthermore the four amplifiers used in the coherent beam combining experiments showed similar behavior, which allows to combine the beams coherently without an active correction of the changing astigmatism. The condition however is that the devices in the setup have to operate at equal bias conditions so that the dynamic change in the astigmatism is *synchronized* in all beams. As a consequence, the dynamic change in the astigmatism is transferred to the coherently combined beam and may be impractical in certain cases, for example for fiber coupling. Unfortunately, there is no straightforward method to correct or circumvent this effect. Strategies to reduce the effect of the wandering astigmatism in the tapered amplifiers include the use of long tapered sections or improved packaging, both targeting a reduced thermal resistance of the device and therefore limiting the influence of thermal effects [Kelemen 04].

Piston phase drift The effective optical path length in the amplifier is also changing during the QCW pulses, which leads to a drift of the accumulated piston phase in the amplifier. The phase drift was measured in the experimental setup shown in Fig. IV.7 (a), which was identical to the setup used for the phase noise measurements discussed in chapter II (section 3.2.4). During the QCW pulse, the piston-phase in the amplifier is changing while the piston phase in the second arm of the interferometer remains unchanged. This leads consequently to a beating of the in-phase (I) and quadrature (Q) signal components during the QCW pulse as shown in Fig. IV.7 (b). One can see that the period of the beating signal is increasing with time but a clear piston phase variation is detectable also at the end of the QCW pulse. The piston phase drift $\varphi(t)$ is directly related to the I and Q signals by the simple relation $\varphi(t) = -\arctan[Q(t)/I(t)]$ (cf. Equ. II.11) and is shown for measurements at different currents I_{tp} into the tapered section in Fig. IV.8 (a). The amplitude of the piston phase drift increased with I_{tp} and was accurately reproduced using the following fit function:

$$\varphi(t) = \varphi_0 + C \times t - \Delta\varphi_1 \times \exp\left[\frac{-t}{\tau_1}\right] - \Delta\varphi_2 \times \exp\left[\frac{-t}{\tau_2}\right]. \tag{IV.1}$$

The time constants τ_1 and τ_2 of the two exponential functions were found by numerical fitting to be 0.1 ms and 1 ms respectively and there were independent of the current I_{tp}. It was verified that the shorter time constant, here 0.1 ms, was related to the rise time of the current into the tapered section. The longer time constant was found to be related to the packaging. The amplitudes of the exponential contributions $\Delta\varphi_1$ and $\Delta\varphi_2$ are proportional to I_{tp} and roughly equal for the two exponential contributions. The linear term $C \times t$ describes a linear increase in the average heatsink temperature during the pulse and is

also proportional to I_{tp}. The amplitude of the overall piston phase drift is large, reaching 30 π at 13 A for 5 ms long pulses.
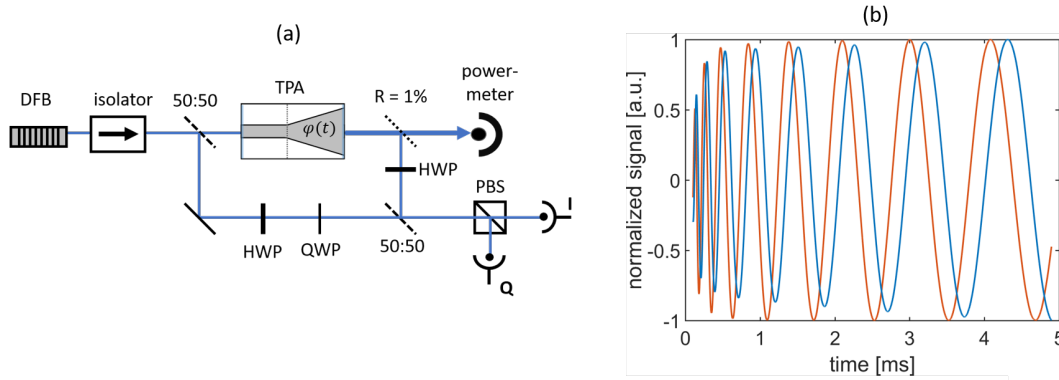
Figure IV.7 – Experimental setup for the measurement of the piston phase drift. Exemplary in-phase and quadrature signals recorded with the photodiodes I and Q during a 5 ms long QCW pulse (ELoD2 4 mm taper).

As a side-note it is worth mentioning that a piston phase drift is equivalent to a slightly changing frequency of the amplified signal $\nu(t) = \nu_{DFB} + \Delta\nu(t)$, where ν_{DFB} is the frequency of the seed laser. The chirp is related to the piston phase drift by

$$\Delta\nu(t) = \frac{1}{2\pi} \times \frac{d\varphi(t)}{dt},\tag{IV.2}$$

and is shown in Fig. IV.8 for $I_{tp} = 13$ A. The frequency differences are in the kHz regime only and decrease rapidly with time. The frequency chirp is not relevant in this case as the line-width of the used DFB seed laser is in the order of a few MHz (over 5 μs), which means that the QCW operation of the tapered amplifier is not significantly increasing the spectral line-width of the complete MOPA setup. In other configurations, if a ECDL with a line-width in the kHz range is used as the master oscillator, this might however be a significant effect.
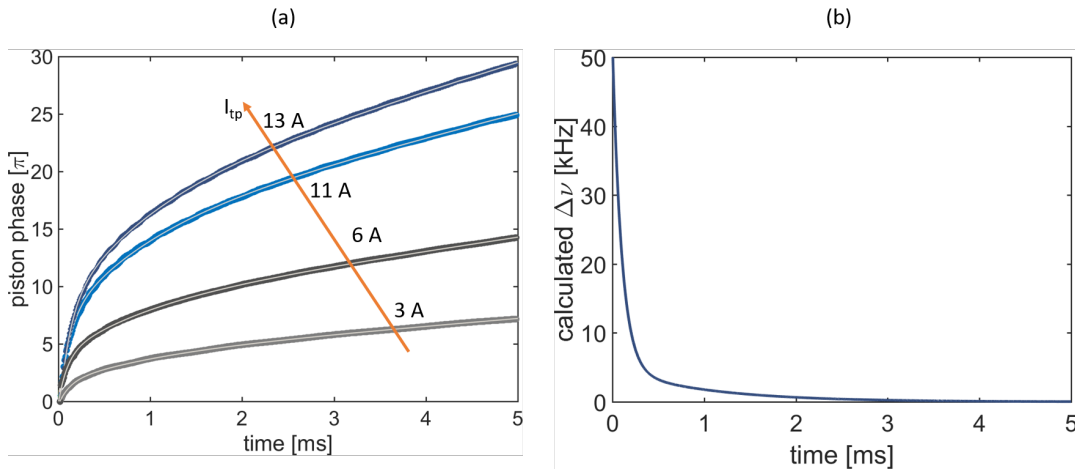
Figure IV.8 – (a) Measured piston phase drift for different currents into the tapered section. The experimental data is shown as thick solid lines and the numerical fit following Eq. IV.1 is shown as thin solid lines. (b) Calculated frequency chirp for the piston phase drift at $I_{tp} = 13$ A (QCW, 5 ms pulses at 10% duty cycle, $I_{rw} = 400$ mA, $P_{in} = 20$ mW. A 5 mm long ELoD2 (50% stripes) tapered amplifier was used).

Phase matching during the entire pulse duration is required for coherent superposition of several tapered amplifiers operated in QCW mode. It is therefore important to understand what factors determine

the described dynamic piston phase drift. The investigation was split in three parts:

(a) How does the amplifier design influence the piston phase drift in QCW operation?

(b) How repeatable is the piston phase drift for different devices with identical amplifier design?

(c) How stable is the piston phase drift in one amplifier from pulse to pulse?

(a) Influence of the amplifier design on the piston phase drift   The piston phase drift was measured for the ELoD2 amplifiers with different lengths of the tapered section (baseline: 3 mm long tapered section, 50% stripes: 4 mm long tapered section with stripe patterned electrical contact), and 4 mm taper (4 mm long tapered section with conventional electrical contact)[1] and compared to a measurement with a Reference epitaxial structure amplifier (4 mm long tapered section - cf. II.2). The measurement shown in Fig. IV.9 (a) shows that a large tapered section is beneficial to reduce the piston phase drift and that the difference between different lateral amplifier designs can be quite significant. Both the thermal resistance and the density of the heat-load decrease with increasing length of the tapered section, which leads to a reduced phase drift. The time constants $\tau_{1,2}$ of the fit function (cf. Equ. IV.1) were however found to be approximately identical (0.1 ms and 1 ms respectively) for all amplifier designs. There was no significant difference of the piston phase drift for devices with and without a stripe patterned electrical contact (cf. solid blue line and dotted black line in Fig. IV.9). The piston phase drift for a tapered amplifier with the reference epitaxial design (also 4 mm long tapered section) that has a slightly better PCE, was slightly lower when compared to the ELoD2 4 mm taper amplifier. These observations lead to the conclusion that a design with a high PCE (resulting in a low heat-load in the device) and a large tapered section (resulting in a low thermal resistance) has a lower piston phase drift in QCW operation. Furthermore, the packaging may also influence the piston phase drift which was however not investigated here.

(b) Repeatability for amplifiers with identical design   The piston phase drift of the four tapered amplifiers (ELoD2 4 mm taper) used in the coherent beam combining experiments was measured and compared to each other. As shown in Figure IV.9 (b), it is possible to achieve an almost perfectly synchronized piston phase drift even at high bias. The current into the tapered section was slightly adjusted (± 0.5 A) in order to achieve the same amplitude of the phase drift in the different amplifiers. The inset in figure IV.9 (b) shows a zoom into the data and indicates that the difference in between the different measurements is in the order of $\pi/10$ only.

The conclusion of this observation is that it is possible to synchronize the piston phase drift of several tapered amplifiers (with identical amplifier design) by fine-tuning of the current into the tapered section. An active control of the relative phase within the pulse may not be required as the differences in the measured phase drift are small. Active phase control is however required to correct slow phase fluctuations of the interferometer and the amplifiers that are dominated by very low frequencies (below 100 Hz, cf. II.3.2.4) and can be easily corrected from pulse to pulse.

(c) Repeatability from pulse to pulse   The piston phase drift was measured for 40 consecutive QCW pulses for one amplifier (ELoD2 4 mm taper). The experimental data illustrated in Fig. IV.10 indicates that the piston phase drift is very repeatable for consecutive pulses. Peak-to-peak variations within 40 consecutive pulses were found to be in the order of $\pi/20$ only. The conclusion of this observation is that it is possible to use a very simple pulse-to-pulse approach for the optimization of the phase-matching in the coherent beam combining interferometer (cf. section 1.4).

---

[1]See Fig. II.19 on page 60 for an overview of the different EloD2 amplifier designs.
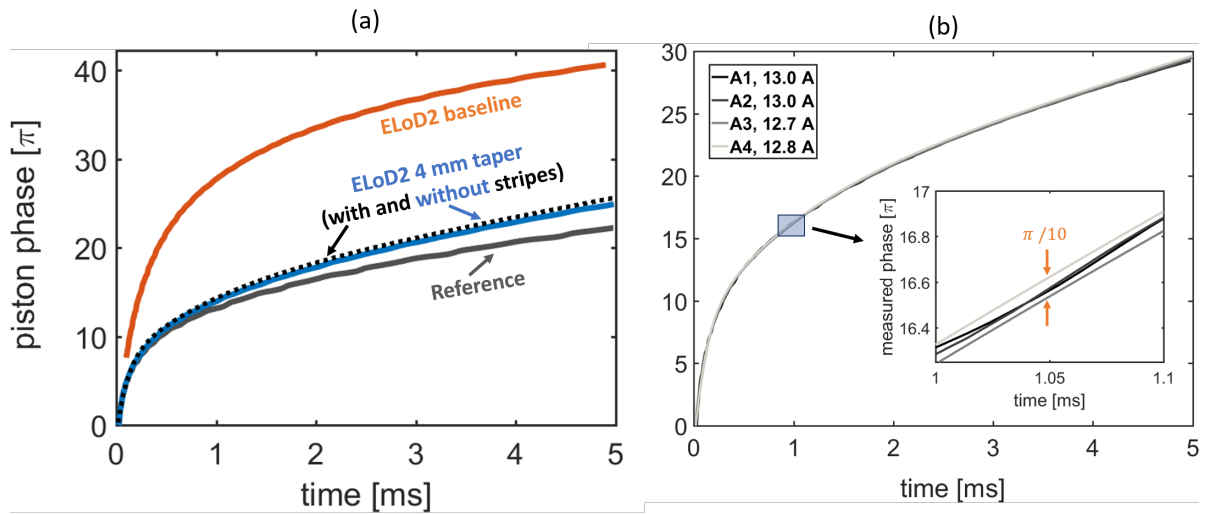
Figure IV.9 – (a) Measured piston phase drift for tapered amplifiers with different device designs at $I_{tp} = 11$ A. Orange - ELoD2 baseline (2 mm RW + 3 mm TP), blue - ELoD2 4mm taper (2 mm RW + 3 mm TP), black dotted line - ELoD2 50% stripes (2 mm RW + 3 mm TP with stripes) and gray - Reference TPA (2 mm RW + 4 mm TP). (b) Measured piston phase drift for four ELoD2 amplifiers with identical device design (1 mm RW, 4 mm TP, no stripes) at $I_{tp} \approx 13$ A. The inset shows a zoom into the data at $t \approx 1$ ms. Bias conditions for all measurements in a and b: QCW, 5 ms pulses at 10% duty cycle, $I_{rw} = 400$ mA, $P_{in} = 20$ mW.
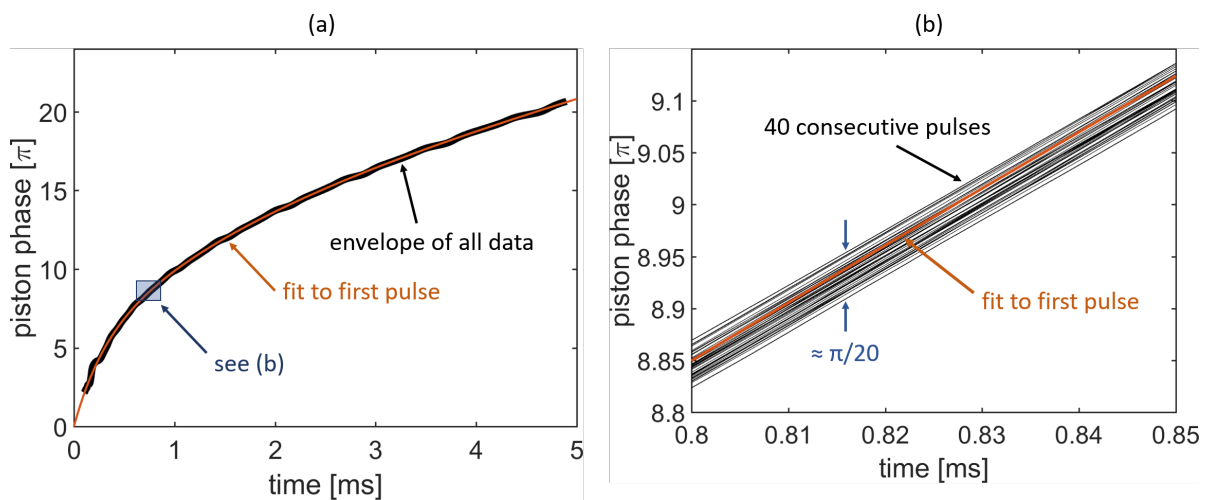
Figure IV.10 – (a) Measured piston phase drift for 40 consecutive QCW pulses at $I_{tp} = 11$ A. Envelope of measurement data (all 40 pulses) is represented in black, the fit to the first pulse is represented in orange. (b) Zoom into the experimental data and each thin black line represents one measurement. (QCW, 5 ms pulses at 10% duty cycle, $I_{rw} = 400$ mA, $P_{in} = 20$ mW. A 5 mm long ELoD2 (4 mm taper) tapered amplifier was used).

Resonances in the amplifier The temporal pulse shape in QCW mode should be approximately rectangular. Measurements however evidenced oscillations in the output power as shown in Fig. IV.11 (a). The period of the oscillations is increasing with time and decreasing with the current into the tapered section. There were minor differences between amplifiers with identical device design. The best ones (see amplifier 1, black lines) showed significant but stable oscillations at very high currents only. The peak-to-peak amplitude of the oscillations measured at 16 A for amplifier 1 were below 6% of the average power. Devices with slightly lower performance (see amplifier 2, blue lines) tended to show stronger oscillations at moderate currents and the oscillations became chaotic at high currents (e.g. 16 A) with a peak-to-peak amplitude of about 12% [Albrodt 19b].

(a)   (b)
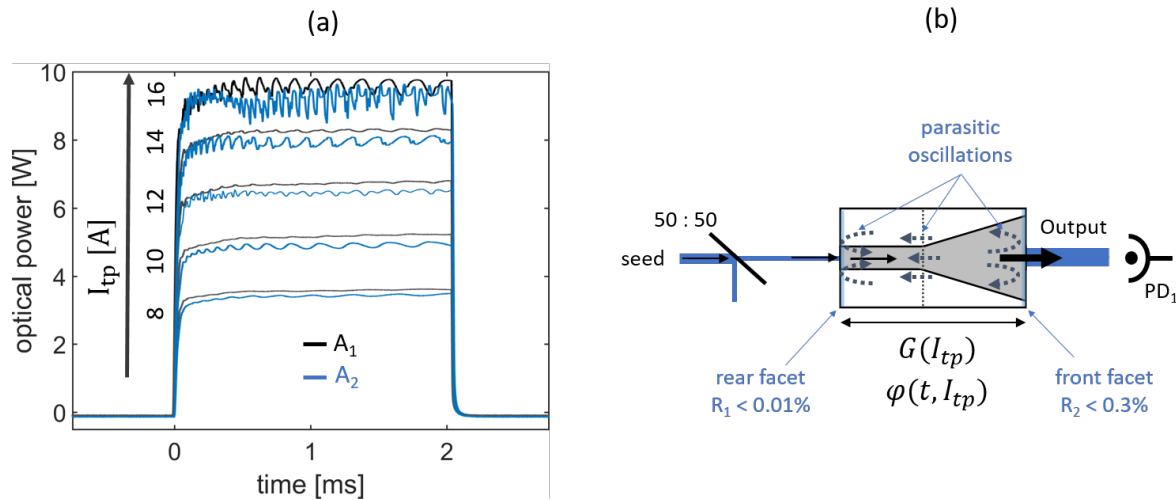
Figure IV.11 – (a) Measured pulse shapes for two amplifiers at 8-16 A current into the tapered section (QCW, 2 ms pulses at 10% duty cycle, $I_{rw} = 400$ mA, $P_{in} = 20$ mW. Two 5 mm long ELoD2 (4 mm taper) tapered amplifiers were used). (b) Simplified schematic of the parasitic Fabry-Perot cavity in the amplifier. A photodiode (PD) was used to measure the power oscillations at the output.

These quasi-periodic oscillations are attributed to parasitic resonances of the narrow spectral line seed signal within the amplifier (see Fig. IV.11 (b)). The amplifier behaves as a low-finesse Fabry-Perot cavity, which filters the seed laser line. The facets of the amplifier are AR coated ($R_1 < 0.01\%$ and $R_2 < 0.3\%$) but the gain in the device $G(I_{tp})$ increases the quality factor of the parasitic cavity, especially at high current levels. Furthermore, the piston phase drift in the amplifiers leads to a scanning effect as it shifts the resonance peaks during the QCW pulses and is causing the observed quasi-periodic oscillations in the output power. The modulation depth of the oscillations increases with the current into the tapered section as the gain in the amplifier is increasing. The slight disparities within the two devices shown in Fig. IV.11 were attributed to small differences in the coating reflectivity, coupling efficiency and gain in the devices.

It would be desirable for further studies into pulsed-mode coherent beam combining to use amplifiers with the best possible AR-coating on both facets in order to avoid those parasitic resonance effects in the amplifier. The reflectivity of the front facet was with $R_2 < 0.3\%$ still quite high and not ideal. The reason for that was that these devices were originally fabricated as DBR-TPLs where low reflectivity of the front facet was required [Crump 15]. The DBR-grating was then cleaved off and the back facet was AR coated in order to use the devices in an amplifier configuration. ELoD2 amplifiers with AR coatings on both facets were unfortunately not available during this work for practical reasons. Furthermore, advanced recent design approaches of tapered lasers and amplifiers that include a small angle between ridge waveguide and tapered section may be helpful to prevent parasitic resonances in the amplifier [Zink 19].

1.3 Optical feedback from over-driven tapered amplifiers in QCW mode

The influence of optical feedback coming from the tapered amplifiers on the DFB laser frequency were previously discussed in chapter III in the context of section 2.3. Feedback effects are critical when the tapered amplifiers are operated at high-currents in QCW mode for two reasons:

- operation at high currents leads to a high level of feedback

- the piston-phase drift in the amplifier leads to an optical feedback with a rapidly changing phase over several tens of π in a few milliseconds.

The initial experimental setup for QCW CBC combining was realized with a double-stage Faraday isolator (55 dB optical isolation). Measurements of the DFB seed laser frequency with a Fabry-Perot interferometer (similar to the measurements described in chapter III section 2.3) evidenced a strong perturbation of the frequency during the QCW pulse, as shown in Fig. IV.12(a). The optical feedback from the tapered amplifier led to a frequency shift and quasi-periodic frequency hopping with an amplitude of about 80 MHz. The period of the frequency hopping clearly decreased during the pulse, which appears to be linked to the piston-phase drift of the tapered amplifiers during a QCW pulse (cf. Eq. IV.1).
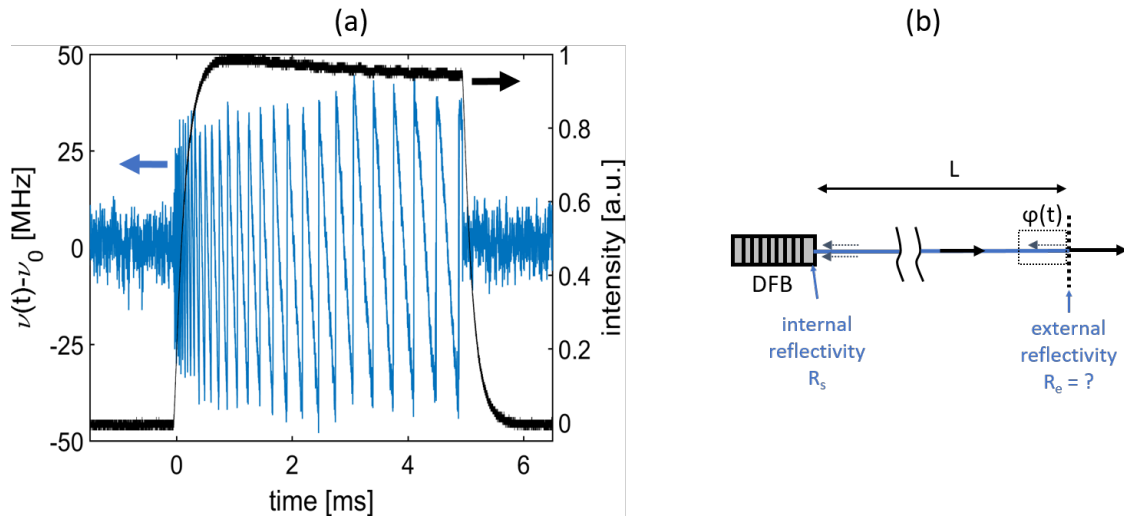
Figure IV.12 – (a) Measurement of the seed laser frequency perturbations $\nu(t) - \nu_0$ (blue) induced by optical feedback from a single tapered amplifier (A$_1$) operated at $I_{tp} = 13$ A. The optical isolation was 55 dB for this experiment. An ELoD2 (4 mm taper) amplifier was used. $I_{rw} = 400$ mA, $P_{in} = 20$ mW. (b) Equivalent representation for a system where the optical feedback comes from a passive external reflector with the reflectivity R_e at the distance L. Furthermore, the single-pass piston phase drift $\varphi(t)$ of the tapered amplifier can be taken into account as a $\frac{\varphi(t)\lambda}{\pi c}$ increase of the external round-trip time.

In order to understand this observation, it is helpful to investigate the effect of an optical feedback with a changing phase $\varphi(t)$ numerically for the simplified equivalent optical setup illustrated in Fig. IV.12(b). A few general equations describing the effect of optical feedback on the DFB laser frequency have been discussed earlier, Eq. III.7 is reformulated here for clarity:

$$\Delta\nu(t) \equiv \nu(t) - \nu_0 = -\frac{\kappa}{2\pi}\Big(\sin(2\pi\nu(t)\tau_e(t)) + \alpha\cos(2\pi\nu(t)\tau_e(t)) \Big). \tag{IV.3}$$

The maximum change in the DFB laser frequency is proportional to the coupling factor κ which is itself proportional to $\sqrt{R_e}$, the square root of an equivalent external reflectivity. The value of R_e is increasing with the operating current as the gain in the device is increasing. Furthermore, the term

$\nu(t)\tau_e(t)$ includes the time dependent external round-trip time $\tau_e(t)$, which can be written as

$$\tau_e(t) = \tau_e(0) + \frac{\varphi(t)}{\pi}\frac{\lambda}{c}, \tag{IV.4}$$

where τ_e is the external round-trip time at the start of the QCW pulse and $\varphi(t)$ is the single-pass piston-phase drift linked to the QCW operation of the amplifier (cf. Eq. IV.1). The numerically found solutions of Eq. IV.3 are shown in Fig. IV.13 for a case where the product $\sqrt{1+\alpha^2}\kappa\tau_e$ was equal to about 2.44, which leads to multiple solutions for certain feedback phases (multiple solutions exist if the value of the product is > 1). Frequency hopping may be observed anywhere in the region with multiple solutions but occurs most likely close to the lower angular point if the phase of the feedback is monotonically increased from 0 to π as indicated in Fig. IV.13.
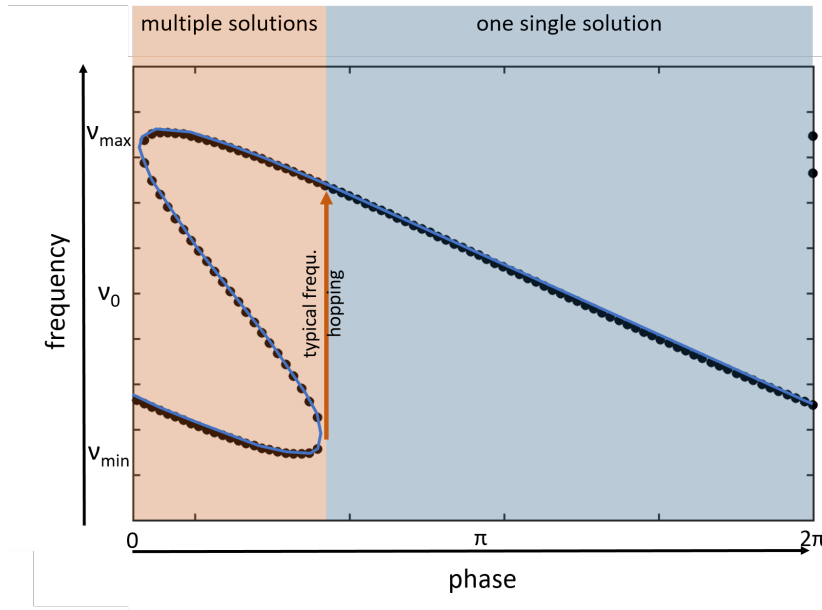
Figure IV.13 – Plot of change in laser frequency for varied feedback phase.

The numerical solution of Eq. IV.3 was fitted to the measured frequency drift (see Fig. IV.12(a)) by optimization of the parameter R_e and using reasonable values for the other parameters that are unknown and determine κ (e.g. α - the line-width enhancement factor, or R_s the reflectivity of the seed laser cavity). The measured and simulated evolution of the seed laser frequency shown in Fig. IV.14 are in good agreement. The quasi-periodic frequency hopping was accurately reproduced in amplitude and periodicity.

The optical isolation in the experimental setup was increased after the study of this effect. Following the simulation results, it was estimated that frequency hopping, related to the bi-stability of $\Delta\nu(t)$, can be avoided for an increased optical isolation of about 63 dB ($\kappa \propto \sqrt{R_e}$). The change in frequency would be below 10 MHz (roughly corresponding to the detection limit of the used setup) for an optical isolation increased to 73 dB. The experiments were repeated after adding an additional optical isolator leading to a total isolation better than 75 dB and no effect on the seed laser frequency was detectable with the used Fabry-Perot spectrum analyzer.

These investigations show that very high optical isolation has to be used to preserve the narrow spectral width of the MO in a QCW coherent beam combining setup. The use of three optical isolators makes the setup bulky and costly. The sensitivity to optical feedback could be reduced in an integrated optical setup (to minimize $\tau_e(0)$), by increasing the reflectivity R_s of the seed laser and by further improvement of the AR coatings of the tapered amplifier (to reduce R_e). Furthermore, small perturbations of the seed laser frequency in the range of 80 MHz are not necessarily a problem for stable coherent beam combining in QCW mode as the corresponding coherence length is still in the order of 1 m, but is critical for applications requiring a stable frequency [Albrodt 19b].
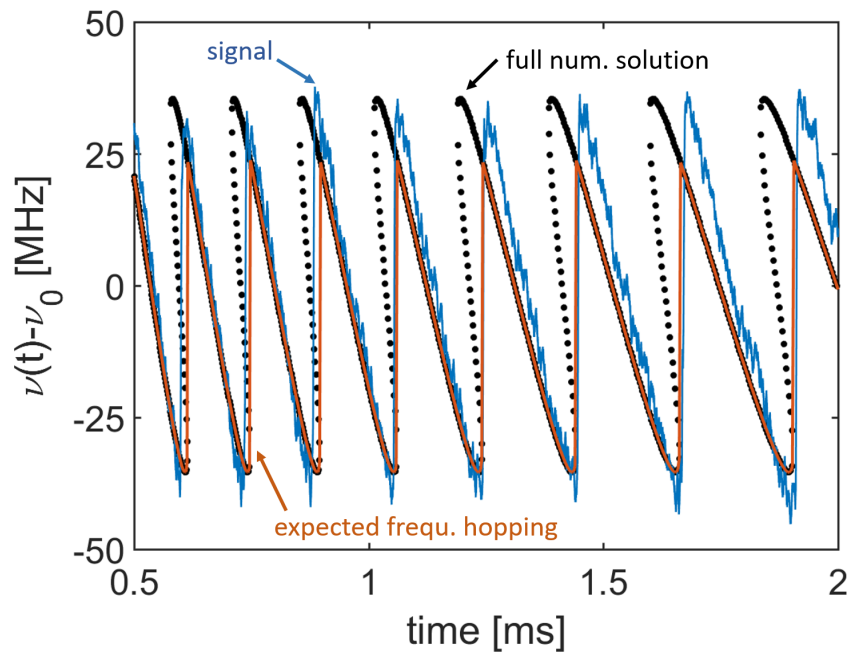
Figure IV.14 – Measured signal (blue), the calculated solutions (black dots) and the expected evolution of the laser frequency with frequency hopping in the multi-stable regime (orange). The optical isolation was 55 dB for this experiment. An ELoD2 (4 mm taper) amplifier was used. $I_{rw} = 400$ mA, $P_{in} = 20$ mW. The used simulation parameters were: $\alpha = 5$, $R_s = 0.01$, $R_e = 9 \times 10^{-10}$, $\tau_e(0) = 10$ ns, $\varphi(t)$ was taken from Fig. IV.8 at $I_{tp} = 13$ A. This corresponds to $\sqrt{1 + \alpha^2}\kappa\tau_e = 2.44$

1.4 Demonstration of QCW coherent beam combining

Coherent beam combining of four tapered amplifiers (all ELoD2 4mm taper) was demonstrated in QCW regime. The chosen pulse duration was 2 ms and the duty cycle was 10% (50 Hz repetition rate). The phase control is discussed below and the experimental results are summarized after that in terms of power and combining efficiency, beam quality and stability.

Phase control   A simplified version of the hill-climbing algorithm was used for the phase control in QCW mode. Figure IV.15 illustrates the approach of the phase control. The hill-climbing algorithm was triggered to the pulse-train and only a single step for the current into one amplifier was done per pulse. The step was applied after 50% of the pulse duration. The power was measured with a photodiode a few μs before and after the hill climbing step in order to measure if the power is increasing or decreasing and the *direction* of the adjustment of I_{rw} was changed if the power was decreasing. Steps of 5 mA were used at the beginning of the optimization and steps of 0.5 mA were used when the current was already close to the optimum value ($\pm$ 35 mA corresponds to a π phase-shift). The convergence criterion was linked to the difference of the two power-measurements and a defined threshold value. The algorithm optimized this way first the current into the RW of A_2 (cf. Fig. IV.2), then similarly for A_3 and finally for A_4. This procedure was repeated in a loop continuously. The rise time of the power was typically below 5 s.
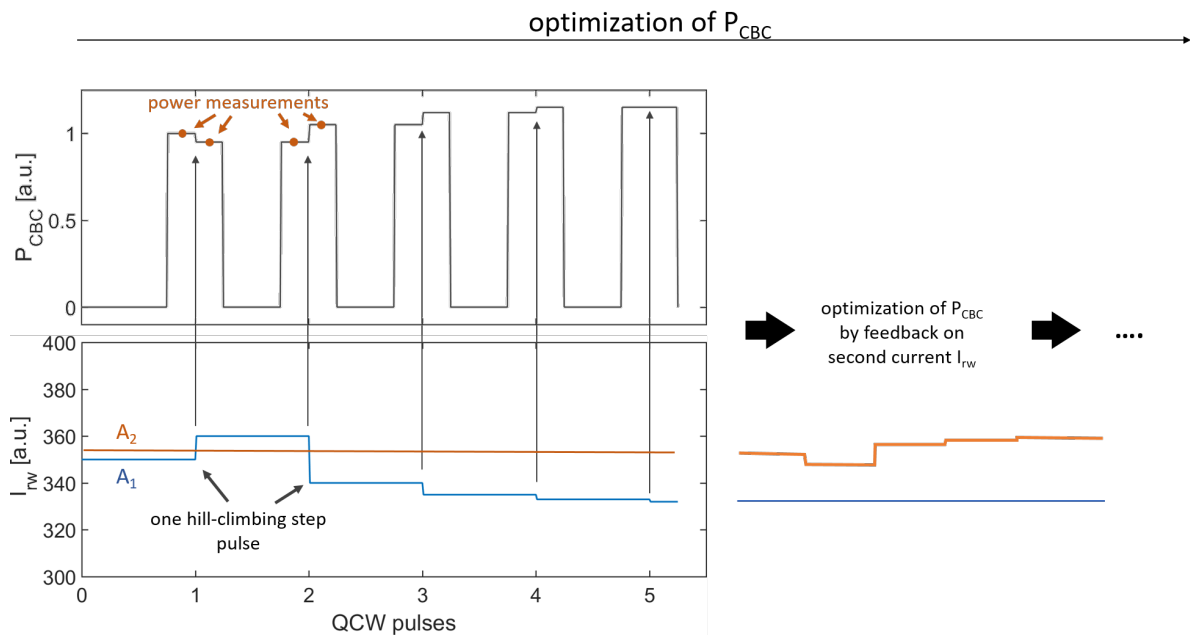
Figure IV.15 – Simplified visualization of the phase control in QCW mode. Only one hill-climbing step for only one amplifier per pulse was used. The currents into the amplifiers $A_{2\text{-}4}$ were optimized sequentially.

Power and combining efficiency   The combined power P_{CBC} and the combining efficiency were measured in QCW operation at four different current levels ($I_{tp} = 10\text{-}14.5$ A). Operation at currents above 14.5 A was unstable as the hill-climbing algorithm was disturbed by the degraded power stability of the individual amplifiers (cf. Fig. IV.11). Both the values for coherent superposition of two amplifiers (CBC of A_1 and A_2, cf. Fig. IV.2) and for coherent superposition of all four amplifiers were measured and are summarized in Table IV.1 below.

The values for coherent beam combining in CW regime are given as a point of reference. The experimental results lead in terms of power and combining efficiency to the following conclusions:

Table IV.1 – Measured combined power P_{CBC} and combining efficiency for coherent superposition of two (A_{1+2}) and four ($A_{1+2+3+4}$) amplifiers at different current levels. (Bias conditions for all measurements: P_{in} = 20 mW, I_{rw} = 300-400 mA, T = 25°C, QCW: 2 ms, 10 % duty cycle).

| | QCW | | | | CW | |
| | 2 amplifiers | | 4 amplifiers | | 4 amplifiers | |
I_{tp} [A]	P_{CBC} [W]	η_{CBC} [%]	P_{CBC} [W]	η_{CBC} [%]	P_{CBC} [W]	η_{CBC} [%]
8	-	-	-	-	10.8	72
10	9.77	84	16.8	71	14.4	71
12.3	12.4	85	20.4	68	**16.9**	**71**
13	12.7	81	21.7	69	-	-
14.5	13.7	79	**22.7**	**64**	-	-

- The maximum output power of 22.7 W (QCW, 10% duty cycle) is to date the highest power reported for coherent superposition of tapered lasers and amplifiers. The coherently combined power per emitter is for the first time >5 W which underlines the significant power advantage in using tapered amplifiers for coherent beam combining architectures when compared to similar work with single mode SCOWAs [Creedon 12].

- QCW operation allowed to scale the output power from 16.9 W (CW) to 22.7 W, which corresponds roughly to a 1.3-fold increase. Although this is already significant, further power scaling by QCW operation seems to be achievable with optimized tapered amplifiers. Resonance effects in the amplifiers linked to an un-ideal AR coating of the front facet were limiting the current into the tapered section to 14.5 A which was only slightly higher than the highest current used in CW operation (12.3 A). Operation at higher currents in the order of 16-20 A with optimized reflection AR coatings on the amplifier may enable output powers > 30 W.

- The combining efficiency in QCW and CW mode was comparable and in the order of 70% for coherent superposition of all four amplifiers at moderate drive currents (10-12 A). This shows that coherent beam combining in QCW mode can be as efficient as in CW mode by careful matching of the turn-on dynamics (piston-phase drift and wandering astigmatism) in between the different devices. The combining efficiency was >64% at the highest power, which can be attributed to the beam quality degradation at high bias. Coherent superposition of only two amplifiers yielded however close to 80% combining efficiency at the highest operating current, which underlines again the advantage of the ELoD2 epitaxial design in terms of beam quality and combining efficiency.

Beam quality   The beam quality was investigated by an ISO compliant caustic measurement (see Fig. IV.4 (a)) at the highest output power (22.7 W). The beam profiles were measured 1 ms after the start of the pulse in order to limit the influence of the wandering astigmatism (cf. Fig. IV.6) on the measurement. The M^2 beam propagation factors, evaluated by numerical fitting, were found to be 1.2 ± 0.1 in FA and 4.7 ± 0.4 in SA. The evaluated second moment beam radius in SA is in some cases slightly off the theoretical fit, which can be attributed to measurement errors[1]. The central lobe power content was found to be 92%, which is an excellent value and comparable to previous experiments in

---

[1]It is quite challenging to measure the beam caustic in QCW mode accurately along with a CCD sensor as the maximal exposure time is limited by the pulse duration (here maximum exposure 1 ms) on the one hand and by the speed of the camera (minimal exposure 50 μs) on the other hand.

CW mode (cf. chapter III section 3). The central lobe power was consequently >20 W (QCW, 10% duty cycle), which is to date the highest central lobe power from a single-frequency laser system based on tapered lasers or amplifiers.
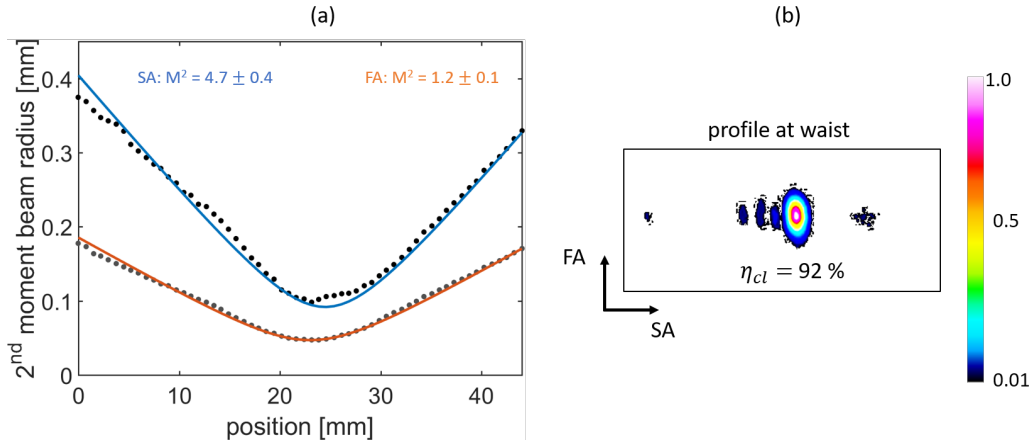
Figure IV.16 – (a) Measured caustic in SA (blue) and FA (orange). The M^2 beam propagation parameters were evaluated by numerical fitting. (b) Measured beam profile at waist. (QCW, 2 ms pulses at 10% duty cycle, I_{rw} controlled actively in the range 300-400 mA, $P_{in} = 20$ mW. $I_{tp} = 12.3$ A)

Stability The stability was investigated by measuring the temporal pulse envelope (minimum and maximum value at each instant) and the average temporal pulse form over one minute. Figure IV.17 shows three exemplary results at different current levels. The temporal pulse shape of the coherently combined beam was nearly rectangular at 10 A with only minor power fluctuations (peak-to-valley fluctuation in the order of 7% of the average power). The temporal pulse shape of the combined power showed quasi-periodic parasitic oscillations at higher bias (see curve for 12.3 A and 14.5 A). These oscillations were attributed to the parasitic resonances in the individual amplifiers and not caused by temporary mismatched piston phases. The increasing period of the oscillations matched the previously described observations (cf. IV.11). The peak-to-valley power fluctuations in the stabilized power level were in the order of 12.5% of the average power at 14.5 A and mostly caused by the oscillating power of each amplifier. This was problematic, as the high power fluctuations disturb the phase matching algorithm and limited the maximum operating current to 14.5 A. Coherent beam combining at even higher bias was clearly unstable. These oscillations are indeed much higher than the small residual power fluctuations for coherent beam combining in CW mode. But the power stability of the average power in QCW mode was also excellent with residual fluctuations in the order of 1% rms (over one minute for $I_{tp} < 14.5$ A).

Conclusions Coherent beam combining in QCW mode was successfully demonstrated at high bias for the first time. The coherently combined power was higher than in any other coherent beam combining setups using tapered lasers or amplifiers. The detailed analyses of the turn-on dynamics revealed a few problematic aspects of the QCW operation of tapered lasers (e.g. the wandering astigmatism within the pulse) that should be addressed in further studies. Tapered amplifiers with a large tapered section (here 4 mm long, 6° angle) performed favorably when compared to amplifiers with smaller tapered sections. Furthermore, parasitic resonances in the amplifier were identified as the physical cause for power instabilities at high bias. Power scaling by QCW operation at high drive currents was limited by power instabilities linked to these effects. Further increase in power seems to be achievable by improvements of the amplifier design, in particular the AR coating at the front facet.
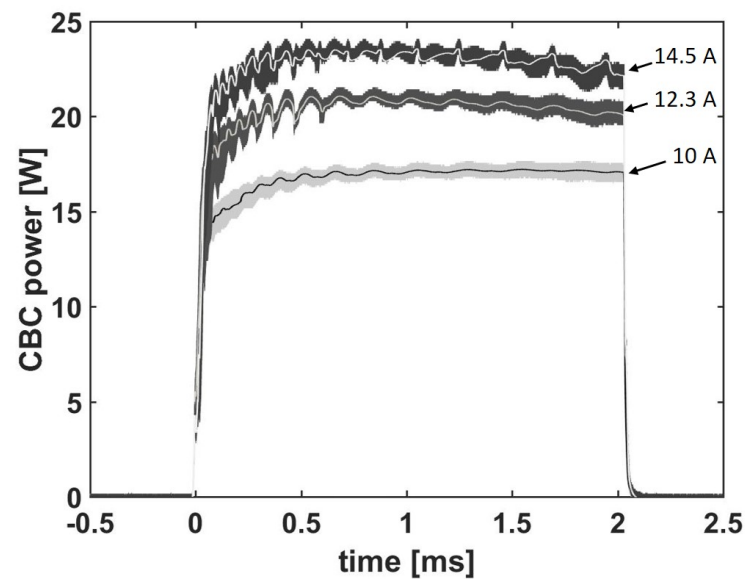
Figure IV.17 – Measured pulse shape at the output of the interferometer at 10 A, 12.3 A and 14.5 A. The pulse envelope is shown in thick lines (1 min integration time) and the average pulse shape is shown with thin lines for each bias. (QCW, 2 ms pulses at 10% duty cycle, I_{rw} controlled actively in the range 300-400 mA, $P_{in} = 20$ mW.)

2 Perspectives for coherent beam combining with nanosecond to microsecond pulse duration

Many applications require much shorter pulse duration than the millisecond-long pulses of the QCW experiments discussed above. Perspectives and preliminary experiments for coherent beam combining of ELoD2 tapered amplifiers with pulse durations in range from 100 ns to 1 μs are discussed in this section. These pulse durations are still quite long compared to the typical carrier lifetime (in the order of a few nanoseconds), so that the experimental principles are similar to the QCW experiments discussed above. It requires nevertheless a few adaptions to the experimental setup that will be discussed in section 2.2. Note that systems based on tapered amplifiers with pulse duration of a few nanoseconds [Vu 14] or even the picosecond-range also exist [Schwertfeger 11], they however require specific device design and advanced pulse drivers and such short pulse durations are not required for the applications discussed below.

High power pulsed diode laser sources are in demand for remote sensing applications in the field of atmospheric lidar (light detection and ranging) techniques with different requirements regarding wavelength and pulse energy [Victori 19]. The advantages of diode lasers in this context are the compactness, low maintenance and high repetition-rate. In many cases however, the available power from a single emitter is not sufficient to reach the required pulse energy. Coherent beam combining of pulsed high brightness tapered amplifiers may be a promising approach to increase the available power from diode laser based sources. The focus of these preliminary investigations lied on a currently planned design of a microsecond range amplification stage for future applications in a differential absorption lidar (DIAL) system for water vapor profiling. The motivation for this application and a few general principles of a DIAL system are discussed below.

2.1 Requirements for laser micro-differential-absorption lidars

Motivation   Some of the most dramatic consequences of climate change are linked to the increasing water vapor concentration in the lower and middle troposphere. The consequences are numerous and observable on both short and long timescales. Extreme weather events like spontaneous heavy rainfall leading to dangerous flash floods can for example be attributed to abnormal high water vapor concentrations [Stott 16]. Long timescale trends, like the dependence of arctic sea-ice melting on low altitude humidity were also observed [Serreze 12]. In both cases, it is important to have access to measurement data of the water vapor concentration in order to predict extreme weather events more precisely or in order to improve large scale climate models. The problem however is that the water vapor concentration is currently monitored by satellite sensors with insufficient temporal and spatial resolution. Atmospheric lidars can deliver additional data with high temporal and spatial resolution and help to improve the understanding of extreme weather events and climate change in general.

Principle   A differential absorption lidar (DIAL) consists in probing the atmosphere with a narrow-line-width laser pulse exactly on a water-vapor absorption line (λ_{on}) and comparing the recorded signal with a reference signal for a second laser pulse with a wavelength λ_{off} that is just slightly off the absorption line. The difference of the recorded signals can then be attributed to molecular absorption. Water vapor has many absorption lines in the infrared. In the literature, the 828 nm line has for example been used in a diode laser based field-deployable DIAL system ($\lambda_{on} = 828.2$ nm and $\lambda_{off} = 828.3$ nm), which is shown in Fig. IV.18 [Spuler 15]. Two DBR lasers were used for the on and offline signals, which were amplified in a pulsed tapered amplifier. A tapered amplifier was used as an excellent beam quality is required in this context. The pulse duration was 0.9 μs at 9 kHz repetition rate and 5 μJ pulse energy (corresponding to roughly 5 W peak power). The integration time per measurement was 10 min. The advantage of this concept is the simplicity and robustness of the laser source especially when compared to Ti:sapphire lasers [Ertel 05] that are commonly used in other water vapor DIAL setups.
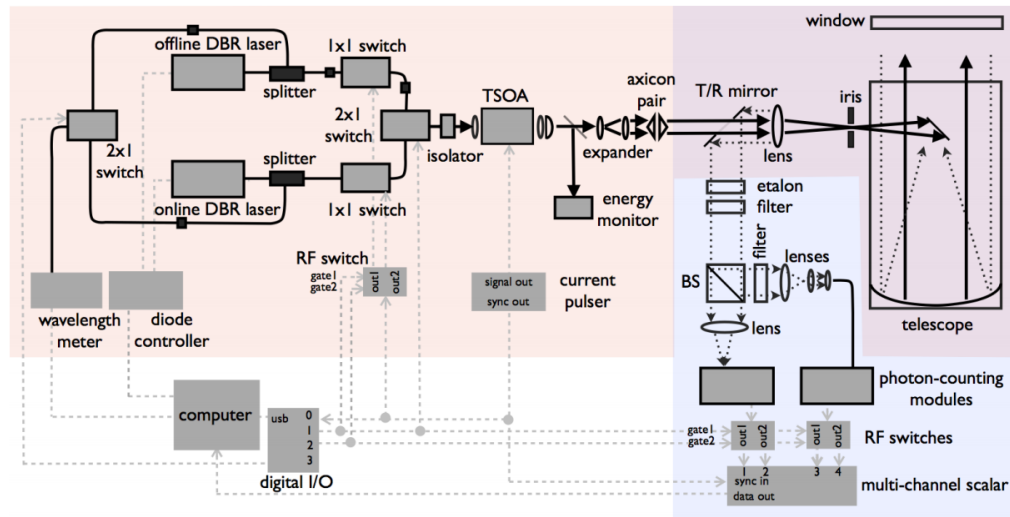
Figure IV.18 – . Schematic of a diode laser based water vapor DIAL system. BS is the beam splitter, T/R is transmit/receive, and I/O is input/output. A tapered amplifier (TSOA) is used to reach the required power level. Taken from [Spuler 15].

Potential benefit from CBC   How could coherent beam combining of tapered amplifiers further improve the performance of such setups? Coherent beam combining and using optimized tapered-amplifier designs may enable significantly increased pulse energy. Taking the QCW coherent beam combining experiments discussed in the previous section as a reference, pulse energies > 20 μJ (20 W, 1 μs) seem to be a realistic estimate for coherent beam combining of four high brightness tapered amplifiers with μs-range pulse duration. This would allow to increase the measurement range or to reduce the integration time significantly. While long integration times are acceptable for stationary DIAL systems, short integration times are strictly required for airborne DIAL systems where an airplane is used to measure the water vapor concentration in a certain area (e.g. for the survey of a cyclone). Airborne water vapor DIAL systems are therefore currently based on other more powerful but also more complex and maintenance intensive laser systems (Ti:sapphire and alexandrite lasers or optical parametric oscillators). In consequence, there are only a few airborne water vapor DIAL systems available which is currently not sufficient for the intensive study of specific extreme weather events.

Three main tasks of research and engineering concerning the semiconductor amplification stage are necessary for the design of such systems: First, coherent beam combining with pulse micro-second pulse duration has to be investigated and demonstrated. Second, the wavelength has to be adapted from currently 976 nm to 828 nm or any other water-vapor absorption line. And finally one has to transfer the coherent beam combining experiments from the laboratory to a robust setup capable of autonomous operation on an airplane. Here in this work, preliminary experimental investigation of only the first task (CBC with ≈ 1 μs pulse duration) are discussed and the other points will be addressed in future work.

2.2   Experimental setup for the short-pulse operation of tapered amplifiers

The experimental setup used for QCW coherent beam combining with the ELoD2 tapered amplifiers was adapted for operation with shorter pulse duration. The ELoD2 4 mm taper design (cf. chapter II) was used. The seed laser, the current into the ridge waveguide remained in CW mode and only the current into the tapered section of the amplifier was pulsed (as in QCW). The pulse driver has to be located near the tapered amplifier in order to limit the rise time of the electrical current. As shown in Fig. IV.19, the pulse driver was placed directly above the tapered amplifier and a short (5 cm) low impedance copper strip-line cable was used for the pulsed current I_{tp}. A commercially available ultra compact pulse driver capable of delivering currents up to 50 A with 8 ns to 10 μs pulse duration was

used and was controlled by a programmable unit. The strip-line was soldered to the electrical contact of the tapered amplifier (p-side) and to the copper heatsink (n-side). Active temperature control with a Peltier element was necessary even for low pulse repetition rates as the RW was operated in CW mode here. The optics used for coupling and collimation were identical to those used in the previously discussed experiments. The lateral footprint of the setup was 4.4×7.3 cm^2.
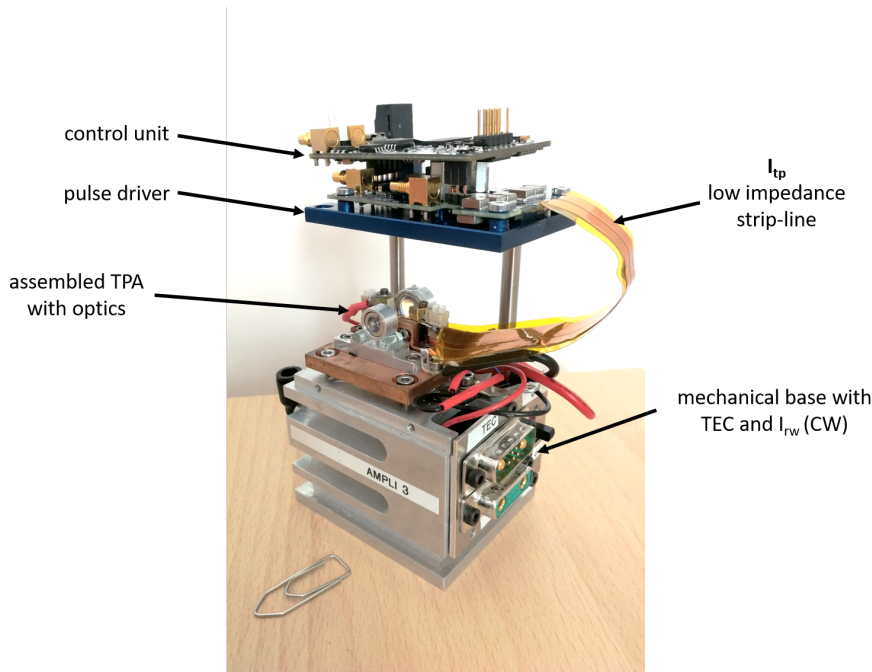
Figure IV.19 – Photograph of a mounted ELoD2 tapered amplifier with optics for coupling and collimation, mechanical mount for temperature control and the connected pulse driver for short pulse operation of the tapered section. The pulse driver (Picolas LDP-V 50-100) is controlled by a programmable control unit (Picolas PLCS-21) and connected with a low-impedance copper-strip-line to the tapered amplifier.

2.3   Preliminary experimental investigations

Most of the dynamic effects in QCW mode (turn-on dynamics) discussed previously were related to temperature effects on a millisecond-timescale. The target of the preliminary experiments described below was to investigate if similar effects are also observable on a microsecond-timescale, where temperature effects are expected to play a less important role.

Power and beam quality   The optical output power and beam quality was investigated for one tapered amplifier in pulsed operation (1 μs, 1 kHz). The temporal pulse envelope was measured with a fast photodiode for a few different drive currents as shown in Fig. IV.20 (a). The measured peak power was in the range from 1 to 4 W (thus pulse energies from 1 to 4 μJ). Unfortunately, there was an experimental problem with the current-monitor port of the pulse-driver, so that value of the numerical value of the current into the tapered section remained unclear. The devices were therefore operated at moderate bias conditions (corresponding to 1-4 W output power) only in order to avoid un-intentional device damage. The rise time of the current into the amplifier was in the order of 100 ns. Minor residual oscillations of the optical power were measured within the first 200 ns of the pulse, and after that the optical output power was stable. The beam profile at waist was measured with a CCD camera and is shown in Fig. IV.20 (b). As the shortest integration time of the used CCD sensor (Dataray Inc. WinCamD) was in the order of 50 μs, it was not possible to measure dynamic changes of the beam profile at waist during the pulse. The measurement given in Fig. IV.20 (b) corresponds to the average

pulse shape averaged over 10 consecutive pulses (10 ms integration time). It has to be investigated in detail if a dynamic change in the beam shape is observable on a μs time-scale, which was not possible withing these preliminary investigations. The central lobe power content was $> 70\%$ which was lower than for measurements at similar power in QCW or CW operation ($> 85\%$ central lobe power content, cf. section II.3). The slow axis beam profile (Fig. IV.20 (c)) showed indeed several side lobes contributing to the decreased central lobe power content. The beam quality in pulsed regime is currently investigated in details as it remained unclear to this point if the long integration time of the CCD sensor results in significant measurement errors of the central lobe power content.
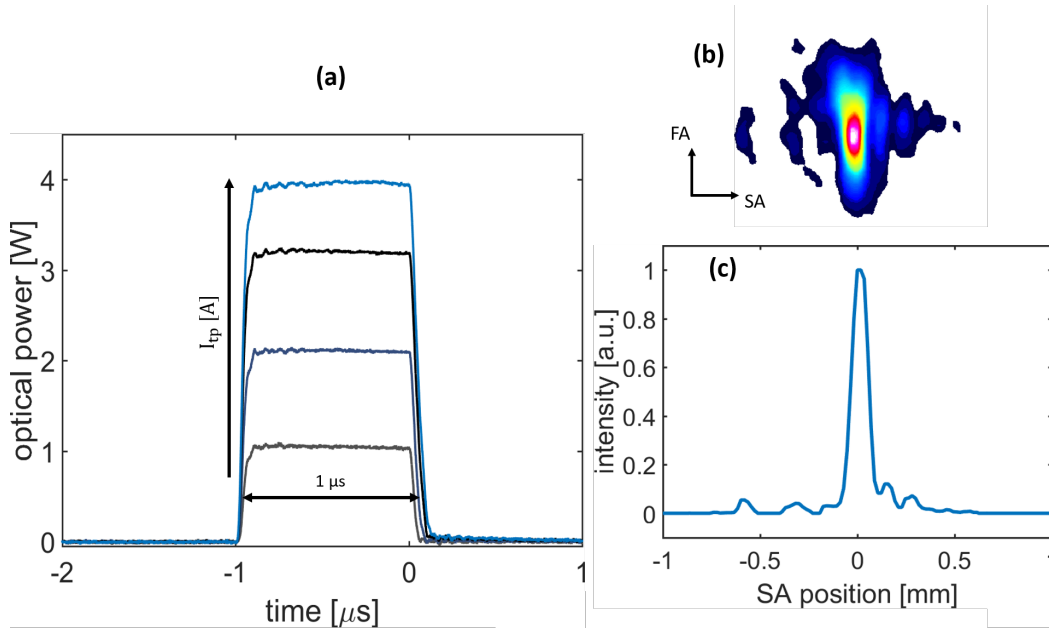
Figure IV.20 – (a) Measured temporal pulse shapes for different drive currents I_{tp} into the tapered section. (b) Measured beam profile at waist (astigmatism corrected) for the highest current into the tapered section on the left. (4 W peak power). (c) Slow axis intensity profile of the beam shown above. The pulse duration was 1 μs and the repetition rate was 1 kHz. $I_{rw} = 350$ mA, $P_{in} = 20$ mW, $T = 31°$C. An ELoD2 tapered amplifier was used (4 mm taper design).

Piston phase   The piston phase drift was investigated similarly to the measurements in QCW regime (cf. section 1.2.2) in a simple Mach-Zehnder interferometer (see. Fig. IV.21 (a)). The measured piston phase drift is shown for two different pulse-energy levels in Fig. IV.21 (b). The phase drift was quasi-linear over 1 μs and increased with the current into the tapered section. The amplitude of the variation was in the order of 0.8 π over 1 μs at 3 W output power. The measured phase drift in this μs-range experiment was much faster compared to the phase drift in QCW regime that was described by the fit-function IV.1 on page 116 (cf. also Fig. IV.8). This was evidenced by comparing the measured data to a fictive reference, which was an extrapolation to the microsecond range measurement data (following Eq. IV.1). This results from the significantly reduced rise-time of I_{tp} (here approx. 100 ns rise time, in previous QCW experiments approx. 100 μs), favoring faster temperature variations in the waveguide. It is worth mentioning that a temperature increase of only 1 K in the 4 mm long tapered section corresponds roughly to a piston-phase drift of π. It is therefore likely that an increasing temperature is contributing to the observed phase-shift even if the time-scale is an order of magnitude lower than for the previously discussed experiments. Furthermore, there may be additional physical effects on this timescale that have to be investigated in detail. The phase drift was however as deterministic and repeatable in the μs-range than in the ms-range.

The relative phase difference of two tapered amplifiers was estimated during preliminary coherent beam combining experiments with two pulsed tapered amplifiers in the experimental setup illustrated
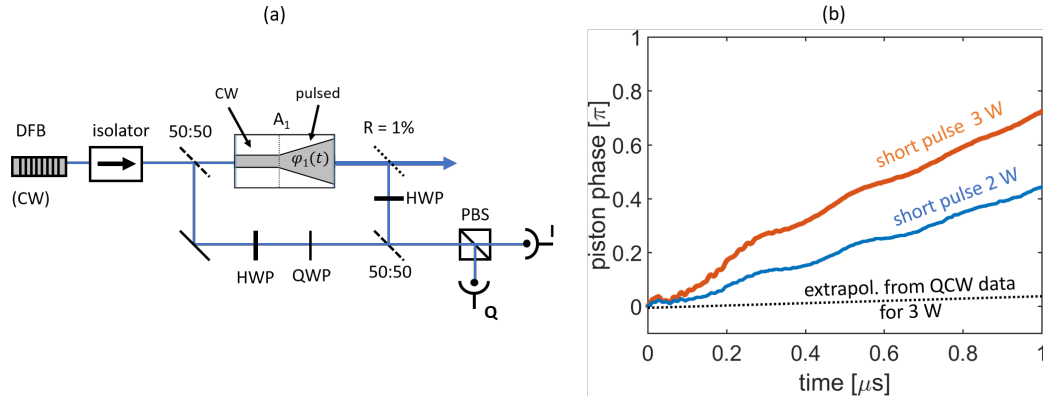
Figure IV.21 – (a) Experimental setup for the measurement of the piston phase drift. (b) Measured piston phase drift for two different pulse energies at the output of the amplifier.

in Fig. IV.22 (a). The two amplifiers A_1 and A_2 were mounted as described in Fig. IV.19 and the pulsed currents into the tapered section were synchronized. The beams were overlapped on the beamsplitter the power at the output of the interferometer, which is as a reminder (cf. Eq. III.2)

$$P_{CBC} = \frac{1}{2}\Big[P_1 + P_2 + 2\sqrt{P_1 P_2} \times C \times cos(\Delta\varphi)\Big], \tag{IV.5}$$

was measured with a photodiode. The relative phase difference in the two arms of the interferometer during the pulse $\Delta\varphi(t) = \varphi_1(t) - \varphi_2(t)$ can be estimated by analyzing the interference signal at the output. This is possible only for relative phase differences far below π and requires the approximation that the powers of the individual beams $P_{1,2}$ and the overlap factor C are considered as constant during the pulse. With these approximations, the relative phase difference between two pulsed amplifiers was found to be below $\pm 0.05\pi \equiv \pm\lambda/40$ at 2 W optical output power as shown in Fig. IV.22 (b). Temporal phase mismatches of this order of magnitude are negligible for the coherent beam combining efficiency. This preliminary investigation confirms that the phase-drift is indeed almost identical between independent amplifiers with independent pulse-drivers on a microsecond timescale. Further investigations for shorter and longer pulse durations and operation at higher currents are currently in progress.
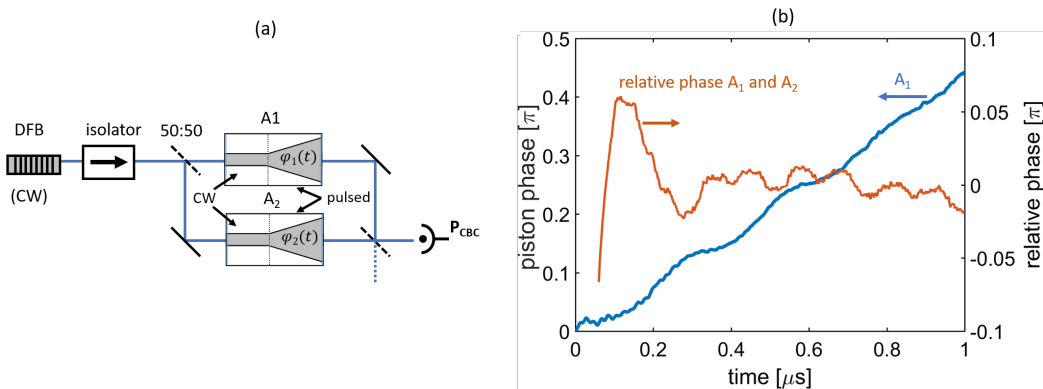
Figure IV.22 – (a) Experimental setup for a preliminary coherent beam combining demonstration of two tapered amplifiers. (b) Piston phase drift for A_1 (taken from Fig. IV.21 (b)) and measured relative phase difference of the two amplifiers for 2 W optical output power per emitter.

Combined power and combining efficiency   The current into the ridge waveguide of A_2 was then optimized manually for maximizing the output power. Coherent beam combining of the two amplifiers

with 2 W output power per emitter yielded 2.8 W as shown in Fig. IV.23, which corresponds to roughly 70% combining efficiency. The combining efficiency was not limited by temporal-phase mismatches but by a poor spatial overlap factor of the beams in this preliminary experiment. The combining efficiency during the pulse evaluated as $\eta_{CBC}(t) = P_{CBC}(t)/(P_1(t) + P_2(t))$ was nearly constant for 200 ns < t < 1μs. The slightly lower combining efficiency in the first 200 ns of the pulse was attributed to un-optimal synchronization of the pulse drivers. These results were achieved without automatic phase control (the current into the RW of A_2 was optimized manually) and the stability of the setup was nevertheless sufficient for basic experimental investigation. This shows that coherent beam combining with pulse durations in the order of 1 μs can be as straightforward as in the long-pulse millisecond-regime (cf. section 1). A phase control within the pulses seems to be not necessary and it appears to be sufficient to optimize the average output power with a basic hill-climbing algorithm.
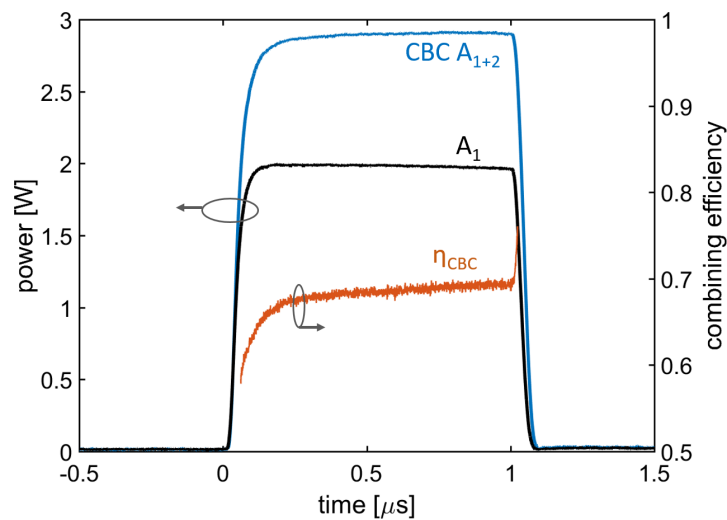
Figure IV.23 – Measured temporal pulse profile for one individual amplifier (A_1 - black line), for the coherently combined beam at the output of the interferometer (CBC A_{1+2}) and evaluated combining efficiency during the pulse (orange).

Perspectives   The first results on coherent beam combining with pulse durations in the μs range are promising as it has been shown that the dynamics in the device are deterministic and very similar to previous observations on a ms-timescale. Further increase in power by operation at higher currents and by combining four amplifiers is currently sought. The target of the ongoing studies is to validate the experimental approach for efficient coherent superposition at high powers in this laboratory-scale proof-of-principle experiment. After that, the next steps would be the design of compact and robust setup, similar to the setup discussed in III.4, and the transfer to 828 nm for potential future applications in DIAL systems. Furthermore, operation with pulse durations below 100 ns is also planned for further peak-power scaling and other applications in the context of atmospheric lidars.

Conclusions and Perspectives

The coherent beam combining experiments demonstrated in this work are summarized and put in relation with the state of the art below. After that, potential pathways for improvement of such systems and methods for further power scaling are discussed. Finally, perspectives for the application of high brightness laser systems based on coherent beam combining of semiconductor amplifiers are pointed out.

Summary of the coherent beam combining results

This work targeted the development coherent beam combining setups that remain simple but enable high output powers. Phase-locking in a MOPA configuration, was used to ensure a high degree of coherence at high powers. Tapered amplifiers were used, as they are by far the brightest emitters available and allow to achieve high powers with a reasonable number of channels and are therefore the ideal amplifier for the development of simple coherent beam combining setups. Different designs of cutting-edge tapered amplifiers, developed and fabricated at the Ferdinand-Braun-Institut (Berlin, Germany), were investigated in terms of power, efficiency, beam quality and noise properties in order to identify the best choice for high power coherent beam combining (cf. chapter II). Experimental demonstrations of coherent beam combining in continuous wave regime with different designs of cutting-edge tapered amplifiers were discussed in chapter III. Additionally, the realization of a compact and modular experimental setup using commercially available off-the-shelf amplifiers and optical elements only was described. It has been shown that coherent beam combining of tapered amplifiers in a MOPA configuration is straightforward and that simple hill-climbing algorithms, adapted for operation on embedded systems, allow to achieve excellent long-term stability. After that, similar approaches were used to investigate coherent beam combining for pulsed operation of the amplifiers (cf. chapter IV). Coherent beam combining in the quasi-continuous-wave regime was successfully demonstrated and preliminary experiments for the operation at shorter pulse duration were described.

Even though the general approach of the coherent beam combining experiments followed the same general principles outlined above, each experiment was nevertheless slightly different as different amplifiers were used and the number of the channels was slightly varied. The key-figures of the different experiments are summarized in Table V.I. The overview of the results lead to the following conclusions:

- **The highest coherently combined power in CW** was 16.9 W in a single beam. This is to date the highest power (in CW) for coherent beam combining using tapered lasers or amplifiers. Only four high brightness tapered amplifiers were used which corresponds to 4.25 W combined power per amplifier.

- **The highest coherently combined power in QCW** was 22.7 W in a single beam. The combined power per emitter was > 5 W for the first time in coherent beam combining setup with semiconductor lasers or amplifiers. This is the first demonstration of high power coherent beam combining in QCW mode and a few interesting observations of the turn-on dynamics in tapered amplifiers were made. Further power scaling in QCW seems to be achievable as parasitic resonances in the amplifiers were limiting the maximal operating current in this work.

- **The highest combining efficiency at maximum bias** was 82% (at 12 A) using two tapered

Table V.1 – Overview of the demonstrated coherent beam combining setups in this work. Each row is linked to a data-point in Fig. V.1 by the roman numerals (I-VI) given in the first column. The specified typical PCE do not take the power consumption of the RW section and the DFB seed lasers into account. The specified M^2 beam propagation factors were measured by iso-compliant measurements of the second-moment beam diameters. The overall PCE takes the PCE of the amplifiers and the combining efficiency into account and is given for the full coherently combined beam and for the central lobe power content of the coherently combined beam. All values are given with two significant digits.

	Emitters				CBC - parameters		Beam quality at output				Overall PCE	
	n	type	mode	typical PCE [%]	P_{CBC} [W]	η_{CBC} [%]	η_{CL} [%]	$M_{FA}^2 \times M_{SA}^2$	B^* [MW cm⁻² sr⁻¹]	B^{**} [MW cm⁻² sr⁻¹]	full beam [%]	central lobe [%]
I	2	FBH: Reference TPA	CW	32	9.7	74	80	1.1 x 4.0	230	700	24	19
II	3	FBH: Reference TPA	CW	32	13	65	83	1.1 x 3.5	340	930	21	17
III	2	FBH: ELoD2 TPA	CW	28	10	89	88	1.2 x 4.5	210	730	25	22
IV	4	FBH: ELoD2 TPA	CW	28	17	71	92	1.2 x 4.0	360	1200	20	18
V	4	FBH: ELoD2 TPA	QCW	30	23	64	92	1.2 x 4.7	430	1600	19	18
VI	4	DILAS TPA	CW	28	9.7	66	85	1.8 x 2.7	200	700	20	17

B*: Brightness calculated with ISO-compliant second moment M^2 beam propagation factors
B**: Brightness calculated with estimated M^2 beam propagation factor using the $1/e^2$ beam diameters (not ISO-compliant)

amplifiers with the ELoD2 epitaxial design. Values above 90% were measured at moderate drive currents. The high combining efficiency was linked to the high central lobe power content of the used amplifiers. The combining efficiency was > 71% for coherent beam combining of four ELoD2 amplifiers. The reason for the slightly lower combining efficiency for configurations with more than one combining step is that the beam clean-up leads to additional losses at the second combining step. Furthermore alignment tolerances of the FA collimation were identified as the most critical experimental parameter and was limiting the combining efficiency slightly.

- **The beam quality** of the coherently combined beam was significantly improved when compared to typical beam quality of the used tapered amplifiers. The highest central lobe power content was > 92%. The measured ISO-compliant second moment beam propagation factors were in the order of 1.1 to 1.3 in FA and 3.5 to 4.7 in SA, which are excellent values for high power diode laser systems. The beam propagation factors estimated with the $1/e^2$ beam diameters were close to unity for all systems but are of limited physical significance. It should however be clear that there is still room for improvement of the beam quality and that the output of coherently combined laser systems is not necessarily a diffraction limited Gaussian beam. The central lobe power has indeed a higher spatial quality than the full beam but should not taken as a rigorous synonym for the diffraction-limited power.

- **The highest brightness** was achieved for coherent beam combining of four ELoD2 tapered amplifiers and was 360 MW cm^{-2} sr^{-1} in CW and 430 MW cm^{-2} sr^{-1} in QCW, calculated following Eq. I.2 using the ISO-compliant second moment M^2 values (cf. B^* in Table V.I). This has to be understood as the average brightness over the full second moment beam width of the beam. It is questionable if this definition, even though it is the international standard, makes sense as the second moment beam propagation factors can be significantly increased by comparably small amounts of power in higher order modes. As $B \propto (M_{FA}^2 \times M_{SA}^2)^{-1}$, one can find significantly higher values, up to 1600 MW cm^{-2} sr^{-1} in QCW, using the not-ISO-compliant definition of the $1/e^2$ beam propagation factors (cf. B^{**} in Table V.I). Both values for the brightness are specified for all experiments for completeness and to allow comparison with the state of the art of single emitters (cf. I.1 and Table I.1).

- **The overall PCE** taking into account the PCE of the amplifiers and the combining efficiency were in the order of 19 to 25%. This is a major drawback compared to the excellent power conversion efficiency of systems based on incoherently combined broad area lasers (typical PCE > 60%). Furthermore high power fiber lasers pumped by efficient diode lasers are commercially available with kW-level output power, diffraction-limited beam quality and wall-plug efficiencies > 45%[1] Future work on coherently combined semiconductor lasers should target besides the increase of power also the increase in PCE, which is a very important parameter for large scale industrial applications.

Strategies for further improvement of power, beam quality and efficiency will be discussed in the following section. Before that, it is worth comparing the achieved experimental results to the state of the art for coherent combining of semiconductor lasers and amplifiers. Figure C.1 shows the output power as a function of the number of emitters for the systems developed in this work (orange) compared to previous results in MOPA configuration (black) and extended cavity configuration (blue), which were taken from Fig. I.23 (cf. chapter I). The achieved experimental results show by far the highest output power for systems relying on a limited number (< 10) of coherently combined emitters. The power record for coherent beam combining of semiconductor lasers, established by Creedon et al. with 47 coherently combined SCOWAs and 40 W output power [Creedon 12] was not reached in systems relying on tapered lasers. One should however keep in mind that the number of emitters has a major influence on the complexity of the setup. Even though the phase noise in semiconductor amplifiers

---

[1]For example: IPG Photonics YLS-SM 1-10 kW product series (https://www.ipgphotonics.com/en/products/lasers/high-power-cw-fiber-lasers, accessed: 15/10/2019).

is low, there is still a need for an active phase control of each channel, which is not straightforward for a large number of emitters. It makes therefore sense to target a high combined power per emitter, which was with > 5 W more than five-fold increased when compared to coherent beam combining using single mode SCOWAs.
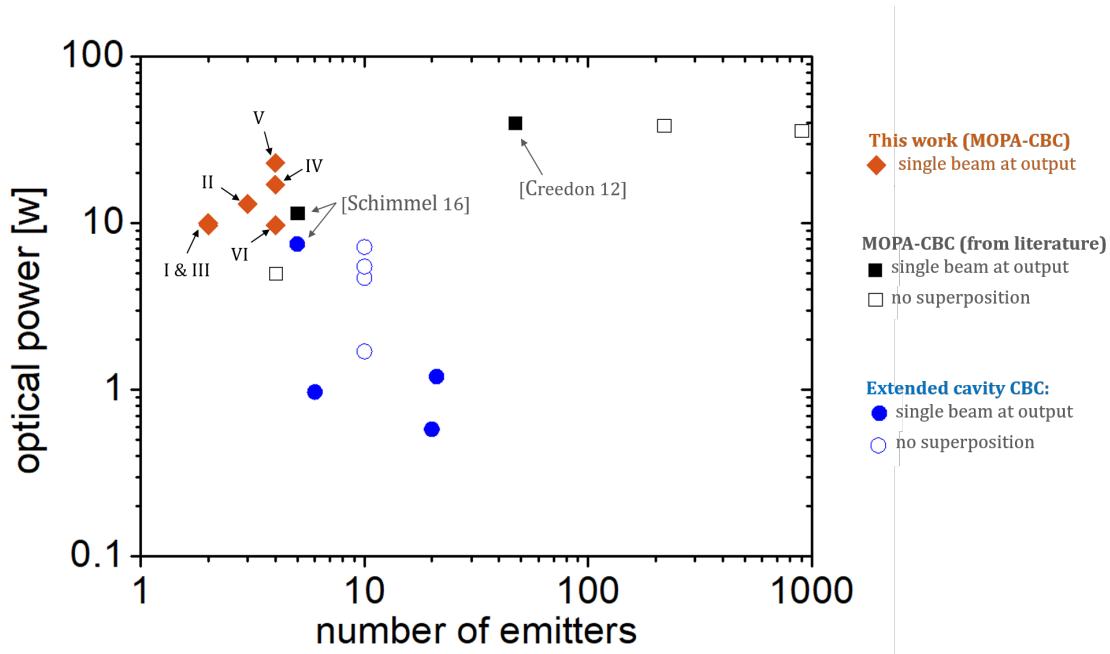
Figure C.1 – Overview of state of the art for coherent beam combining with edge emitting NIR semi-conductor lasers. The experimental results of this work are shown in orange. The other data points were taken from Fig. I.23 in chapter I of this manuscript. The filled symbols represent work, where coherent superposition into a single beam was demonstrated. The key-figures of each experiment are summarized in Table V.1 (see roman numerals).

The single-emitter approach followed in this work allowed to operate the tapered amplifiers at higher currents when compared to similar experiments where a mini-bar of five tapered amplifiers was used [Schimmel 16] (maximum operating current was limited by thermal effects in the bar). The maximum power reached in the minibar experiments was 11.5 W (CW) which is much lower than the power of 16.9 W (CW) reached in this work (cf. Fig. C.1). Furthermore, the architecture based on a mini-bar of amplifiers was quite complicated, bulky and required custom mounting and customized diffractive optical elements. The architectures studied in this work are modular, simple and rely on standard optical elements only.

The simplicity of the setups, the high power and brightness and the good stability of the coherent beam combining architectures discussed in this work underline that coherent beam combining is a promising approach for the development of new high brightness laser systems based on semiconductor emitters only.

Perspectives

Compact setups One major advantage of semiconductor lasers and amplifiers is the compactness of the emitters. The footprint of most architectures used for coherent beam combining of semiconductor lasers and amplifiers in the past was however quite large [Lucas-Leclin 19]. This was also the case in the initial experiments described in this work, where the footprint of the interferometer was in the order of 2 m^2. As the proposed architectures is however particular simple, it was possible to reduce the size of the coherent beam combining setup dramatically to the approximate lateral dimensions of an standard A4 page ($\approx 20{\times}30$ cm^2 - cf. Fig. C.2). Further miniaturization is possible and may lead to ultra compact coherent beam combining interferometer with a lateral footprint in the order of the size of a standard credit card ($\approx 5{\times}8$ cm^2). The miniaturization however requires advanced micro-positioning technology. Research-groups at the Ferdinand-Braun-Institut have successfully demonstrated several different high power ultra-compact laser modules for incoherent superposition of diode lasers[1] and modules for coherent beam combining could be realized with similar technology. Ultra compact modules would also be beneficial as a fully micro-integrated multi-arm interferometer will automatically further decrease the phase-noise in the system. An important issue to address regarding the potential for miniaturization of the setup is however the encountered experimental problem regarding optical feedback from the tapered amplifiers. Improved design of amplifiers and seed source should reduce the required isolation levels.

A compact and robust setup for a CBC-interferometer with about four tapered amplifiers could be easily implemented in experimental setups where tapered amplifiers are commonly used (e.g. SHG light sources based on a MOPA NIR pump sources [Jechow 10], amplification of narrow-line-width signal for quantum technology [Schkolnik 16] etc.) in order to increase the output power by a factor of 3-4. Furthermore, a compact setup with coherently combined tapered amplifiers in an interferometer with balanced optical path lengths could also be used as a high power amplification stage for tunable seed lasers with narrow spectral line-width. High power tunable laser sources are required in the field of absorption spectroscopy and biomedical imaging [Coldren 04]. Coherent beam combining is a promising approach to reach a 3-4 fold increased output power when compared to setups where the tunable seed laser is amplified in a single tapered amplifier [Tawfieq 17].

The experimental setups investigated in this manuscript are also transferable to any other wavelength withing the large wavelength-coverage of GaInP and GaInAs based tapered lasers and amplifiers from 630 nm to 1180 nm [Sumpf 18]. A simple coherent beam combining setup is especially attractive for wavelengths in the 6xx nm spectral range, where the highest power per emitter are limited to roughly 1 W.

Improvement of the overall PCE The overall PCE efficiency of the system should be improved in the future by increasing the individual PCE of the emitters on the one hand and the combining efficiency in the system on the other hand. The PCE of the used ELoD2 tapered amplifiers was limited due to a high threshold current. Future device development of tapered amplifiers for coherent beam combining should target an improved PCE of the ELoD2 design by lowering the threshold current while maintaining the excellent beam quality at high bias. Furthermore, improved cooling by p-side down mounting and using larger heat-sinks will increase the PCE slightly by avoiding a thermal rollover. Additional improvement of the combining efficiency in the order of a few percent seem to be achievable by better control of the FA collimation during the alignment process. Altogether, one can expect to increase the overall PCE from currently $\approx 20\%$ to $> 35\%$, which would for example correspond to $> 45\%$ PCE of the tapered amplifiers at high bias and $> 80\%$ combining efficiency. It will however be challenging to achieve even higher overall efficiencies as the PCE of tapered lasers or amplifiers is commonly not as high as for broad area lasers and as the beam clean-up effect inevitably leads to

---

[1]e.g. a compact module for polarization coupling of two high brightness tapered lasers:
https://www.fbh-berlin.de/forschung/forschungsnews/detail/micro-integrated-high-power-infrared-laser-source-for-short-pulse-pumping-applications, accessed 15/10/2019
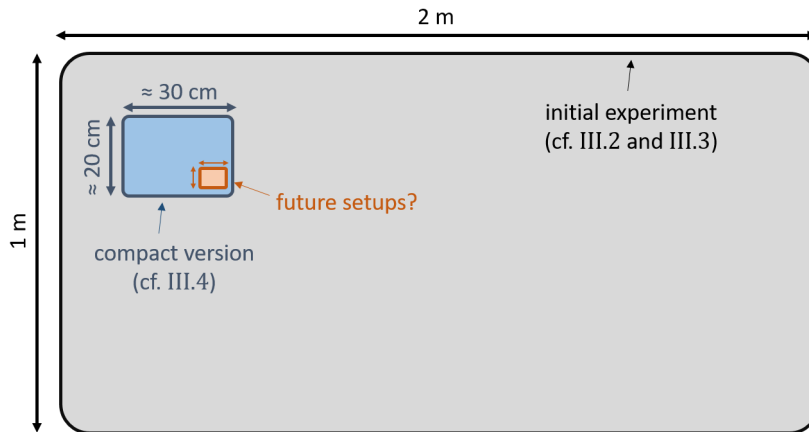
Figure C.2 – Simplified illustration of the lateral dimensions of the coherent beam combining setups studied in this work.

combining losses.

Further power and brightness scaling   The use of more emitters is the most natural approach for further power and brightness scaling. The MOPA approach for phase-locking is extremely robust and can easily be scaled to a larger number of amplifiers if necessary. Tapered amplifiers require typically 10-30 mW of seed power, so that one DBR-TPL (> 5 W) as the seed source of a larger setup would be sufficient to phase-lock a large number of amplifiers. The scaling of the sequential two-by-two filled-aperture superposition of the beams becomes however unpractical for a large number of channels. The number of channels may however easily be increased to 8 as shown in Fig. C.3(a) or to 16 especially if compact modules with 4 amplifiers each are used in a building-block system. Beyond that, it is questionable if the sequential filled aperture combining approach studied in this work is the best choice.
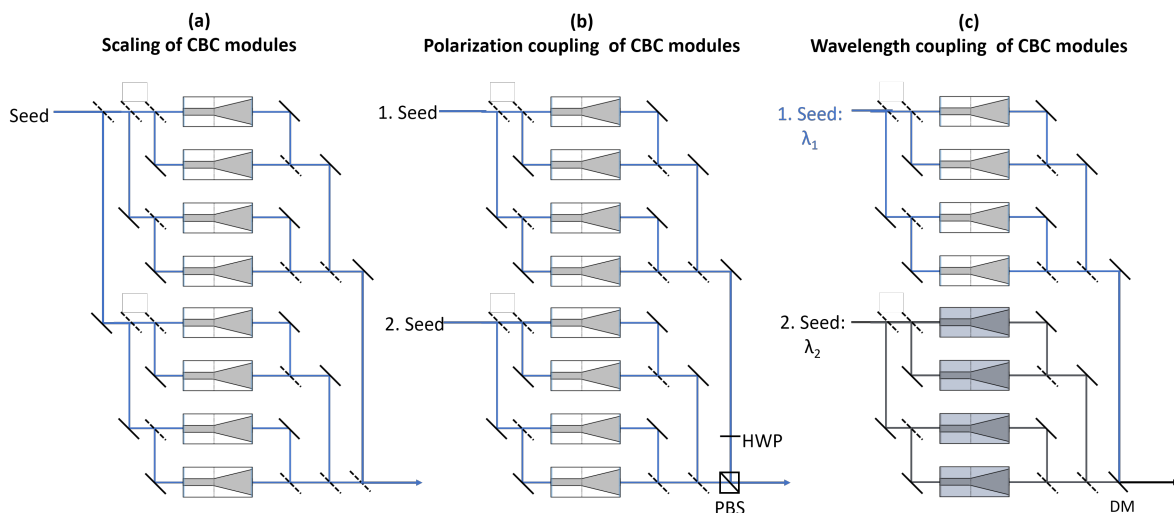
Figure C.3 – Three concepts for further scaling of power and brightness using compact coherent beam combining modules with four tapered amplifiers as the basic building-block. HWP: half-wave-plate, PBS: polarizing-beam-splitter, DM: dichroic mirror.

It is however possible to use coherent beam combining as a tool to increase the power within one linear polarization and one wavelength channel to its maximum in a simple building-block-like setup. The power of several of such coherently combined sub-systems can then be added by incoherent polarization coupling (cf. Fig. C.3(b)) and wavelength coupling (cf. Fig. C.3(c)). While polarization

coupling is limited to one stage where two beams can be coupled, coarse wavelength beam combining is straightforward with more channels. Of course, it is possible to use both approaches in one large setup in order to increase the total number of channels. This way, the power from diode laser based systems can be scaled easily without the need for complex phase-locking methods of a large number of channels as it is sufficient to ensure phase locking in the coherently-combined sub-systems.

These points considered, what would be a realistic scenario based on the experimental results of this work for the realization of feasible setup with 100 W in a single beam with nearly diffraction limited power?

1. Coherent beam combining of 4 ELoD2 tapered amplifiers yielded in about 17 W output power. Extrapolated for a coherent beam combining of 8 channels, one may achieve > 30 W at the output power if the combining efficiency at the additional combining step is > 88%.

2. Polarization coupling of two independent sources with 8 high brightness tapered amplifiers each may enable > 55 W output power if the efficiency of this combining step is > 92% (conservative estimation).

3. An additional wavelength coupling step of two setups build following step 1 and 2 at slightly different wavelengths may finally yield in 100 W output power if the efficiency of the wavelength combining step is > 90% (conservative estimation).

This approach is illustrated in Fig. C.4. Any additional increase of the power by further optimization of the amplifiers, packaging technology and the combining efficiency may enable even higher powers. Furthermore, the use of high power truncated-tapered amplifiers, enabling > 17 W central lobe power per emitter [Wang 13], is one potential pathway for the development of high brightness diode laser systems with output powers far above 100 W.

All things considered, the development of commercial high brightness diode laser systems making use of coherent beam combining appears more realistic and less utopian after this work. To come back to the picture of the marvelous animal, that Germans call "eierlegende Wollmilchsau", one can say that diode lasers may become even more versatile enabled by coherent beam combining.
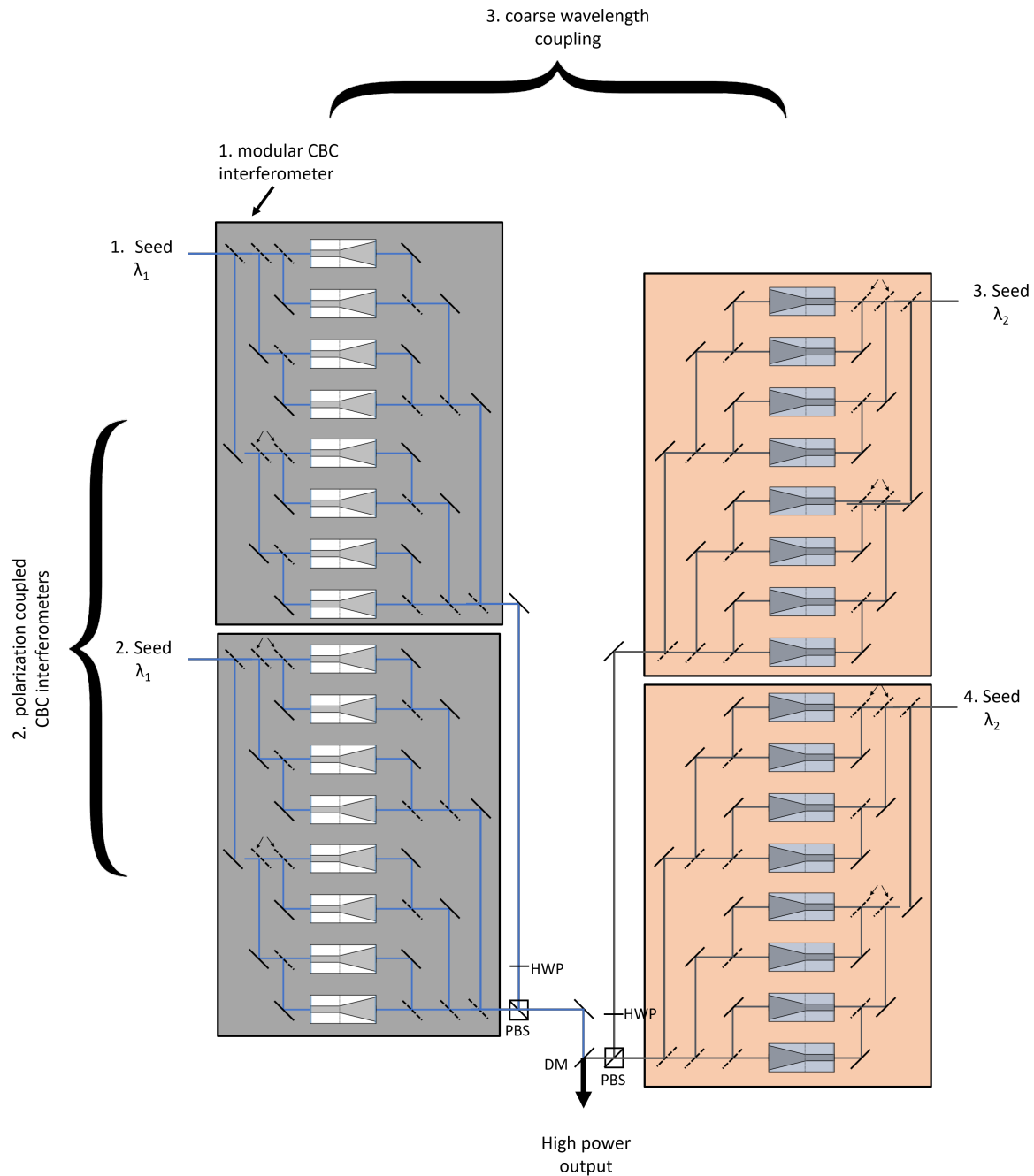
Figure C.4 – Simplified schematic view of a potential experimental setup based on coherent beam combining modules for > 100 W output power. HWP: Half-wave-plate, PBS: polarizing beamsplitter, DM: dichroic mirror.

Annex

Annex A: Hill-climbing algrorithm

The micro-controller based hill-climbing algorithm was based on a periodic dither test. The dither was realized by a small perturbation (e.g. ± 5 mA) of the current into the ridge waveguide. The power at the output of the interferometer was measured and the local slope was evaluated. The hill-climbing step is calculated as a function of the measured slope (similar to SPGD [Redmond 13]). The parameters of the hill-climbing algorithm are listed in table A1. A simplified flow-chart of the algorithm is given in Figure A2. Comments are highlighted in orange.

Table A1 – parameters used in the hill-climbing algorithm

parameter	comment	typical value
$n_{channel}$	number of controlled channels	1-3
ΔI_j	dither amplitude in current loop	-
ΔI_{start}	dither amplitude at start	5 mA
I_{max}	maximum current	400 mA
I_{min}	minimum current	300 mA
I_{jump}	offset corresponding to a π phase-shift	35 mA
η	test factor for avoiding slowly deriving power	0.95
k	gain parameter	2
$P_{j,ref}$	max. power	-
t_{wait}	wait time when system is converged	0.5 s

Start

Initialize
$\Delta I_j = \Delta I_{start}$; $P_{j,ref}$; t_{wait}; I_{max}; I_{min}; I_{jump}; η; k; $n_{channel}$; $n_{iterations}$

parameters defined by user

$t = t_{wait}$

$n = 1$

$n = n + 1$

for n = 1:$n_{channel}$ if n = $n_{channel}$

if $|I_j - I_{max}| < \Delta I_j$ yes $I_j = I_j - 2\,I_{jump}$

if $|I_j - I_{min}| < \Delta I_j$ yes $I_j = I_j + 2\,I_{jump}$

Jump away if too close to min. or max.

PD $P_{j,init}(V_j)$ *first power measurement*

if $P_{j,init} < \eta \cdot P_{j,ref}$ yes $\Delta I_j = \Delta I_{start}$

$P_{j,ref} = P_{j,init}$

dither

PD $P_j^+(I_j + \Delta I_j)$ slope 1: $s_1 = \dfrac{P_j^+ - P_{j,init}}{\Delta I_j}$ if $|P_j^+ - P_{j,init}| <$ noiselevel   yes $s_1 = 0$

PD $P_j^-(V_j - \Delta V_j)$ slope 2: $s_2 = \dfrac{P_j^- - P_{j,init}}{\Delta I_j}$ if $|P_j^- - P_{j,init}| <$ noiselevel   yes $s_2 = 0$

$I_j = I_j + I_{ump}$ yes

$I = I_j - I_{jump}$ no

if $|I_{max} - I_j| < |I_{min} - I_j|$ yes   if $s_1 > 0$ AND $s_2 < 0$ *close to minimum, jump to a maximum (I_{jump})*

no

positive slope   if $s_1 > 0$ AND $s_2 > 0$ yes $I_j = I_j + \Delta I_j \cdot k \cdot \dfrac{s_1}{s_2}$

no

negative slope   if $s_1 < 0$ AND $s_2 < 0$ yes $I_j = I_j - \Delta I_j \cdot k \cdot \dfrac{s_2}{s_1}$

hill-climbing-step

no

converged, go to next channel   yes   if $s_1 = 0$ AND $s_2 = 0$

$\Delta I_j = \dfrac{\Delta I_j}{2}$

no

$s_1 < 0$ and $s_2 > 0$
close to maximum

if $|s_1| < |s_2|$ yes $I_j = I_j + \dfrac{\Delta I_j}{2}\left(1 - \left|\dfrac{s_1}{s_2}\right|\right)$

no $I_j = I_j - \dfrac{\Delta I_j}{2}\left(1 - \left|\dfrac{s_2}{s_1}\right|\right)$

Fig. annex 2 – simplified flow-chart of the hill-climbing algorithm. Taken from [Hamperl 19] and modified.

Bibliography

[Achtenhagen 06]   M. Achtenhagen, A. Hardy, et C. Harder. *Coherent kinks in high-power ridge waveguide laser diodes*. Journal of Lightwave Technology, vol. 24, no. 5, pages 2225–2232, May 2006.

[Albrodt 18a]   P. Albrodt, X. Delen, M. Besbes, F. Lesparre, et P. Georges. *Simulation and experimental investigation of beam distortions in end-pumped laser rod amplifiers*. JOSA B, vol. 35, no. 12, pages 3004–3013, 2018.

[Albrodt 18b]   P. Albrodt, M. Hanna, F. Moron, J. Decker, M. Winterfeldt, G. Blume, G. Erbert, P. Crump, P. Georges, et G. Lucas-Leclin. *Coherent combining of high brightness tapered lasers in master oscillator power amplifier configuration*. In High-Power Diode Laser Technology XVI, volume 10514, page 105140T. International Society for Optics and Photonics, 2018.

[Albrodt 19a]   P. Albrodt, M. T. Jamal, A. K. Hansen, O. B. Jensen, G. Blume, K. Paschke, P. Crump, P. Georges, et G. Lucas-Leclin. *Coherent combining of high brightness tapered amplifiers for efficient non-linear conversion*. Optics Express, vol. 27, no. 2, pages 928–937, January 2019.

[Albrodt 19b]   P. Albrodt, M. Niemeyer, P. Crump, J. Hamperl, F. Moron, P. Georges, et G. Lucas-Leclin. *Coherent beam combining of high power quasi continuous wave tapered amplifiers*. Optics Express, vol. 27, no. 20, pages 27891–27901, 2019.

[Barthelemy 92]   A. Barthelemy, F. Louradour, et V. Couderc. *Wavelength-tunable diffraction-limited operation of a standard high-power diode-laser array using an off-centred extended cavity*. Electronics Letters, vol. 28, no. 22, pages 2038–2040, 1992.

[Becker 18]   D. Becker, M. D. Lachmann, S. T. Seidel, H. Ahlers, A. N. Dinkelaker, J. Grosse, O. Hellmig, H. Müntinga, V. Schkolnik, T. Wendrich, et al. *Space-borne Bose–Einstein condensation for precision interferometry*. Nature, vol. 562, no. 7727, page 391, 2018.

[Bendelli 91]   G. Bendelli, K. Komori, S. Arai, et Y. Suematsu. *A new structure for high-power TW-SLA (Travelling wave semiconductor laser amplifier)*. IEEE Photonics technology letters, vol. 3, no. 1, pages 42–44, 1991.

[Borruel 04]   L. Borruel, S. Sujecki, P. Moreno, J. Wykes, P. Sewell, T. M. Benson, E. C. Larkins, et I. Esquivias. *Modeling of patterned contacts in tapered lasers*. IEEE journal of quantum electronics, vol. 40, no. 10, pages 1384–1388, 2004.

[Botez 91]   D. Botez, M. Jansen, L. J. Mawst, G. Peterson, et T. J. Roth. *Watt-range, coherent, uniphase powers from phase-locked arrays of antiguided diode lasers*. Applied Physics Letters, vol. 58, no. 19, pages 2070–2072, May 1991.

[Bourderionnet 11]   J. Bourderionnet, C. Bellanger, J. Primot, et A. Brignon. *Collective coherent phase combining of 64 fibers*. Optics express, vol. 19, no. 18, pages 17053–17058, 2011.

[Boyd 68]   G. D. Boyd et D. A. Kleinman. *Parametric interaction of focused Gaussian light beams*. Journal of Applied Physics, vol. 39, no. 8, pages 3597–3639, 1968.

[Boyd 03]   R. W. Boyd. Nonlinear optics. Elsevier, 2003.

[Brauch 00]   U. Brauch, P. Loosen, et H. Opower. *High-Power Diode Lasers for Direct Applications*. In High-Power Diode Lasers, Topics in Applied Physics, pages 303–368. Springer, Berlin, Heidelberg, 2000.

[Brignon 13]   A. Brignon. Coherent Laser Beam Combining. John Wiley & Sons, November 2013.

[Christensen 17]   M. Christensen, A. K. Hansen, D. Noordegraaf, O. B. Jensen, et P. M. W. Skovgaard. *Deep modulation of second-harmonic light by wavelength detuning of a laser diode*. Applied Optics, vol. 56, no. 8, page 2250, March 2017.

[Coldren 95]   L. A. Coldren, S. W. Corzine, et M. L. Mashanovitch. Diode lasers and photonic integrated circuits, volume 218. John Wiley & Sons, 1995.

[Coldren 04]   L. A. Coldren, G. Fish, Y. Akulova, J. Barton, L. Johansson, et C. Coldren. *Tunable semiconductor lasers: A tutorial*. Journal of Lightwave Technology, vol. 22, no. 1, page 193, 2004.

[Creedon 12]   K. J. Creedon, S. M. Redmond, G. M. Smith, L. J. Missaggia, M. K. Connors, J. E. Kansky, T. Y. Fan, G. W. Turner, et A. Sanchez-Rubio. *High efficiency coherent beam combining of semiconductor optical amplifiers*. Optics letters, vol. 37, no. 23, pages 5006–5008, 2012.

[Crump 06]   P. Crump, M. Grimshaw, Jun Wang, Weimin Dong, Shiguo Zhang, Suhit Das, J. Farmer, M. DeVito, L. S. Meng, et J. K. Brasseur. *85% power conversion efficiency 975-nm broad area diode lasers at − 50°C, 76 % at 10°C*. In 2006 Conference on Lasers and Electro-Optics and 2006 Quantum Electronics and Laser Science Conference, pages 1–2, Long Beach, CA, USA, 2006. IEEE.

[Crump 12]   P. Crump, H. Wenzel, G. Erbert, et G. Tränkle. *Progress in increasing the maximum achievable output power of broad area diode lasers*. In High-Power Diode Laser Technology and Applications X, volume 8241, page 82410U. International Society for Optics and Photonics, February 2012.

[Crump 13a]   P. Crump, G. Erbert, H. Wenzel, C. Frevert, C. M. Schultz, K.-H. Hasler, R. Staske, B. Sumpf, A. Maaßdorf, F. Bugge, S. Knigge, et G. Tränkle. *Efficient High-Power Laser Diodes*. IEEE Journal of Selected Topics in Quantum Electronics, vol. 19, no. 4, pages 1501211–1501211, July 2013.

[Crump 13b]   P. Crump, S. Knigge, A. Maaßdorf, F. Bugge, S. Hengesbach, U. Witte, H.-D. Hoffmann, B. Köhler, R. Hubrich, H. Kissel, J. Biesenbach, G. Erbert, et G. Tränkle. *Low-loss smile-insensitive external frequency-stabilization of high power diode lasers enabled by vertical designs with extremely low divergence angle and high efficiency*. In High-Power Diode Laser Technology and Applications XI, volume 8605, page 86050T. International Society for Optics and Photonics, February 2013.

[Crump 15]   P. Crump, J. Decker, M. Winterfeldt, J. Fricke, A. Maaßdorf, G. Erbert, et G. Tränkle. *Development of high-power diode lasers with beam parameter product below*

2 mm$\times$ mrad within the BRIDLE project. In High-Power Diode Laser Technology and Applications XIII, volume 9348, page 93480D. International Society for Optics and Photonics, 2015.

[Crump 19]   P. Crump. Private Communication, 2019.

[Decker 14]   J. Decker, P. Crump, J. Fricke, A. Maaßdorf, G. Erbert, et G. Trankle. *Narrow Stripe Broad Area Lasers With High Order Distributed Feedback Surface Gratings*. IEEE Photonics Technology Letters, vol. 26, no. 8, pages 829–832, April 2014.

[DILAS 19]   DILAS. *COHERENT / DILAS Diodenlaser GmbH: http://www.dilas.com/products/search/single-emitters-open*, 2019.

[Epperlein 13a]   Epperlein. *Basic Diode Laser Engineering Principles*. In Semiconductor Laser Engineering, Reliability and Diagnostics, pages 3–100. John Wiley & Sons Ltd, Oxford, UK, January 2013.

[Epperlein 13b]   Epperlein. *Design Considerations for High-Power Single Spatial Mode Operation*. In Semiconductor Laser Engineering, Reliability and Diagnostics, pages 101–210. John Wiley & Sons Ltd, Oxford, UK, January 2013.

[Ertel 05]   K. Ertel, H. Linné, et J. Bösenberg. *Injection-seeded pulsed Ti: sapphire laser with novel stabilization scheme and capability of dual-wavelength operation*. Applied optics, vol. 44, no. 24, pages 5120–5126, 2005.

[Fan 05]   T. Y. Fan. *Laser beam combining for high-power, high-radiance sources*. IEEE Journal of Selected Topics in Quantum Electronics, vol. 11, no. 3, pages 567–577, May 2005.

[Fiebig 08]   C. Fiebig, G. Blume, C. Kaspari, D. Feise, J. Fricke, M. Matalla, W. John, H. Wenzel, K. Paschke, et G. Erbert. *12 W high-brightness single-frequency DBR tapered diode laser*. Electronics Letters, vol. 44, no. 21, pages 1253–1255, October 2008.

[Fiebig 09a]   C. Fiebig, G. Blume, M. Uebernickel, D. Feise, C. Kaspari, K. Paschke, J. Fricke, H. Wenzel, et G. Erbert. *High-Power DBR-Tapered Laser at 980 nm for Single-Path Second Harmonic Generation*. IEEE Journal of Selected Topics in Quantum Electronics, vol. 15, no. 3, pages 978–983, 2009.

[Fiebig 09b]   C. Fiebig, D. Feise, B. Eppich, K. Paschke, et G. Erbert. *Tapered diode laser with reverse bias absorber section*. IEEE Photonics Technology Letters, vol. 21, no. 23, pages 1755–1757, 2009.

[Flores 13]   A. Flores, B. Pulford, C. Robin, C. A. Lu, et T. M. Shay. *Coherent Beam Combining of Fiber Amplifiers via LOCSET*. In Coherent Laser Beam Combining, pages 45–73. John Wiley & Sons, Ltd, 2013.

[Fritsche 14]   H. Fritsche, R. Koch, B. Krusche, F. Ferrario, A. Grohe, S. Pflueger, et W. Gries. *Generating a high brightness multi-kilowatt laser by dense spectral combination of VBG stabilized single emitter laser diodes*. page 91340U, Brussels, Belgium, May 2014.

[Gehrsitz 00]   S. Gehrsitz, F. Reinhart, C. Gourgon, N. Herres, A. Vonlanthen, et H. Sigg. *The refractive index of Al x Ga 1- x As below the band gap: accurate determination and empirical modeling*. Journal of Applied Physics, vol. 87, no. 11, pages 7825–7837, 2000.

[Goldberg 92]   L. Goldberg et D. Mehuys. *21 W broad area near-diffraction-limited semicon-ductor amplifier*. Applied Physics Letters, vol. 61, no. 6, pages 633–635, August 1992.

[Goldberg 93]   L. Goldberg, M. R. Surette, et D. Mehuys. *Filament formation in a tapered GaAlAs optical amplifier*. Applied Physics Letters, vol. 62, no. 19, pages 2304–2306, May 1993.

[Goldwin 02]   J. Goldwin, S. Papp, B. DeMarco, et D. Jin. *Two-species magneto-optical trap with 40 K and 87 Rb*. Physical Review A, vol. 65, no. 2, page 021402, 2002.

[Goodno 10]   G. D. Goodno, C.-C. Shih, et J. E. Rothenberg. *Perturbative analysis of coherent combining efficiency with mismatched lasers*. Optics express, vol. 18, no. 24, pages 25403–25414, 2010.

[Hamperl 19]   J. Hamperl. Coherent combining of high-brightness tapered semiconductor ampli-fiers. Master's thesis, Friedrich-Schiller-Universität Jena, Jena, Germany, 2019.

[Heilmann 18]   A. Heilmann. *Highly scalable femtosecond coherent beam combining system of high power fiber amplifiers*. thesis, Paris Saclay, December 2018.

[Helal 17]   M. A. Helal, S. N. Nyirenda-Kaunga, S. Bull, et E. C. Larkins. *Beam quality degradation processes in tapered lasers and DBR tapered lasers*. In 2017 IEEE High Power Diode Lasers and Systems Conference (HPD), pages 25–26, Coventry, October 2017. IEEE.

[Huang 03]   R. K. Huang, J. P. Donnelly, L. J. Missaggia, C. T. Harris, J. Plant, D. E. Mull, et W. D. Goodhue. *High-power nearly diffraction-limited AlGaAs-InGaAs semicon-ductor slab-coupled optical waveguide laser*. IEEE Photonics Technology Letters, vol. 15, no. 7, pages 900–902, July 2003.

[Huang 09]   R. K. Huang, B. Chann, L. J. Missaggia, S. J. Augst, M. K. Connors, G. W. Turner, A. Sanchez-Rubio, J. P. Donnelly, J. L. Hostetler, et C. Miester. *Coherent combi-nation of slab-coupled optical waveguide lasers*. In Novel In-Plane Semiconduc-tor Lasers VIII, volume 7230, page 72301G. International Society for Optics and Photonics, 2009.

[Jechow 10]   A. Jechow, R. Menzel, K. Paschke, et G. Erbert. *Blue-green light generation using high brilliance edge emitting diode lasers*. Laser & Photonics Reviews, vol. 4, no. 5, pages 633–655, 2010.

[Jensen 14]   O. B. Jensen, A. K. Hansen, A. Muller, B. Sumpf, A. Unterhuber, W. Drexler, P. M. Petersen, et P. E. Andersen. *Power Scaling of Nonlinear Frequency Con-verted Tapered Diode Lasers for Biophotonics*. IEEE Journal of Selected Topics in Quantum Electronics, vol. 20, no. 2, pages 307–321, March 2014.

[Jensen 17]   O. B. Jensen, A. K. Hansen, A. Müller, B. Sumpf, P. M. Petersen, et P. E. Ander-sen. *Efficient generation of 3.5W laser light at 515nm by frequency doubling a single-frequency high power DBR tapered diode laser*. Optics Communications, vol. 392, pages 167–170, June 2017.

[Kabeya 15]   D. Kabeya, V. Kermene, M. Fabert, J. Benoist, A. Desfarges-Berthelemot, et A. Barthelemy. *Active coherent combining of laser beam arrays by means of phase-intensity mapping in an optimization loop*. Optics Express, vol. 23, no. 24, page 31059, November 2015.

[Kelemen 04]   M. T. Kelemen, J. Weber, S. Kallenbach, C. Pfahler, M. Mikulla, et G. Weimann. *Astigmatism and beam quality of high-brightness tapered diode lasers*. In Semiconductor Lasers and Laser Dynamics, volume 5452, pages 233–243. International Society for Optics and Photonics, 2004.

[Khajavikhan 13]   M. Khajavikhan et J. R. Leger. *Modal Theory of Coupled Resonators for External Cavity Beam Combining*. In Coherent Laser Beam Combining, pages 303–343. John Wiley & Sons, Ltd, 2013.

[Klenke 18]   A. Klenke, M. Müller, H. Stark, M. Kienel, C. Jauregui, A. Tünnermann, et J. Limpert. *Coherent Beam Combination of Ultrafast Fiber Lasers*. IEEE Journal of Selected Topics in Quantum Electronics, vol. 24, no. 5, pages 1–9, September 2018.

[Kumar 09]   S. C. Kumar, G. Samanta, et M. Ebrahim-Zadeh. *High-power, single-frequency, continuous-wave second-harmonic-generation of ytterbium fiber laser in PPKTP and MgO: sPPLT*. Optics express, vol. 17, no. 16, pages 13711–13726, 2009.

[Kumar 11]   S. C. Kumar, G. K. Samanta, K. Devi, et M. Ebrahim-Zadeh. *High-efficiency, multicrystal, single-pass, continuous-wave second harmonic generation*. Optics Express, vol. 19, no. 12, page 11152, June 2011.

[Lang 80]   R. Lang et K. Kobayashi. *External optical feedback effects on semiconductor injection laser properties*. IEEE Journal of Quantum Electronics, vol. 16, no. 3, pages 347–355, March 1980.

[Larkins 19]   E. Larkins. Private Communication, 2019.

[Levy 95]   J. L. Levy et K. Roh. *Coherent array of 900 semiconductor laser amplifiers*. In Laser Diodes and Applications, volume 2382, pages 58–70. International Society for Optics and Photonics, April 1995.

[Liao 04]   Z. M. Liao, S. A. Payne, J. Dawson, A. Drobshoff, C. Ebbers, D. Pennington, et L. Taylor. *Thermally induced dephasing in periodically poled KTP frequency-doubling crystals*. JOSA B, vol. 21, no. 12, pages 2191–2196, 2004.

[Lim 09]   J. J. Lim, S. Sujecki, L. Lang, Z. Zhang, D. Paboeuf, G. Pauliat, G. Lucas-Leclin, P. Georges, R. C. MacKenzie, P. Bream, et al. *Design and simulation of next-generation high-power, high-brightness laser diodes*. IEEE Journal of Selected Topics in Quantum Electronics, vol. 15, no. 3, pages 993–1008, 2009.

[Lim 14]   J. J. Lim, E. C. Larkins, S. N. Kaunga-Nyirenda, K.-H. Hasler, S. Bull, et J. Fricke. *Factors influencing brightness and beam quality of conventional and distributed Bragg reflector tapered laser diodes in absence of self-heating*. IET Optoelectronics, vol. 8, no. 2, pages 99–107, April 2014.

[Liu 04]   X. Liu, M. H. Hu, H. K. Nguyen, C. G. Caneau, M. H. Rasmussen, R. W. Davis, et C.-E. Zah. *Comparison between epi-down and epi-up bonded high-power single-mode 980-nm semiconductor lasers*. IEEE Transactions on Advanced Packaging, vol. 27, no. 4, pages 640–646, 2004.

[Liu 08]   B. Liu, Y. Liu, et Y. Braiman. *Coherent addition of high power laser diode array with a V-shape external Talbot cavity*. Optics Express, vol. 16, no. 25, page 20935, December 2008.

[Liu 10]   B. Liu, Y. Liu, et Y. Braiman. *Coherent beam combining of high power broad-area laser diode array with a closed-V-shape external Talbot cavity.* Optics Express, vol. 18, no. 7, page 7361, March 2010.

[Liu 13]   L. Liu, J. Zhang, S. Ma, A. Qi, H. Qu, Y. Zhang, et W. Zheng. *High-brightness diode laser arrays integrated with a phase shifter designed for single-lobe far-field pattern.* Optics Letters, vol. 38, no. 15, page 2770, August 2013.

[Liu 18]   B. Liu et Y. Braiman. *Coherent addition of high power broad-area laser diodes with a compact VBG V-shaped external Talbot cavity.* Optics Communications, vol. 414, pages 202–206, May 2018.

[Lombard 13]   L. Lombard, J. L. Gouët, P. Bourdon, et G. Canat. *Coherent Beam Combining of Pulsed Fiber Amplifiers in the Long-Pulse Regime (Nano-to Microseconds).* Coherent Laser Beam Combining, pages 231–276, 2013.

[Loosen 00]   P. Loosen. *Cooling and Packaging of High-Power Diode Lasers.* In R. Diehl, editeur, High-Power Diode Lasers: Fundamentals, Technology, Applications: With Contributions by Numerous Experts, Topics in Applied Physics, pages 289–301. Springer Berlin Heidelberg, Berlin, Heidelberg, 2000.

[Lucas-Leclin 19] G. Lucas-Leclin, P. Albrodt, G. Schimmel, D. Paboeuf, et P. Georges. *Coherent beam combining architectures for high-power laser diodes.* In I. Divliansky, editeur, Advances In High-Power Fiber And Diode Laser Engineering, volume 1 of *1.* IET Publishing, 1 edition, 11 2019.

[Montoya 12]   J. Montoya, S. J. Augst, K. Creedon, J. Kansky, T. Y. Fan, et A. Sanchez-Rubio. *External cavity beam combining of 21 semiconductor lasers using SPGD.* Applied optics, vol. 51, no. 11, pages 1724–1728, 2012.

[Müller 13]   A. Müller, S. Marschall, O. B. Jensen, J. Fricke, H. Wenzel, B. Sumpf, et P. E. Andersen. *Diode laser based light sources for biomedical applications.* Laser & Photonics Reviews, vol. 7, no. 5, pages 605–627, 2013.

[Müller 17]   A. Müller, C. Zink, J. Fricke, F. Bugge, G. Erbert, B. Sumpf, et G. Tränkle. *Efficient, High Brightness 1030 nm DBR Tapered Diode Lasers With Optimized Lateral Layout.* IEEE Journal of Selected Topics in Quantum Electronics, vol. 23, no. 6, pages 1–7, November 2017.

[Müller 18]   M. Müller, A. Klenke, A. Steinkopff, H. Stark, A. Tünnermann, et J. Limpert. *3.5 kW coherently combined ultrafast fiber laser.* Optics Letters, vol. 43, no. 24, page 6037, December 2018.

[Nehrir 11]   A. R. Nehrir, K. S. Repasky, et J. L. Carlsten. *Eye-Safe Diode-Laser-Based Micropulse Differential Absorption Lidar (DIAL) for Water Vapor Profiling in the Lower Troposphere.* Journal of Atmospheric and Oceanic Technology, vol. 28, no. 2, pages 131–147, February 2011.

[Nehrir 12]   A. R. Nehrir, K. S. Repasky, et J. L. Carlsten. *Micropulse water vapor differential absorption lidar: transmitter design and performance.* Optics Express, vol. 20, no. 22, page 25137, October 2012.

[Nyman 06]   R. A. Nyman, G. Varoquaux, B. Villier, D. Sacchet, F. Moron, Y. Le Coq, A. Aspect, et P. Bouyer. *Tapered-amplified antireflection-coated laser diodes for potassium and rubidium atomic-physics experiments.* Review of Scientific Instruments, vol. 77, no. 3, page 033105, 2006.

[Osinski 95]   J. S. Osinski, D. Mehuys, D. F. Welch, R. G. Waarts, J. S. Major, K. M. Dzurko, et R. J. Lang. *Phased array of high-power, coherent, monolithic flared amplifier master oscillator power amplifiers*. Applied Physics Letters, vol. 66, no. 5, pages 556–558, January 1995.

[Paboeuf 08]   D. Paboeuf, G. Lucas-Leclin, P. Georges, N. Michel, M. Krakowski, J. Lim, S. Sujecki, et E. Larkins. *Narrow-line coherently combined tapered laser diodes in a Talbot external cavity with a volume Bragg grating*. Applied Physics Letters, vol. 93, no. 21, page 211102, 2008.

[Pabœuf 11]   D. Pabœuf, D. Vijayakumar, O. B. Jensen, B. Thestrup, J. Lim, S. Sujecki, E. Larkins, G. Lucas-Leclin, et P. Georges. *Volume Bragg grating external cavities for the passive phase locking of high-brightness diode laser arrays: theoretical and experimental study*. JOSA B, vol. 28, no. 5, pages 1289–1299, 2011.

[Platz 14]   R. Platz, B. Eppich, P. Crump, W. Pittroff, S. Knigge, A. Maaßdorf, et G. Erbert. *940-nm Broad Area Diode Lasers Optimized for High Pulse-Power Fiber Coupled Applications*. IEEE Photonics Technology Letters, vol. 26, no. 6, pages 625–628, March 2014.

[Redmond 11]   S. M. Redmond, J. E. Kansky, K. J. Creedon, L. J. Missaggia, M. K. Connors, G. W. Turner, T. Y. Fan, et A. Sanchez-Rubio. *Active coherent combination of> 200 semiconductor amplifiers using a SPGD algorithm*. In Lasers and Electro-Optics (CLEO), 2011 Conference on, pages 1–2. IEEE, 2011.

[Redmond 13]   S. Redmond, K. Creedon, T. Y. Fan, A. Sanchez-Rubio, C. Yu, et J. Donnelly. *Active Coherent Combination Using Hill Climbing-Based Algorithms for Fiber and Semiconductor Amplifiers*. Coherent Laser Beam Combining, pages 103–136, 2013.

[Sabouri 13]   S. G. Sabouri, S. C. Kumar, A. Khorsandi, et M. Ebrahim-Zadeh. *Thermal effects in high-power continuous-wave single-pass second harmonic generation*. IEEE Journal of Selected Topics in Quantum Electronics, vol. 20, no. 5, pages 563–572, 2013.

[Sahm 18]   A. Sahm, N. Werner, J. Hofmann, R. Bege, et K. Paschke. *Compact Miniaturized Laser Module Emitting More Than 1.6 W of Yellow Light at 576 nm*. IEEE Photonics Technology Letters, vol. 30, no. 21, pages 1878–1881, November 2018.

[Saleh 19]   B. E. A. Saleh et M. C. Teich. Fundamentals of Photonics. John Wiley & Sons, February 2019.

[Sanders 94]   S. Sanders, R. Waarts, D. Nam, D. Welch, D. Scifres, J. C. Ehlert, W. J. Cassarly, J. M. Finlan, et K. M. Flood. *High power coherent two-dimensional semiconductor laser array*. Applied physics letters, vol. 64, no. 12, pages 1478–1480, 1994.

[Schimmel 16]   G. Schimmel. *Combinaison cohérente de diodes laser de puissance*. Manuscrit de Th, Université-Paris Saclay, 2016.

[Schimmel 17]   G. Schimmel, S. Janicot, M. Hanna, J. Decker, P. Crump, G. Erbert, U. Witte, M. Traub, P. Georges, et G. Lucas-Leclin. *Coherent beam combining architectures for high power tapered laser arrays*. In High-Power Diode Laser Technology XV, volume 10086, page 100860O. International Society for Optics and Photonics, 2017.

[Schkolnik 16]   V. Schkolnik, O. Hellmig, A. Wenzlawski, J. Grosse, A. Kohfeldt, K. Döringshoff, A. Wicht, P. Windpassinger, K. Sengstock, C. Braxmaier, et al. *A compact and robust diode laser system for atom interferometry on a sounding rocket*. Applied Physics B, vol. 122, no. 8, page 217, 2016.

[Schwertfeger 11]   S. Schwertfeger, A. Klehr, T. Hoffmann, A. Liero, H. Wenzel, et G. Erbert. *Picosecond pulses with 50 W peak power and reduced ASE background from an all-semiconductor MOPA system*. Applied Physics B, vol. 103, no. 3, pages 603–607, 2011.

[Serreze 12]   M. C. Serreze, A. P. Barrett, et J. Stroeve. *Recent changes in tropospheric water vapor over the Arctic as assessed from radiosondes and atmospheric reanalyses*. Journal of Geophysical Research: Atmospheres, vol. 117, no. D10, 2012.

[Shukla 15]   P. Shukla, J. Lawrence, et Y. Zhang. *Understanding laser beam brightness: A review and new prospective in material processing*. Optics & Laser Technology, vol. 75, pages 40–51, 2015.

[Siegman 93]   A. Siegman. *Analysis of laser beam quality degradation caused by quartic phase aberrations*. Applied optics, vol. 32, no. 30, pages 5893–5901, 1993.

[Siegman 98]   A. E. Siegman. *How to (Maybe) Measure Laser Beam Quality*. In DPSS (Diode Pumped Solid State) Lasers: Applications and Issues, page MQ1. Optical Society of America, 1998.

[Smith 11]   G. M. Smith, J. P. Donnelly, L. J. Missaggia, M. K. Connors, S. M. Redmond, D. C. Mathewson, R. B. Swint, A. Sanchez-Rubio, et G. W. Turner. *High-power slab-coupled optical waveguide amplifiers*. In IEEE Photonic Society 24th Annual Meeting, pages 579–580, October 2011.

[Spuler 15]   S. M. Spuler, K. S. Repasky, B. Morley, D. Moen, M. Hayman, et A. R. Nehrir. *Field-deployable diode-laser-based differential absorption lidar (DIAL) for profiling water vapor*. Atmospheric Measurement Techniques, vol. 8, no. 3, pages 1073–1087, 2015.

[Stott 16]   P. A. Stott, N. Christidis, F. E. Otto, Y. Sun, J.-P. Vanderlinden, G. J. Van Oldenborgh, R. Vautard, H. Von Storch, P. Walton, P. Yiou, et al. *Attribution of extreme weather and climate-related events*. Wiley Interdisciplinary Reviews: Climate Change, vol. 7, no. 1, pages 23–41, 2016.

[Sujecki 03]   S. Sujecki, L. Borruel, J. Wykes, P. Moreno, B. Sumpf, P. Sewell, H. Wenzel, T. Benson, G. Erbert, I. Esquivias, et E. Larkins. *Nonlinear properties of tapered laser cavities*. IEEE Journal of Selected Topics in Quantum Electronics, vol. 9, no. 3, pages 823–834, May 2003.

[Sumpf 18]   B. Sumpf et K. Paschke. *Spectrally stabilized high-power high-brightness DBR-tapered lasers in the VIS and NIR range*. In Proc. SPIE, volume 10518, page 1051817. International Society for Optics and Photonics, February 2018.

[Tawfieq 17]   M. Tawfieq, A. Muller, J. Fricke, P. Della Casa, P. Ressel, A. Ginolas, D. Feise, B. Sumpf, et G. Trankle. *Compact High Power Diode Laser MOPA System With 5.5 nm Wavelength Tunability*. IEEE Photonics Technology Letters, vol. 29, no. 22, pages 1983–1986, November 2017.

[Thompson 72]   G. Thompson. *A theory for filamentation in semiconductor lasers including the dependence of dielectric constant on injected carrier density*. Opto-electronics, vol. 4, no. 3, pages 257–310, 1972.

[Tkach 86]   R. Tkach et A. Chraplyvy. *Regimes of feedback effects in 1.5-µm distributed feed-back lasers.* Journal of Lightwave Technology, vol. 4, no. 11, pages 1655–1661, November 1986.

[Tomm 11]   J. Tomm, M. Ziegler, M. Hempel, et T. Elsaesser. *Mechanisms and fast kinetics of the catastrophic optical damage (COD) in GaAs-based diode lasers.* Laser & Photonics Reviews, vol. 5, no. 3, pages 422–441, May 2011.

[Toptica 19]   Toptica. *Toptica Photonics AG: https://www.toptica.com/products/,* July 2019.

[Unger 13]   A. Unger, T. Brand, S. Bull, E. C. Larkins, M. Traub, S. Hengesbach, P. Uusimaa, V. Vilokkinen, P. Crump, G. Erbert, G. Lucas-Leclin, P. Georges, T. Rataj, et E. Deichsel. *The BRIDLE project: High brilliance diode lasers for industrial applications.* In 2013 High Power Diode Lasers and Systems Conference (HPD), pages 28–29, October 2013.

[Victori 19]   S. Victori. *The requirements on pulsed laser diodes for use in atmospheric LiDAR.* In High Power Diode Lasers and Systems Conference (HPD), 2019 IEEE, pages 3–5. IEEE, 2019.

[Vorontsov 98] M. A. Vorontsov et V. P. Sivokon. *Stochastic parallel-gradient-descent technique for high-resolution wave-front phase-distortion correction.* Journal of the Optical Society of America A, vol. 15, no. 10, page 2745, October 1998.

[Vu 14]   T. N. Vu, A. Klehr, B. Sumpf, H. Wenzel, G. Erbert, et G. Tränkle. *Wavelength stabilized ns-MOPA diode laser system with 16 W peak power and a spectral line width below 10 pm.* Semiconductor Science and Technology, vol. 29, no. 3, page 035012, 2014.

[Walpole 92]   J. N. Walpole, E. S. Kintzer, S. R. Chinn, C. A. Wang, et L. J. Missaggia. *High-power strained-layer InGaAs/AlGaAs tapered traveling wave amplifier.* Applied Physics Letters, vol. 61, no. 7, pages 740–742, August 1992.

[Walpole 02]   J. Walpole, J. Donnelly, P. Taylor, L. Missaggia, C. Harris, R. Bailey, A. Napoleone, S. Groves, S. Chinn, R. Huang, et J. Plant. *Slab-coupled 1.3-m semiconductor laser with single-spatial large-diameter mode.* IEEE Photonics Technology Letters, vol. 14, no. 6, pages 756–758, June 2002.

[Wan 12]   C. Wan et J. R. Leger. *Experimental Measurements of Path Length Sensitivity in Coherent Beam Combining by Spatial Filtering.* IEEE Journal of Quantum Electronics, vol. 48, no. 8, pages 1045–1051, August 2012.

[Wang 12]   X. Wang, G. Erbert, H. Wenzel, B. Eppich, P. Crump, A. Ginolas, J. Fricke, F. Bugge, M. Spreemann, et G. Tränkle. *High-power, spectrally stabilized, near-diffraction-limited 970 nm laser light source based on truncated-tapered semiconductor optical amplifiers with low confinement factors.* Semiconductor Science and Technology, vol. 27, no. 1, page 015010, January 2012.

[Wang 13]   X. Wang, G. Erbert, H. Wenzel, P. Crump, B. Eppich, S. Knigge, P. Ressel, A. Ginolas, A. Maaßdorf, et G. Trankle. *17-W Near-Diffraction-Limited 970-nm Output From a Tapered Semiconductor Optical Amplifier.* IEEE Photonics Technology Letters, vol. 25, no. 2, pages 115–118, January 2013.

[Welch 92]   D. Welch, R. Parke, D. Mehuys, A. Hardy, R. Lang, S. O'Brien, et S. Scifres. *1.1 W CW, diffraction-limited operation of a monolithically integrated flared-amplifier master oscillator power amplifier.* Electronics Letters, vol. 28, no. 21, page 2011, 1992.

[Wenzel 07]   H. Wenzel, K. Paschke, O. Brox, F. Bugge, J. Fricke, A. Ginolas, A. Knauer, P. Ressel, et G. Erbert. *10 W continuous-wave monolithically integrated master-oscillator power-amplifier*. Electronics Letters, vol. 43, no. 3, page 160, 2007.

[Wenzel 08]   H. Wenzel, F. Bugge, M. Dallmer, F. Dittmar, J. Fricke, K. H. Hasler, et G. Erbert. *Fundamental-Lateral Mode Stabilized High-Power Ridge-Waveguide Lasers With a Low Beam Divergence*. IEEE Photonics Technology Letters, vol. 20, no. 3, pages 214–216, February 2008.

[Wenzel 13]   H. Wenzel, P. Crump, J. Fricke, P. Ressel, et G. Erbert. *Suppression of higher-order lateral modes in broad-area diode lasers by resonant anti-guiding*. IEEE Journal of Quantum Electronics, vol. 49, no. 12, pages 1102–1108, 2013.

[Wilkens 18]   M. Wilkens, H. Wenzel, J. Fricke, A. Maaßdorf, P. Ressel, S. Strohmaier, A. Knigge, G. Erbert, et G. Tränkle. *High-efficiency broad-ridge waveguide lasers*. IEEE Photonics Technology Letters, vol. 30, no. 6, pages 545–548, 2018.

[Wilkens 19]   M. Wilkens, G. Erbert, H. Wenzel, A. Maaßdorf, J. Fricke, P. Ressel, A. Knigge, et P. Crump. *Efficient Narrow Stripe Ridge Waveguide Lasers for Single-Spatial Mode Operation up to 2.5 W*. In 2019 Conference on Lasers and Electro-Optics Europe and European Quantum Electronics Conference, page cb.5.3. Optical Society of America, 2019.

[Winterfeldt 14] M. Winterfeldt, P. Crump, H. Wenzel, G. Erbert, et G. Tränkle. *Experimental investigation of factors limiting slow axis beam quality in 9xx nm high power broad area diode lasers*. Journal of Applied Physics, vol. 116, no. 6, page 063103, August 2014.

[Yu 06]   C. X. Yu, J. E. Kansky, S. E. J. Shaw, D. V. Murphy, et C. Higgs. *Coherent beam combining of large number of PM fibres in 2-D fibre array*. Electronics Letters, vol. 42, no. 18, page 1, 2006.

[Zhou 19]   W. Zhou, Q.-Y. Lu, D.-H. Wu, S. Slivken, et M. Razeghi. *High-power, continuous-wave, phase-locked quantum cascade laser arrays emitting at 8 µm*. Optics Express, vol. 27, no. 11, page 15776, May 2019.

[Zhu 17]   Y. Zhu, Y. Zhao, et L. Zhu. *Two-dimensional photonic crystal Bragg lasers with triangular lattice for monolithic coherent beam combining*. Scientific Reports, vol. 7, no. 1, December 2017.

[Zink 19]   C. Zink, M. Maiwald, H. Wenzel, B. Sumpf, et G. Tränkle. *Monolithic master oscillator with tapered power amplifier diode laser at 1060 nm with additional control section for high power operation*. In 2019 Conference on Lasers and Electro-Optics Europe and European Quantum Electronics Conference, page cb.3.1. Optical Society of America, 2019.

Publications of the author

Parts of the work described in this manuscript have previously been published in the following publications:

Journal Articles

Coherent beam combining of high power quasi continuous wave tapered amplifiers
P. Albrodt, M. Niemeyer, P. Crump, J. Hamperl, F. Moron, P. Georges, and G. Lucas-Leclin
Optics Express 27(20), pp. 27891-27901 (2019)

Coherent combining of high brightness tapered amplifiers for efficient non-linear conversion
P. Albrodt, M. T. Jamal, A. K. Hansen, O. B. Jensen, G. Blume, K. Paschke, P. Crump, P. Georges, and G. Lucas-Leclin
Optics Express 27(2), pp. 928-937 (2019)

Low-index quantum-barrier single-pass tapered semiconductor optical amplifiers for efficient coherent beam combining
P. Albrodt, M. Niemeyer, M. Ellatar, J. Hamperl, G. Blume, A. Ginolas, J. Fricke, A. Maassdorf, P. Georges, G. Lucas-Leclin, K. Paschke and P. Crump
submitted to Semiconductor Science and Technology, provisional acceptance, not yet published (02/03/2020)

Book Chapter

Coherent beam combining architectures for high-power laser diodes
G. Lucas-Leclin, P. Albrodt, G. Schimmel, D. Paboeuf, and P. Georges
In I. Divliansky (ed.) *Advances In High-Power Fiber And Diode Laser Engineering*, IET Publishing, in press (expected 11/2019).

International Conferences

Coherent beam combining of tapered amplifiers under QCW regime
P. Albrodt, M. Niemeyer, P. Crump, J. Hamperl, F. Moron, P. Georges, and G. Lucas-Leclin
IEEE High Power Diode Lasers and Systems Conference (HPD), Coventry - UK, pp. 22-23 (2019)

Compact module for high power coherent beam combining of tapered amplifiers
J. Hamperl, P. Albrodt, P. Georges and G. Lucas-Leclin
IEEE High Power Diode Lasers and Systems Conference (HPD), Coventry - UK, pp. 35-36 (2019)

Coherent superposition of pulsed high-brightness tapered amplifiers
P. Albrodt, J. Hamperl, M. Niemeyer, P. Crump, P. Georges, and G. Lucas-Leclin

Conference on Lasers and Electro-Optics Europe and European Quantum Electronics Conference, OSA Technical Digest, paper cb 4.6 (2019).

Recent progress in brightness scaling by coherent beam combining of tapered amplifiers for efficient high power frequency doubling
P. Albrodt, M. T. Jamal, A. K. Hansen, O. B. Jensen, M. Niemeyer, G. Blume, K. Paschke, P. Crump, P. Georges, and G. Lucas-Leclin
SPIE Photonics West, San Francisco - USA, High-Power Diode Laser Technology XVII, Proc. SPIE 10900, p. 109000O (2019)

High power single-mode 488 nm emission by second harmonic generation of coherently-combined high-brightness tapered lasers
P. Albrodt, M. T. Jamal, A. K. Hansen, O. B. Jensen, G. Blume, K. Paschke, P. Crump, P. Georges, and G. Lucas-Leclin
8th EPS-QEOD Europhoton Conference EUROPHOTON, Barcelona - Spain (2018)

Coherent combining of high brightness tapered lasers in master oscillator power amplifier configuration
P. Albrodt, M. Hanna, F. Moron, J. Decker, M. Winterfeldt, G. Blume, G. Erbert, P. Crump, P. Georges, G. Lucas-Leclin
SPIE Photonics West, San Francisco - USA, High-Power Diode Laser Technology XVI, Proc. SPIE 10514, p. 105140T (2018)

Coherent beam combining of high-power tapered amplifiers
P. Albrodt, M. Hanna, F. Moron, J. Decker, M. Winterfeldt, G. Blume, P. Crump, P. Georges, G. Lucas-Leclin
IEEE High Power Diode Lasers and Systems Conference (HPD), Coventry - UK, pp. 15-16 (2017)

Coherent combining architectures for high-brightness laser diodes
G. Lucas-Leclin, G. Schimmel, P. Albrodt, M. Hanna, P. Georges
IEEE High Power Diode Lasers and Systems Conference (HPD), Coventry - UK, pp. 49-50 (2017)

Coherent combining of high brightness tapered amplifiers for efficient non-linear conversion

P. ALBRODT,[1] M. T. JAMAL,[2] A. K. HANSEN,[2] O. B. JENSEN,[2] G. BLUME,[3] K. PASCHKE,[3] P. CRUMP,[3] P. GEORGES,[1] AND G. LUCAS-LECLIN[1,*]

[1]*Laboratoire Charles Fabry, Institut d'Optique Graduate School, CNRS, Université Paris Saclay 91127 Palaiseau Cedex, France*
[2]*DTU Fotonik, Department of Photonics Engineering, Technical University of Denmark, Frederiksborgvej 399 4000 Roskilde, Denmark*
[3]*Ferdinand-Braun-Institut, Leibniz-Institut für Höchstfrequenztechnik, Gustav-Kirchhoff-Str. 4 12489 Berlin, Germany*
*gaelle.lucas-leclin@institutoptique.fr

Abstract: We report on a coherent beam combination of three high-brightness tapered amplifiers, which are seeded by a single-frequency laser at $\lambda = 976$ nm in a simple architecture with efficiently cooled emitters. The maximal combined power of 12.9 W is achieved at a combining efficiency of > 65%, which is limited by the amplifiers' intrinsic beam quality. The coherent combination cleans up the spatial profile, as the central lobe's power content increases by up to 86%. This high-brightness infrared beam is converted into the visible by second harmonic generation. This results in a high non-linear conversion efficiency of 4.5%/W and a maximum power over 2 W at 488 nm, which is limited by thermal effects in the periodically poled lithium niobate (PPLN).

1. Introduction

High-power high-brightness diode lasers are in strong demand for many applications and benefit from their efficiency, reliability and compactness [1]. However, the power limit of diode lasers is much lower in the visible spectral range than in the near infrared and not all wavelengths are directly accessible with diode lasers. Nonlinear frequency conversion, like second harmonic generation (SHG) is an important technology for the development of high power laser sources in the visible spectral range. Efficient SHG requires a good beam quality, a narrow spectral linewidth and a high input power [2]. High conversion efficiencies are commonly achieved with diode pumped solid state and fiber lasers [3,4], however diode laser based visible light sources have become increasingly attractive for biomedical applications [5] to fulfill the need for compact and efficient visible laser sources. Different high-brightness diode laser architectures are used for blue-green light generation [6]. Among those, tapered lasers (TPL) and tapered amplifiers (TPA) are the most promising architecture since they combine high power and acceptable beam quality in one device.

TPL and TPA devices consist of a single mode ridge waveguide (RW) followed by flared gain-guided amplifier section. Spectrally stabilized TPL are available in the visible (VIS) and near-infrared (NIR) spectral range and reach output powers up to 15 W per device [7] and can be converted to multiple watts of VIS light [8] by making use of a cascade of two SHG crystals [9,10]. Further power scaling can be achieved using an increased NIR pump laser power enabled by research on highly efficient high power diode lasers [11]. Power can also be scaled by beam combining techniques. Incoherent spectral beam combining of tapered diode lasers is a straightforward concept for this power scaling [12], however the ultimate limitation is the available output power per wavelength channel. Coherent beam combining

(CBC) of light from several devices is the only way to achieve much higher powers within a single beam that retains excellent spatial and spectral beam quality [13].

We describe in this paper the CBC of three high-brightness tapered amplifiers in a simple optical setup. Furthermore, we demonstrate the importance of CBC for the development of high power visible light sources by demonstrating a significant improvement of the achievable nonlinear conversion efficiency for single pass SHG in a bulk periodically poled lithium niobate (PPLN) crystal.

2. Coherent beam combining

CBC is the superposition of multiple laser beams by constructive interference. It requires a proper and stable phase relationship of the sampled gain medium. Different approaches have been demonstrated: active phase locking of amplifiers seeded by a single frequency laser split into several beams or passive phase locking of emitters in an extended cavity [14]. Impressive results for CBC using a limited number of high power fiber amplifiers (P > 100W per channel) show the potential of power scaling by CBC reaching kW level powers [15,16]. CBC with diode lasers and amplifiers is still limited to lower power levels but has been demonstrated in various configurations. CBC of arrays of diode lasers in an external cavity [17–19] has been demonstrated but did not lead to a significant increase of the available NIR power since the combined power was limited to a few watts. CBC in MOPA configuration has been demonstrated for larger arrays of amplifiers [20,21] and led to a significant increase of the available NIR power of diode laser architectures reaching about 40 W for CBC of 47 Slab Coupled Optical Waveguide Amplifiers (SCOWA) [22].

Our approach to make CBC of diode lasers more attractive for future applications is to make use of high-brightness tapered amplifiers in order to reach similar power levels but with a reduced number of elements. Tapered laser diodes are a promising building block for CBC architectures as they can deliver high power in a close to diffraction limited beam out of one monolithic device. However, one important drawback to tapered devices is the slightly degraded beam quality at high powers with about 70% power-content in the diffraction limited central lobe while the rest of the power is distributed in side lobes. TPAs are nevertheless our preferred choice for power scaling by CBC to simplify the optical setup by using only a limited number of high-power amplifiers. At the same time as demonstrated in this study, CBC is one way to reduce the relative power content in the side lobes since CBC with non-perfect Gaussian beams favors the diffraction-limited power content leading to an improved beam quality [23]. In our previous studies, an output power of 11.5 W was reached by CBC of a monolithically integrated array of five TPAs, but it was limited by thermal effects caused by emitter to emitter heating of the laser bar [24]. For this reason, we make use of separate individual amplifiers that can be efficiently cooled in order to be able to operate them at higher currents and achieve a higher combined power per element [25]. Additionally one can develop a simplified optical setup with standard optical elements, as splitting and combining the beam is simpler.

2.1 Experimental setup

We used 6 mm long TPAs mounted p-side up on CuW-heat spreaders and C-mounts. We made use of amplifiers identical to lasers previously described in [26] but with a 2 mm long RW instead of the internal grating. Two amplifiers had a 5 μm wide single-mode RW entry section and the third amplifier a 4.5 μm wide entry section, limited by the availability of the amplifiers. Currents in RW (I_{rw}) and tapered section (I_{tp}) can be controlled independently, allowing decoupled control of the phase (via I_{rw}) and the power (via I_{tp}) in each amplifier. The amplifiers are saturated for ridge currents I_{rw} > 300 mA. We use small variations of I_{rw} above this limit in order to control the phase with limited impact on the optical power. The maximum power extracted from the amplifiers reaches 6.5 W at 10 A and is limited by thermal rollover due to poor thermal resistance of the c-mount packaging. The power content

in the central lobe is >70%. A detailed analysis of the amplifiers used is given in [25] showing that the phase noise of the amplifier is dominated by low frequencies (f < 10 Hz).

The CBC interferometer used in this work is sketched in Fig. 1 and is based on three arms. The seed laser, a narrow linewidth DFB laser at 976 nm (P_{max} = 100 mW), was isolated by a double stage optical isolator with an isolation > 50 dB. The beam was split and recombined using non-polarizing 50:50 beam splitters (BS). The beam was coupled into the ridge waveguides (RW) using aspheric lenses (L_2: f = 8 mm, NA = 0.5) and recollimated in the fast axis (FA) by an aspheric lens (L_3: f = 2.75 mm, NA = 0.55) and in the slow axis by a cylindrical lens (L_4: f = 19 mm). We note that the injection powers into the amplifiers were slightly different due to the asymmetry of the setup and the used 50:50 beam splitter coatings. However, this did not affect the performance of the setup since the input powers into all amplifiers (P_{in} ≥10 mW) were high enough to saturate them. The beams of amplifiers A_1 and A_2 interfered on a 50:50 beam combiner (BS_1). The combined beam was then directed to the second 50:50 beam combiner (BS_2) where it interfered with the beam from A_3. One path at each element of combination, representing the combining losses B_1 and B_2, was absorbed by a beam block. We note that the use of two 50:50 beam combiners leads to unbalanced intensities on the second combiner resulting in minor losses smaller than 3% in the combining setup [24]. The power of the combined beam is measured by a fast photodiode and a control loop is used to maximize and stabilize the output power by active feedback on the ridge currents of A_2 and A_3 sequentially. We used a standard hill climbing algorithm for the phase control, which is characterized in details in [25].

The output of the CBC interferometer was used for single pass SHG, which will be described later in section 3.
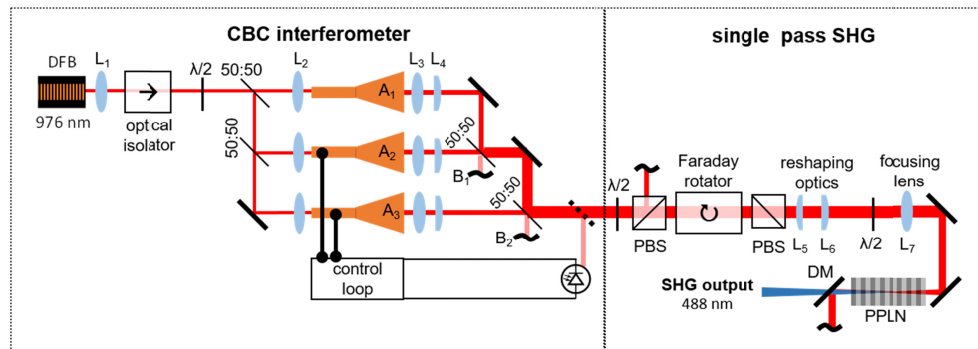

Fig. 1. Experimental setup of the CBC interferometer and the single pass SHG in a MgO:PPLN bulk crystal; BS: 50:50 beam splitters; PBS: polarizing beam splitters.

2.2 Combined power

We measured the coherently combined power P_{CBC} behind the combining elements at different currents into the tapered section, corresponding to the superposition of two and three beams, respectively (see Fig. 2). The positions of the cylindrical lenses for SA-collimation (Fig. 1) were adapted at each operating point to correct the astigmatism and to ensure a good beam overlap on the beam combiners. The combining efficiency is defined by the ratio of the coherently combined power over the sum of the extracted optical powers, which is equivalent to $\eta = P_{CBC}/\left(P_{CBC} + P_{B1} + P_{B2}\right)$ for the superposition of A_{1+2+3} neglecting the losses at the optical elements. As shown in Fig. 2 we reached a maximum power of 12.9 W at I_{tp} = 10 A. This is higher than the 11.5 W previously achieved by CBC of 5 TPAs on a minibar limited by thermal effects [24]. Though the design of amplifiers in [24] was slightly different to those used in this work, it still appears that individual mounting of emitters allows the operation of the elements at higher currents since they can be cooled more efficiently.

Measurements of combination of only the first two amplifiers (A_{1+2}) show a higher combining efficiency (ranging from 85% at 2 A to 74% at 10 A). The combining efficiency of the total setup was > 65%. The combining efficiency decreases for higher currents in the tapered section caused by the degradation of the individual beam quality of each emitter, which will be discussed in the following subsection.

Measurements of the spectrum showed that the spectral properties of the DFB seed laser (976 nm) were maintained. The side mode suppression ratio was better than 40 dB. The full width at half maximum (FWHM) was smaller than 20 pm, limited by the resolution of the optical spectrum analyzer.
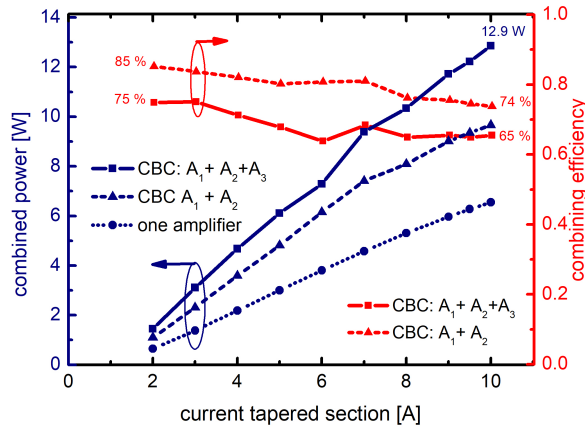

Fig. 2. Combined power at output and total combining efficiency as a function of the currents in the tapered section. The ridge currents were actively controlled in the range of 250 to 400 mA, the heatsink temperature was T = 20 °C. The astigmatism of the amplifiers was corrected at each operating current.

2.3 Beam quality and combining efficiency

Since the beam quality of the TPA is not diffraction limited in the slow axis (SA), one has to investigate the achievable combining efficiency together with the resulting beam quality of the combined beam. Two beams with a slightly different profile interfere at each combining element in the CBC interferometer (Fig. 1). The combining efficiency η at each combining step can be written as

$$\eta = \frac{\iint \eta'(x,y)\big[I_1(x,y)+I_2(x,y)\big]\,dxdy}{\iint I_1(x,y)+I_2(x,y)\,dxdy}, \qquad (1)$$

with the local combining efficiency

$$\eta'(x,y) = \frac{1}{2}\frac{\left|\sqrt{I_1(x,y)}\,e^{i\varphi_1(x,y)}+\sqrt{I_2(x,y)}\,e^{i\varphi_2(x,y)}\right|^2}{\left|\sqrt{I_1(x,y)}\,e^{i\varphi_1(x,y)}\right|^2+\left|\sqrt{I_2(x,y)}\,e^{i\varphi_2(x,y)}\right|^2}, \qquad (2)$$

defined by the overlap of the incident spatial amplitude and phase profiles $I_{1,2}(x,y)$ and $\varphi_{1,2}(x,y)$ respectively [27].

One can consider the beam of a tapered laser as a sum of the fundamental mode, corresponding to the central lobe, and emission at high angle ("side lobes"). The central lobes of each beam are very similar and interfere constructively with a high combining efficiency.

But the high-order modes exhibit a significantly higher beam mismatch and get therefore partially filtered during the CBC. Furthermore, amplified spontaneous emission is incoherent to the seed source and is therefore weakened by 50% at each beam combiner. Consequently, CBC of beams from tapered lasers leads to a clean-up of the spatial beam profile where the central lobe is maintained and the high angle non diffraction-limited emission is suppressed. The beam profile measurements shown in Figs. 3(a)-3(c) illustrate this effect. The shown beam profiles correspond to the beam waist after the focusing lens with a $1/e^2$ waist diameter of about 95 µm. One can clearly see that the side lobes in SA get filtered by the two CBC steps. The power content in the central lobe gets increased from 71% for one individual amplifier to 81% for CBC of A_{1+2} and 86% for CBC of A_{1+2+3}. As a result the beam quality factor is reduced from $M^2_{4\sigma} < 1.3 \times 4$ for one individual amplifier to $M^2_{4\sigma} < 1.1 \times 2.5$ for the final beam. Consequently the experimental combining efficiency of our setup is mostly limited by the power losses induced by this beam clean-up, which removes the undesired high-angle side lobes of the amplifier beams.


	one individual amplifier: A_2 only	CBC step 1: $A_1 + A_2$	CBC step 2: $A_1 + A_2 + A_3$
	(a)	(b)	(c)
power	6.5 W	9.8 W	12.9 W
in central lobe	71 %	81 %	86 %
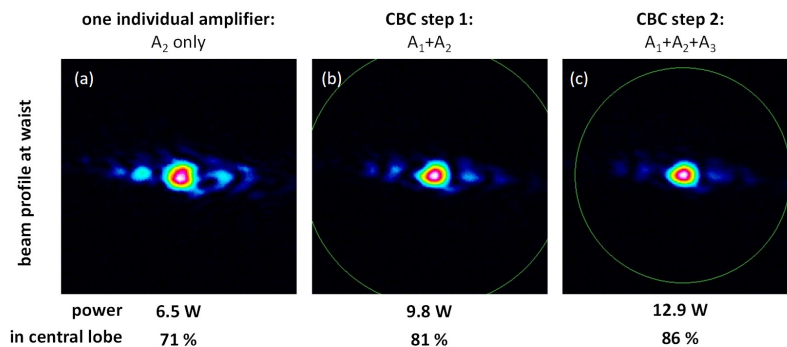
Fig. 3. Beam profiles at waist for (a) one individual amplifier A_2, (b) CBC of two amplifiers A_{1+2} and (c) the final CBC step of all three amplifiers A_{1+2+3}. Measurement for I_{tp} = 10 A, T = 20 °C and actively controlled ridge currents in the range of 250 to 400 mA. The FA is in vertical and the SA is in horizontal direction. The given central lobe power content was calculated by fitting a Gaussian beam profile to the central lobe of the beam and calculating the power content within the fitted profile.

In order to estimate the combining efficiency of the central lobes alone, we used intensity and wavefront measurements of the individual beams at maximum power. The combining efficiency is then calculated following Eqs. (1) and (2). We applied a strong clipping criterion at $1/e^2$ intensity level to the experimental data as a rough estimation for the central lobe and analyzed the overlap of the intensity and phase profiles within this area. We identified a mismatch of the intensity profile in SA caused by slightly different widths of the ridge section as mentioned earlier in section 2.1. Furthermore small differences in the collimation of each beam lead to a mismatch of the intensity profile in FA. Both effects reduce the achievable combining efficiency by 7-10% at each combining step. Furthermore, the wavefront measurements were used to evaluate combining losses linked to differences in the phase profile in between the beams. Those differences are small and had a limited impact smaller than 3% on the achievable combining efficiency of the central lobe.

Altogether, the calculated combining efficiency is η = 91% for the first CBC step (A_{1+2}) and η = 87% for the second step (A_{1+2+3}), resulting in an overall combining efficiency of 82% for the central lobe power content at the maximum current of 10 A. Our lower experimental combining efficiency of >65% considering the whole beam is thus clearly related to the power content in the fundamental mode of the individual amplifier beams.

3. Second harmonic generation

The increase of the brightness in the NIR by CBC of laser diodes can be useful for many applications requiring high power as well as good spectral and spatial beam quality. Especially for CW single-pass SHG, the conversion efficiency is strongly influenced by the focusing conditions in the nonlinear crystal, as described by Boyd and Kleinman [28]. Furthermore, the spatial quality of the pump beam directly impacts the achievable conversion efficiency [29]. We demonstrate in the following the improvement of single pass SHG efficiency resulting from the scaled brightness by coherent combining, and the subsequent increase of the visible power.

3.1 Description of the experiment

The output of the CBC-interferometer was used for single pass SHG as shown in Fig. 1. In order to test the nonlinear conversion efficiency at different levels of brightness, we did modify the CBC setup slightly in order to use the beam from either a single amplifier (A_1) or from the CBC of two (A_{1+2}) or three power amplifiers (A_{1+2+3}) as the input pump beam for the SHG. This was done by replacing the relevant combining elements with highly reflective mirrors. During the SHG experiments all three amplifiers were operated at constant current into the tapered section (I_{tp} = 9 A) and the power used for SHG was adjusted by turning the polarization before the first polarizing beam splitter (PBS). The optical isolation between the CBC interferometer and the SHG experiment was >25 dB. After reshaping optics (L_5: f = 50 mm and L_6: f = 100 mm) for beam size adjustment and astigmatism correction, another half-wave plate is used to align the polarization of the NIR beam with the crystallographic Z-axis of the nonlinear crystal which is parallel to the thickness of the crystal in this case. The NIR beam was then focused with a lens (L_7: f = 150 mm) into the 40 mm long periodically poled MgO:LiNbO$_3$ (PPLN). The $1/e^2$ waist diameter of the focused beam inside the crystal was measured to be ~95 µm, which was experimentally verified to be the optimum focusing condition at the highest input power. The focusing conditions were identical for all pump source configurations. The PPLN crystal was mounted into a temperature-controlled closed-top oven. The temperature was measured with a temperature sensor in the oven and corresponds to an average temperature. It was optimized at each pump power level. The spectral components were separated by a dichroic mirror (DM).

3.2 Experimental results

The SHG power was measured for three source configurations: a single amplifier (A_1), CBC of two amplifiers (A_{1+2}) and CBC of three amplifiers (A_{1+2+3}). Results are shown in Fig. 4. We fitted the pump depletion approximation [30]

$$P_{2\omega} = P_\omega \times \tanh^2(\sqrt{\eta P_\omega}), \tag{3}$$

where η is the nonlinear conversion efficiency, to the experimental values for pump powers < 6 W. The nonlinear conversion efficiencies in case A_1, A_{1+2} and A_{1+2+3} obtained by numerical fitting are 2.6%/W, 3.7%/W and 4.5%/W, respectively. This corresponds to an increase of up to 73% enhanced by the beam clean-up and the scaled brightness. We attribute the deviation of measured SHG power from the theoretical fit for $P_\omega \geq 6$ W to thermal dephasing due to localized heating caused by SH absorption [9]. This limited the maximum SHG output power to 2.09 W for 9.2 W of NIR input power (conversion efficiency >22%). However it is so far the highest power achieved at λ = 488 nm by single-pass SHG of a diode-laser-based system, thanks to the simultaneous increase of power and brightness provided by the coherent combining architecture.
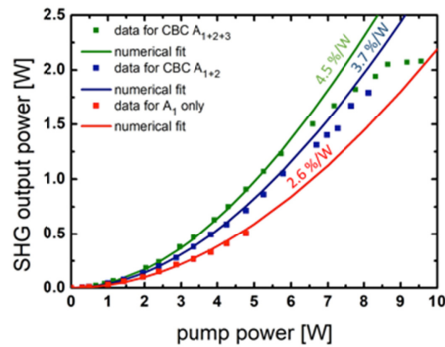
Fig. 4. SHG output power ($P_{2\omega}$) vs. fundamental pump power (P_ω) with corresponding numerical fits using pump depletion approximation.

A further investigation regarding the effects of thermal dephasing on the SHG power was performed by mechanical low frequency chopping (~0.7 Hz, 50% duty cycle) of the NIR beam at different pump power levels. Figure 5(a) shows a photodiode measurement of the SHG power and chopped pump beam with 7 W peak pump power. The results show a clear degradation in the SH power level during each pulse. This degradation in the SHG power indicates the onset of thermal dephasing. This effect was observed for pump powers higher than 6 W. The peak power of SHG can be considered as the SHG power level prior to adverse effects of thermal dephasing. When the peak power of SHG is plotted against the fundamental input power for $P_\omega > 6$ W, it followed the numerical fit nicely as shown in Fig. 5(b). This supports our conclusion that further increase of the SH power was limited by thermal effects in the PPLN crystal and not by the available pump power or the pump beam quality.
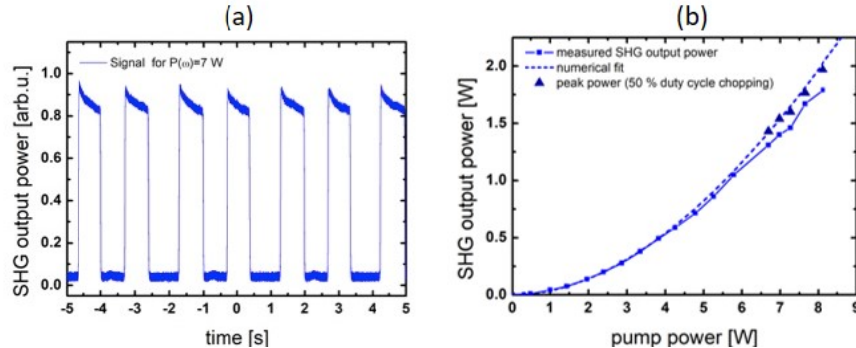
Fig. 5. (a) Photodiode measurements of the SHG output power with chopped pump beam. (b) SHG output power in CW and SHG peak power in QCW (50% duty cycle) operation. The used pump beam was generated by CBC of A_{1+2}.

The crystal temperature acceptance bandwidth measured at $P_\omega = 1$ W (blue curve) and $P_\omega = 7$ W (red curve) is shown in Fig. 6. The FWHM temperature bandwidth was about 0.6°C. The down shift of 0.4°C in the crystal phase matching temperature also indicates the overheating of the crystal due to SH absorption at high pump powers [4]. These thermal effects can be reduced by using nonlinear crystals with better thermal handling in a cascade scheme as described in [9,10].
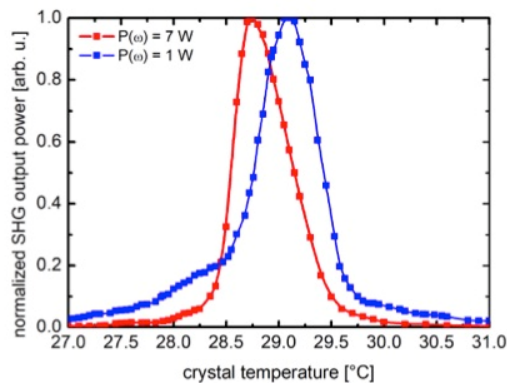
Fig. 6. Normalized SHG power vs. crystal temperature at P_ω = 1 W (blue curve) and P_ω = 7 W (red curve) under CW operation.

The measured spectral FWHM linewidth of the generated blue-green light (488 nm) was less than 20 pm limited by the resolution of the optical spectrum analyzer. The beam quality of SHG was close to diffraction-limited ($M^2_{4\sigma} < 1.2$). The improved beam quality of the SHG beam compared to the fundamental input beam ($M^2_{4\sigma} < 2.5$) is caused by the so-called nonlinear beam clean-up [31].

4. Conclusion and perspectives

Coherent beam combining is an important approach for power scaling of diode laser systems when high spatial quality and narrow linewidth are required. In this work, we used a simple architecture and only three amplifiers allowing to combine 12.9 W in one single beam. The beam quality was significantly increased by a beam cleanup inherent to the CBC process, resulting in a beam quality factor of $M^2_{4\sigma} < 1.1 \times 2.5$ and 86% power content in the central lobe. Those results compare favorably with previous demonstrations of CBC with diode lasers [17–24], regarding both the combined power per amplifier and the simplicity of the setup. Furthermore, the multi-arm MOPA configuration used here could easily be scaled to a larger number of amplifiers, should a larger NIR power be required.

The coherently combined beam was used for single pass nonlinear frequency conversion in a PPLN crystal. As compared to direct SHG of single tapered devices, the improved beam quality of the combined beam in the infrared increases significantly the nonlinear conversion efficiency. A maximum SH power of 2.09 W at 488 nm was reached, limited by thermal dephasing of the PPLN, as confirmed using a pulsed pump beam. Further increase of the output power in the visible spectral range would firstly require the use of different nonlinear crystals in order to deal with the thermal roll-over of the conversion efficiency.

The CBC architecture demonstrated here relies only on off-the-shelf optical elements combined with state of art TPAs. As tapered amplifiers are now available at a wide range of wavelengths, from to the red to the NIR [7], our setup can easily be adapted for other applications. Besides its use for nonlinear frequency conversion towards the visible, our approach would also be effective to develop powerful pump sources for high-brightness pumping of fibre or bulk-crystal amplifiers. The output power could even be further increased by dense spectral beam combining of several similar CBC interferometers operating at slightly different wavelengths, as commonly used with single emitters and bars [32] offering a potential path to future CBC-based direct diode high brightness material processing systems.

References

1. F. Bachmann, P. Loosen, and R. Poprawe, *High Power Diode Lasers: Technology and Applications* (Springer Series in Optical Sciences, 2007).
2. R. W. Boyd, *Nonlinear Optics* (Elsevier, 2003).
3. G. D. Miller, R. G. Batchko, W. M. Tulloch, D. R. Weise, M. M. Fejer, and R. L. Byer, "42%-efficient single-pass cw second-harmonic generation in periodically poled lithium niobate," Opt. Lett. **22**(24), 1834–1836 (1997).
4. S. C. Kumar, G. K. Samanta, and M. Ebrahim-Zadeh, "High-power, single-frequency, continuous-wave second-harmonic-generation of ytterbium fiber laser in PPKTP and MgO:sPPLT," Opt. Express **17**(16), 13711–13726 (2009).
5. A. Müller, S. Marschall, O. B. Jensen, J. Fricke, H. Wenzel, B. Sumpf, and P. E. Andersen, "Diode laser based light sources for biomedical applications," Laser Photonics Rev. **7**(5), 605–627 (2013).
6. A. Jechow, R. Menzel, K. Paschke, and G. Erbert, "Blue-green light generation using high brilliance edge emitting diode lasers," Laser Photonics Rev. **4**(5), 633–655 (2010).
7. B. Sumpf and K. Paschke, "Spectrally stabilized high-power high-brightness DBR-tapered lasers in the VIS and NIR range," Proc. SPIE **10518**, 44 (2018).
8. O. B. Jensen, A. K. Hansen, A. Müller, B. Sumpf, P. M. Petersen, and P. E. Andersen, "Efficient generation of 3.5W laser light at 515nm by frequency doubling a single-frequency high power DBR tapered diode laser," Opt. Commun. **392**, 167–170 (2017).
9. A. K. Hansen, M. Tawfieq, O. B. Jensen, P. E. Andersen, B. Sumpf, G. Erbert, and P. M. Petersen, "Concept for power scaling second harmonic generation using a cascade of nonlinear crystals," Opt. Express **23**(12), 15921–15934 (2015).
10. S. C. Kumar, G. K. Samanta, K. Devi, and M. Ebrahim-Zadeh, "High-efficiency, multicrystal, single-pass, continuous-wave second harmonic generation," Opt. Express **19**(12), 11152–11169 (2011).
11. P. Crump, G. Erbert, H. Wenzel, C. Frevert, C. M. Schultz, K.-H. Hasler, R. Staske, B. Sumpf, A. Maassdorf, F. Bugge, S. Knigge, and G. Trankle, "Efficient High-Power Laser Diodes," IEEE J. Sel. Top. Quantum Electron. **19**(4), 1501211 (2013).
12. O. B. Jensen, A. K. Hansen, A. Muller, B. Sumpf, A. Unterhuber, W. Drexler, P. M. Petersen, and P. E. Andersen, "Power Scaling of Nonlinear Frequency Converted Tapered Diode Lasers for Biophotonics," IEEE J. Sel. Top. Quantum Electron. **20**(2), 307–321 (2014).
13. T. Y. Fan, "Laser beam combining for high-power, high-radiance sources," IEEE J. Sel. Top. Quantum Electron. **11**(3), 567–577 (2005).
14. G. D. Goodno and J. E. Rothenberg, "Engineering of Coherently Combined, High-Power Laser Systems," in *Coherent Laser Beam Combining* (Wiley-Blackwell, 2013), pp. 1–44.
15. A. Klenke, M. Müller, H. Stark, M. Kienel, C. Jauregui, A. Tünnermann, and J. Limpert, "Coherent Beam Combination of Ultrafast Fiber Lasers," IEEE J. Sel. Top. Quantum Electron. **24**(5), 1–9 (2018).
16. S. M. Redmond, D. J. Ripin, C. X. Yu, S. J. Augst, T. Y. Fan, P. A. Thielen, J. E. Rothenberg, and G. D. Goodno, "Diffractive coherent combining of a 2.5 kW fiber laser array into a 1.9 kW Gaussian beam," Opt. Lett. **37**(14), 2832–2834 (2012).
17. R. K. Huang, B. Chann, L. J. Missaggia, S. J. Augst, M. K. Connors, G. W. Turner, A. Sanchez-Rubio, J. P. Donnelly, J. L. Hostetler, C. Miester, and F. Dorsch, "Coherent combination of slab-coupled optical waveguide lasers," Proc. SPIE **7230**, 72301G (2009).
18. J. Montoya, S. J. Augst, K. Creedon, J. Kansky, T. Y. Fan, and A. Sanchez-Rubio, "External cavity beam combining of 21 semiconductor lasers using SPGD," Appl. Opt. **51**(11), 1724–1728 (2012).
19. B. Liu and Y. Braiman, "Coherent addition of high power broad-area laser diodes with a compact VBG V-shaped external Talbot cavity," Opt. Commun. **414**, 202–206 (2018).
20. S. M. Redmond, K. J. Creedon, J. E. Kansky, S. J. Augst, L. J. Missaggia, M. K. Connors, R. K. Huang, B. Chann, T. Y. Fan, G. W. Turner, and A. Sanchez-Rubio, "Active coherent beam combining of diode lasers," Opt. Lett. **36**(6), 999–1001 (2011).
21. J. L. Levy and K. Roh, "Coherent array of 900 semiconductor laser amplifiers," Proc. SPIE **2382**, 58–70 (1995).
22. K. J. Creedon, S. M. Redmond, G. M. Smith, L. J. Missaggia, M. K. Connors, J. E. Kansky, T. Y. Fan, G. W. Turner, and A. Sanchez-Rubio, "High efficiency coherent beam combining of semiconductor optical amplifiers," Opt. Lett. **37**(23), 5006–5008 (2012).

23. G. Schimmel, I. Doyen-Moldovan, S. Janicot, M. Hanna, J. Decker, P. Crump, G. Blume, G. Erbert, P. Georges, and G. Lucas-Leclin, "Rear-side resonator architecture for the passive coherent combining of high-brightness laser diodes," Opt. Lett. **41**(5), 950–953 (2016).
24. G. Schimmel, S. Janicot, M. Hanna, J. Decker, P. Crump, G. Erbert, U. Witte, M. Traub, P. Geaorges, and G. Lucals-Leclin, "Coherent beam combining architectures for high power tapered laser arrays," Proc. SPIE **10084**, 1008600 (2017).
25. P. Albrodt, M. Hanna, F. Moron, J. Decker, M. Winterfeldt, G. Blume, G. Erbert, P. Crump, P. Georges, and G. Lucas-Leclin, "Coherent combining of high brightness tapered lasers in master oscillator power amplifier configuration," Proc. SPIE **10514**, 105140T (2018).
26. C. Fiebig, G. Blume, C. Kaspari, D. Feise, J. Fricke, M. Matalla, W. John, H. Wenzel, K. Paschke, and G. Erbert, "12 W high-brightness single-frequency DBR tapered diode laser," Electron. Lett. **44**(21), 1253–1255 (2008).
27. G. D. Goodno, C.-C. Shih, and J. E. Rothenberg, "Perturbative analysis of coherent combining efficiency with mismatched lasers," Opt. Express **18**(24), 25403–25414 (2010).
28. G. D. Boyd and D. A. Kleinman, "Parametric interaction of focused Gaussian light beams," J. Appl. Phys. **39**(8), 3597–3639 (1968).
29. M. Uebernickel, R. Güther, G. Blume, C. Fiebig, K. Paschke, and G. Erbert, "Study of the properties of the SHG with diode lasers," Appl. Phys. B **99**(3), 457–464 (2010).
30. W. P. Risk, *Compact Blue-Green Lasers* (Cambridge University, 2003)
31. E. Karamehmedović, C. Pedersen, O. B. Jensen, and P. Tidemand-Lichtenberg, "Nonlinear beam clean-up using resonantly enhanced sum-frequency mixing," Appl. Phys. B **96**(2-3), 409–413 (2009).
32. U. Witte, F. Schneider, M. Traub, D. Hoffmann, S. Drovs, T. Brand, and A. Unger, "kW-class direct diode laser for sheet metal cutting based on DWDM of pump modules by use of ultra-steep dielectric filters," Opt. Express **24**(20), 22917–22929 (2016).

Coherent beam combining of high power quasi continuous wave tapered amplifiers

P. Albrodt,[1] M. Niemeyer,[2] P. Crump,[2] J. Hamperl,[1] F. Moron,[1] P. Georges,[1] and G. Lucas-Leclin[1],*

[1]*Laboratoire Charles Fabry, Institut d'Optique Graduate School, CNRS, Université Paris-Saclay, 2 Avenue Augustin-Fresnel, 91127 Palaiseau, France*
[2]*Ferdinand-Braun-Institut, Leibniz-Institut für Höchstfrequenztechnik, Gustav-Kirchhoff-Str. 4, 12489 Berlin, Germany*
gaelle.lucas-leclin@institutoptique.fr

Abstract: We demonstrate coherent beam combining of four high brightness tapered amplifiers in pulsed, quasi continuous wave (QCW) operation, seeded by a 976 nm laser diode. The maximum power of 22.7 W was achieved with > 64% combining efficiency in a close to diffraction limited beam. We discuss turn-on dynamics of tapered amplifiers operated in pulsed mode in detail.

1. Introduction

The power and brightness of laser diodes are continuously increasing and as the cost per watt is decreasing at the same time, they become more attractive for industrial application requiring high brightness [1]. It is however necessary to make use of beam combining technologies in order to meet the power requirements in this regard [2]. Especially spectral beam combining is a widely used approach for development of high brightness diode laser systems [3,4], the ultimate limitation is however the power available within a certain spectral linewidth. Coherent beam combining (CBC) relies on constructive interference of several separate beams and allows to scale the power available within a very narrow spectral bandwidth in a beam with nearly diffraction limited beam quality. CBC with diode lasers has been demonstrated in many different external cavity configurations [5–9] and in master oscillator power amplifier (MOPA) configurations [10,11]. The highest combined power has been achieved in a MOPA setup using large arrays of single mode amplifiers [11]. Using a few high brightness tapered amplifiers is a promising approach to reduce the complexity of CBC setups and yields a higher power per element [12,13]. Operating those amplifiers in pulsed, quasi continuous wave (QCW) mode, allows even higher powers per amplifier to be reached as the devices are no longer limited by thermal rollover. However CBC of diode lasers has commonly been demonstrated in continuous wave (CW) operation and there are only few demonstrations of CBC of pulsed diode lasers [14]. Pulsed (QCW) semiconductor amplifiers are not in steady state but exhibit dynamic temperature changes. This consequently leads to a dynamic change of the accumulated phase and of the beam propagation parameters, which makes CBC with pulsed amplifiers more challenging. Additionally, high brightness pulsed sources with high spectral purity are in demand as NIR pump sources of solid state lasers and for nonlinear frequency conversion to address medical applications of modulated high power visible laser sources [15–17]. Furthermore CBC of pulsed tapered amplifiers may improve the performance of diode-laser-based portable differential absorption lidar systems used for atmospheric measurements [18,19].

We use a master oscillator power amplifier (MOPA) configuration with four parallel tapered amplifiers operated in QCW mode. Their coherent superposition is achieved in a filled aperture approach using standard beamsplitters as the combiner elements. The experimental setup is described in section 2. The performance of the tapered amplifiers is characterized in section 3

especially regarding the dynamic change in phase as the devices are turned on. We observe and analyze effects associated with the operation of the pulsed amplifiers at high bias, which induce strong peak power fluctuations and deteriorate the seed line stability. Finally we demonstrate CBC of four high brightness tapered amplifiers in QCW mode and compare the results to operation in CW mode (see section 4).

2. Experimental setup

We used 5 mm long amplifiers consisting of a 1 mm long 4 µm wide ridge waveguide (RW) followed by a 4 mm long tapered section (TP, 6° taper angle). The facets of the devices were passivated and anti-reflection coated ($R_1 = 0.01\%$ for RW facet and $R_2 = 0.05\%$ for TP facet) [20] The epitaxial design of the devices was the so called ELOD2 design [21], having an extremely low vertical divergence, that has proven to maintain good beam quality at high drive currents in tapered laser format [21], with good results also in related designs in truncated tapered amplifier format [22]. We used individually mounted emitters instead of an array of amplifiers to achieve a simple modular setup and benefit from the efficient heat removal in each heatsink. The devices were mounted p-side up on CuW heat sinks onto C-mounts with separate electrical contacts for the currents I_{rw} into the RW and I_{tp} into the tapered section of each device respectively. An additional CuW heat spreader was also attached to the p-side of the tapered amplifier section for improved cooling. The C-mounts were fixed on individual temperature-stabilized mechanical mounts. The current into the RW was not pulsed as it has low impact on the total heat load of the device (< 1 W). We used small variations (+/- 50 mA) of the continuous current into the ridge section of each amplifier for phase-control [23]. We used Arroyo 4320-QCW laser diode drivers for the current into the tapered section of each device.

The pulse durations were in the order of a few milliseconds (typically $\Delta t_{QCW} = 2$ ms) and a duty cycle of 10%. The amplifiers were arranged in a multiarm-interferometer as shown in Fig. 1 similar to the experimental setup used in previous work [13]. The seed source was a 100 mW CW narrow linewidth (< 20 MHz) DFB laser at 976 nm. After optical isolation the beam was split using non-polarizing 50:50 beamsplitters. The seed power incident for each amplifier was 20 mW. The amplified beams were collimated in slow axis (SA) and fast axis (FA) individually and the astigmatism was corrected depending on the current into the tapered section. We used
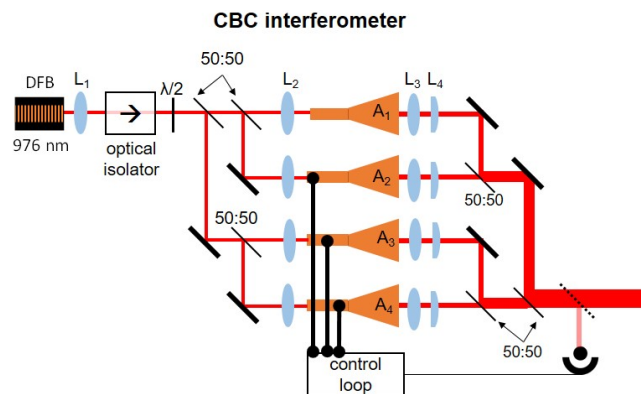
**Fig. 1.** Experimental setup of the CBC-interferometer with four high brightness tapered amplifiers (A_{1-4}). The currents into the DFB seed laser and the RWs of the amplifiers were continuous and only the currents into the tapered section of each amplifier were pulsed. (L_1 and L_2 aspheric lens f = 8 mm NA = 0.5, L_3 aspheric lens f = 2.35 mm NA = 0.55, L_4 cylindrical lens f = 19 mm).

also 50:50 plate beamsplitters for recombining the beams in a filled aperture approach. The intensity of a small part of the output beam (less than 0.5%) was measured with a photodiode, delivering the signal for the microcontroller based closed-loop phase correction.

3. Investigation of the dynamics of the amplifiers

3.1. Optical power and beam quality

The QCW operation of the amplifiers with pulse lengths in the ms-range and duty cycles typically below 10% allows testing the devices beyond the limitations normally set by CW thermal rollover. The influence of the reduced heat load in QCW on the optical output power is clearly visible in the measurements plotted in Fig. 2(a). While there is an onset of the thermal rollover for all four amplifiers at about 10 A in CW mode (dashed lines), this is not the case for QCW operation (solid lines) and the slope efficiency remains constant at about 0.7 W/A resulting in an output power > 9 W for all four amplifiers at 16 A. The output power for moderate currents < 8 A is identical in CW and QCW operation. The beam shapes at the imaged beam waist are shown for one typical amplifier (A3) in Fig. 2(b) for different currents into the tapered section in CW and QCW mode. The beam shapes shown in Fig. 2(b) in QCW mode were measured 0.8 ms after the start of the pulse with 50 μs integration time. At this time, the device temperature and beam shape is stabilized. The observed shapes are typical for tapered amplifiers, with a close to diffraction limited central lobe containing most of the energy and lower intensity higher angle side lobes in the slow axis (SA). The intensity of the side lobes gradually increases at higher currents into the taper leading to decreased power content in the central lobe, which is given in percent for each bias point in Fig. 2(b). The differences in the beam shapes between CW and QCW operation are minor at moderate currents but one can observe a significant degradation of the beam quality when the amplifiers are overdriven in QCW operation leading to a central lobe power content of 73% at 13 A. The beam shapes of the four amplifiers were quite similar with minor differences in the central lobe power content at equal bias conditions (+/- 5%), considering that the beam quality also depends on alignment tolerances for the coupling into the narrow RW.
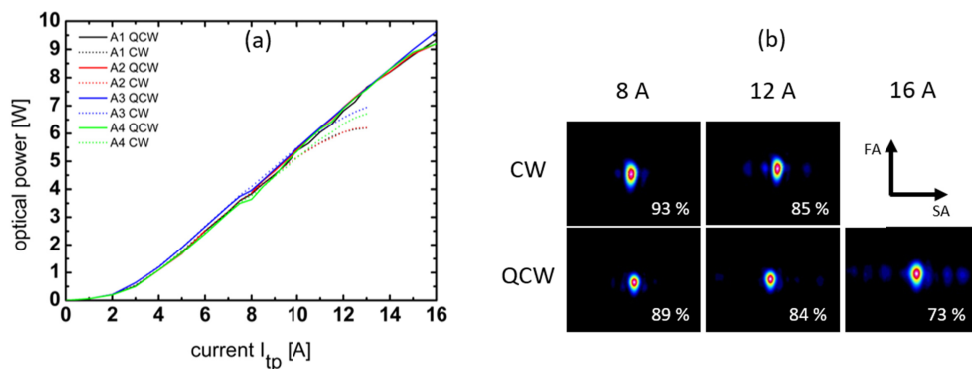
Fig. 2. (a) Optical output power versus drive current into the tapered section for the four amplifiers in CW and QCW operation. (b) Measurements of the beam shape at waist at different bias conditions. The power content in the central lobe was calculated with a 2D Gaussian fit of the central lobe. The integration time of the CCD camera was 50 μs. (Bias conditions for all measurements: $P_{in} = 20$ mW, $I_{rw} = 350$ mA, T = 25°C, $\Delta t_{qcw} = 1$ ms, 10% duty cycle). See **Visualization 1** for the spatial turn-on dynamics in QCW mode. The video shows 20 images of the beam shape measured with 50 μs integration time from the start to the end of the pulse.

Tapered lasers and amplifiers have a temperature induced wandering astigmatism that depends on the current into the tapered section [24,25]. This leads to a dynamic change in the beam shape in SA at the start of each QCW pulse. This effect is shown in the supplementary Visualization 1. We sampled 20 images of the beam shape into a short video showing that the beam is focusing rapidly at the beginning of the pulse and then converges to a stable shape after about 500 µs. The measured 2nd moment beam diameter decreases from 1100 µm to 875 µm, which corresponds to a displacement of the waist in SA by about 80% of the corresponding Rayleigh length at a current of 13 A into the tapered section. The spatial dynamics were similar for all four amplifiers in our setup. In order to ensure a good spatial overlap of the beams during the full pulse duration, it is therefore necessary to operate the different amplifiers at similar bias conditions in order to optimize the coherent beam combining efficiency.

3.2. Temperature - driven piston phase drift of pulsed amplifiers

The rise in temperature as the device is turned on does also increases the effective optical path length in the amplifier and leads to a drift of the accumulated phase in each amplifier. The piston phase drift is approximately proportional to the change in temperature. We measured the phase drift during the QCW pulses by overlapping the output beam from an amplifier with a reference beam as described in detail in [26]. Figure 3(a) shows the measurements for one amplifier at different currents into the tapered section. The amplitude of the piston phase drift increases with the current, and the experimentally measured phase drift was reproduced accurately at all bias points using the following fit function (Eq. 1), as seen in Fig. 3(a):

$$\varphi(t) = \varphi_0 + C \times t - \Delta\varphi_1 \times \exp\left[\frac{-t}{\tau_1}\right] - \Delta\varphi_2 \times \exp\left[\frac{-t}{\tau_2}\right]. \tag{1}$$

The time constants $\tau_{1,2}$ of the two exponential functions were found by fitting to be 0.1 ms and 1 ms respectively and these were independent of the current into the tapered section I_{tp}. The amplitudes of the exponential contributions $\Delta\varphi_{1,2}$ are proportional to I_{tp} and roughly equal for the two exponential contributions. The linear term $C \times t$ describes a linear increase in the average temperature of the heatsink during the pulse and is also proportional to I_{tp}. The amplitude of the overall change in piston is large, reaching 30 π at 13 A for 5 ms long pulses. The dynamic variation in phase is however highly reproducible, consistent between samples and we propose it to be defined by the geometry and efficiency of the amplifiers, the heatsink and the rise-time of the current driver. We thus achieved a very good overlap of the piston phase drifts in all four amplifiers of the interferometer as shown in Fig. 3(b). We used small adjustments (+/- 0.5 A) of the pulsed current into the taper sections in order to achieve a piston phase drift of the same magnitude for all four amplifiers. The inset in Fig. 3(b) shows a zoom into the same data, where one can see that the relative differences in phase between the four amplifiers are in the range of $\pi/10$ only.

3.3. Power stability in QCW mode

We measured the pulse stability at different currents into the tapered section and observed oscillations in the output power as shown in Fig. 4. The period of the oscillations is increasing with time and decreasing with the current into the taper, although there were minor differences between the amplifiers used. The best ones (see amplifier 1, black lines) show significant but stable oscillations at very high currents only. The peak-to-peak amplitude of the oscillations measured at 16 A for amplifier 1 are below 6% of the average power. Devices with a slightly lower performance (see amplifier 2 above) tended to show stronger oscillations at moderate currents (10-12 A) and the oscillations become chaotic at high currents (e.g. 16 A) with a peak-to-peak amplitude of about 12%.
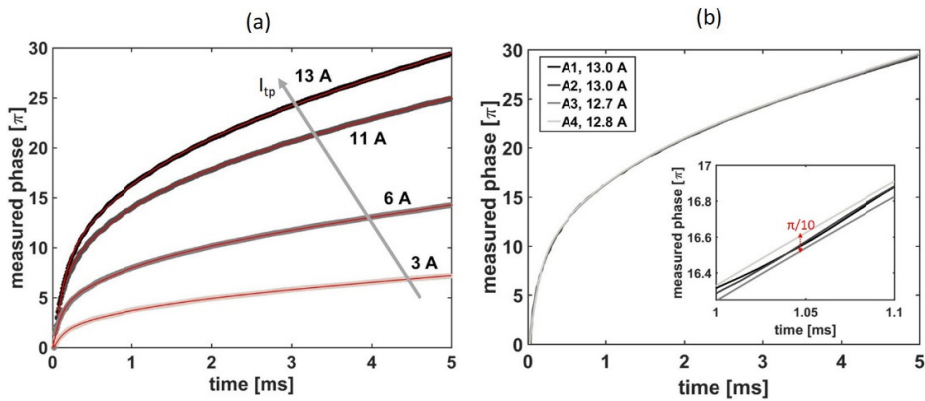
Fig. 3. (a) Measured piston phase drift during QCW operation of amplifier 1 at different currents into the tapered section. The experimental data is plotted as thick grayscale data points and the fitted function as a red solid line. (b) Measured phase drift during QCW operation for all four amplifiers. The currents into the tapered section were slightly adjusted around 13 A in order to achieve the same phase drift and balance slight differences in the efficiency of the devices. The inset shows a zoom into the same data in order to distinguish the different solid lines. (Bias conditions for all measurements: $P_{in} = 20\,mW$, $I_{rw} = 350\,mA$, $T = 25°C$, $\Delta t_{QCW} = 5\,ms$, 10% duty cycle)
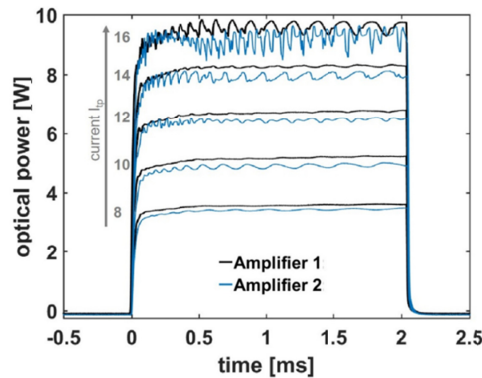

Fig. 4. Measured pulse shape for two amplifiers at 8-16 A current into the tapered section (Bias conditions for all measurements: $P_{in} = 20\,mW$, $I_{rw} = 350\,mA$, $T = 25°C$, $\Delta t_{qcw} = 2\,ms$, 10% duty cycle).

These quasi-periodic oscillations are attributed to parasitic resonances of the narrow spectral line seed signal ($\Delta\nu_{FWHM} < 20\,MHz$) within the amplifier. Indeed though both device facets are AR coated ($R_1 = 0.01\%$ and $R_2 = 0.05\%$), the amplifier acts as a low-finesse scanning Fabry-Perot cavity whose resonance peaks shift during the current pulse following the dynamic phase drift $\varphi(t)$ discussed earlier. Consequently, the period of the oscillations increases during the pulse (cf. Figure 3 and Eq. 1). Furthermore the cavity finesse is enhanced with the amplifier gain, leading to an increase of the modulation depth. The slight disparities in the behavior of the different devices are therefore attributed to small differences in the coating reflectivity, coupling efficiency and gain in the device.

It would be desirable for further studies to use amplifiers with the best possible AR-coating on both facets in order to push the onset of these oscillations to even higher powers, which was not

possible in the framework of this work. Besides the degradation of the beam quality at high bias, the poor pulse stability is another limitation for power scaling by QCW operation in QCW mode. Especially regarding coherent superposition, it is important to have a reasonable stability of the power within the pulse. We therefore limited the current in the tapered section to below 14.5 A for the subsequent CBC experiments, as the pulse stability was insufficient at higher currents.

3.4. Optical feedback from overdriven tapered amplifiers

It is well known that optical feedback from a distant reflector may perturb the lasing properties of a DFB laser, such as frequency, spectral linewidth and power [27]. In particular, weak time-dependent feedback may lead to a rich variety of effects including frequency hopping. We started our experiment with one double-stage Faraday isolator (-55 dB optical isolation) between the seed DFB laser diode and the CBC interferometer to limit reflection effects. A small part of the amplified beam gets reflected at the output facet ($R_2 = 0.5\%$) of the amplifier and propagates backwards through the setup towards the seed laser. This optical feedback is spectrally identical to the seed laser with only minor ASE contribution. As several parallel overdriven tapered amplifiers lead to high levels of absolute optical feedback, it appears that this isolation was not sufficient to prevent perturbations of the seed laser. Indeed we measured the seed laser frequency using a Fabry-Perot interferometer (Thorlabs SA210-8B, FSR = 10 GHz, finesse > 150). Figure 5(a) shows the measured seed laser frequency perturbations (blue line) induced by optical feedback from one tapered amplifier during a 5 ms-long QCW pulse (black line). The feedback leads to a frequency shift and a frequency hopping up to 80 MHz. The decreasing period of the observed frequency hopping appears to be linked to the phase dynamics discussed in section 3.2.
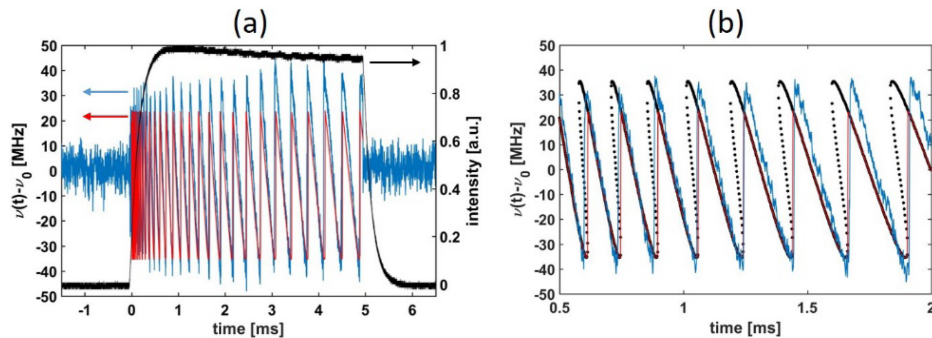

Fig. 5. (a) Measurement of the seed laser frequency perturbations $\nu(t) - \nu_0$ (blue), and simulated laser frequency perturbations (red) induced by optical feedback from a single tapered amplifier (A1) operated at $I_{tp} = 13$ A (black). (b) Zoom into the measured frequency change with the calculated solutions (black dots) for the seed laser frequency considering the phase change in the amplifier and the expected frequency hopping in the multi-stable regime (red solid line). The simulation parameters used were: $\alpha = 5$, $R_s = 0.01$, $R_e = 9 \times 10^{-10}$, $\tau_s = 50$ ps, $\tau_e(t) = 10$ $ns + \frac{\lambda \, \varphi(t)_{13A}}{\pi c}$, where $\varphi(t)_{13A}$ was taken from Fig. 3(a)). The optical isolation was -55 dB.

In the presence of an optical feedback, the frequency shift of a single-mode laser is described by [27]

$$\Delta\nu(t) = \nu(t) - \nu_0 = -\frac{\kappa}{2\pi}[\sin(2\pi \, \nu(t) \times \tau_e(t)) + \alpha \times \cos(2\pi \, \nu(t) \times \tau_e(t))], \qquad (2)$$

with the coupling coefficient

$$\kappa = \frac{(1 - R_s)\sqrt{R_e}}{\tau_s\sqrt{R_s}}, \tag{3}$$

where R_s is the reflectivity of the laser output facet, R_e is the effective reflectivity of the external optical setup, τ_s is the roundtrip time in the laser, $\tau_e(t)$ is the time dependent round trip time of the feedback and α is the linewidth enhancement factor. Frequency hopping occurs for higher levels of the product $\kappa\tau_e$ when there are multiple solutions for Eq. 2. We calculated the frequency change using the measurement of the phase drift at $I_{tp} = 13$ A given in Fig. 3(a) for defining $\tau_e(t)$ with $\tau_e(0) = 10$ ns related to the distance from the seed laser to the amplifier (about 1.5 m in this laboratory scale experiment). We compared in Figs. 5(a) and 5(b) the experimental evolution of the seed frequency during the pulse with a numerical resolution of Eq. 2. Each black dot in Fig. 5(b) is one calculated solution to this equation. We can easily identify regimes with multiple solutions where frequency hopping is likely to occur. The red line represents the expected evolution of the seed laser frequency, assuming that the frequency hopping occurs when the change in the laser frequency has reached the local minimum. Figure 5(a) shows that the measurement (blue) and simulation (red) are in good agreement during the whole pulse. The value for the external reflection of the extended cavity $R_e = 9 \times 10^{-10}$ used in these simulations may appear low but corresponds to the small part of the optical feedback from the amplifier that couples back into the seed laser. Indeed feedback from a distant reflector is critical even at very low level (see [27]). In comparison feedback from near passive optical elements (such as L_1 in Fig. 1.) may have a similar level, but would be less critical as it would be induced at short distance and would result in a stable piston phase.

Equation (2) has multiple solutions, resulting in frequency hopping, if $\sqrt{1 + \alpha^2}\kappa\tau_e > 1$. With our simulation parameters, the product $\sqrt{1 + \alpha^2}\kappa\tau_e$ was equal to about 2.44. As $\kappa \propto \sqrt{R_e}$ we estimate that the optical isolation in our experimental conditions should be better than -62.7 dB to avoid those frequency hops. Furthermore the maximum change in frequency would be below 10 MHz for an optical isolation better than -73 dB considering that $\Delta\nu \propto \sqrt{R_e}$. We repeated our experiment after increasing the optical isolation from -55 dB to -75 dB by using a third stage of optical isolation and did no longer measure any effect on the laser frequency during the QCW pulses. We conclude that the requirements regarding the optical isolation of a narrow linewidth seed laser can be extremely high in CBC architectures, especially when the amplifiers are overdriven and generate therefore a high level of feedback. The sensitivity to optical feedback could be reduced in an integrated optical setup (to minimize τ_e), by increasing the reflectivity R_s of the seed laser and by further improvement of the AR coatings of the tapered amplifiers (to reduce R_e). Small perturbations of the seed laser frequency in the range of 80 MHz (see Fig. 5(a)) are not necessarily a problem for successful CBC, as this corresponds still to a coherence length in the range of 1 m, but is critical for applications requiring a stable frequency.

4. Coherent beam combining in QCW operation

The phase matching between the four amplified beams in the coherent beam combining experiment was achieved by a sequential hill-climbing algorithm with stepwise adjustment of the current into the RW from pulse to pulse. The error signal was measured with a fast photodiode (see Fig. 1) measuring the power at the CBC output. The currents into the amplifiers were optimized separately: the current into the RW of A2 was optimized first from pulse to pulse, then the current into A3 similarly and finally the current into A4. A variation of $\pm$ 35 mA corresponded to a phase shift of $\pm\pi$ and we used steps of 0.75 mA for the hill-climbing algorithm. Phase control with this simple sequential pulse-to-pulse algorithm was sufficient as the phase noise in the interferometer was dominated by very low frequencies (<1 Hz). The feedback loop was triggered to maximize the power of the combined beam after 50% of the pulse duration as the

pulse stability was better in the second half of the pulse (cf. Fig. 4). The pulse duration was adjustable from 1 to 10 ms and the duty cycle from 0.01 to 10% (we typically used 2 ms pulses and a duty cycle of 10%). The achieved coherently combined power P_{CBC} and the corresponding combining efficiency, defined as the ratio of the combined power over the sum of the individual powers ($\eta_{CBC} = P_{CBC} \big/ \sum_1^4 P_i$), are summarized in Table 1. Power and combining efficiency for operation in continuous wave mode are also given for comparison. The current values I_{tp} into the tapered section correspond to the average of the four currents, which were slightly adjusted in order to optimize the phase matching during the pulse (see Fig. 3(b)). For each measurement, the SA cylindrical lenses (L_4 see Fig. 1) were positioned to compensate for the amplifier astigmatism and optimize the overlap of the beams during the current pulse despite the wandering SA waist position mentioned in section 3.1.

Table 1. Measured combined power P$_{CBC}$ and combining efficiency for coherent superposition of two (A1 + A2) and four (A1 + A2 + A3 + A4) amplifiers at different currents into the tapered sections. Operating conditions for each individual amplifier: P$_{in}$ = 20 mW, I$_{rw}$ = 300-400 mA, T = 25 °C, Δt$_{qcw}$ = 2 ms, 10% duty cycle.

	QCW				CW	
	2 amplifiers		4 amplifiers		4 amplifiers	
I_{tp} [A]	P$_{CBC}$ [W]	η_{CBC} [%]	P$_{CBC}$ [W]	η_{CBC} [%]	P$_{CBC}$ [W]	η_{CBC} [%]
8	-		-		10.8	72
10	9.77	84	16.8	71	14.4	71
12.3	12.4	85	20.4	68	**16.9**	**71**
13	12.7	81	21.7	69	-	-
14.5	13.7	79	**22.7**	**64**	-	-

At the maximum operating current I_{tp} = 14.5 A per amplifier the QCW output power of the coherently combined output beam reached 22.7 W. This is the highest power reported for CBC of tapered lasers or amplifiers. In contrast we measured 16.9 W as the highest power in CW, which is about 25% lower than the maximum QCW power. The combining efficiency at the highest bias was > 64% limited by the degradation of the beam quality at high currents. The combining efficiency at moderate currents was measured to be > 70% and almost identical for QCW and CW operation. The combining efficiency of the coherent superposition of only two amplifiers was slightly higher, in the range of 79-84%, as each combining step adds combining losses.

A large part of the combining losses were attributed to a spatial clean-up of the beam. The beam from each amplifier has a central lobe power content in the order of 75% (cf. Fig. 2), which is significantly lower than the central lobe power content of the coherently combined beam of 92% as shown in Fig. 6. The M^2 beam propagation factor of the combined beam was below 1.3 in both directions considering the $1/e^2$ beam diameters. The more accurate and standard definition of the M^2 factor, using the 2nd moment beam diameters, resulted in 1.3 in FA and 5 in SA : this is below the beam propagation factor of the individual amplifiers $M^2 > 10$ in SA at high bias. The improved beam quality of the combined beam (evidenced by higher central lobe power content and improved M^2) is typical for coherent beam combining of tapered lasers and amplifiers [12,13]. It is related to a high mismatch in amplitude and phase of the higher order modal content in the individual beams, whereas the central lobes of those individual beams have a high spatial overlap and interfere efficiently. The combining efficiency considering the central lobe powers only was >80% for the whole setup. Slight mismatches in the FA collimation and the parasitic resonances (cf. section 3.3 and Fig. 4) were identified as the limitation for further increase in combining efficiency.

Figure 6 shows the measured pulse stability at three different bias points. We measured the envelope of the pulses over one minute (see thick lines) and the average pulse shapes (see thin
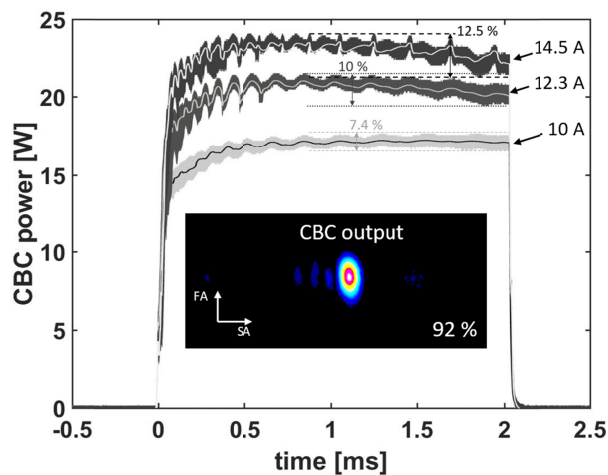
Fig. 6. Measured pulse shape at the output of the CBC interferometer at 10 A, 12.3 A and 14.5 A into each tapered section. At each bias we measured the envelope (1 min integration time) (see thick lines) and the average pulse shape (thin line). The inset shows the waist of the combined beam at the highest bias current and the measured power content in the central lobe. (Bias conditions for all measurements: $P_{in} = 20\,mW$, $I_{rw} = 300\text{-}400\,mA$, $T = 25°C$, $\Delta t_{qcw} = 2\,ms$, 10% duty cycle).

lines). The peak to valley roughness of the pulse envelope increases from 7.4% at 10 A to 12.5% at 14.5 A, mainly caused by the resonance effects in the amplifiers analyzed in section 3.3, with (feedback-induced) instability in the seed source eliminated by using high levels of optical isolation (-75 dB). CBC at even higher bias was unstable as the internal resonance effects perturb the phase control and the oscillations get chaotic. The beam quality of the combined beam was close to the diffraction limit and improved compared to the beam quality of an individual amplifier. This beam clean-up is a typical effect of CBC with tapered lasers or amplifiers [9,13]. The power content in the central lobe of the output beam was > 92%, with only a few higher angle side lobes in SA. The evaluated central lobe power was > 20 W at 14.5 W, which is the highest diffraction limited power reported for a single coherent beam from tapered lasers or amplifiers and is an extremely high value for a single frequency semiconductor based system.

5. Conclusion

In this paper we investigated the dynamics of high power tapered amplifiers in pulsed quasi-continuous operation. The rise in temperature as the device is turned on leads to a change in the beam shape in SA caused by a wandering astigmatism. The phase drift is also related to the rising temperature in the device and was measured for different bias currents in the tapered section. It was shown that good phase matching with residual errors below $\pi/10$ can be achieved even at high currents. Power instabilities in the QCW pulses occur at high bias as resonances in the device interfere with the seed laser beam. Further increase of the current into the taper was limited by the pulse stability and the decreasing beam quality.

CBC of four tapered amplifiers in QCW lead to a total power of 22.7 W with 64% combining efficiency. The advantage in using tapered amplifiers for CBC is the extremely high power per device (here 5.67 W per amplifier) that exceeds the power achievable with single-mode amplifiers by more than a factor of 5. Higher total powers have so far only been achieved by coherent beam combining of large arrays of single-mode amplifiers at the cost of an increased complexity (CBC of 47 single-mode slab-coupled optical waveguide amplifiers yielded 40 W [11]). The achieved

power in the central lobe of the combined beam is higher than 20 W (92% of total power). This is the highest power in a diffraction-limited beam ever reported from a single-frequency system based on tapered lasers or amplifiers. The operation in QCW mode allowed to overcome thermal limitations and to reach about 25% higher power in comparison to CW operation.

The power could be further increased by using more efficient semiconductor structures, either directly as here or fabricated as single-contact truncated tapered amplifiers, which provide the highest reported diffraction limited power (QCW power in the central lobe up to 17 W per device [22]). Higher powers are also likely to be possible by using lower reflectivity coatings and tilted facets on the tapered amplifiers to suppress internal oscillations. Combining these approaches offers a potential path for the development of compact CBC modules exceeding 50 W output power with close to diffraction limited beam quality. Efforts to reduce the pulse durations to the microsecond and nanosecond regime are also promising for potential applications in biomedicine [15,16] and remote sensing [18,19].

Acknowledgments

References

1. F. Bachmann, P. Loosen, and R. Poprawe, eds., *High Power Diode Lasers: Technology and Applications*, Springer Series in Optical Sciences (Springer-Verlag, 2007).
2. T. Y. Fan, "Laser beam combining for high-power, high-radiance sources," IEEE J. Sel. Top. Quantum Electron. **11**(3), 567–577 (2005).
3. S. Strohmaier, C. Tillkorn, P. Olschowsky, and J. Hostetler, "High-power, high-brightness direct-diode lasers," Opt. Photonics News **21**(10), 24–29 (2010).
4. V. Daneu, A. Sanchez, T. Y. Fan, H. K. Choi, G. W. Turner, and C. C. Cook, "Spectral beam combining of a broad-stripe diode laser array in an external cavity," Opt. Lett. **25**(6), 405–407 (2000).
5. L. Bartelt-Berger, U. Brauch, A. Giesen, H. Huegel, and H. Opower, "Power-scalable system of phase-locked single-mode diode lasers," Appl. Opt. **38**(27), 5752–5760 (1999).
6. B. Liu, Y. Liu, and Y. Braiman, "Coherent addition of high power laser diode array with a V-shape external Talbot cavity," Opt. Express **16**(25), 20935–20942 (2008).
7. D. Paboeuf, G. Lucas-Leclin, P. Georges, N. Michel, M. Krakowski, J. Lim, S. Sujecki, and E. Larkins, "Narrow-line coherently combined tapered laser diodes in a Talbot external cavity with a volume Bragg grating," Appl. Phys. Lett. **93**(21), 211102 (2008).
8. J. Montoya, S. J. Augst, K. Creedon, J. Kansky, T. Y. Fan, and A. Sanchez-Rubio, "External cavity beam combining of 21 semiconductor lasers using SPGD," Appl. Opt. **51**(11), 1724–1728 (2012).
9. G. Schimmel, I. Doyen-Moldovan, S. Janicot, M. Hanna, J. Decker, P. Crump, G. Blume, G. Erbert, P. Georges, and G. Lucas-Leclin, "Rear-side resonator architecture for the passive coherent combining of high-brightness laser diodes," Opt. Lett. **41**(5), 950–953 (2016).
10. S. M. Redmond, K. J. Creedon, J. E. Kansky, S. J. Augst, L. J. Missaggia, M. K. Connors, R. K. Huang, B. Chann, T. Y. Fan, and G. W. Turner, "Active coherent beam combining of diode lasers," Opt. Lett. **36**(6), 999–1001 (2011).
11. K. J. Creedon, S. M. Redmond, G. M. Smith, L. J. Missaggia, M. K. Connors, J. E. Kansky, T. Y. Fan, G. W. Turner, and A. Sanchez-Rubio, "High efficiency coherent beam combining of semiconductor optical amplifiers," Opt. Lett. **37**(23), 5006–5008 (2012).
12. G. Schimmel, S. Janicot, M. Hanna, J. Decker, P. Crump, G. Erbert, U. Witte, M. Traub, P. Georges, and G. Lucas-Leclin, "Coherent beam combining architectures for high power tapered laser arrays," Proc. SPIE **10086**, 100860O (2017).
13. P. Albrodt, M. T. Jamal, A. K. Hansen, O. B. Jensen, G. Blume, K. Paschke, P. Crump, P. Georges, and G. Lucas-Leclin, "Coherent combining of high brightness tapered amplifiers for efficient non-linear conversion," Opt. Express **27**(2), 928–937 (2019).
14. J. S. Osinski, D. Mehuys, D. F. Welch, R. G. Waarts, J. S. Major, K. M. Dzurko, and R. J. Lang, "Phased array of high-power, coherent, monolithic flared amplifier master oscillator power amplifiers," Appl. Phys. Lett. **66**(5), 556–558 (1995).
15. B. Gupta, M. Elagouz, D. McHugh, V. Chong, and S. Sivaprasad, "Micropulse diode laser photocoagulation for central serous chorio-retinopathy," Clin. Exp. Ophthalmol. **37**(8), 801–805 (2009).
16. L. Chehade, G. Chidlow, J. Wood, and R. J. Casson, "Short-pulse duration retinal lasers: a review," Clin. Exp. Ophthalmol. **44**(8), 714–721 (2016).

17. M. Christensen, A. K. Hansen, D. Noordegraaf, O. B. Jensen, and P. M. W. Skovgaard, "Deep modulation of second-harmonic light by wavelength detuning of a laser diode," Appl. Opt. **56**(8), 2250–2254 (2017).

18. A. R. Nehrir, K. S. Repasky, and J. L. Carlsten, "Eye-Safe Diode-Laser-Based Micropulse Differential Absorption Lidar (DIAL) for Water Vapor Profiling in the Lower Troposphere," J. Atmos. Oceanic Technol. **28**(2), 131–147 (2011).

19. A. R. Nehrir, K. S. Repasky, and J. L. Carlsten, "Micropulse water vapor differential absorption lidar: transmitter design and performance," Opt. Express **20**(22), 25137–25151 (2012).

20. R_2 was slightly higher as these amplifiers have been designed for backside extended cavity configurations in the first place, where a weak feedback from R_2 was necessary.

21. P. Crump, J. Decker, M. Winterfeldt, J. Fricke, A. Maaßdorf, G. Erbert, and G. Tränkle, "Development of high-power diode lasers with beam parameter product below 2 mm mrad within the BRIDLE project," Proc. SPIE **9348**, 93480D (2015).

22. X. Wang, G. Erbert, H. Wenzel, P. Crump, B. Eppich, S. Knigge, P. Ressel, A. Ginolas, A. Maassdorf, and G. Trankle, "17-W Near-Diffraction-Limited 970-nm Output From a Tapered Semiconductor Optical Amplifier," IEEE Photonics Technol. Lett. **25**(2), 115–118 (2013).

23. P. Albrodt, M. Hanna, F. Moron, J. Decker, M. Winterfeldt, G. Blume, G. Erbert, P. Crump, P. Georges, and G. Lucas-Leclin, "Coherent combining of high brightness tapered lasers in master oscillator power amplifier configuration," Proc. SPIE **10514**, 28 (2018).

24. L. Borruel, S. Sujecki, P. Moreno, J. Wykes, M. Krakowski, B. Sumpf, P. Sewell, S.-C. Auzanneau, H. Wenzel, D. Rodriguez, T. M. Benson, E. C. Larkins, and I. Esquivias, "Quasi-3-D simulation of high-brightness tapered lasers," IEEE J. Quantum Electron. **40**(5), 463–472 (2004).

25. M. T. Kelemen, J. Weber, S. Kallenbach, C. Pfahler, M. Mikulla, and G. Weimann, "Astigmatism and beam quality of high-brightness tapered diode lasers," Proc. SPIE **5452**, 233 (2004).

26. P. Albrodt, M. T. Jamal, A. K. Hansen, O. B. Jensen, M. Niemeyer, G. Blume, K. Paschke, P. Crump, J. Hamperl, P. Georges, and G. Lucas-Leclin, "Recent progress in brightness scaling by coherent beam combining of tapered amplifiers for efficient high power frequency doubling," Proc. SPIE **10900**, 109000O (2019).

27. R. Tkach and A. Chraplyvy, "Regimes of feedback effects in 1.5-μm distributed feedback lasers," J. Lightwave Technol. **4**(11), 1655–1661 (1986).

Low-index quantum-barrier single-pass tapered semiconductor optical amplifiers for efficient coherent beam combining

(Preliminary version – **unpublished preprint** - Provisional acceptance for publication in SST)

P. Albrodt[1], M. Niemeyer[2], M. Elattar[2], J. Hamperl[1], G. Blume[2], A. Ginolas[2], J. Fricke[2], A. Maaßdorf[2], P. Georges[1], G. Lucas-Leclin[1], K. Paschke[2] and P. Crump[2]

[1.] Université Paris-Saclay, Institut d'Optique Graduate School, CNRS, Laboratoire Charles Fabry, 91127, Palaiseau, France
[2.] Ferdinand-Braun-Institut, Leibniz-Institut für Höchstfrequenztechnik, Gustav-Kirchhoff Str. 4, D-12489 Berlin, Germany

E-mail: paul.crump@fbh-berlin.de

Abstract

The requirements for coherent combination of high power GaAs-based single-pass tapered amplifiers are studied. Changes to the epitaxial layer structure are shown to bring higher beam quality and hence improved combining efficiency for one fixed device geometry. Specifically, structures with large vertical near field and low wave-guiding from the active region show 10% higher beam quality and coherent combining efficiency than reference devices. As a result, coherent combining efficiency is shown to be limited by beam quality, being directly proportional to the power content in the central lobe across a wide range of devices with different construction. In contrast, changes to the in-plane structure did not improve beam quality or combining efficiency. Although poor beam quality does correlate with increased optical intensities near the input aperture, locating monolithically-integrated absorption regions in these areas did not lead to any performance improvement. However, large area devices with subsequently improved cooling do achieve higher output powers. Phase noise can limit coherent combining, but this is shown to be small and independent of device design. Overall, tapered amplifiers are well suited for high power coherent combining applications.

_____

1. Introduction

GaAs-based high power diode lasers are key components for commercial laser systems, and continuous improvements in their brightness is sought, in terms of watts of optical output per solid angle of emission [1,2]. Sources with narrow spectral width $\Delta\lambda_{95\%}$ are preferred, for pumping narrow lines, for spectroscopy and sensing applications such as LIDAR, and for later spectral combining via a grating for further enhanced brightness [2]. Coherent combining is a technique that allows the emission from many semiconductor sources to be combined within a single beam, scaling optical output power P_{opt} delivered within a narrow spectral line without degrading beam quality, so has high potential for use in a variety of optical systems [2]. Coherent combining can be performed by actively regulating the phase of each element, as studied here. Alternatively, the phase can be tied together using various passive techniques, as reviewed recently in [3,4]. In previous studies, the authors have shown that single-pass tapered semiconductor amplifiers with $P_{opt} = 4...5$ W can be efficiently coherently combined using active phase control into beams with $P_{opt} > 20$ W, in continuous wave (CW) and quasi-continuous wave (QCW) mode, and used to generate high intensities of green light, using frequency conversion techniques [5,6,7]. These previous studies

primarily focused on developing techniques for the effective coherent combining of tapered amplifiers.

In contrast, we review here the impact of changes in the device design and construction on tapered amplifiers operating close to a wavelength $\lambda = 976$ nm. In studies by other groups, active coherent combining has been successfully performed in large arrays of ridge waveguide amplifiers that are limited to a single optical mode by design, through the use of a well-defined lateral waveguide [8,9]. Such systems are restricted to around 1 W per emitter. In contrast, tapered amplifiers that use various different designs can deliver diffraction limited power $P_{DL} = 5...10$ W in CW mode, $P_{DL} > 15$ W in QCW mode (100 µs) [10] and $P_{DL} > 70$ W for < 10 ps wide pulses [11], enabling higher overall power levels per device, for large reductions in size, complexity and cost. However, tapered amplifiers typically are fabricated with more than 50× larger surface area than a comparable ridge waveguide laser, and do not include any lateral waveguiding, meaning they are potentially more susceptible to the onset of instabilities such as filamentation [12,13] that could lead to phase instability or degraded coherent combining efficiency. In recent studies on modern, low-defect broad area lasers, experimental and theoretical studies find little indication for filamentation playing a significant role in their beam properties [13-16]. Coherent combination is however a more demanding application.

In previous work by the authors on single-pass tapered amplifiers, both higher overall P_{DL} and a higher fraction of nearly diffraction limited emission $\eta_{CL} = P_{DL}/P_{tot}$ was sought, where P_{tot} is the total spatially integrated optical output power. Higher P_{DL} and η_{CL} was achieved by using epitaxial layer designs with low confinement factor in the active region Γ for low modal gain factor Γg_0 and extremely low vertical divergence angle, $\Theta_V^{95\%}$ (with 95% power content) [10,17]. The use of an active region containing low-index quantum barriers (LIQB) was also proposed as being beneficial, as this potentially limits the impact of any variation in refractive index of the active region (due to oscillations in carrier density or temperature) on the propagating field [10]. In addition, devices with larger surface areas were found to achieve higher overall power and hence higher P_{DL} due to their better cooling [10]. Similar results were reported in free-standing tapered lasers [18].

Following these studies, we present here a comparison of the impact of epitaxial layer design and lateral (in-plane) structuring on the performance of tapered amplifiers in coherent combination, for a fixed coherent combination scheme taken from [5,6]. We start with an analysis of the impact of epitaxial layer structure, first quantifying the impact of LIQB on lateral waveguiding in simulation. We then fabricate and test comparable tapered amplifiers using two related epitaxial layer designs, one extremely low divergence (ELoD) design that uses LIQB and one similar reference design without LIQB, and show that the beam quality and coherent combining efficiency in ELoD-based amplifiers is improved. We next analyze the impact of changes in the lateral (in-plane) design for ELoD-based amplifiers, increasing surface area, seeking higher powers (following [10]), and implementing absorber regions around the input aperture (following [19]), seeking improved beam quality and P_{DL}. We then conclude with an overview, showing that the coherent combining efficiency correlates directly to P_{DL}/P_{tot}, independent of vertical and lateral device design. We also show that phase noise is low ($< \lambda/100$), and independent of device design, and does not restrict coherent combining. Overall, tapered amplifiers are confirmed to enable reproducible, stable coherent combining, and hence be suitable sources for future compact, efficient laser systems.

2. Device Configuration

2.1 Vertical epitaxial laser design for CBC

Diode lasers using two different vertical layer designs are compared in this paper, both with operating wavelength close to $\lambda = 976$ nm. A reference design is used, taken from [20], whose active zone, AZ, contains a double InGaAs quantum well with $GaAs_xP_{1-x}$ barriers, where $x = 80\%$. The AZ is located asymmetrically within a 4.8 µm thick $Al_yGa_{1-y}As$ waveguide, where $y = 35\%$. The vertical far field is $\Theta_V^{95\%} = 46°$ and the near field width is $W_{95\%} = 2.19$ µm (at 95% power content) (see Fig. 1 left). The reference design is compared here to a second design with narrower vertical far field, achieved by using a modified vertical waveguide design for extremely low vertical divergence (ELoD) that makes use of low-index quantum barriers LIQB, as described in [21], specifically the higher performance "ELoD2" variant, taken from [22]. The ELoD2 AZ includes a triple InGaAs quantum well separated by $GaAs_xP_{1-x}$ barriers, with $x = 0.66$. The AZ is located asymmetrically within a 4.8 µm thick $Al_yGa_{1-y}As$ waveguide, where $y = 15\%$. The high phosphorus content in

the barriers lowers their refractive index below that of the low-aluminum waveguide, compensating for the high refractive index of the InGaAs wells, and reducing the influence of the AZ on the vertical field, leading to narrower $\Theta_V^{95\%} = 26°$ and $W_{95\%} = 3.05$ µm. The vertical refractive index profile and calculated profile of the first guided optical mode are shown in Fig. 1 for both structures. Total confinement in the AZ is (by design) $\Gamma = 1.95\pm0.1\%$ in both cases, summed across all wells, with the ELoD2 design compensating for the broader near field by adding an extra quantum well.
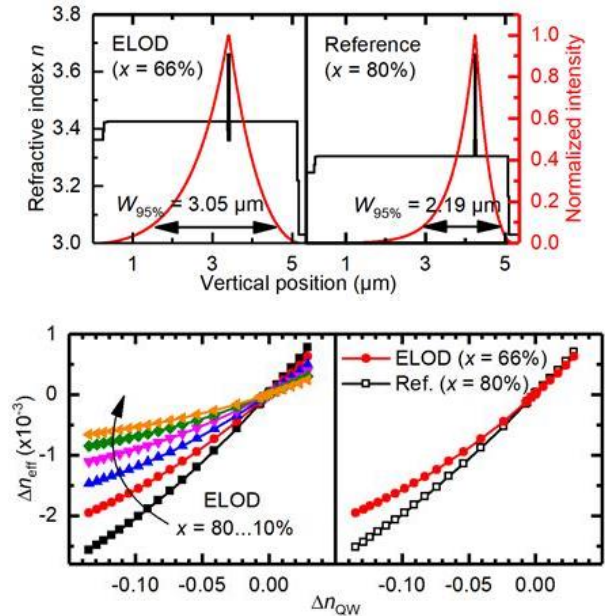

Figure 1. Vertical layer designs. Top: Vertical refractive index as function of vertical position and resulting calculated optical intensity profile of the fundamental mode for the two vertical epitaxial layer designs studied here (ELOD and reference). Bottom: Calculated lateral contrast in effective index arising due to variation in the local refractive index of the quantum well, for ELOD and reference designs. In the case of the ELOD design, calculations are repeated for a variation in the composition of the low-index barrier layers located around the quantum well.

Broad area lasers were fabricated for both vertical layer designs using a simplified wafer process to obtain characteristic parameters, by measuring the variation of threshold and slope from a series of unmounted bars in pulsed mode, following [21]. Values are summarized in Table 1. The characteristic parameters were similar for both designs, with a modal gain parameter $\Gamma g_0 = 21$ cm^{-1} and optical loss $\alpha_i = 0.6$ cm^{-1} for the ELoD2-based lasers and $\Gamma g_0 = 20$ cm^{-1} and $\alpha_i = 0.9$ cm^{-1} for the reference material. These parameters lead to a similar overall single-pass peak gain at transparency (amplifier bias equivalent to $J = J_{transp}$) of $(\Gamma g_0 - \alpha_i)L_a = 8.2$ and 7.6 for an ELoD2 and reference amplifier respectively, for amplifier length of $L_a = 4$ mm. In the following, we assume that de-tuning from gain peak is small and that differences in the gain spectrum due to changes in the active region play no role. Further studies are needed to confirm this assumption.

Both designs show not just comparable peak gain, but also similar internal differential efficiency $\eta_i > 95\%$. However, in contrast, the ELoD2 material has increased transparency current density of $J_{transp} = 220$ A/cm^2, compared to $J_{transp} = 137$ A/cm^2 for the reference material, due to the need to pump three rather than two quantum wells. The lower aluminum concentration in the $Al_yGa_{1-y}As$ waveguide in the ELoD2 structure leads to higher electron and hole mobility

which also reduces the electrical resistance.

As noted in [10], the use of LIQBs will reduce the impact of oscillations in carrier density and temperature in the AZ on the optical field. Following [23], the refractive index n of the AZ varies approximately with temperature at a rate of $dn/dT \sim 2.4 \times 10^{-4}$ K^{-1}, and with carrier density n_c, at a rate of $dn/dn_c \sim 10^{-20}$ cm^3, so that oscillations in local temperature and carrier density of $\Delta T = 40$ K and $\Delta n_c = 10^{18}$ cm^{-3} in the quantum well respectively would lead to oscillations in the refractive index of around $\Delta n_{QW} \sim 0.01$. These oscillations can potentially arise spontaneously in semiconductor amplifiers [12]. Significant local variation in carrier density also occurs due to current spreading and non-clamping at the edges of the injection region, where lateral carrier accumulation is seen in both simulation and measurement [24,25]. We quantify the potential impact of such oscillations on lateral wave guiding here by calculating the vertical effective index n_{eff} of the fundamental mode as a function of the refractive index of the quantum well and Fig. 1 (right) shows the variation in effective index Δn_{eff} as a function of change in refractive index of the quantum well Δn_{QW}, for a well thickness of 8.5 nm. The calculations are repeated for the ELoD2 design for GaAs$_x$P$_{1-x}$ barriers with $x = 10\%...80\%$. Reducing x from 80% (no LIQB effect, black solid squares) to 66% (strong negative step in index, structure "as grown", red solid circles), reduces the impact on Δn_{eff} by around 20% within the simulated range of Δn_{QW}, with $x = 10\%$ reducing the impact around four-fold. The calculation was then repeated for the reference design (with $y = 35\%$ in the Al$_y$Ga$_{1-y}$As waveguide, but the same well thickness) and this is directly compared to the "as grown" ELoD2 design in Fig. 1. The ELoD2 design reduces the impact of variation in quantum well refractive index on Δn_{eff} by around 15% when compared directly to the baseline design. Overall, the ELoD2 design has lower sensitivity to index variations than the baseline and larger vertical near field at the price of higher threshold current. We expect that this should result in a lower sensitivity to beam filamentation in the lateral profile and hence higher beam quality, as will be investigated in the following section.

Layer Design	Modal gain parameter Γg_0 (cm^{-1})	Optical loss, α_i (cm^{-1})	Transparency current density, J_{transp} (A/cm^2)	Single pass net gain at transparency $(\Gamma g_0 - \alpha_i)L_a$ ($L_a = 4$ mm)
Reference	20	0.9	137	7.6
ELoD2	21	0.6	220	8.2

Table 1. *Measured characteristic device parameters and resulting calculated expected single pass net gain at transparency for the two epitaxial layer designs studied here. The measured internal differential efficiency was $\eta_i > 95\%$ in both cases.*

2.2 Lateral (in-plane) tapered amplifier design

Epitaxial wafers to ELoD2 and reference designs were grown using metalorganic vapor phase epitaxy, and processed using standard techniques into tapered amplifiers, following [10,17,20]. The amplifiers included a laterally single mode ridge waveguide input with 4...5 µm ridge width at the rear facet and a separately contacted tapered amplifier section, shown schematically in Fig. 2. The taper has a flare angle in all cases of 6°, and the facets are passivated for high power operation then dielectric coated for front and rear reflectivities $R_F = 0.3\%$ and $R_R = 0.01\%$ respectively (nominal

values based on measured coating layer thicknesses and calculated value of n_{eff}). The baseline lateral design has a taper length $L_a = 3$ mm and a ridge waveguide length of $L_{RW} = 2$ mm. As reported in [19], free-standing tapered lasers with highly reflective rear facets can show improved beam quality and higher η_{CL} when reverse bias absorber sections are included on either side of the ridge section, to suppress intensity in backwards propagating modes. Even when low facet reflectivities are used, the residual backwards propagating field has been predicted to play a role in limiting beam quality [26], especially when it induces bleaching around the ridge waveguide section, hindering its effectiveness as a mode filter. We therefore assess the benefit here of similar absorber sections on the beam quality, resulting coherent combining efficiency and phase noise, monolithically implemented here using highly absorbing Ge-layers that are designed to resonantly absorb any guided mode, using the designs process reported in [27], which has successfully suppressed higher order lateral modes and improved beam quality in high power broad area lasers. These absorbing regions are located 15 µm laterally offset from the ridge section, as shown in Fig. 2, equivalent to the location of the reverse-biased absorbers in [19]. Finally, we assess the benefit of larger surface area tapered amplifiers, increasing L_a to 4 mm for improved cooling and larger single-pass net gain, with reduced ridge waveguide length of $L_{RW} = 1$ mm. The reference amplifiers were solely fabricated with $L_a = 4$ mm and $L_{RW} = 2$ mm. All devices were mounted junction-side up onto an expansion matched CuW (10:90) submount, itself soldered onto a C-Mount, with a CuW (10:90) heat spreader soldered onto the tapered section. The C-mount length was matched in each case to the total device length, to retain reasonable cooling and so that both facets were accessible for experiments in single-pass amplifier configuration.
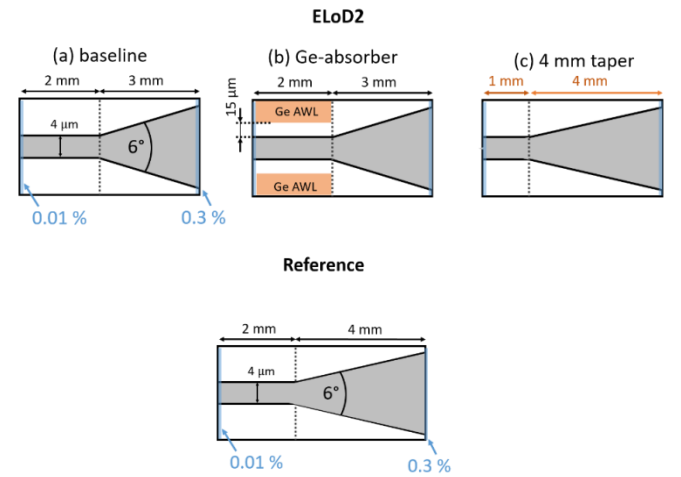

Figure 2. *Schematic overview of the lateral (in-plane) device geometries tested for the ELOD2 epitaxial design*

3. **Comparisons between devices with different vertical and lateral designs**

The tapered amplifiers described in the previous section were investigated experimentally in two steps. The characterization of individual amplifiers is described in this section in terms of optical output power P_{opt} and conversion efficiency *PCE*, beam quality and phase noise properties. Three designs were then chosen for simple coherent beam combining experiments described in section 4. A 976 nm DFB seed laser diode was used as the seed laser for the following amplifier characterizations. The seed wavelength

was consistent and within 10 nm of the peak of the amplified spontaneous emission spectrum, to ensure broadly comparable net gain (the ELoD2 material had ~ 9 nm shorter gain wavelength). The optical isolation and optics used for coupling and collimation were identical to those used in the coherent beam combining setup which is described in detail in section 4

3.1 Optical output power and conversion efficiency

The electro-optic characteristics of the two investigated epitaxial structures are shown in Fig. 3, for ridge waveguide current of $I_{rw} = 400$ mA and seed power of $P_{in} = 15\text{-}20$ mW (sufficient for saturation). Both devices have a $L_a = 4$ mm long tapered section. We define PCE here in terms of the total output power and the current I_{tp} and voltage V_{tp} for the tapered amplifier section, $PCE = P_{opt} / (I_{tp} \times V_{tp})$. We neglect the contributions of the seed laser and ridge waveguide section, as the power consumed here is small by comparison (< 5% of total). The optical output power of the reference device was higher than for the ELoD2 amplifier and reached 6.5 W at taper current of $I_{tp} = 10$ A ($PCE_{max} \approx 36\%$ at $I_{tp} = 6$ A). The higher transparency current density for the ELoD2 amplifier (cf. section II.A) leads to an increased turn-on current of the amplifier, which was in the order of 2.5 A for the 4 mm long tapered section device. It results in a reduced optical power of 5.5 W at $I_{tp} = 10$ A and reduced efficiency ($PCE_{max} \approx 30\%$ at $I_{tp} = 9.5$ A) when compared to the reference design. The series resistance was however slightly reduced, as evidenced by a slightly lower voltage at high drive currents (cf. section II.A). The slope efficiency was in the order of 0.7 W/A for both epitaxial designs for taper bias up to $I_{tp} = 10$ A.
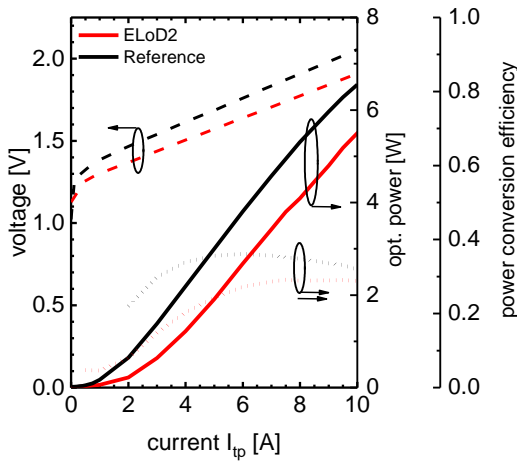

Figure 3. *Measured CW 20°C taper voltage (dashed lines), optical output power (solid lines) and conversion efficiency (dotted lines) as a function of taper current under fixed injection conditions ($P_{in} = 15 - 20$ mW [saturation], $I_{rw} = 400$ mA) for reference (black) and ELoD2 (red) tapered amplifiers with $L_a = 4$ mm.*

The electro optic characteristics for ELoD2 amplifiers with the three different lateral (in plane) device configurations are shown in Fig. 4. Devices with the shorter ($L_a = 3$ mm) tapered section (baseline and Ge-absorber) showed a low turn-on current in the order of $I_{tp} = 1.5$ A and a slightly higher power conversion efficiency when compared to the device with $L_a = 4$ mm. The maximal output power for the baseline design configuration was however limited to 4.4 W by the onset of a thermal rollover at $I_{tp} = 8$ A. The device configuration with the monolithically integrated Ge-absorber layers suffered from an early thermal rollover at $I_{tp} = 6$ A attributed to additional losses in the RW section, comparable to those seen in preliminary studies of narrow stripe lasers with Ge-absorber layers [18]. The 4 mm taper device

configuration showed the most stable electrooptic characteristics and enabled 6.6 W output power at $I_{tp} = 12$ A. Indeed the increased area of the tapered section reduces the thermal resistance of the device by a factor of about 40%, and decreases its electrical series resistance too as can be seen on the V(I) evolution. Thus the $L_a = 4$ mm taper section device can be considered as the most favorable ELoD2 configuration for achieving highest CW powers.

3.2 Investigation of the beam quality

The fast axis (FA, vertical) beam quality was nearly diffraction limited for all designs with $M^2_{4\sigma} < 1.3$. The slow axis (SA, lateral, in the plane of the amplifier) beam quality of the different amplifier configurations was investigated using ISO-compliant caustic measurements (second order moments beam diameter) to determine the $M^2_{4\sigma}$ beam propagation factors and the central lobe power content η_{cl}. at Specifically, the central lobe power content was determined by fitting an ideal Gaussian intensity profile to the measured intensity profile at waist (2D analysis) and inferring its power content P_{Gauss} at a given P_{opt}, to derive $\eta_{cl} = P_{Gauss}/P_{opt}$.
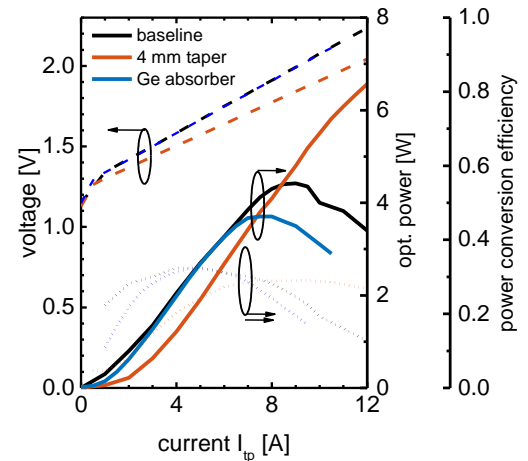

Figure 4. *Measured CW 20°C taper voltage (dashed lines), optical output power (solid lines) and conversion efficiency (dotted lines) as a function of taper current under fixed injection conditions ($P_{in} = 20$ mW [saturation], $I_{rw} = 400$ mA) for ELoD2 tapered amplifiers with baseline (black), 4 mm taper (red) and Ge-absorber lateral geometry (cf. Fig. 2).*

The variation in spatial quality in the horizontal direction (slow axis, SA) for the various amplifier designs is summarized in Fig. 5 for an example bias current in the tapered section $I_{tp} = 5$ A, which is the highest current before thermal rollover effects start to become important. The beam profile for an exemplary single emitter is shown in Fig. 5, and mean and standard deviation values are given for the beam quality parameters (M^2 and η_{CL}) taken from several emitters of the same design. The reference design amplifier showed good beam quality with only minor side-lobes at waist, for $\eta_{cl} = 73\%$. The most favorable beam quality at this bias point was achieved with the ELoD2 baseline and $L_a = 4$ mm taper design configurations although as will be shown later, the beam quality of ELoD2 amplifiers with $L_a = 3$ mm and 4 mm was broadly comparable. In these ELoD2 structures, the central lobe power content was > 84% and the ISO-compliant beam propagation factor was in the order of 3.5 - 4.0 in SA, which are excellent values for tapered amplifiers [10,17] and significantly better than the beam quality achievable with the reference epitaxial design. The design variant including Ge absorber layer showed however poor beam quality in SA with significant side-lobes, appreciably increased beam

propagation factor and low central lobe power content. From this comparative study it seems that the monolithically integrated Ge-absorber region deteriorated the beam quality of the tapered amplifier. This conclusion contradicts previous results obtained in both broad area lasers [18,26] and in free-standing tapered lasers including absorbing regions located on either side of the stripe, that have proven to improve the beam quality of such devices [19].

In order to understand this discrepancy, we experimentally investigated the operation of the RW mode filter in our tapered amplifiers. The RW section is actually critical as its role consists in both pre-amplification of the low-power input signal, and in mode filtering. One known

reflected at the output facet (AR coating $R_f = 0.3\%$) have the potential to excite higher-order modes in the ridge, for degraded overall beam quality.

Figure 5. *Measured CW 20°C optical intensity as a function of lateral position for images of the lateral beam at the slow-axis waist, for all device configurations assessed (Fig. 2). Central lobe power content and beam propagation factors are noted, consistent operating conditions are used ($I_{tp} = 5 A$, $P_{in} = 15\text{-}20 mW$ [saturation], $I_{rw} = 400 mA$). A normalized lateral length-scale is used, where w_0 corresponds to the $1/e^2$ radius of the central lobe.*

In order to investigate this hypothesis, we made an image of the rear facet of an ELoD2 device with $L_a = 4$ mm taper under
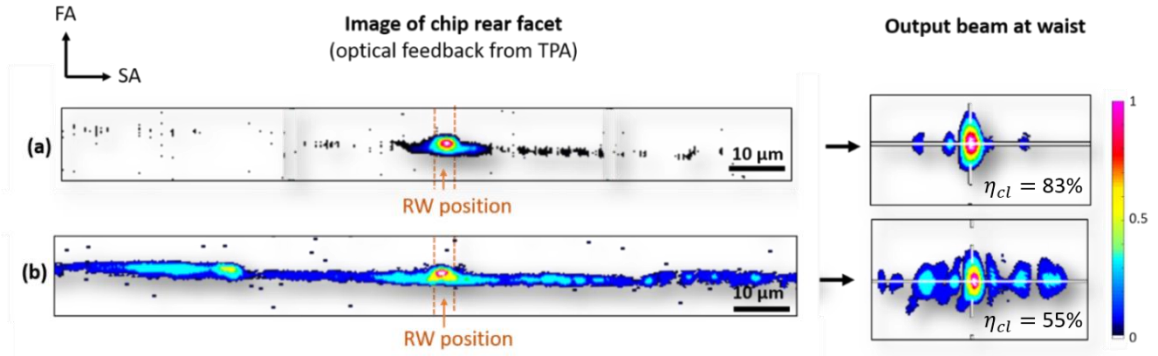

Figure 6. *Measured spatial distribution of the optical feedback and corresponding output beam at waist (astigmatism corrected) for a normally pumped RW section ($I_{rw} = 400 mA$), see (a), and an under-pumped RW section ($I_{rw} = 300 mA$), see (b). Operating conditions: $I_{tp} = 12 A$, $P_{in} = 20 mW$, $T = 20°C$. An ELoD2 tapered amplifier (4 mm taper design variant) was used. The measurements were taken with identical gain and integration time of the CCD sensor, with intensity normalized and presented as a linearly-scaled false color plot.*
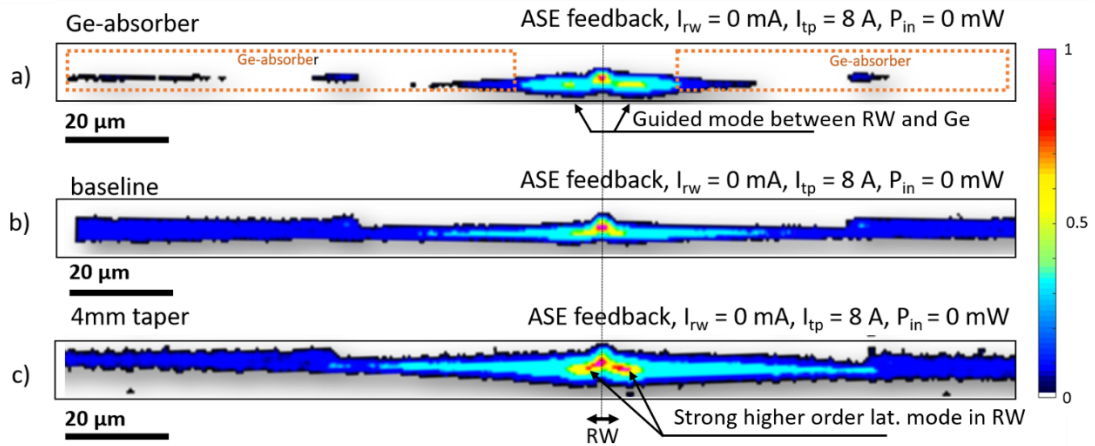

Figure 7. *Measured spatial distribution of the optical intensity at the chip rear facet, with backwards propagating ASE from the tapered front region used to excite guided modes around the ridge waveguide ($P_{in} = 0 mW$, $I_{tp} = 8 A$ QCW 2 ms 10 Hz, $I_{rw} = 0 mA$ and $T = 20°C$) for three different lateral designs of the ELoD2 tapered amplifier: (a) Ge-absorber, (b) baseline and (c) 4 mm taper (cf. Fig. 2). The measurements were taken with identical gain and integration time of the CCD sensor, with intensity normalized and presented as a linearly-scaled false color plot.*

explanation for beam quality degradation effects in tapered lasers is the influence of parasitic round-trip effects in the amplifier leading to a dysfunction of the RW mode filter [24-26]. Such parasitic round trip effects can be effectively suppressed by implementing absorber regions on either side of the ridge [16]. Alternatively, DBR gratings can be implemented in the ridge section (to provide the rear-facet optical feedback for round-trip operation) and then anti-reflection coating applied to the rear facet, which strongly suppresses the parasitic-backwards propagating field. It is proposed that the backwards propagating field remains a significant limit to beam quality in single pass-tapered amplifiers [26]. In this case, the backwards propagating amplified spontaneous emission (ASE) field and the field

different injection currents into the RW section. Simultaneously we measured the beam profile of the amplified beam at waist. If the RW mode filter works effectively, we would expect the optical feedback signal (at the rear facet) to have a (close-to) Gaussian beam profile corresponding to the fundamental mode guided by the ridge waveguide. This occurs only at the highest injection current $I_{rw} = 400$ mA (as illustrated in the experimental data shown in Fig. 6), when the beam quality at the output facet is close to the diffraction limit with high central lobe power content. In contrast, at a lower injection current the optical field spreads over tens of micrometers on both sides of the ridge section, correlating to a poor beam quality of the amplified output beam from the front facet, with multiple side-lobes at

waist leading to decreased central lobe power content. This spatial distribution of the optical power on the rear facet of the chip attests that the passive (unbiased) absorbing regions on either side of the RW mode filter are bleached and do not function as an effective filter. It remains however unclear at this point if the observed filter dysfunction is the cause or the effect of the distorted output beam quality

The various lateral designs of the ELoD2 tapered amplifiers available in this study (cf. Fig. 2) allow the mode filtering properties of the RW section to be further investigated. To this end, the spatial distribution of the beam profile at the rear facet was measured for an un-biased ridge, without using a seed laser ($I_{rw} = 0$ mA, $P_{in} = 0$). The tapered section was driven under QCW (2 ms, 5 Hz) conditions at moderate current $I_{tp} = 8$ A (Figure 7), with the backward propagating optical field effectively used to excite the guided modes in the ridge waveguide region. The resulting optical fields are shown in Fig. 7. For both the baseline ($L_a = 3$ mm, Fig. 7b) and the $L_a = 4$ mm taper designs (Fig. 7c), the backward ASE is widely spread at the rear facet, far away from the ridge waveguide and the passively absorbing regions around the RW section are strongly bleached. The $L_a = 4$ mm taper design, with a shorter ridge section and a larger gain volume, delivers a higher ASE-level into the ridge waveguide section, leading to a higher-order lateral mode to be excited (with two lobes), confirming that high levels of backward feedback can degrade the beam in the ridge section, a known cause of poor overall beam quality.

Repeating the same test on devices with Ge-absorber layers clarifies why these devices do not show better overall beam quality. The Ge-absorber layers very effectively absorb the backward propagating ASE across the entire region where they are located (the absorber starts ± 15 μm laterally offset from the RW), and no optical intensity is observed there (see Fig. 7a), in striking contrast to the baseline structure (Fig. 7b). However, an extra laterally two-lobed optical feature is seen in the region between Ge and RW (labelled). We propose that this is either a higher order mode of the RW or an additional or a deformed guided mode naturally arising due to coupling between the Ge-region (with large imaginary refractive index) and the RW. Either effect will degrade the beam quality of the overall system. If the guided modes in the RW are deformed by the use of a Ge-absorber, then high bias of the RW will only have limited benefit on beam quality. Therefore, although the implementation of a Ge-absorber region very effectively suppresses the backward propagating field, we propose that in the process, the modes guided around the ridge are themselves degraded, leading to poor overall beam quality. Further measurements and simulations would be needed to fully confirm this. Overall, changes in the vertical structure strongly improved the beam quality, attributed to a suppression of filamentation in the tapered section. In contrast, the assessed changes to the lateral structure did not bring any improvement in beam quality, but did help clarify one key additional source of beam degradation – namely, the onset of higher order modes around the ridge section.

3.3 Investigation of the phase noise

Operation with low phase noise is essential to achieve and sustain high coherent combining efficiency. Therefore, the phase noise was investigated by injecting a 976 nm seed laser in a simple Mach-Zehnder interferometer, where a tapered amplifier was placed in one arm and a quarter-wave plate was placed in the other arm. In-phase and quadrature

components can then be separated at the output of the interferometer allowing the relative phase drift $\Delta\varphi(t)$ of the two arms in the interferometer to be determined [29]. Figure 8 shows the amplifiers integrated phase noise spectrum $S_\varphi(f) = \sqrt{\int_f^{10\ kHz} PSD_\varphi(f)\ df}$, where $PSD_\varphi(f)$ is the one-sided power spectral density of the measured relative phase drift. A reference measurement, where the tapered amplifier was removed is shown and allows us to determine the phase noise of the external optical setup. The overall noise level is low, dominated by frequencies below 10 Hz and overall comparable to the phase noise in low power single mode ridge waveguide amplifiers [29]. The contribution of the tapered amplifier was in the order of $\lambda/100$ (integrated from 0.1 Hz to 10 kHz), which is extremely low and can be almost entirely attributed to the temperature stability of the active temperature control (Arroyo 52400 TEC: $\Delta T < 0.01\ K$). Differences within the different vertical and lateral amplifier designs were in the order of the measurement precision and there was no evidence for an influence of the device design on the measured phase noise in our study. Note that measurements were done in a well-controlled laboratory environment with minimal influence of external noise sources and that the noise in the interferometer itself may overlay the actual phase noise in the amplifier in other less protected environments. In conclusion one can say that high power tapered amplifiers contribute only marginally to the phase noise in the experimental setup, and any impact of device construction was below measurement accuracy and not significant for device operation. Simple phase control methods with a bandwidth in the order of 100 Hz are more than sufficient to correct the residual phase fluctuations. One straightforward way for phase control in tapered amplifier is an active feedback on the current into the RW of the amplifier as previously demonstrated in [3,5], which was also used in the coherent beam combining experiments discussed below.
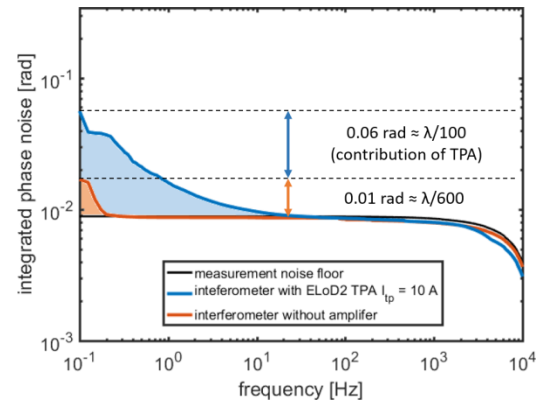

Figure 8. *Integrated phase noise as function of frequency. Interferometer with tapered amplifier (ELoD2, 4 mm taper config., $I_{tp} = 10$ A, $I_{rw} = 400$ mA, $P_{in} = 20$ mW) in blue. Reference measurement without amplifier in orange. Measurement noise floor in black.*

4. Coherent beam combining of high brightness amplifiers

The experimental setup used to compare the different amplifier designs in a simple coherent beam combining setup is shown in Fig. 9 and consists of a two-arm Mach-Zehnder interferometer. A narrow linewidth DFB laser ($\lambda = 976$ nm, short-time linewidth $\Delta\nu_{10\mu s} < 20$ MHz, $P_{out} = 100$ mW) optically isolated by a double stage Faraday isolator (60 dB optical isolation) was used as the master oscillator. The beam

was split and recombined by a standard nonpolarising 50:50 beamsplitter. Each amplifier was mounted on a temperature controlled baseplate which supported also the optics for injection into the RW (cf. L_2), and collimation in FA and SA (cf. L_3 and L_4). Phase control was achieved by active feedback of the current into the ridge waveguide of one amplifier using a simple hill-climbing algorithm, with I_{rw} = 300-400 mA. The experimental setup was similar to our previously published work on coherent beam combining of tapered amplifiers [5,6]. In this work, the focus lay on the investigation of factors limiting the combining efficiency (defined as $\eta_{CBC} = \frac{P_{CBC}}{P_1+P_2}$) by measuring η_{CBC} with the different amplifier configurations. The combining efficiency of two coherent beams is also linked to the spatial overlap factor of the two fields. Beam quality degradation effects lead to non-ideal overlap of the beams and to combining losses [28]. Amplifiers with improved spatial properties enable an improved overlap of the fields, which was experimentally studied here.
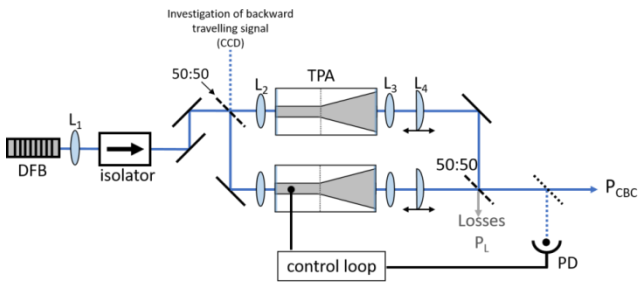

Figure 9. Simplified schematic of the experimental setup. L_1 and L_2: aspherical lens f = 8 mm, NA = 0.55; L_3: aspherical lens f = 2.3 mm, NA = 0.55; L_4: cylindrical lens f = 19 mm. PD: Photodiode, TPA: tapered semiconductor optical amplifier. The control loop was implemented using a microcontroller.

The combining efficiency was characterized experimentally at different current levels for tapered amplifiers with the reference epitaxial layer structure and the ELoD2 epitaxial structure. Two lateral design variations were tested for the ELoD2 amplifiers (L_a = 3 mm and 4 mm, devices with Ge-absorber omitted due to poor performance). The results are summarized in Fig. 10 for the reference epitaxial structure design (black) with the 4 mm-long lateral tapered geometry, the ELoD2 baseline (blue) and the EloD2 4 mm taper design (red). The reference design enabled high combined output power (~ 10 W at 10 A) but with a moderate combining efficiency (76% at 8 A) that is attributed to the moderate beam quality of the individual amplifiers.
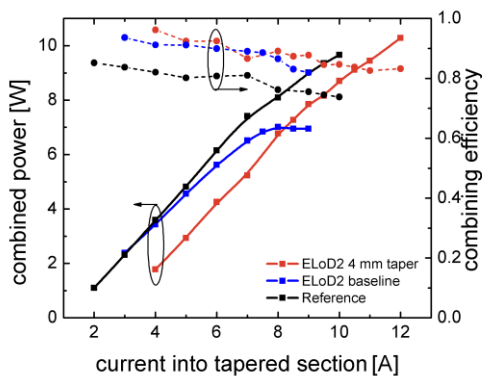

Figure 10. Measured CW 20°C combined output power (solid lines) P_{CBC} and corresponding combining efficiency η_{CBC} (dotted lines) for CBC of two single-pass tapered amplifiers. Black: Reference structure; Blue: ELoD2 baseline geometry; Red: ELoD with L_a = 4 mm, under fixed injection conditions (P_{in} = 20 mW [saturation], I_{rw} = 300-400 mA)..

In contract, Fig. 10 also shows that the EloD2 amplifiers allow more efficient coherent beam combining with η_{CBC} > 84% at 8 A and η_{CBC} ~ 100% at low currents. No significant difference in combining efficiency was observed for the two different lateral amplifier designs assessed. The ELoD2 devices with baseline taper design (L_a = 3 mm) enables output power comparable to the reference design at low drive currents (I_{tp} < 8 A), the power then however saturated as this amplifier design was limited by an early thermal rollover (cf. Fig. 10). The coherently combined power did not plateau for the 4 mm taper design as expected from the amplifier P(I) curve in Fig. 4. The highest combined power of 10.2 W was thus reached with this taper design, in spite of it having the highest turn-on current (largest contact area, high transparency current). It is noteworthy that for both vertical designs the maximum power for coherent beam combining of two amplifiers was similar, but the ELoD2 design achieved 10% higher combining efficiency across the full measured range.

The combining efficiency η_{CBC} is next plotted as a function of the relative central lobe power content η_{cl} of one of the two combined beams as shown in Fig. 11, corresponding to the measurements in Fig. 10 (η_{CL} is within 3% for the ELoD2 TPAs and for the reference TPAs, so the choice of emitter does not affect the figure). All test data falls onto a single line. Overall, the higher η_{CBC} observed for the ELoD2 tapered amplifiers is solely due to their improved beam quality. Epitaxial design changes, lateral structure changes and changes in device operating condition in this study only affect η_{CBC} to the extent that they influence the beam quality, quantified using η_{CL}. Nonetheless the overall system efficiency $\eta_{tot} = PCE \times \eta_{CBC}$, taking into account the power conversion efficiency (PCE) of the amplifiers and the combining efficiency, is similar for both the reference (24% at 10 A) and ELoD2 designs (23% at 10 A).
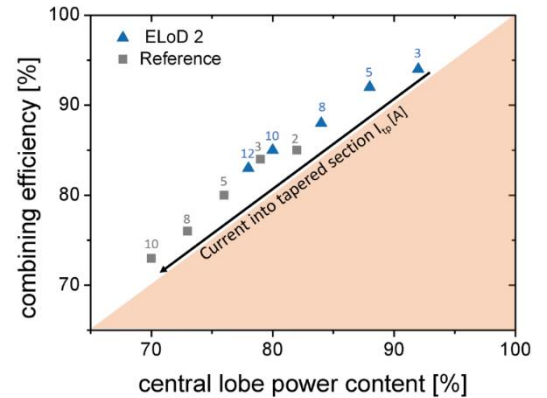

Figure 11. Measured combining efficiency η_{CBC} as a function of the central lobe power content η_{CL}. Reference epitaxial structure in gray and ELoD2 4 mm taper design variant in blue, for results taken from Fig. 11. The corresponding drive current into the tapered section is given in Ampere for each data point.

5. Conclusions and next steps

A study was presented into the impact of semiconductor device design on coherent combining in high power single pass tapered amplifiers operating around λ = 975 nm. The coherent combining efficiency η_{CBC} was shown to be limited by the beam quality of the amplifier used, with device design and operation mode only relevant to η_{CBC} to the extent that they affect the proportion of power in the diffraction limited central lobe, η_{CL}. Comparison of two epitaxial layer designs

shows that ELoD2 structures with extremely low vertical divergence achieve around 10% higher η_{CL} and hence η_{CBC} than a reference design. The improved η_{CL} is proposed as being primarily due to the use of low index quantum barriers, which reduce the impact of variations in the refractive index of the active region on lateral waveguiding. A comparison of lateral taper designs did not lead to increased brightness but did clearly indicate that a high quality single-mode input beam is required, and that any effects that compromise this (for example, onset of higher order modes triggered by back-coupled ASE, or beam deformation triggered by the introduction of highly lossy mode filters) directly degrade η_{CL} and hence η_{CBC}. Phase noise was shown to be low, semiconductor device structure independent (within measurement accuracy), and in no way a limit to coherent combining.

Power per device could be increased by improving thermal resistance (larger area device) or increasing conversion efficiency. Overall, high powered tapered amplifiers were confirmed to be stable, reproducible and robust sources, suitable for use in coherent combining. The high level of stability and reproducibility observed is anticipated to allow coherent combining to be used as a power-scaling tool in many systems, especially those where overall conversion efficiency is not a key factor. Further increases in coherently combined power per device and wider exploitation are expected if the role of the active region in waveguiding can be further suppressed (higher η_{CL}), if the single mode input section can be more thoroughly protected from the onset of higher order modes (higher η_{CL}), and if higher conversion efficiency and improved cooling can be achieved (higher power).

Acknowledgments

References

[1] P. Crump et al. 2019 in *Advances in High-Power Fiber and Diode Laser Engineering*, The Institution of Engineering and Technology, ISBN 978-1-78561-751-5, Chapter 5

[2] T. Y. Fan 2005 *IEEE J. Sel. Top. Quant. Electron.* **11**(3) 567

[3] G. Lucas et al. 2019 in *Advances in High-Power Fiber and Diode Laser Engineering*, The Institution of Engineering and Technology, ISBN 978-1-78561-751-5, Chapter 2

[4] D. V. Vysotsky and A. P. Napartovich 2019 *Quantum Electron.* **49**(11) 989-1007

[5] P. Albrodt et al. 2019 *Opt. Express* **27**(2) 928-937

[6] P. Albrodt et al. 2019 *Opt. Express* **27**(20) 27891

[7] G. Schimmel et al. 2017 Proc. SPIE **10086** 100860O-1

[8] K. J. Creedon et al. 2012 *Optics letters* **37** 5006–5008

[9] S. M. Redmond et al. 2011 *Optics letters* **36**, 999–1001

[10] X. Wang et al. 2013 *IEEE Photon. Techn. Lett* **25**(2) 115

[11] H. Wenzel et al. 2012 Proc. SPIE **8241** 82410V1

[12] R. J. Lang et. al 1993 *Appl. Phys. Lett.* **62**(11) 1209

[13] M. Winterfeldt et al. 2015 *Proc. IEEE Photonics Conf. Reston VA USA* 567-568

[14] P. Crump et al. 2016 *Proc. SPIE* **9767** 97671L

[15] A. Zeghuzi et al. 2019 *IEEE J. Sel. Top. Quantum Electron.* **25**(6), 1502310

[16] A. Zeghuzi et al. 2019 *IEEE J. Quantum Electron.* **55**(2) 2000207

[17] X. Wang et al. 2012 *Semicond. Sci. Technol.* **27** 015010

[18] P. Crump et al. 2015 *Proc. SPIE* **9348** 93480D

[19] C. Fiebig et al. 2009 *IEEE Photon. Technol. Lett.* **21**(23) 1755

[20] C. Fiebig et al. 2008 *Electron. Lett.* **44**(21) 1253

[21] P. Crump et al. 2010 *Appl. Phys. Lett.* **96** 131110

[22] P. Crump et al. 2013 *Proc. SPIE* **8605** 86050T

[23] A.I. Bawamia et al. 2009 *Appl. Phys. B* **97** 95–101

[24] S. Bull et al. 2006 *IEE Proc.-Optoelectron.* **153**(1) 2

[25] J. J. Lim et al. 2009 *IEEE J. Sel. Top. Quant. Electron.* **15**(3) 993.

[26] M. A. Helal et al. 2017 in *Handbook of Optoelectronic Device Modeling and Simulation* CRC Press 81-108

[27] H. Wenzel et al. 2013 *IEEE J. Quant. Electron.* **49**(12), 1102

[28] G. Goodno et al. 2010 *Opt. Express* **18** 25403-25414

[29] R. K. Huang et al. 2009 *Proc. SPIE* **7230**, 72301G

Résumé de la thèse en français

Combinaison cohérente d'amplificateurs optiques à semi-conducteurs à section évasée

Des sources laser à semiconducteur avec une forte luminance sont requises pour de nombreuses applications directes et indirectes. L'augmentation de la puissance émise au-delà des limitations liées aux seuils de dommage se fait par des techniques de combinaison. La combinaison cohérente permet d'augmenter la puissance tout en préservant les propriétés physiques des émetteurs individuels et est donc le concept idéal pour l'augmentation de la luminance. Les amplificateurs optiques avec une section évasée permettent d'atteindre des puissances élevées par émetteur tout en gardant une bonne qualité spatiale et sont donc très bien adaptés pour l'augmentation de la luminance par combinaison cohérente. L'objectif de ce travail est le développement d'architectures simples et robustes pour la combinaison cohérente d'un petit nombre d'émetteurs de forte luminance.

Les travaux de cette thèse s'inscrivent dans le cadre d'une collaboration entre le groupe Laser du Laboratoire Charles Fabry (Université Paris-Saclay) et le High Power Diode Lasers Lab – Ferdinand-Braun-Institut (Leibniz Institut für Höchstfrequenztechnik, Berlin, Allemagne).

Le manuscrit contient une introduction générale, quatre chapitres, une conclusion générale et une annexe.

Le **chapitre I** couvre tous les aspects fondamentaux utiles pour cette thèse, ainsi que l'état de l'art des émetteurs semi-conducteurs de forte luminance et la combinaison cohérente.

Le **chapitre II** commence par une analyse théorique des faisceaux légèrement multimodes typiques pour les amplificateurs à section évasées. Puis, différents schémas d'amplificateurs à section évasée, développés et fabriqués par le Ferdinand-Braun-Institut, sont évalués dans le contexte de la combinaison cohérente.

Le **chapitre III** résume les résultats expérimentaux de différentes expériences de combinaison cohérente à forte puissance en régime continu. Les paramètres ayant une influence importante sur l'efficacité de combinaison sont analysés en détail. La proportion de puissance dans le lobe central est identifiée comme un paramètre clé pour assurer une superposition cohérente de bonne efficacité. Le système développé se compare de manière avantageuse à d'autres expériences de combinaison cohérente de diodes laser en termes de complexité et de stabilité du dispositif expérimental. L'intérêt de la combinaison cohérente pour des applications nécessitant de fortes luminances est démontré par une augmentation de l'efficacité non-linéaire dans le cadre d'une expérience de doublement de fréquence. De plus, des architectures modulaires et compactes avec une très bonne stabilité sont développées et caractérisées.

Le **chapitre IV** contient une analyse d'expériences similaires menées en régime impulsionnel. Dans un premier temps, le fonctionnement en régime quasi-continu (QCW) avec une durée d'impulsions de l'ordre de la milliseconde est étudié. Le régime QCW permet de réduire la charge thermique dans les amplificateurs pour faire fonctionner les amplificateurs à très fort courant. Cependant le fonction-

nement en QCW conduit aussi à des effets dynamiques au début des impulsions, tels qu'une dynamique spatiale du faisceau et une dynamique temporelle du piston de phase. Ces phénomènes causent, entre autres, des effets parasites avec une influence importante sur la stabilité des impulsions. La combinaison cohérente de quatre amplificateurs est démontrée pour la première fois à très forte puissance et conduit à une puissance optique de 23 W dans un faisceau présentant une très bonne qualité spatiale. Cette valeur est un record en terme de puissance optique pour une architecture basée sur la combinaison cohérente d'amplificateurs semi-conducteurs à section évasée. Le chapitre IV contient aussi une étude préliminaire de la combinaison cohérente avec des impulsions plus courtes (durée des impulsions dans l'ordre de la microseconde, donc environ trois ordres de grandeurs plus courtes qu'en QCW).

Tous les résultats expérimentaux sont regroupés dans la **conclusion** et mis en contexte avec l'état de l'art, et les perspectives pour la suite de ces travaux de thèse sont mis en avant. L'**annexe** contient une description de l'algorithme de mise en phase.

Titre : Combinaison cohérente d'amplificateurs optiques à semi-conducteurs à section évasée

Mots clés : Combinaison cohérente, diodes lasers à forte luminance

Résumé Des sources laser à semiconducteur avec une forte luminance sont requises pour de nombreuses applications directes et indirectes. L'augmentation de la puissance au-delà des limitations liées aux seuils de dommage se fait par des techniques de combinaison. La combinaison cohérente permet l'augmentation de la puissance tout en préservant les propriétés physiques des émetteurs individuels et est donc le concept idéal pour l'augmentation de la luminance. Les amplificateurs optiques avec une section évasée permettent d'atteindre des puissances élevées par émetteur tout en gardant une bonne qualité spatiale et sont donc les émetteurs idéaux pour l'augmentation de la luminance par combinaison cohérente.

L'objectif de ce travail est le développement d'architectures simples et robustes pour la combinaison cohérente d'un petit nombre d'émetteurs de forte luminance.

Différents designs d'amplificateurs à section évasée, développés et fabriqués par le Ferdinand-Braun-Institut (Berlin, Allemagne) dans le cadre d'une collaboration de recherche, sont évalués dans le contexte de la combinaison cohérente. La combinaison cohérente à forte puissance est étudiée en détail et démontrée en régime continu et impulsionnel. Le système développé, avec une puissance maximale de 23 W dans un faisceau présentant une qualité spatiale très élevée, se compare de manière avantageuse à d'autres expériences de combinaison cohérente de diodes laser.

L'intérêt de la combinaison cohérente pour des applications nécessitant de fortes luminances est démontré par une augmentation de l'efficacité non-linéaire dans le cadre d'une expérience de doublement de fréquence. De plus, des architectures modulaires et compactes avec une très bonne stabilité sont développées et caractérisées.

Title : Coherent beam combining of high brightness tapered semiconductor optical amplifiers

Keywords : Coherent beam combining, high brightness diode lasers and amplifiers

Abstract Compact and efficient high-brightness semiconductor laser systems are demanded for direct and indirect applications. Power scaling beyond the limitations of material damage threshold requires combining multiple beams from independent emitters. Unlike other beam combining techniques, coherent beam combining (CBC) allows power and brightness scaling while maintaining all physical properties of the individual emitters and is therefore the ideal approach for brightness scaling. As they provide high powers with good beam quality, semi-conductor tapered lasers and amplifiers are a good starting block for power and brightness scaling in coherent beam combining setups

This work targets the development of simple and robust coherent beam combining setups based on a few high power tapered amplifiers with optimized design.

Different amplifier designs developed and fabricated within the framework of common research activities with the Ferdinand-Braun-Institut (Berlin, Germany) are investigated in details and tested in coherent beam combining architectures. Both continuous wave and pulsed quasi-continuous wave CBC is demonstrated and investigated at high powers. The achieved maximum power (23 W in QCW) in a nearly diffraction limited beam compares favourably to previous work on CBC with semiconductor emitters.

The usefulness of CBC for applications requiring high brightness is demonstrated by an increased nonlinear conversion efficiency in single pass SHG setups. Furthermore, the work also targets the development of integrated modular setups with reduced footprint and improved stability.